Preparation of a TiO2 porous layer by molding of polymer beads for perovskite solar cells application

Kubra Yasaroglu Yasaroglu Unal

UNIVERSITÉ DE STRASBOURG
FREIBURG UNIVERSTÄT

ECOLE DOCTORALE pcp

École Doctorale de Physique et Chimie-Physique (ED182)

Institut de Physique et Chimie des Matériaux de Strasbourg (UMR 7504-CNRS)

Fraunhofer ISE - Institüt für Solar Energy system (Freiburg, Allemagne)

THÈSE présentée par :

Kubra YASAROGLU UNAL

soutenance prévue le: **18 novembre 2019**

pour obtenir le grade de : **Docteur de l'Université de Strasbourg et de l'Université de Freiburg**

Discipline/ Spécialité: Ingénierie des Matériaux et Nanoscience

Préparation de couches poreuses de TiO_2 par moulage de billes de polymères pour des applications dans des cellules solaires à base de pérovskites

THÈSE dirigée par:

M. Aziz DINIA	Professeur, Université de Strasbourg, France
M. Stefan GLUNZ	Professeur, Université de Freiburg, Allemagne

MEMBRES RAPPORTEURS:

Mme Mónica LIRA-CANTÚ	Professeur, IC2N, Barcelone, Espagne
M. Guillaume WANTZ	Maitre de conférences, ENSCB, Bordeaux, France

---

MEMBRES EXAMINATEURS:

M. Jean-Luc REHSPRINGER	Directeur de recherche (DR2), IPCMS CNRS, Strasbourg, France
M. Andreas HINSCH	Chargé de recherche, Fraunhofer ISE, Freiburg, Allemagne
M. Saliba MICHAEL	Professeur, Technische Universität, Darmstadt, Allemagne

MEMBRES INVITES:

Mme Anne HEBRAUD	Maitre de conférences, ICPEES CNRS, Strasbourg, France
M. Simone MASTROIANNI	Chercheur, Fraunhofer ISE, Freiburg, Allemagne

English title:

Preparation of a TiO_2 Porous Layer by Molding of Polymer Beads for Perovskite Solar Cells Application

“I have no doubt that we will be successful in harnessing the sun's energy… If sunbeams were weapons of war, we would have had solar energy centuries ago.”

Sir George Porter (1973)

Remerciements

A l'issue de la rédaction de ce travail de recherche, je suis convaincue que la thèse est loin d'être un travail solitaire. En effet, je n'aurais jamais pu réaliser ce travail doctoral sans le soutien d'un grand nombre de personnes dont la générosité, la bonne humeur et l'intérêt manifestés à l'égard de ma recherche m'ont permis de progresser dans cette phase délicate de « l'apprenti-chercheur ».

En premier lieu, je tiens à remercier mes directeurs de thèses, professeur Aziz Dinia de l'Université de Strasbourg et professeur Stefan Glunz de l'Université de Freiburg, pour la confiance qu'ils m'ont accordée en acceptant d'encadrer ce travail doctoral ainsi que pour leurs multiples conseils et pour toutes les heures qu'il a consacrées à diriger cette recherche.
Je remercie également Monica Lira Cantu et Guillaume Wantz m'ont fait l'honneur d'être rapporteurs de ma thèse, ils ont pris le temps de m'écouter et de discuter avec moi avec une grande gentillesse. Leurs remarques constructives m'ont permis d'envisager mon travail sous un autre angle. Pour tout cela je les remercie.
Je tiens à remercier Michael Saliba, Andreas Hinsch, Jean-Luc Rehspringer, Anne Hebraud et Simone Mastroianni pour avoir accepté de participer à mon jury de thèse et pour leur participation scientifique ainsi que le temps précieux qu'ils ont consacré à ma recherche.
Je remercie encore tous ces membres pour l'honneur qu'ils m'ont fait d'être dans mon jury de thèse.

Concernant le travail de recherche, Il me sera très difficile de remercier tout le monde car c'est grâce à l'aide de nombreuses personnes que j'ai pu mener cette thèse à son terme. Mais je vais essayer d'oublier personne dans le cas contraire je présente mes excuses pour les personnes omises dans ces remerciements.

Je tiens à remercier particulièrement Jean-Luc Rehspringer et Andreas Hinsch de m'avoir encadré dans l'élaboration de mon travail de recherches, pour toutes les discussions et conseils qui m'ont accompagné tout au long de cette co-tutelle.
J'aimerais également leur dire à quel point j'ai apprécié leur grande disponibilité et leur intérêt pour le monde de la recherche scientifique. Enfin, j'ai été extrêmement sensible à leurs qualités humaines d'écoute et de compréhension tout au long de ce travail doctoral.
Il m'est impossible aussi d'oublier Simone Mastroinanni et Anne Hebraud pour leur grande contribution dans la réalisation de ce projet et surtout pour les préparations expérimentales. Ils ont toujours fait tout leur possible pour m'aider.

Je voudrais aussi remercier grandement Guy Schmerber ingénieur de recherche à l'IPCMS pour toute son aide. Je suis ravi d'avoir travaillé en sa compagnie car outre son appui scientifique, il a toujours été là pour me soutenir et me conseiller au cours de l'élaboration de cette thèse.
J'exprime ma reconnaissance à Silviu Colis qui a su être critique dans l'analyse de mon travail et qui a apporté une aide indispensable dans la préparation de papiers scientifique.

Je souhaite aussi exprimer ma gratitude à Abdelillah Slaoui et les membres de son équipe, Thomas Fix, Nicolas Zimmerman et Stéfane Roques pour l'intérêt dont ils ont fait preuve envers ma recherche, les moyens qu'il a mis en œuvre pour me donner accès au terrain ainsi que pour leur accueil dans leur laboratoire de caractérisations des cellules solaires. Je tiens à leur témoigner toute ma reconnaissance pour leur aide dans les mesures expérimentales essentielles à l'élaboration de ce projet.

Je souhaite remercier énormément tous les ingénieurs de microscopies Jutta Zielonka, Cédric Levrey et Corinne Bouillet qui ont fourni des éléments indispensables à la compréhension et acheminement de ce travail.

Une grande partie de mes remerciements sont dédiés également à tous les membres de chaque institut impliqué dans cette co-tutelle qui ont apporté leur contribution dans ce travail ainsi que

tous étudiants de Doctorat et de Master pour leur travail honorable ; Marc Lenertz, Didier Burger, Amir Khamari, Gayathri Mathiazhagan, Lukas Wagner, Konrad Fisher, Kevin Eble, Dimitry Bogachuk, Sinem Aydemir, Jae Kun Lim, Mohamed Elshamy, Salma Zouhair, Wissal Belayachi, Salma Boujmiraj et Khaoula Kissi.

Je remercie également les gestionnaires et le service IT pour leur soutien administratif et logistique toujours dans la bonne humeur et la gentillesse absolue.

Ces remerciements seraient incomplets si je n'en adressais pas à l'ensemble des doctorants du DCMI avec qui j'ai partagé d'excellents moments que ce soit dans le cadre du travail ou en dehors. Je remercie plus particulièrement mes collègues de bureau Mathias Dolci, Elodie Martin, Florian Gelle, Suvidyakumar Homkar et Pier Berling avec qui j'ai vécu des scènes mémorables de fous rires et avec qui chaque occasion était bonne pour manger. Un petit clin d'œil supplémentaire à Florian Gelle qui a soutenu une dizaine de jours après mois et qui a été un vrai coach pour moi dans la finalisation de ce projet de thèse, un grand merci encore !

Aussi, je remercie énormément tous les participants des « cooking circle » organisé avec les membres du Fraunhofer, un concept génial durant lequel on cuisine, discute et rigole toujours aussi bien avec des amis qui feront toujours parti de ma vie.

Pour finir mes remerciements mais qui ne sont pas des moindres, ma reconnaissance va à ceux qui ont plus particulièrement assuré le soutien affectif de ce travail doctoral : ma famille, mon mari, ma belle-famille ainsi que mes amies qui sont devenues des membres de familles à part entière. Je remercie chaleureusement chaque membre que j'aime énormément mais mes remerciements je fais une dédicace spéciale à mon papa d'amour qui m'a toujours soutenu tout au long de mes études et qui a toujours cru en moi.

Table of Contents

List of Abbreviations

η	Efficiency
AFM	Atomic Force Microscopy
AM	Air Mass
c-PSC	Carbon-based Perovskite Solar Cell
c-TiO_2	compact Titanium dioxide
CB	Conduction Band
DLS	Dynamic Light Scattering
DMF	Dimethylformamide
DMSO	Dimethylsulfoxide
e^-	Negative charge (electron)
EDX	Energy-dispersive X-ray spectroscopy
Eg	Band Gap
ETL	Electron Transporting Layer
FAI	Formamidinium Iodide
FF	Fill Factor
FFT	Fast Fourrier Transform
FIB	Focused Ion Beam
FTO	Fluorine doped Tin Oxide
GBL	γ-Butyrolactone
h^+	Positive charge (hole)
HTL	Hole Transporting Layer
I-V	Courant-Tension
ITO	Indium Tin oxide
J_{SC}	Short-circuit courant
m-TiO_2	mesoporous Titanium dioxide
MAI	Methylammonium Iodide
MAPI-$MAPbI_3$	Methylammonium Lead Iodide
MPP	Maximum Power Point
P50+	PMMA particles size around 70 nm of diameter
P100+	PMMA particles size around 150 nm of diameter
P200+	PMMA particles size around 280 nm of diameter
PCE	Power Conversion Efficiency
PL	Photoluminescence
PMMA	Poly(methyl methacrylate)
PSC	Perovskite Solar Cell
PV	Photovoltaic

rpm	rotation per minute
R_{SH}	Shunt resistance
R_S	Series resistance
SC	Solar Cell
SEM	Scanning Electron Microscopy
SPD	Spray Pyrolysis Deposition
STEM	Scanning Transmission Electron Microscopy
TCO	Transparent Conductive Oxide
TEM	Transmission Electron Microscopy
TGA	Thermogravimetric Analysis
UV-Vis	Ultra-Violet-Visible spectroscopy
VB	Valence Band
V_{MPP}	Voltage at Maximum Power Point
V_{OC}	Open-circuit Voltage
XRD	X-Ray Diffraction
ZrO_2	Zirconium dioxide

Table of Illustrations

I. Introduction

In the last few years, Perovskite Solar Cells (PSC) have shown a great potential in the field of new generation solar cells emphasized with the rapid improvement of conversion efficiency [1]. A perovskite solar cell is a type of solar cell that includes a perovskite structured compound (ABX_3 with X a halogen), most commonly composed of hybrid organic-inorganic lead or tin halide as the light-harvesting active material. Such materials (i.e. the most common methylammonium lead halides $CH_3NH_3PbI_3$-$MAPbI_3$-MAPI) are cheap to produce and relatively simple to manufacture. Although the evolution of power conversion efficiency (PCE) has been extraordinary, there is still a barrier hindering the commercialization of PSC, which is their high sensitivity to moisture and oxygen leading to the fast degradation of the perovskite absorber-material [2]. To tackle these issues, one idea is to use an inorganic scaffold architecture replacing the use of organic layers such spiro-OMeTAD and metal electrodes (Gold or Silver). It is well known, in fact, that metal ions diffuse into the absorber material causing the cell degradation [3]. In literature such a cell structure has been proposed by using a triple stack of two inorganic layers (e.g. TiO_2 and ZrO_2) and a carbon layer [4], [5]. The PSC with such a scaffold design is composed of different layers deposited successively on Fluorine Tin Oxide (FTO) coated glass commercials substrates. The FTO plays the role of front-contact and transparent electrode (anode). The first deposited layer is a n-type, thin and compact TiO_2 layer (~ 20 nm) for electron extraction from the photo-absorber material to the anode; it is usually a thin film obtained by spray pyrolysis deposition. The next steps are to build the mesoscopic TiO_2 (m-TiO_2) and ZrO_2 porous layers, usually by screen-printing techniques [6]. To complete the cell structure, graphite is deposited on the top by the same process as previously; the graphite is used for the extraction of the holes and the back-contact electrode (cathode). Finally, the solution containing the perovskite precursors is infiltrated by a drop-casting method through the scaffolded films to form the perovskite photo-active crystals (as $MAPbI_3$). The graphite-based perovskite solar cell configuration and the energy levels of TiO_2, $CH_3NH_3PbI_3$, and Carbon are illustrated as below:

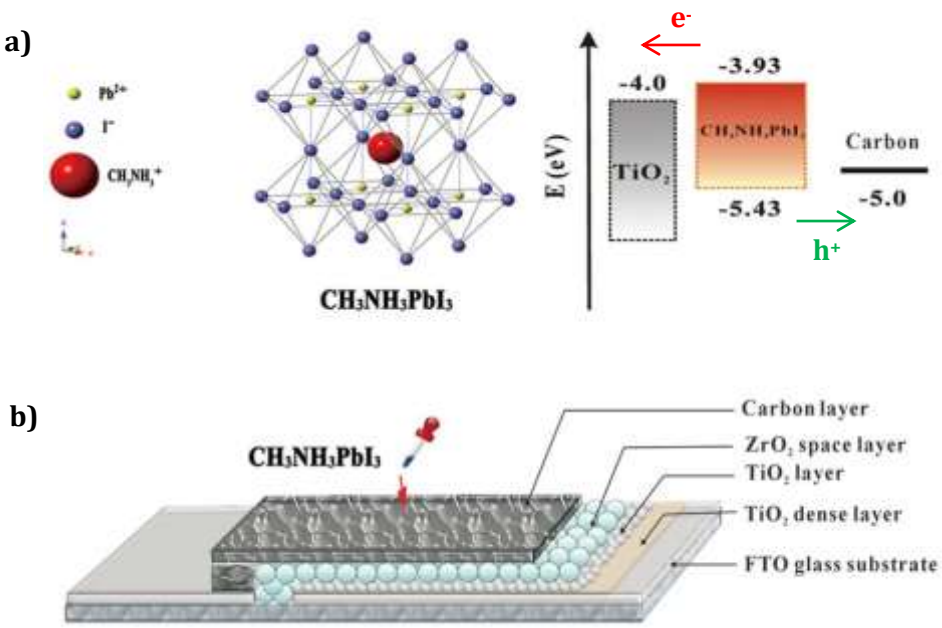

Figure I-1: (a) The crystal structure of $CH_3NH_3PbI_3$ perovskite and the corresponding energy levels of TiO_2, $CH_3NH_3PbI_3$, and Carbon. (b) A schematic structure of a carbon based monolithic device [6]

The m-TiO_2 layer is generally deposited by spin-coating or screen-printing process using a commercial paste containing TiO_2 nanoparticles with diameter of ca. 20 nm to form a 200–500 nm thick mesoporous film with high surface area [5]. The perovskite crystals grown in such

mesoporous TiO_2 scaffolds often suffer from incomplete crystallite formation and inhomogeneous pore filling [7]. In order to better control the morphological parameters of the scaffold and the quality formation of the active material, different strategies based on sol-gel reactions using structure-directing soft templates (such as surfactants and block copolymers) have been developed to prepare a crystalline TiO_2 layer with well-defined mesopores. Yue *et al.* [8] used single continuous poly(methyl methacrylate) (PMMA) layers as templating agent to form crack-free mesoporous TiO_2 films by a sol-gel method. It was shown that the pore size and morphology obtained upon annealing can be controlled by varying the amount of PMMA. Larger mesopores were shown to lead to larger solar cell efficiencies. This morphology promotes better performances in comparison to similar devices prepared with conventional TiO_2 nanoparticle pastes or by the same sol-gel method without adding PMMA.

Regarding the described issues and possible alternative as cited above, it appeared promising to elaborate in this work TiO_2 scaffolds with a macroporous structure, using the polymer-assisted sol-gel approach. For a better control of the porosity, polymer particles are preferred in the place of single continuous layers. A suspension of poly(methyl methacrylate) polymer beads with different diameter (from 80 nm-small particles to 280 nm-large particles) is used as unique templating agent to form the TiO_2 scaffolded layer with controlled porosity sizes directly related to polymer particles size by molding process.

The pore morphologies of the layer were found to be successfully controllable by varying the PMMA particles diameter. Scanning electron microscopy (SEM) analyses have been performed on the TiO_2 porous layers (200 – 300 nm thick) obtained with this molding process. They have successfully shown the relationship between the PMMA beads diameter and the pore size. In addition, X-ray diffraction measurements of the TiO_2 porous layers confirmed that the later are well crystallized as TiO_2 anatase.

In summary, in this work I firstly focused in the pore size engineering of TiO_2 layer by PMMA beads molding process. Here, the polymer spheres are used as a pattern with different diameter to control the pore size from 80 nm up to 280 nm. The aim is to obtain a layer that gives rise to: (i) the efficient electron transfer and (ii) the high TiO_2/perovskite interface quality and (iii) allowing the control of an optimal perovskite precursors infiltration.

The second scientific question investigated in this work tackles the stabilization of short-term cell efficiency. A promising alternative to $MAPbI_3$ has been widely shown in literature via the use of mixed-cation systems (for example, including inorganic cations such as rubidium or cesium) to enhance both long-term stability and efficiency. The first perovskite cells exceeding 20 % power efficiency used a mixed organic cation system, and many of the highest-efficiency systems recently published use inorganic components [9]. Based on the various properties of the different perovskite components, researchers focused on the combination of different cations and halides in order to combine their advantages. Moreover, the addition of a small amount of inorganic cesium in a "double or triple cation" perovskite structure (Cs-Cesium/MA-Methylammonium/FA-Formamidinium) resulted in high-quality monolithic grains of perovskite [10]. In this work we have followed a similar approach by replacing the commonly used $MAPbI_3$ perovskite light absorber by a $(CH_5N_2)_xCs_{1-x}PbBr_yI_{3-y}$ (Formamidinium-Cesium-Lead-Bromide with $x = 0.83$ and $y = 0.8$) crystal.

To resume, in this thesis I have developed a structural "macroporous" TiO_2 layer and I have introduced the mixed cations/halides perovskite structure ($FA_{0.83}Cs_{0.17}PbBr_{0.8}I_{2.2}$) in graphite based PSC. A thorough characterization has been performed for the complete analysis of chemical

and physical cell parameters with the aim to demonstrate the advantages of the innovative PSC architecture developed, its increased performance and stabilized efficiency enhancement. The integration of the macro-porous TiO_2 layer prepared by pore size engineering and the use of $FA_{0.83}Cs_{0.17}PbBr_{0.8}I_{2.2}$ perovskite resulted in a steep improvement of graphite based PSC with a reported efficiency of 14.7%.

This manuscript is organized into three distinct sections comprising five chapters in total. In the first section, the state of the art of PSC is presented, which comprises the perovskite cell working principle, the possible cell configurations, the precursor deposition techniques, the stability issues and finally the approach of the thesis. In the experimental section, the processes for the fabrication of graphite-based perovskite solar cell is described with the porous TiO_2 layer preparation by PMMA beads molding method. The last section reports the experimental process for the integration of thus TiO_2 porous layer in the complete c-PSC and the measured electrical performances. Throughout these chapters, the characterization results will be analyzed and discussed. The thesis synopsis is presented in the diagram below (Figure I-2).

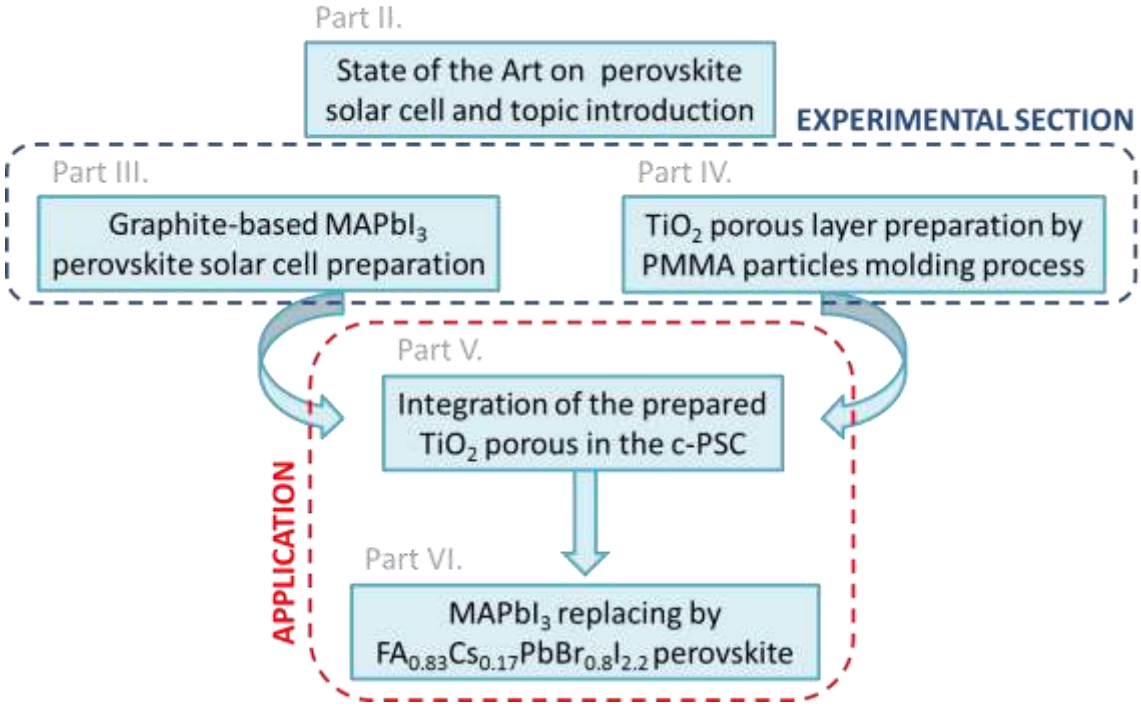

Figure I-2: Diagram representing the thesis synopsis

II. State of the Art

II.1. The Context and Motivations to PV Cells

In the 21st century, the energy sector will face a huge number and large range of intertwining challenges. These mostly include economic, political, geological, technological, and environmental challenges. The continuously increasing population growth, especially in developing countries, raises the need of energy. The energy needs of billions of supplementary people living in urban as well as rural areas must be met. According to the international energy agency, the current global energy consumption is around 14,000 Mtoe (million tons of oil equivalent) and is expected to reach about 18,000 Mtoe by 2040 as shown in Figure II-1 [11]. The conventional energy resources use such as oil and coil are expected to stagnate while the energy demand is expected to increase. In fact, the worldwide increase in energy consumption has led to the start of a depletion of energy resources. The energy demand of the world will not be able to be covered by fossil fuel resources only. Meeting the global demand will necessitate very extensive lead times.

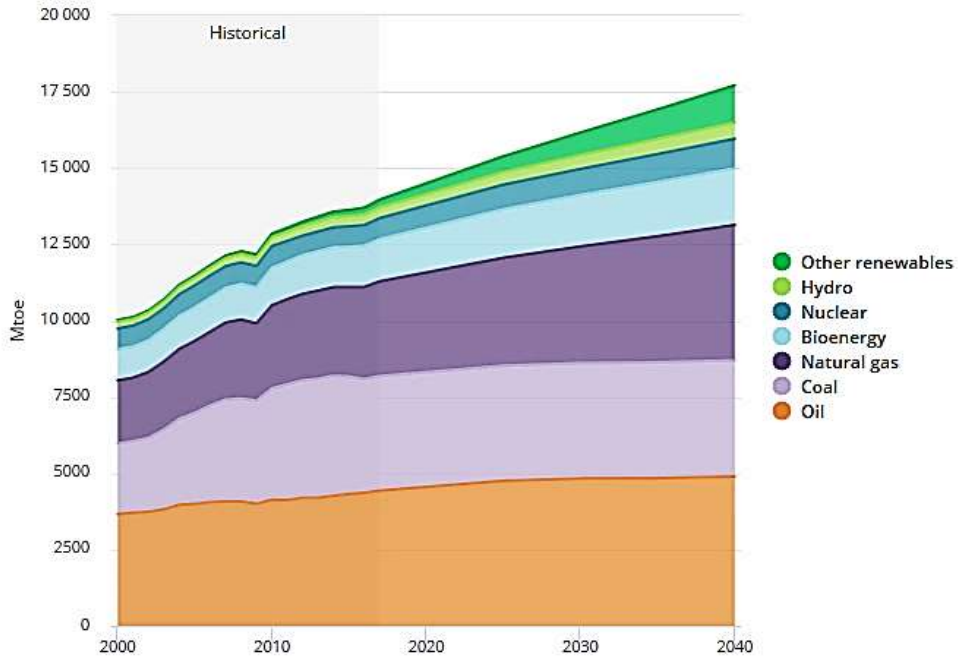

Figure II-1: Global total primary energy demand by source [12]

The greatest energy potential comes from sunlight. At the surface of the earth, this source has an energy potential of 1.8 x 10^{14} kW [11]. Solar energy can be transformed into electrical or thermal energy with negligible environmental impacts. One of the most promising technologies used to convert solar energy to electrical energy is the photovoltaic (PV) technology.

II.2. The PV Effect Principle

As its name implies, the photovoltaics effect is the direct conversion of light (photo) into electricity (voltaic) using semiconducting materials [13]. The principal light source in PV activity is the sunlight also characterized as a radiant energy. This chapter describes the properties of sunlight and its interaction with matter to generate carriers and therefore electricity.

II.2.1. The Sun as Abundant and Free Energy Source

The total power emitted from the sun is not composed of a single wavelength, but of many wavelengths and particles called "photons" [14], [15]; therefore, depending on the situation, a photon may appear as either a wave or as a particle and this concept is called "wave-particle duality" [16].

A photon is denoted by λ or equivalently energy, denoted by E. There is an inverse relationship between the energy of a photon (E) and the wavelength of the light (λ) given by the equation:

$$E = \frac{h\,c}{\lambda} = h\,\nu$$

(With c the speed of light: 3×10^8 m.s^{-1} and ν the photon frequency)

There are several key characteristics of the incident solar energy which are critical in determining how the incident sunlight interacts with a photovoltaic converter or any other object. The important characteristics of the incident solar energy are:

- the spectral content of the incident light,
- the radiant power density from the sun,
- the angle at which the incident solar radiation strikes a photovoltaic module, and
- the radiant energy from the sun throughout a year or day for a particular surface.

The spectral irradiance as a function of photon wavelength (or energy), is the most common way to characterize a light source. It gives the power density at a particular wavelength. The Air Mass (AM) quantifies the reduction in the power of light as it passes through the atmosphere and is absorbed by air and dust. The Air Mass is defined as: $AM = \frac{1}{\cos\Theta}$

where θ is the angle from the vertical (zenith angle)[17]. When the sun is directly overhead, the Air Mass is 1 which means less loss from the radiant power density from the sun (Figure II-2) [8].

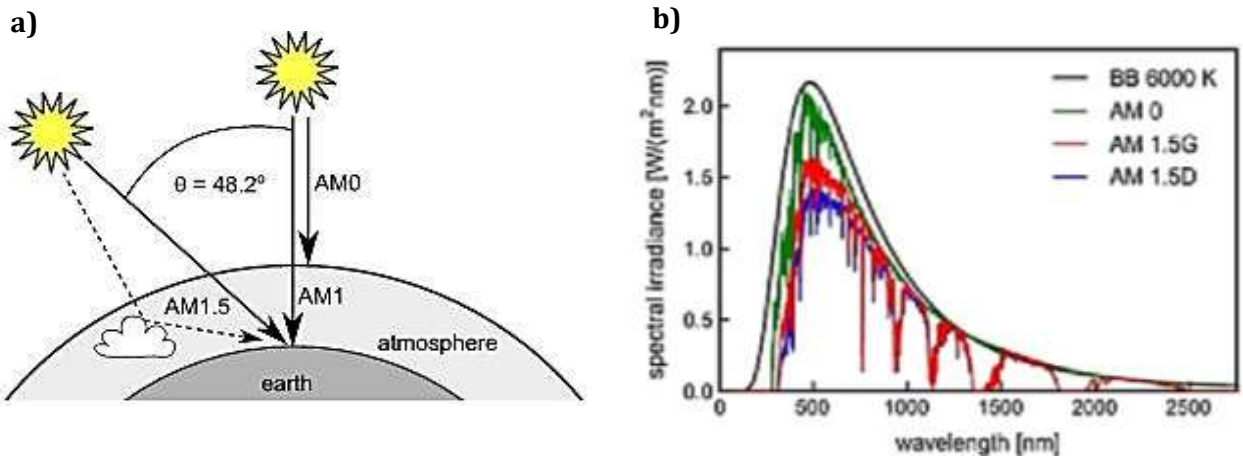

Figure II-2: a) Air Mass (AM) conditions illustration with ɵ the zenith angle b) Standard solar spectra. Most solar reference cells are measured under condition AM 1.5 G (Global) [7]

II.2.2. Semiconductor as Photo-Active Material for PV

Solid-state materials are commonly grouped into three classes: insulators, semiconductors, and conductors. A semiconductor (SC) material has an electrical conductivity value falling between that of a conductor, such as metallic copper, and an insulator, such as glass. The wide range of semiconductor applications comes from the ability to easily change their conductivity. Semiconductor devices can display a range of useful properties such as passing current more easily in one direction than the other, showing variable resistance, and sensitivity to light or heat. Because the electrical properties of a semiconductor material can be modified by doping or by the application of electrical fields or light, devices made from SC are used in energy conversion [20].

The atoms in a semiconductor are materials from either group I-V of the periodic table, or from a combination of group III and group V (called III-V semiconductors), or of combinations from group II and group VI (called II-VI semiconductors). More common SC used for PV application are single element such as Silicon (Si) or Germanium (Ge); or a compound such as GaAs (Galium Arsenic), InP (Indium Phosphide) or CdTe (Cadmium Telluride) [21].

II.2.2.1. The Optical Band Gap (Eg)

The band gap of a semiconductor is the minimum energy required to excite an electron that is stuck in its bound state into a free state where it can participate in conduction.

The lower energy level of a semiconductor is called the "valence band" (E_V) and the energy level at which an electron can be considered free is called the "conduction band" (E_C). The band gap (E_g) is the gap in energy between the bound state and the free state, between the valence band and conduction band [20]. The different class of materials can be distinguished by this value as illustrated in Figure II-3:

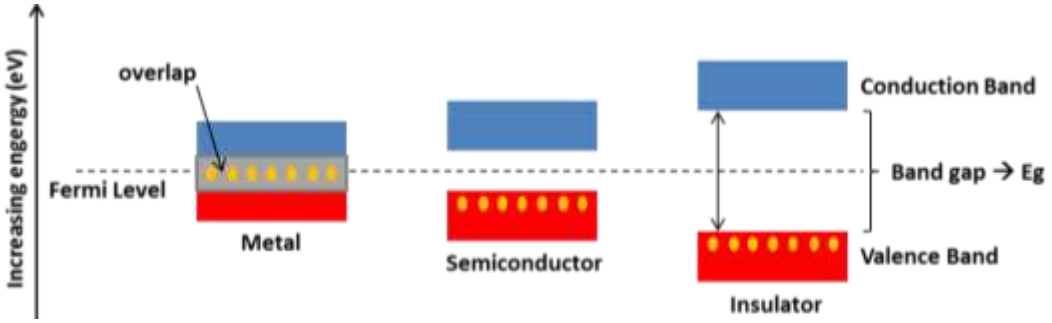

Figure II-3: Scheme illustrating the conduction band and valence band of the three main classes of materials

II.2.2.2. Light Absorption

The photons coming from sunlight can interact in various ways according to the photon energy and the semiconductor E_g. The different possible scenarios are:

1. The photon can pass straight through the semiconductor — this (generally) happens for lower energy photons.

2. The photon can reflect off the surface.

3. The photon can be absorbed by the semiconductor if the photon energy is higher than the SC band gap value. This generates an electron-hole pair and sometimes heat depending on the band structure.

When a photon is absorbed, its energy is given to an electron in the crystal lattice. Usually this electron is in the valence band. The energy given to the electron by the photon "excites" it into the conduction band where it is free to move around within the semiconductor (Figure II-4-a). However, the excitation of an electron to the conduction band will also allow an additional conduction process to take place. The excitation of an electron to the conduction band leaves behind an empty space for an electron. An electron from a neighboring atom can move into this empty space. When this electron moves, it leaves behind another space. The continual movement of the space for an electron, called a "hole" or "h^+", can be illustrated as the movement of a positively charged particle through the crystal structure. It can be said that photons absorbed in the semiconductor create electron-hole pairs (Figure II-4-b). Thus, both the electron and hole can participate in conduction and are called "carriers" [22].

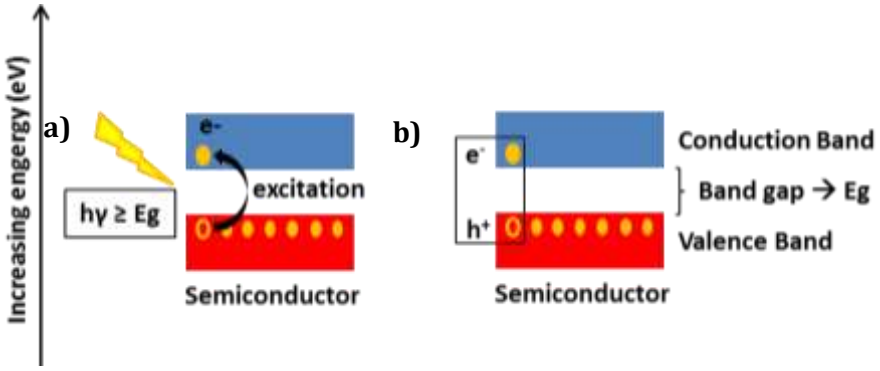

Figure II-4: Diagram depicting the creation of electron-hole pairs by the effect of solar photon excitation on a semiconductor material

II.3. The Solar Cell Working Principle

A Solar cell, also called photovoltaic cell (PV cell) or solar panel is defined by a device that directly converts the energy of light into electrical energy through the photovoltaic effect [23]. There are three generation of solar cells;

1. 1st generation: traditional solar cells made from silicon (single crystal, multi-junction etc.) which are currently the most efficient solar cells available for residential use and account for around 80 % of all the solar panels sold around the world [24], [25].

2. 2nd generation: solar cells which are usually called thin-film solar cells because when compared to crystalline silicon based cells they are made from layers of semiconductor materials only a few micrometers thick. The semiconductors used for this category are usually amorphous silicon or also made from non-silicon materials namely cadmium telluride (CdTe), and copper indium gallium diselenide (CIGS). Together they accounted for around 16.8 % of the panels sold in 2009 and reached over 20 % efficiency nowadays [26]–[28].

3. 3rd generation: cells which refers to PVs using technologies that have the potential to overcome current efficiency and performance limits or are based on novel materials. This 3rd generation of PVs includes DSSC (Dye Sensitized Solar Cell or Grätzel cells), organic

photovoltaic (OPV), quantum dot (QD) PV and perovskite PV [29]–[31]. There are also the tandems cells which combine two photo-active absorber materials with the aim to extend the light spectrum absorption and therefore improve the efficiency as the silicon-perovskite based tandem cells [32].

In this thesis we are interested on this third generation solar cells and in particular perovskite PV and we will discuss specially the general structure of a perovskite solar cell device.

II.3.1. The Solar Cell Structure

Light shining on the solar cell produces both a current and a voltage to generate electric power. This process requires firstly, a material in which the absorption of light raises an electron to a higher energy state (the semiconductor), and secondly materials which allow the movement of this higher energy electron from the solar cell into an external circuit for the charges collection.

The perovskite solar cell (PSC) is composed by an active layer (perovskite structured compound), which is contacted with an n-type material for electron (negative charge) extraction (ETL – Electron Transporting Layer) and a p-type material for hole (positive charge) extraction (HTL – Hole Transporting Layer) as illustrated in Figure II-5 [1].

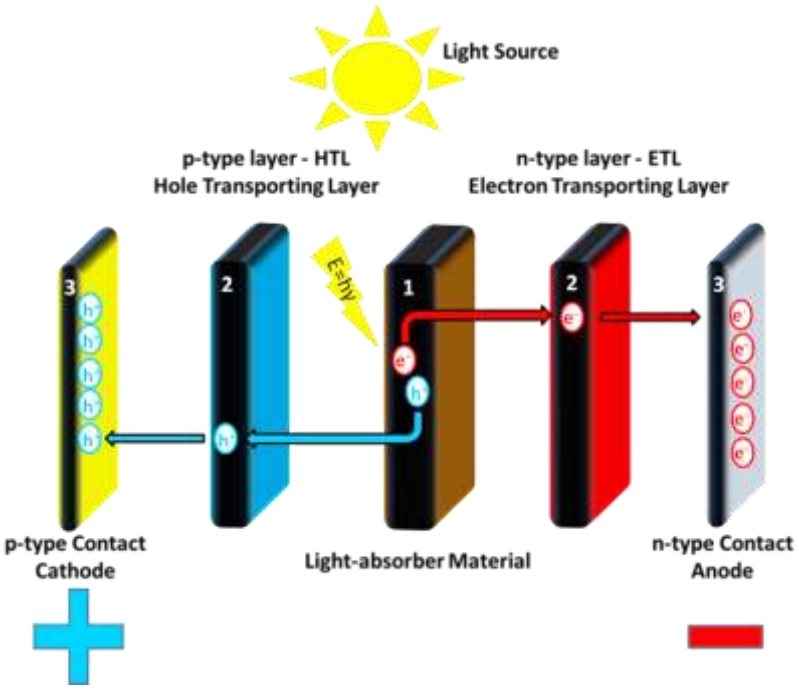

Figure II-5: Scheme illustrating the solar cell structure and principle of the charge carriers transfers

The extracted negative charges are transferred and collected to the anode, which is generally a transparent conductive oxide (TCO either ITO – Indium doped Tin Oxide or FTO – Fluorine-doped Tin Oxide) deposited on a glass substrate. Meanwhile, the positive charges are collected to the cathode (back-contact), which is commonly a Gold (Au), Silver (Ag) or aluminum (Al) electrode [33].

The main electrical characteristics of a PV cell or module are summarized in the relationship between the current and voltage shown in a typical solar cell I-V characteristic curve, which gives information on the solar cell performance. I-V characteristic curves are graphs of output current versus voltage obtained by applying a range of voltage through the electrode in reverse or forward

scan [34]. The reverse bias corresponds to connecting the p-type region to the negative terminal of the generator and the n-type region to the positive terminal and the forward bias is the reverse. The I-V measurement principle is explained in detail in the next part.

II.3.2. The Solar Cell Parameters

Measuring solar cells parameters requires a stable light source that closely matches the conditions of sunlight. Not only the intensity but also the spectrum must be matched to a standard. The most common solution is to use an artificial light source that simulates the sun. The ideal illumination source would have following features;

- a spatial non uniformity of less than 1 %.
- a variation in total irradiance with time of less than 1 %,
- filtered for a given reference spectrum to have a spectral mismatch error of less than 1%.

II.3.2.1. The I-V Curve

The I-V curve of a solar cell is the superposition of the I-V curve of the solar cell diode in the dark with the light-generated current [35]. The light has the effect of shifting the I-V curve down into the fourth quadrant where power can be extracted from the diode (Figure II-6-1).

Illuminating a cell adds a generated current to the normal "dark" current in the diode so that the diode law becomes (Figure II-6-2):

$$I = I_0 \left[\exp\left(\frac{q\,V}{n\,k\,T}\right) - 1\right] - I_L$$

where:
I = the net current flowing through the diode,
$\boldsymbol{I_0}$ = "dark saturation current", the diode leakage current density in the absence of light,
V = applied voltage across the terminals of the diode,
q = absolute value of electron charge,
k = Boltzmann's constant,
T = absolute temperature (K), and
$\boldsymbol{I_L}$ is the generated current

The equation for the I-V curve in the first quadrant is:

$$I = I_L - I_0 \left[\exp\left(\frac{qV}{n\,k\,T}\right) - 1\right]$$

The first term in the above equation can usually be neglected. The exponential term is usually >> 1 except for voltages below 100 mV [36]. Further, at low voltages, the light generated current I_L dominates the "I_0 (...)" term so the first term is not needed under illumination:

$$I = I_L - I_0 \left[\exp\left(\frac{q\,V}{n\,k\,T}\right)\right]$$

Plotting the above equation gives the I-V curve below with the relevant points on the curve labeled in Figure II-7 and described later. The power curve has a maximum where the solar cell should be operated to give the maximum power output. It is also denoted as P_{MAX} or *MPP* (Maximum Power Point) and occurs at a voltage of V_{MP} and a current of I_{MP}. Rearranging the equation above gives the voltage in terms of current:

$$V = \frac{n\,k\,T}{q}\ln\left(\frac{I_L - I_0}{I_0}\right)$$

When $I > I_L$ the term inside the "ln(...)" is negative and undefined. So the solar cell goes into reverse bias (negative voltage) and the cell will dissipate power [37].

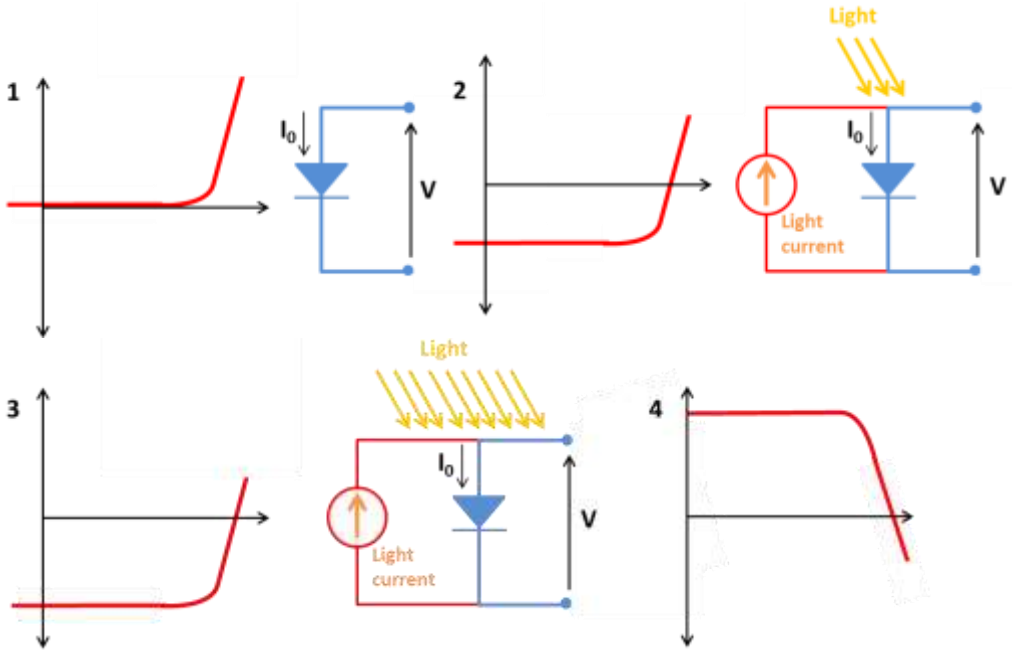

Figure II-6 : The effect of light on the current-voltage characteristics

To summarize, without illumination, a solar cell has the same electrical characteristics as a large diode (Figure II-6-1). When the light shines on the cell, the I-V curve shifts as the cell begins to generate power (Figure II-6-2). The shift intensity depends on the light intensity (Figure II-6-3). Since the cell is generating power the convention is to invert the current axis (Figure II-6-4).

Several important parameters which are used to characterize solar cells are discussed in the following pages. The short-circuit current (***J_{SC}***), the open-circuit voltage (***V_{OC}***), the fill factor (***FF***) and the efficiency are all parameters determined from the I-V curve [38].

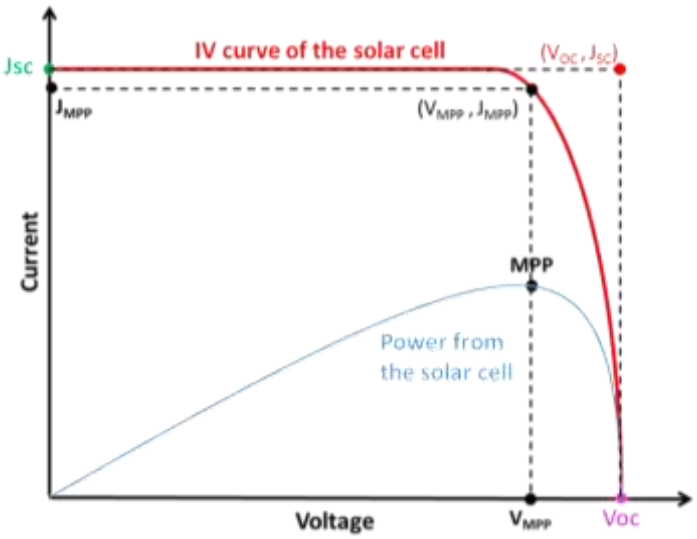

Figure II-7: Graph of cell output current (red line) and power (blue line) as a function of voltage. Also, the short-circuit current (I_{SC}) and open-circuit voltage (V_{OC}) points of the cell are represented, as well as the maximum power point MPP (V_{MP}, I_{MP})

a. The Short-Circuit Current (J_{SC})

The short-circuit current is the current through the solar cell when the voltage across the solar cell is zero (i.e., when the solar cell is short circuited). Usually written as I_{SC}, the short-circuit current is shown in the I-V curve (Figure II-7).

The short-circuit current is due to the generation and collection of light-generated carriers. For an ideal solar cell with most moderate resistive loss mechanisms, the short-circuit current and the light-generated current are identical. Therefore, the short-circuit current is the largest current which may be drawn from the solar cell [39].

The short-circuit current depends on a number of factors which are described below:

- the area of the solar cell. To remove the dependence of the solar cell area, it is more common to list the short-circuit current density (J_{SC} in mA/cm^2 means current divided by the active area) rather than the short-circuit current;
- the number of photons (i.e., the power of the incident light source). I_{SC} from a solar cell is directly dependent on the light intensity as discussed in the section on "Effect of Light Intensity";
- the spectrum of the incident light. For most solar cell measurement, the spectrum is standardized to the AM1.5 spectrum;
- the optical properties (absorption and reflection) of the solar cell (as will be discussed in Optical Losses section); and
- the collection probability of the solar cell, which depends mainly on the surface passivation and the minority carrier lifetime in the base.

When comparing solar cells of the same material type, the most critical material parameter is the diffusion length and surface passivation. In a cell with perfectly passivated surface and uniform generation, the equation for the short-circuit current can be approximated as [40]:

$$J_{SC} = q\ G\ (L_n + L_p)$$

where G is the generation rate, and L_n and L_p are the electron and hole diffusion lengths respectively. Although this equation makes several assumptions, which are not true for the conditions encountered in most solar cells, the above equation nevertheless indicates that the short-circuit current depends strongly on the generation rate and the diffusion length [20].

b. The Open-Circuit Voltage (V_{OC})

The open-circuit voltage, V_{OC}, is the maximum voltage available from a solar cell, and this occurs at zero current. The open-circuit voltage corresponds to the amount of forward bias on the solar cell due to the bias of the solar cell junction with the light-generated current. The open-circuit voltage is shown on the I-V curve (Figure II-7).

An equation for V_{OC} is found by setting the net current equal to zero in the solar cell equation to give:

$$V_{OC} = \frac{n\ k\ T}{q} \ln\left(\frac{I_L}{I_0} + 1\right)$$

A casual inspection of the above equation might indicate that V_{OC} goes up linearly with temperature. However, this is not the case as I_0 increases rapidly with temperature primarily due to changes in the intrinsic carrier concentration n_i. The effect of temperature is complicated and varies with cell technology. V_{OC} decreases with temperature. If the temperature varies, I_0 also varies.

c. The Fill Factor (*FF*)

The short-circuit current and the open-circuit voltage are the maximum current and voltage respectively from a solar cell. However, at both of these operating points, the power from the solar cell is zero. The "fill factor", more commonly known by its abbreviation "*FF*", is a parameter which, in conjunction with V_{OC} and J_{SC}, determines the maximum power from a solar cell. The *FF* is defined as the ratio of the maximum power from the solar cell to the product of V_{OC} and J_{SC}:

$$FF = \frac{P_{MPP}}{V_{OC}\, J_{SC}} = \frac{V_{MPP}\, J_{MPP}}{V_{OC}\, J_{SC}}$$

The *FF* is a measure of the "squareness" of the I-V curve (Figure II-7); thereby a solar cell with a higher voltage has a larger possible *FF* since the "rounded" corner portion of the I-V curve takes up less area and the curve has a squarer shape.

d. The Solar Cell Efficiency (η)

The efficiency is the most commonly used parameter to compare the performance of one solar cell to another. Efficiency is defined as the ratio of energy output from the solar cell to input energy from the sun. In addition to reflecting the performance of the solar cell itself, the efficiency depends on the spectrum and intensity of the incident sunlight and the temperature of the solar cell. Therefore, conditions under which efficiency is measured must be carefully controlled in order to compare the performance of one device to another. Terrestrial solar cells are measured under AM1.5 conditions and at a temperature of 25 °C. Solar cells intended for space use are measured under AM0 conditions [15].

The efficiency of a solar cell is determined as the fraction of incident power which is converted to electricity and is defined as:

$$P_{max} = V_{OC}\, J_{SC}\, FF$$

$$\eta = \frac{P_{max}}{P_{in}} = \frac{V_{OC}\, J_{SC}\, FF}{P_{in}}$$

Where again the:
$\boldsymbol{V_{oc}}$ is the open-circuit voltage;
$\boldsymbol{I_{sc}}$ is the short-circuit current;
FF is the fill factor and
$\boldsymbol{\eta}$ is the efficiency.

The input power (P_{in}) for efficiency calculations is 1 kW/m² or 100 mW/cm².

The solar cell parameters performance value can be reduced either by the charges recombination effect, which means losses due to electrons that lose energy and stabilize back to the valence band, recombining with a hole [41]; or by resistive effects that reduce the efficiency of the solar cell by dissipating power in the resistances [42]. This last point is described in the next part.

II.3.2.2. The Resistive Effects

Resistive effects in solar cells reduce the efficiency of the solar cell by dissipating power in the resistances. The most common parasitic resistances are series resistance and shunt resistance.

a. Series Resistance (R_S)

The Series resistance in a solar cell can be due to several reasons:

1. the movement of current through the emitter and base of the solar cell;
2. the resistance between the interface in the cell structure;
3. the resistance of the top and rear metal contacts.

The main impact of series resistance is to reduce the fill factor, although excessively high values may also reduce the short-circuit current [43], [44].

b. Shunt Resistance (R_{SH})

Significant power losses caused by the presence of a shunt resistance, R_{SH}, are typically due to manufacturing defects, rather than poor solar cell design. An estimate for the value of the shunt resistance of a solar cell can be determined from the slope of the I-V curve near the short-circuit current point. Such a diversion reduces the amount of current flowing through the solar cell junction and reduces the voltage from the solar cell. The effect of a shunt resistance is particularly severe at low light levels, since there will be less light-generated current [45].

In most cases and for typical values of shunt and series resistance, the key impact of parasitic resistance is to reduce the fill factor [46]. The inclusion of the series and shunt resistance on the solar cell model is shown in the figure below;

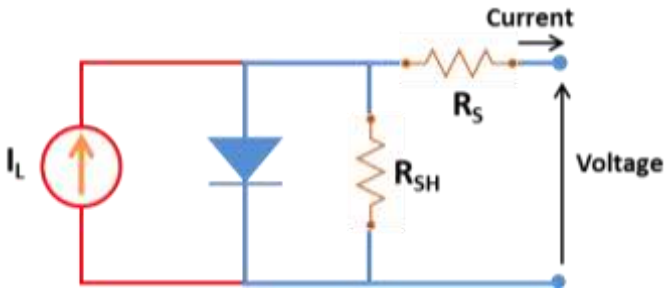

Figure II-8: Schematic of a solar cell with series and shunt resistance

II.4. Introduction of Perovskite Solar Cell in PV Activity

II.4.1. The Tendency toward Perovskite as Photoactive Material

Silicon based PV technologies are widely used and have shown a record-breaking efficiency of 27.6 % [27]. Nonetheless, the fabrication of silicon based PVs deploys harmful chemicals during the purification processes [47]. They also face some limitations related to their integration into buildings because of their unaesthetic appearance and low real efficiencies when used in facades. On the contrary, third-generation solar cells, which include organic photovoltaic (OPV), Dye Sensitized Solar Cells (DSSC), Hybrid organic-inorganic perovskite solar cells (PSC), can be easily adapted to facades thanks to their ability to absorb diffused light [48]–[50]. The use of perovskite

as a light absorber material was presented for the first time in 2009 by Kojima *et al.* reaching a power conversion efficiency (PCE) of 3.8 % [51]. The halide perovskite material with the generic structure $CH_3NH_3PbX_3$ has soon proved to provide a high electron and hole conductivity [52].

These outcomes have given rise to the emergence of a novel thin-film PV category called perovskite solar cells (PSCs), which is one of the most investigated categories of solar cells. This increasing burst of research interest has led to the fast improvement of their PCE from 3.8 % in 2009 up to 25.2 % in 2019 as shown in Figure II-9. This highest recorded PCE was achieved by the Korean Research Institute of Chemical Technology (KRICT) and is until this time not beaten [28].

Amongst the emerging technologies, perovskite solar cells (PSC) are an exceptional discovery, promising to have a very low cost and at the same time allowing easy manufacturing processes and the possibility to fabricate them in many colors. They can reach high Power Conversion Efficiency (PCE) making them very competitive to the well-known silicon based solar cells.

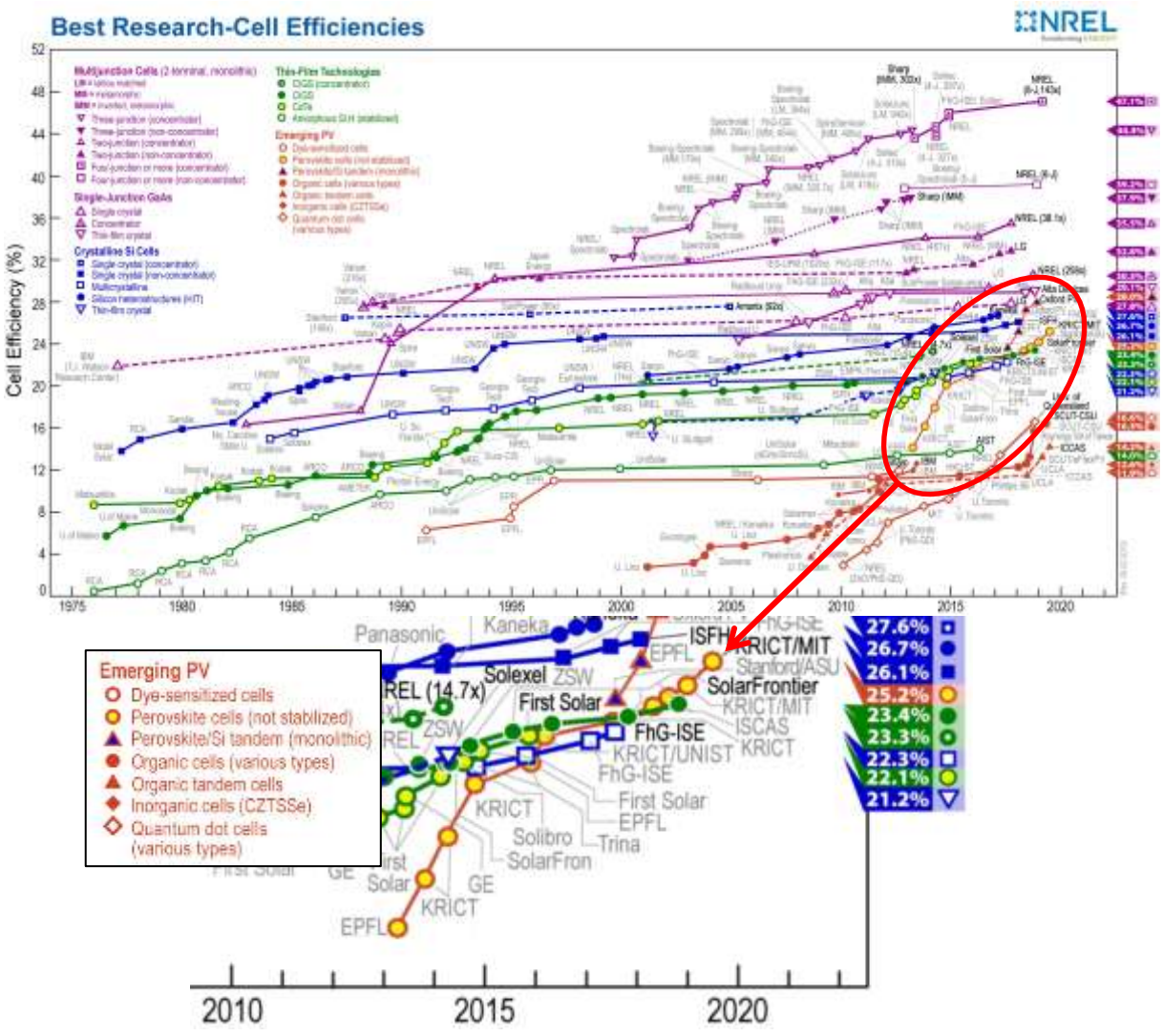

Figure II-9: Best research solar cells efficiencies from NREL [28]

II.4.2. Perovskite Solar Cell Definition and Optical Properties

Perovskite – is a large family of chemical compounds with a common formula: ABX_3 (Figure II-10). The most relevant and studied type of perovskite for PSC application is hybrid organic-inorganic halide perovskites; It has an, organic cation located at the corners of the cubic cell and which is typically $CH_3NH_3^+$ (MA), $HC(NH_2)_2$+ (FA) or $C_2H_5NH_3^+$ (EA) as the organic element. B is a bivalent metal located at the center of the unit cell, such as Pb^{2+}, Sn^{2+} and Cu^{2+} which is the inorganic part. X is a halogen anion located at the face centers of the body, which include I^- and Br^- [53].

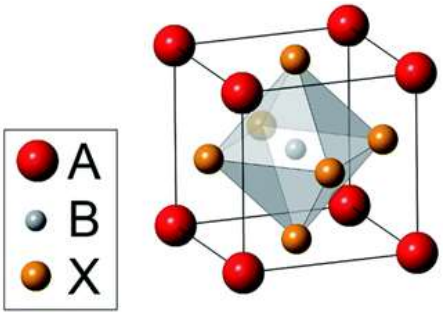

Figure II-10: ABX_3 perovskite crystal structure as the light absorber material of the solar cell

Among numerous perovskite material compositions, the most researched compound is methylammonium lead iodide ($MAPbI_3$ or MAPI). The main optoelectronic properties depend on the B and X atoms in ABX_3 perovskite compounds; the band gap is defined by the electron orbitals overlap between them and determine the Valence Band (VB) maximum and Conduction Band (CB) minimum. Thus by varying B and X ions, one can tune the energy bandgap of perovskite [54].

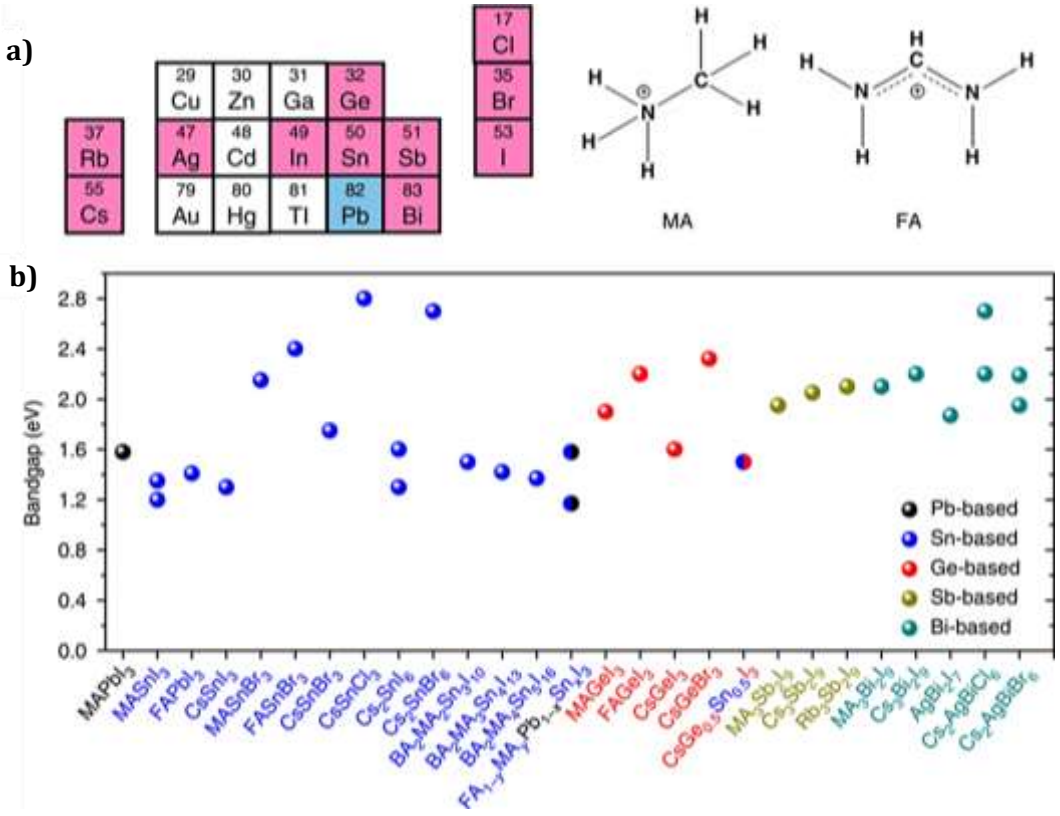

Figure II-11: Potential materials as solar cell absorbers a) Potential A-site cations (organic MA and FA or inorganic Cs and Rb), metals, and halides (I, Br, Cl) for perovskite structure b) Bandgaps of various materials. The suitable materials for solar cells should have direct bandgaps of around 1.1 to 2.0 eV [55]

These types of materials have a range of advantages when used as PV absorber, which are strong optical absorption, high mobility and diffusion length of electrons and holes, low surface recombination rate, favorable grain boundaries, and ideal photovoltaic properties such as an optical band gap of around 1.5 eV [56].

The Shockley–Queisser efficiency limit (also known as the detailed balance limit) refers to the maximum theoretical efficiency of a solar cell using a single p-n junction to collect power from the cell where the only loss mechanism is radiative recombination in the solar cell [13]. Additionally, according to the Shockley Queisser efficiency limit (Figure II-12), perovskite solar cells have a theoretical efficiency around 30 %, which is relatively similar to the Shockley limit of silicon or monolithic gallium arsenide (GaAs) based cells close to maximum theoretical efficiency curve.

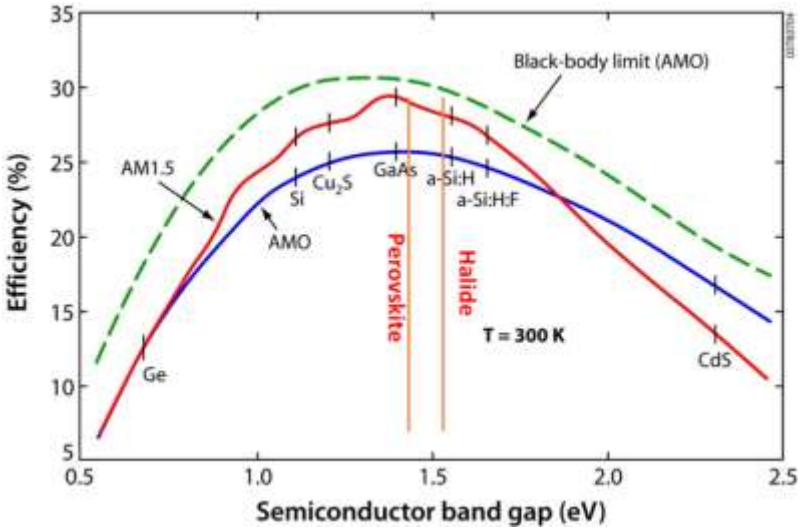

Figure II-12: The Shockley Queisser efficiency limit for solar cells as function of the optical band gap [58]

The spectral energy distribution of solar light has maxima in the visible portion (Figure II-1). This is at around 1.5 eV and hence a semiconductor with a band gap in the range of 1.1 eV to 1.7 eV is preferred for PV cells. Since the maximum in intensity occurs in the visible portion of sunlight, only this portion is useful. The other portion of spectrum is less useful. It produces heat if absorbed and attempts are made to get it reflected. This is one of the reasons of low efficiency of solar cells, as only 46 percent of spectrum corresponds to the visible portion. The perovskite solar cell absorbs mainly in the visible light wavelength range [51], [59]. Figure II-13 indicates that the perovskite layer absorbs the majority of solar photons captured in the active layer, and drop around 780 nm wavelength is found.

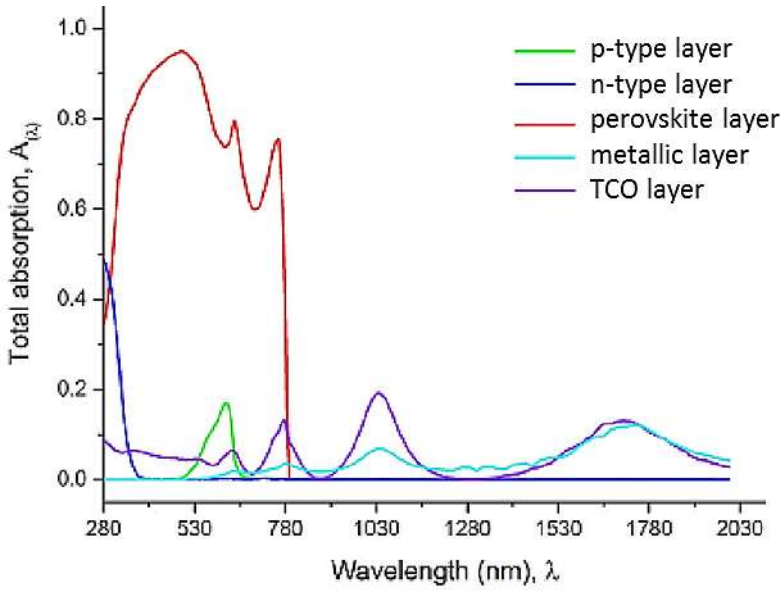

Figure II-13: Separate absorption A(k) layesr present in the complete perovskite solar cell [60]

II.5. The Different Type of Perovskite Solar Cells

Perovskite solar cells hold an advantage over traditional silicon solar cells in the simplicity of their processing and their tolerance to internal defects [61]. The different types of PSC can be classified by their architecture. Depending on the architecture there are various ways to prepare the light absorber material, which is commonly a hybrid material based on organic and inorganic components.

II.5.1. The Different Methods for Perovskite Crystals Preparation

The main issues for practical device fabrication of perovskite solar cells are film quality and thickness. The light-harvesting (active) perovskite layer needs to be several hundred nanometers thick – several times more than for standard organic photovoltaics, and creating such thick layers with high uniformity can be difficult [34], [62]. This is why the deposition conditions and annealing temperature need to be optimized. According to the solvent or the deposition technique such parameters vary but due to the perovskite crystals sensitivity the annealing temperature rarely exceeds 150 °C [63]–[65].

The perovskite photo-active crystals formation methods for PV application can be classified into two main types, the vapor deposition and the solution deposition method (wet chemistry).

II.5.1.1. Vapor Deposition Technique

There are three types of vapor deposition methods, which are the co-evaporation of organic and inorganic component, the sequential evaporation method which is similar to the previous one and the vapor-assisted method. The latter combines first the spin-coating technique to obtain a film with the inorganic element and secondly a vapor formation with organic element for the perovskite film growth. The three different methods are illustrated in Figure II-14.

Co-evaporation deposition method

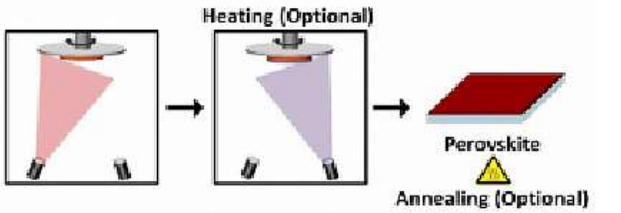

Sequential evaporation deposition method

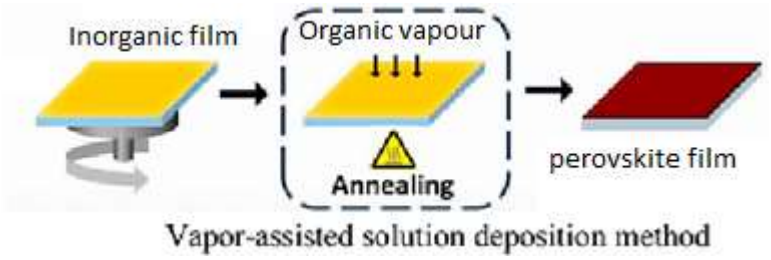

Figure II-14: Illustration of the different vapor deposition methods [66]

For an optimal performance of the PSC, the film quality of perovskite crystals is very important. In the past vacuum-deposited films provided the most efficient devices, but usually this process requires the co-evaporation of the organic components at the same time as the inorganic components, necessitating specialist evaporation chambers that are not available to many researchers. As a result, there have been significant efforts to improve solution-processed devices, as these are simpler and allow low-temperature processing, and these now equal vacuum-deposited cells in terms of efficiency [67].

II.5.1.2. Solution Deposition Technique

The solution deposition method can be again classified into two main categories; the one step deposition technique or the two steps deposition technique. The advantages of the solution processing are the simple and cheap way of elaboration to obtain uniform and good quality perovskite crystals film. The majority of solution preparation is carried out in glovebox conditions to prevent against degradation of the different components, which can be sensitive to humidity[63], [68].

In the one-step solution processing, the organic and inorganic components can be dissolved in a solvent and spin coated onto a substrate. Subsequent evaporation and convective self-assembly during spinning result in dense layers of well crystallized perovskite material, due to the strong ionic interactions within the material as shown in Figure II-15. The organic component also contributes to a lower crystallization temperature [63], [64].

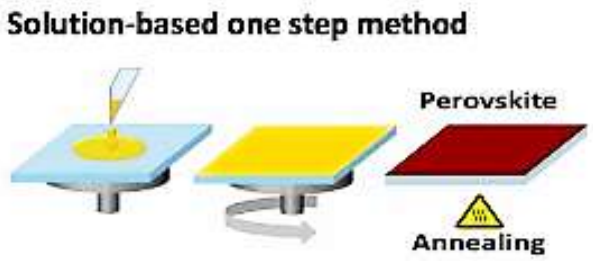

Figure II-15: The One step solution process illustration [64]

The most commonly used solvents are DMF (Dimethylformamide), GBL (Gamma-butyrolactone) and DMSO (Dimethyl sulfoxide). The choice of solvent has important influence on the perovskite film formation and the criteria to choose an ideal solvent could be the high solubilization of perovskite precursors, less volatile solvent to promote a low and good quality of crystallization etc. The solvent effects on perovskite film formation are the focus of various research studies also known as solvent engineering [63], [64]. Also, there is the binary solvent engineering that is a mixture of two solvent, with an alternative allowing to combine the solvents properties advantageously as the formation of intermediate component, which can slow down the

crystallization process [69]. Additionally, the anti-solvent process is also developed, which consists in immediately exposing the perovskite film to small amount of solvent such as chlorobenzene or toluene to induce the crystallization [70]. According to the complexity of this topic the solvent engineering process is not discussed in depth in this thesis.

In the two-step process, the metal halide (such as PbI_2) and organic components (such as CH_3NH_3I) are spin-coated in separate, subsequent films. Alternatively, metal halide films can be immerged in a solution containing the organic precursors (such as MAI salt dissolved is Isopropanol solvent). Figure II-16 illustrates the possible process for the two step deposition method.

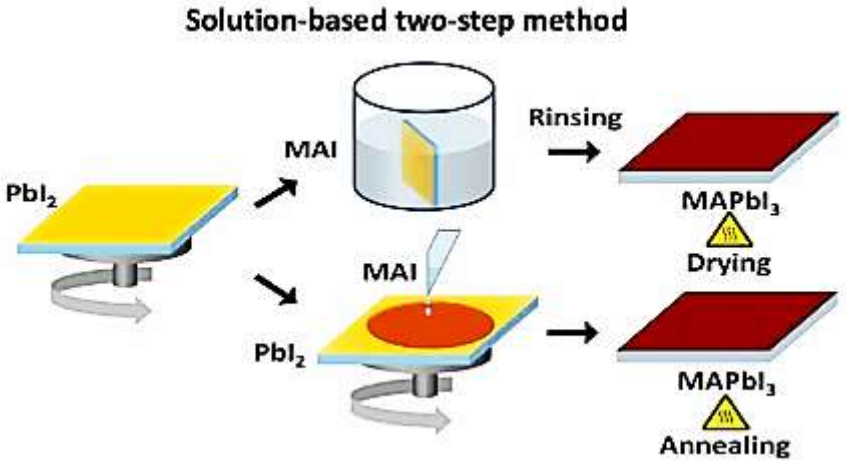

Figure II-16: The two steps depositions process representation [64]

The key point with the two-step deposition is the total conversion of metal halide to perovskite without any residue. The presence of metal halide after the process is completed could create defect and degradation in the PSC [2], [71]. Also, reproducible photovoltaic parameters extracted from statistical analysis were found to have strong correlation with the morphology of the deposited perovskite material. This means that the performances of the PSC is significantly affected by the resulting morphology of the perovskite [68]. Adding a step to the perovskite crystals growth process may impact the uniformity of the film and the performance reproducibility of solar cells series.

During this thesis work we have used essentially the one step solution deposition technique, which will be described in more detail in the experimental chapter.

II.5.2. Design and Configuration of the Different Type of PSC

For solar cells, the device architecture is a key factor to the PV performance [72]. For perovskite solar cells, there are three main configurations through which a perovskite solar cell can be structured. The planar direct configuration (Figure II-17-a), the mesoporous direct configuration (Figure II-17-b) and the inverted configuration (Figure II-17-c) [73], [74].

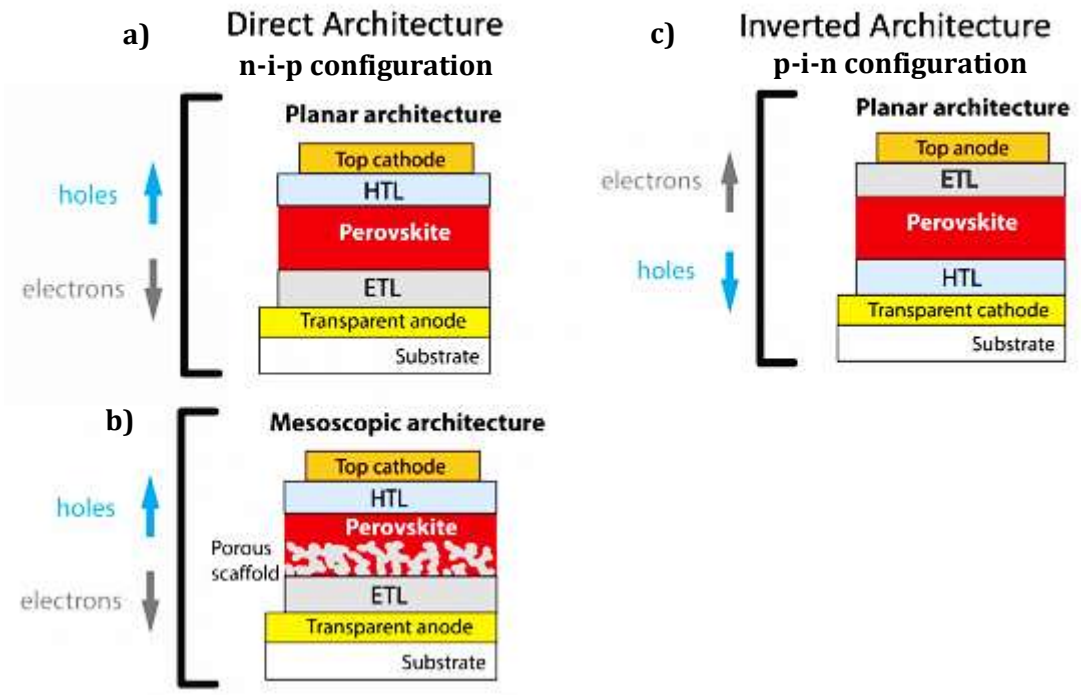

Figure II-17: Representation of the different Type of PSC architecture in n-i-p and p-i-n configuration with a) the direct and planar architecture, b) the direct and mesoscopic or scaffolded architecture and c) the inverted and planar architecture [75]

All these different cell structures have already demonstrated very impressive advances in performance [61]. Depending on the cell architecture (p-i-n or n-i-p) there is a wide choice of materials for n-type electron transporting layer (ETL) and p-type hole transporting layer (HTL) [1], [74], [76]. The structure of the cell is generally built layer by layer from the TCO/glass substrate and the main technique used to deposit the various films present in the cell excepted the metallic electrode is the spin-coating [75]. This is still an approach to cell preparation that is simple to develop and is therefore advantageous. The combination of the different materials present in a PV cell has to follow a coherence of the appropriate energy levels at the interfaces to avoid as much as possible the charge carrier losses and to facilitate their transfer through the different films until they reach the contact electrodes (Figure II-18) [77], [78]. Understanding and optimizing the energy levels and interactions of the different materials at these interfaces offers a very exciting area of research that is still under discussion.

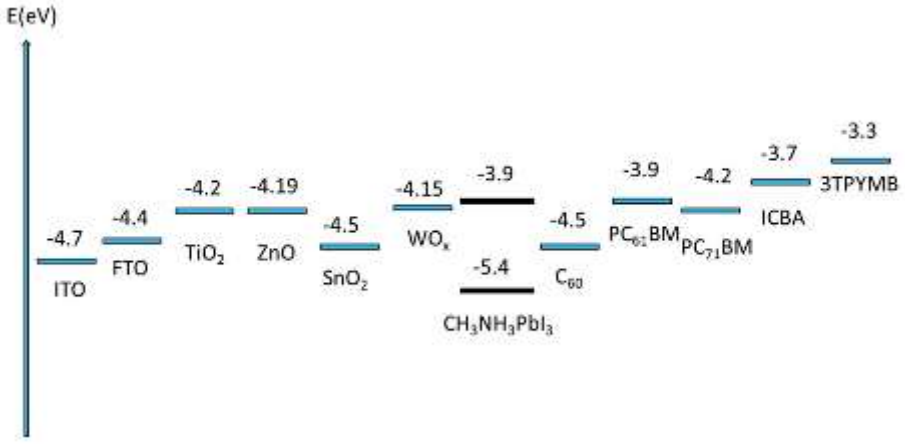

Figure II-18: Energy level diagram showing conduction band levels of various ETL [79]

II.5.2.1. Planar Cells Configuration

a. Inverted Cells

Snaith *et al.* [80] first reported on an "inverted PSC design" (p-i-n architecture) using a p-type organic hole transporting layer (as PEDOT:PSS and NiO) in a solar cell with the layout FTO/PEDOT:PSS/MAPI/PCBM/Al. While in this configuration, holes are collected at the front transparent glass electrode (FTO) via the HTL layer (PEDOT:PSS), electrons are collected via the ETL (n-type, PCBM) at the top counter electrode (Al) [75], [81]. In the p-i-n type devices, photocurrent flows in the reverse direction (photo-induced holes instead of electrons collected through the front conductive glass substrate) and hence the name "inverted structure. In the initial work, the PSC with PEDOT:PSS showed a PCE of 10 % on glass substrates and 6 % on flexible polymer substrates [82]. Since the initial studies, the PCE has been improved up to 18 % [83].

The Planar heterojunction solar cells fabricated with this method demonstrate hysteresis-free or less hysteresis performance, which means that the photocurrent variation with voltage in the forward and reverse sweep directions is almost the same [84].

b. Direct Cells

Most state-of-the-art perovskites solar cells are based on a transparent p-i-n configuration. Contrary to inverted cell architecture, in this configuration electron negative charges are collected at the front transparent glass electrode via the electron transporting layer and holes (h^+) are collected via the HTL at the top counter electrode. Thanks to their appropriate energy levels; a typical hole-transport layer is Spiro-OMeTAD (2,2',7,7'-Tetrakis[N,N-di(4-methoxyphenyl)amino]-9,9'-spirobifluerene) and typical electron-transport layers include TiO_2 or SnO_2 compact thin layer around 20-30 nm thick. The most studied layout n-i-p planar direct configuration is FTO/TiO_2/MAPI/Spiro-OMeTAD/Au [85], [86]. This PSC design has shown high performance but the high price of spiro-OMeTAD is an obvious issue for the commercialization.

II.5.2.2. Mesoporous Cells Configuration

The first scaffolded perovskite solar cells were based on solid state dye-sensitized solar cells (DSSCs or Grätzel cells), and thus used a mesoporous TiO_2 (m-TiO_2) scaffold [49]. The idea consists in having the perovskite infiltrate into the mesoporous layer, to allow for more volume of the perovskite to be deposited into the mesoporous Titania. The purpose is to enhance photon absorption, as this configuration allows for a better electron mobility, which enables fast electron transport within the electron transporting layer [87]. Many cells have consequently followed this template known as the "mesostructured" or "scaffolded" n-i-p architecture [88].

a. The Spiro Cells

These performing perovskite solar cells use a high surface area of mesoporous TiO_2 layer as a scaffold to enhance the embedding of the perovskite light absorber in the PSC device. In view of the very strong absorption coefficient of hybrid halide perovskites in the visible region, the Ti oxide layer can be substantially thinner than that used for liquid electrolyte DSSCs (150–400 nm vs. ≈10 μm in liquid-electrolyte DSSC) [89]. The Mesoporous TiO_2 serves as a large area scaffold for the uniform infiltration of the perovskite and also as an electron-transport layer (ETL) that collects and passes photogenerated electrons to the compact TiO_2 (c-TiO_2) layer and thereby to

the fluorine-doped tin oxide (FTO) collector electrode. The holes (h^+) hop through the hole conducting material layer, usually the spiro-OMeTAD to reach the cathode (gold electrode). PSC with the layout FTO/c-TiO_2/m-TiO_2-MAPI/MAPI/spiro-OMeTAD/Au is the most commonly studied n-i-p mesostructured perovskite photovoltaic device (Figure II-19).

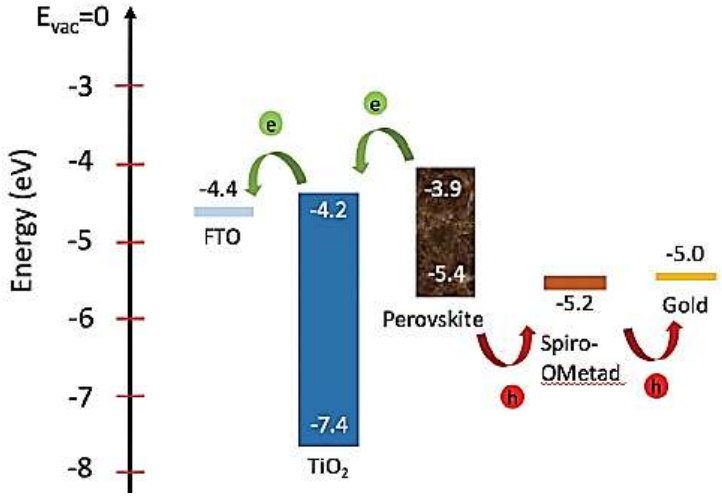

Figure II-19: The corresponding energy levels and charge carriers transfers in the FTO/TiO_2/perovskite/spiro-OMeTAD/Au configuration PSC [85]

b. Monolithic Carbon-based, HTL Free and Fully Printable PSC

An important property of hybrid halide perovskites is the ambipolar nature of charge carrier transport. Here, both electrons and holes exhibit very good mobility, and efficient PSC can be fabricated even without passing through the hole transporting layer such as spiro-OMeTAD [90].

In view of these parameters, the researchers have been developing in the last years an HTL free perovskite solar cell. In 2013 Han demonstrated the first printable PSC with carbon electrode as an alternative to expensive and unstable materials, reaching an efficiency of 6.7 % [6]. Later Mei *et al.* reported an efficiency of 12.8 % of a similar cell with ZrO_2 layer between electron transport layer and a graphite electrode (Figure II-20) [5]. As seen from Figure I-19-b, the ZrO_2 layer acts as an energy barrier for electrons reaching the back contact (Graphite) and in addition ensures that there is no direct contact (shunt) between photo-anode and graphite [91]. Carbon plays a critical role in regulating performance of the PSC collecting charge carriers. In this category of PSC, not only the cost of production is greatly reduced but also due to the hydrophobic nature of carbon, the stability of the device is increased in the presence of humidity and thus the humidity-vulnerable perovskite is substantially protected [92]. The energy level of carbon is conveniently located to absorb holes from perovskite materials [93], [94], thus the expensive and unstable spiro-OMeTAD HTM layer may be eliminated. Since then, various structures have been developed by replacing the ZrO_2 separating layer with Al_2O_3 or NiO with efficiencies of up to 17% [95]–[97].

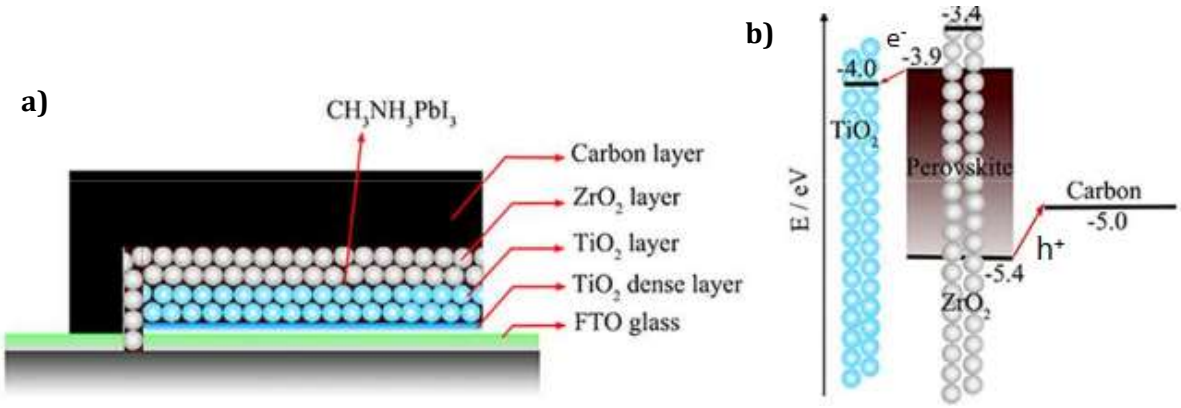

Figure II-20: a) A schematic structure of carbon electrode based mesoscopic perovskite solar cell device. b) The corresponding energy level of TiO_2, perovskite, ZrO_2 and carbon [98]

This new architecture requires only three steps: first the compact TiO_2 deposition, second the mesoporous TiO_2 and ZrO_2 layer (for perovskite infiltration), and third the carbon electrode. Among various kinds of PSC, carbon-based PSC also without hole transport materials (also named as carbon based PSC/c-PSC, monolithic PSC, HTL free PSC or fully printable PSC) seem to be the most promising for addressing the stability issue because carbon materials are stable, inert to ion migration, and inherently water-resistant. Concurrent with the steady rise in PCE of c-PSC, great progresses have also been attained in the device stability and scaling-up fabrication of c-PSC, which should allow the possible commercialization of perovskite solar cells in the near future [99].

The advantage of such architecture is the simple technique of elaboration. Indeed, the cells can be screen-printed (using commercial paste for m-TiO_2, m-ZrO_2 and graphite layers) and thus it is easier to manufacture them. After the cell is printed it is later infiltrated with perovskite precursor solution as all the layers are porous and act as a framework for later crystallization of the material. The perovskite precursor solution is simply filled from the top usually by drop-casting method and then the cells are annealed to promote the perovskites crystals growth through the porous layers [100].

Considering the many advantages of this type of configuration, we have focused the thesis work on the development of the c-PSC structure. Our motivations and strategy for this topic are explained in the next part, which follows the challenging aspect and key issues encountered for this PV activity. Indeed, while the PSC efficiency has been increasing notably , a main barrier is still hindering the commercialization of PSC, which its high sensitivity to moisture and oxygen leading to the fast degradation of the perovskite absorber material that cannot provide stabilized solar cells in a long term period [101].

II.6. Challenging Aspect and Issues

II.6.1. Stability of the PSC

Currently, the most efficient perovskite solar cells (> 20 %) using a variety of materials (including complex and expensive materials) do not present a stable performance over time. Moisture has been considered as the most influential factor challenging the stability of the perovskite material [62]; it causes a degradation of such cells in less than 1000h. Such instability is unsuitable for the

introduction of perovskite solar cells to the market, which requires 20-25 years of stable operation with < 10 % performance drop [102]. But the challenging issue of stability concerns in general all perovskite solar cells and hinders their technology from large scale production due to the rapid degradation under ambient conditions. For example, Lead based PSC are very sensitive to humidity due to the ionic nature. Perovskites with Sn (as an alternative to Pb) are also sensitive to moisture and air. $MAPbI_3$ tend to decompose into MAI and PbI_2, followed by formation of Methylamine and HI from MAI, due to hygroscopic nature of MA cation [103]. Another degradation mechanism is induced by UV light. Similarly to the dye sensitized solar cells, TiO_2 particles act as photocatalyst for iodide oxidation reaction [89].

Although the issue of device stability has drawn more and more the attention of the photovoltaic research community in the last five years, reports on the fundamental causes and mechanisms limiting the material and device stability (e.g., humidity, heat, electrical stress, oxygen, UV light, chemical precursors, processing conditions, etc.) remain scarce [62], [104].

Up to now a lot of efforts have been made in order to solve this fundamental issue in the perovskite activity. Several strategies have been proposed with the aim to improve stability. As discussed previously, one solution has been to remove the HTM material and replace the gold electrode with carbon-based material. Additionally, a promising alternative consists in the modification of the perovskite component. Using mixed-cation systems (for example by including inorganic cations such as rubidium or cesium) has been shown to enhance both stability and efficiency. The first perovskite cells to exceed 20 % efficiency used a mixed organic cation system, and many of the highest-efficiency systems published recently use inorganic components [9], [105].

II.6.2. Infiltration of the Photo-Active Perovskite Precursors

The photovoltaic performance is strongly dependent on the degree of perovskite coverage on the mesoporous TiO_2 layer and morphology of the deposited perovskite in the mesoporous TiO_2 based perovskite solar cells [92]. This is currently due to the lack of control over crystallization kinetics, which leads to a non-uniform absorber layer formation, high recombination rate and poor charge carrier extraction due to non-optimized cell structure [106]. Thus, it needs to be investigated further in order to improve the efficiency of graphite-based perovskite solar cells [107].

The m-TiO_2 layer to be integrated in solar cells is generally prepared by spin-coating or screen-printing process using a commercial paste containing TiO_2 nanoparticles to form a 200–500 nm thick mesoporous film with high surface area [108], [109]. The active material crystals grown in such mesoporous TiO_2 scaffolds often suffer from incomplete crystallite formation, depending on size of the employed TiO_2 nanoparticles [7]. In order to better control the parameters of the scaffold and active material system, different strategies based on sol-gel reactions using structure-directing soft templates (such as surfactants and block copolymers) have been developed in order to prepare crystalline TiO_2 with well-defined mesoporosity. Yue *et al.* [8] used single continuous poly(methyl methacrylate) (PMMA) layers as templating agent to form crack-free mesoporous TiO_2 films by a sol-gel method. The pore size and morphology obtained upon annealing can be controlled by varying the amount of PMMA. Larger mesoporosity were shown to lead to larger solar cell efficiencies [8]. This morphology promotes better performances in comparison to similar devices prepared with conventional TiO_2 nanoparticle pastes or with the same sol-gel method without adding PMMA.

II.6.3. Our Approach Description

Regarding the current issues and alternatives cited above, it appears interesting to elaborate TiO_2 scaffolds with a macro-porous structure, using the polymer-assisted sol-gel approach. For a better control of the porosity, polymer particles will be used instead of single continuous layers.

Furthermore, a recent work on the role of grain boundaries of perovskite has specially investigated the effect of degradation on crystal morphology [2]. It has been demonstrated that smaller grains degrade more rapidly than larger grains, suggesting that the degradation process is directly related to the grain boundaries of the perovskite crystals. We assume therefore that increasing the perovskite crystal size infiltrated within the porous TiO_2 n-type layer could have a positive effect on the cell stability. This will reduce the grain boundaries in the perovskite crystals and therefore the photo-active material degradation, which directly causes the instability of the PSC [110]. As the usual mesoporous TiO_2 layer has small cavity size (< 20 nm) it is impracticable to obtain crystal sizes larger than this value.

Considering these results, a suspension of poly(methyl methacrylate) PMMA polymer beads with different diameter (from 80 nm-small particles up to 280 nm-large particles) is used as unique templating agent to form the TiO_2 scaffolded layer with controlled porosity sizes directly related to polymer particles size by molding process (from small cavity size ≈ 50 nm to larger cavity size ≈ 250 nm). This layer will replace the printed m-TiO_2 present in the carbon-based monolithic perovskite solar cell structure. This approach constitutes a simple and cheap way to obtain macro-porous layers by chemical elaboration process. Such scaffold layers, with optimized and variable porosity used for the fabrication of graphite-based perovskite solar cells, where a good infiltration of the perovskite crystals is mandatory, could improve both efficiency and stability [111]. Indeed, the larger pore size could improve the infiltration of perovskite precursor and thereby the efficiency. Also, it can promote a growth of larger crystals inside the TiO_2 porous layer, which means a reduction of the grains boundaries and thereby less degradation of the perovskite light absorber material. As a reminder, the degradation of the light absorber perovskite crystals is the main cause for the PSC instability.

Another device advantage of the perovskite solar cell is the solution-processing enabling fabrication at low cost. This gives also the opportunity to modify easily the perovskite chemical nature and thereby the properties. Using perovskites with mixed cations and halides has become important because the pure perovskite compounds suitable for PV applications, which are primarily $MAPbX_3$ (Methylammonium lead halide), $FAPbX_3$ (Formamidinium lead halide) and $CsPbX_3$ (Cesium lead halide) where X = Br or I, come with numerous disadvantages. For example the $CsPbBr_3$ perovskite demonstrate an excellent thermal stability; however, does not have an ideal band gap for PV cells [112]. A further example is the $FAPbI_3$ perovskite used instead of $MAPbI_3$ with the advantage of reducing band gap and thus allowing a higher solar light harvesting efficiency [57]; however, pure $FAPbI_3$ shows also structural instability at room temperature as it can crystallize in a phase, which is sensitive to solvents or humidity [77].

Also, a modification of the X halide can control the range of absorption wavelength. The perovskite compound with X = Br is useful for light absorption at shorter wavelengths and the compound with X = I is relatively useful at longer wavelengths [113], [114]. For example, The perovskite phase of $CsPbI_3$ has a more suitable band gap (1.73 eV) compared to $CsPbBr_3$ (2.34 eV) and has been investigated for its good emissive properties [115], [116].

Based on the various properties of the different perovskite component, researchers focus on combination of different cations ("mixed cations") and halides ("mixed halide") in aim to combine their advantages. The use of inorganic cesium in mixed cation perovskites is quite intuitive because it could integrate easily the structure, with an ionic radius of 1.81 Å, which is considerably smaller than MA (2.70 Å) or FA (2.79 Å), [117]. Park *et al.* [118] report on Cs/FA mixtures showing enhanced thermal and humidity stability, reaching a PCE of 16.5 %. Moreover, adding only a small amounts of inorganic cesium in a "double or triple cation" configuration (Cs/MA/FA) results in highly monolithic grains of more pure perovskite [9]. Additionally, the mixed Br and I halide provides a band gap shift, which is particularly suitable for perovskite cells [119].

In this thesis work we have followed a similar approach by replacing the traditional $MAPbI_3$ perovskite light absorber material by a $FA_xCs_{1-x}PbBr_yI_{3-y}$ (Formamidinium-Cesium-Lead-Bromide) crystal in aim to improve the short-term stabilized efficiency and optical properties of the perovskite solar cells.

Conclusion

To resume, this chapter is an introduction to research topic in perovskite solar cells. The thesis work focusses on mesoporous and graphite-based perovskite solar cell architecture in the direct configuration (n-i-p).

The hybrid (organic-inorganic) perovskite solar cells are described here as a new emerging and low cost photovoltaic technology that is inspired by dye sensitized solar cells. The c-PSC can be mass produced through screen-printing technique, and a variety of abundant raw materials can be used for their elaboration. With a theoretical power conversion efficiency of 33 % according to the Shockley Queisser limit, hybrid perovskite solar cells have proved themselves to be the fastest developing photovoltaic technology in the history of solar panels.

Nevertheless, this PV activity is still facing a major issue, which is the high sensitivity to humidity that causes the rapid degradation of the perovskite layer. This makes the perovskite solar cells unstable and non-reliable when exposed to humid air environments, which restricts their scaling up and commercialization. Another issue concerns the uniform and optimal infiltration of the perovskite precursors inside the TiO_2 mesoporous layer present in c-PSC device. Therefore, it has become an important design principle to improve infiltration of light harvesting precursors and use mix cations and halides combining beneficial properties in order to achieve perovskite compounds with improved thermal and structural stability.

Hence, this justifies our intuitive strategy where the m-TiO_2 layer is replaced by a porous layer with larger cavities (size ranging over ≈ 50 nm to ≈ 250 nm) prepared by PMMA particles molding with a sol-gel solution containing Ti precursors.

Furthermore, the traditional $MAPbI_3$ light harvesting is replaced with a mixed cation and halide perovskite. Regarding positive effect of cations mixture; a small amount of inorganic Cesium is used to improve FA perovskite compounds. The X halide part is combined with Br and I element in order to improve the optical properties. Consequently, the classical previous photo-active material becomes a $(CH_5N_2)_xCs_{1-x}PbBr_yI_{3-y}$ mixed perovskite where $x = 0.83$ and $y = 0.8$.

Both, structural (TiO_2 "macroporous" layer) and perovskite type (mixed cations and halides: $FA_xCs_{1-x}PbBr_yI_{3-y}$) modifications will be applied to a referential monolithic graphite-based/$MAPbI_3$ perovskite solar cell in order to study the performance and stabilized efficiency enhancement.

III. Experimental Section of a Referential Carbon-based Monolithic Perovskite Solar Cell Preparation and Characterization

This chapter describes the complete monolithic perovskite solar cell preparation and characterization. The different materials and tools used for the elaboration are described below. The light absorber material composition and structure is depicted in detail. The Electron Transporting layer (c-TiO_2) and the scaffolds layer's (m-TiO_2, ZrO_2 and graphite) thickness and morphologies are characterized. The performances of the manufactured hybrid lead-halide perovskite solar cells are carried out and discussed.

III.1. Monolithic Carbon-based Solar Cell Preparation

The fully printable mesoscopic perovskite solar cells are called "printable" because the main technique used for the manufacturing is the screen printing, and the "mesoscopic" label is due to the porous layers present in the structure of the PSC. The preparation is processed in different steps (Figure III-1) using a commercial glass substrate coated with a Transparent Conductive Oxide (TCO), which is usually the FTO (Fluorine Tin Oxide). The FTO/glass plate dimension is $10 \times 10 cm^2$ (Figure III-1-1). The first step of the process is to ablate by laser lines on the FTO/glass substrate (Figure III-1-2) to separate three main areas. These lines will avoid the overlap of specific layers such as the FTO base layer for the anode, the mesoporous layers - TiO_2 and ZrO_2 (Figure III-1-3 and II-1-4) and finally the carbon cathode (Figure III-1-5). The final step is to cut the plate in sixteen pieces with a scriber to obtain cells of 2.5×2.5 cm^2 size (Figure III-1-6). The cell elaboration is described more in detail in the next part.

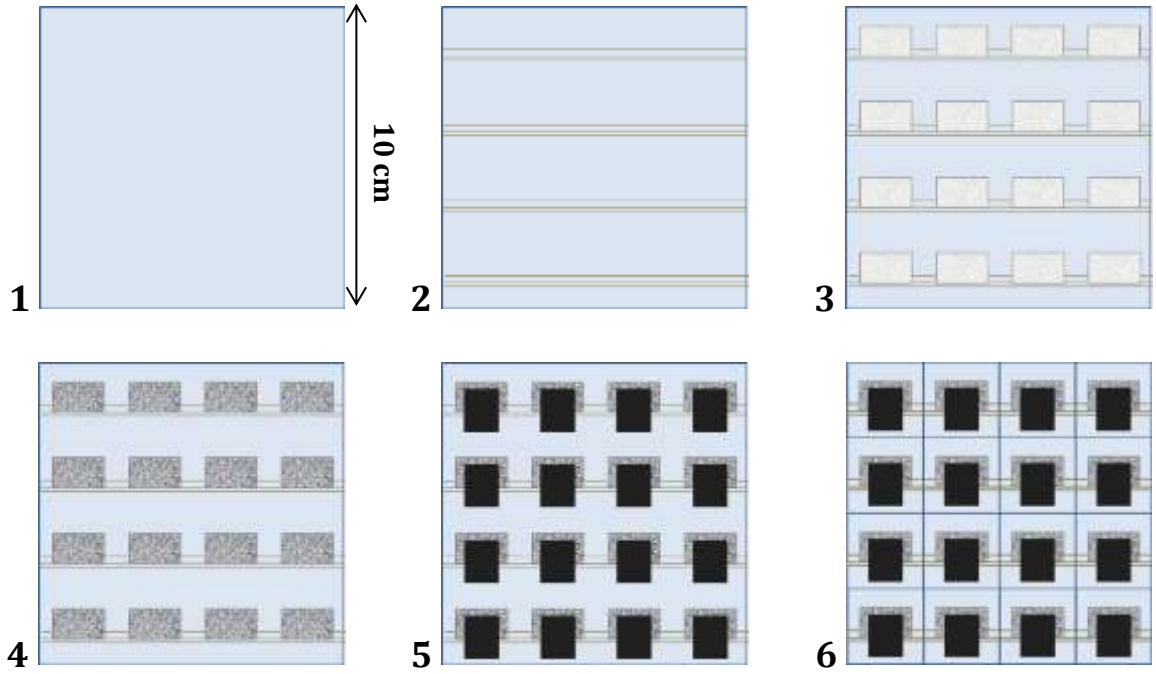

Figure III-1: Schemes representing the different steps for the perovskite solar cells samples preparation using a commercial FTO/glass plate. The different steps are 1) FTO/glass commercial plate cleaning 2) laser lines ablation to define the patterns areas 3) mesoporous TiO_2 4) ZrO_2 and 5) graphite 6) deposition

III.1.1. c-TiO_2 Deposition on Commercial FTO/Glass Substrate

The Electron Transporting Layer (ETL), which is a compact Titanium dioxide (c-TiO_2) is obtained by Spray Pyrolysis Deposition (SPD) technique on FTO/glass substrate.

The Spray pyrolysis consists in a deposition of a nebulized precursor on a hot substrate. In our work we deposit a TiO_2 precursor onto a heated substrate (glass with FTO conductive layer). The substrate is carried at high temperature on hot plate (470 °C) and nebulized solutions decompose to final material on the substrate (Figure III-2). The precursors used for the oxide is a commercial Tetraisopropyl orthotitanate product from TCI. The nanostructure parameters (particle size, shape, thickness) are defined by controlling the spray energy (gas inlet to nebulizer, gas flow pressure), droplet size of the precursors, duration of spray, distance between the spray gun and the substrate, and the temperature of the hot plate and substrate using manual or automated control systems [120]. In this protocol, the SPD is realized manually and temperature, volume and pressure have been optimized to obtain a dense TiO_2 layer on FTO/glass substrate of about 30 nm thickness on average. The Spray pyrolysis is very useful for the preparation of thin films at large scale, it's also a versatile deposition method that is simple, cost effective and can be adapted to large area deposition [121].

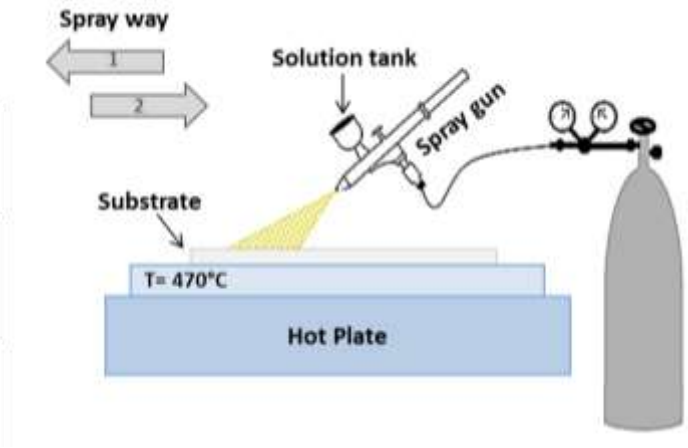

Figure III-2: The Spray Pyrolysis Deposition (SPD) technique illustration for the c-TiO_2 deposition on the FTO/Glass substrate

III.1.2. Deposition of the Different Porous Layer by Screen-Printing Technique

The next layers deposited on the top of the c-TiO_2/FTO/Glass substrate for the perovskite solar cells upscaling are essentially obtained by the same technique, which is the screen-printing.

Screen printing is a deposition process whereby a screen with specific mesh or patterns is used to transfer paste (usually commercial) onto a substrate. A squeegee is moved across the screen to fill the open mesh apertures with paste, and a reverse stroke then causes the screen to touch the substrate momentarily along a line of contact (Figure III-3-1). This causes the paste to wet the substrate and be pulled out of the mesh apertures as the screen springs back after the squeegee has passed (Figure III-3-2). After the screen-printing deposition the substrate is placed in a gas fired dryer (screen-printing conveyor) heated over 100 °C to remove all excess of solvent from the paste to obtain dry patterns (Figure III-3-3). Several screens can be used to produce different designs on the substrate. The thickness and the size of patterns deposited on substrate correspond to the patterns on the screen. The substrates and screens have original patterns to align correctly the device.

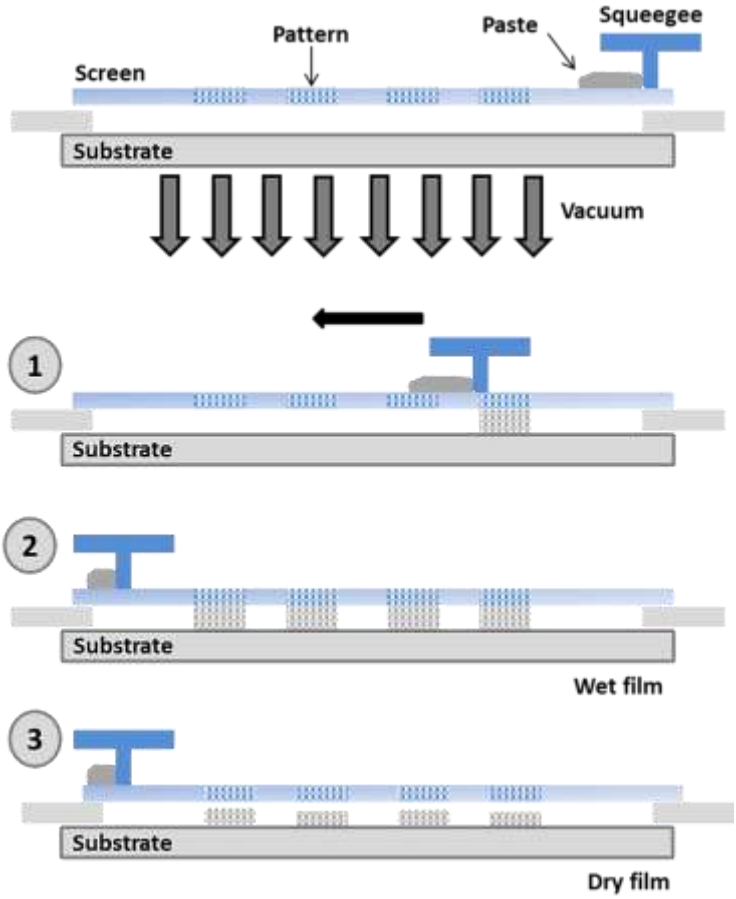

Figure III-3: Image describing the screen-printing deposition principle. (1) Paste deposition onto the substrate through the screen (2) transfer of the screen patterns on samples (3) patterns after drying.

The TiO_2 and ZrO_2 nanopowders paste are deposited successively with the same screen (Figure III-1-2), while the graphite paste has another screen that shifts the layer to the top contact zone (Figure III-1-5). All the used pastes are commercial products from Dyesol or Solaronix companies. After the TiO_2 and ZrO_2 layer deposition, the substrate is dried in a screen-printing conveyor and then annealed at 500 °C while the carbon layers are annealed at 400 °C. This final heating treatment leads to get the mesoporous TiO_2 – ZrO_2 layer and top carbon contact.

Finally, the FTO/glass plate with c-TiO_2/m-TiO_2/m-ZrO_2/graphite deposited onto the delimited surface is separated with a manual glass cutter to obtain sixteen samples of $2.5 \times 2.5 cm^2$ ready to be filled with the perovskite light absorber material for PSC application (Figure III-1-6). The active area of the cells is 0.4 cm^2; the Figure III-4 and the Figure III-5 represent respectively the perovskite solar cell sample from the top view and the side view with the different layer thicknesses of the PSC before any infiltration of perovskite precursors. The advantages of the fully printable carbon based solar cells preparation are the easy process preparation, low cost, good reproducibility of the cells and the infiltration of perovskite after all upscaling elaboration [99], [100], as opposed to the spiro-cells which is a layer by layer deposition with perovskite layers in the middle of the cells [72].

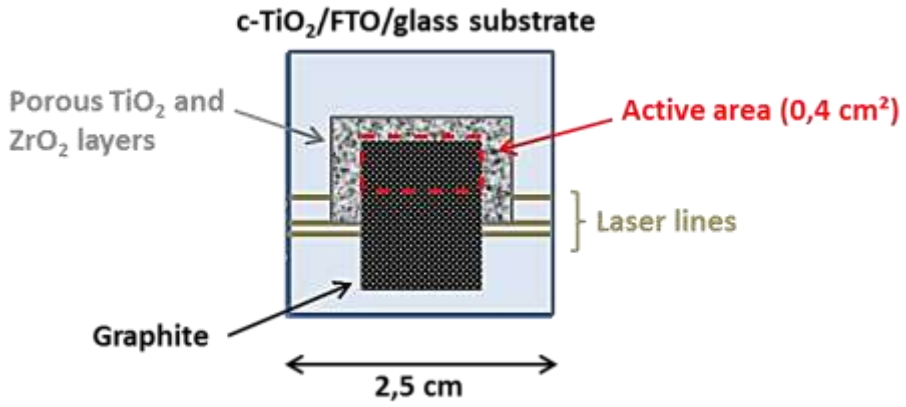

Figure III-4: Representation from the top view of the printed monolithic carbon-based perovskite solar cell ready for light absorber material infiltration

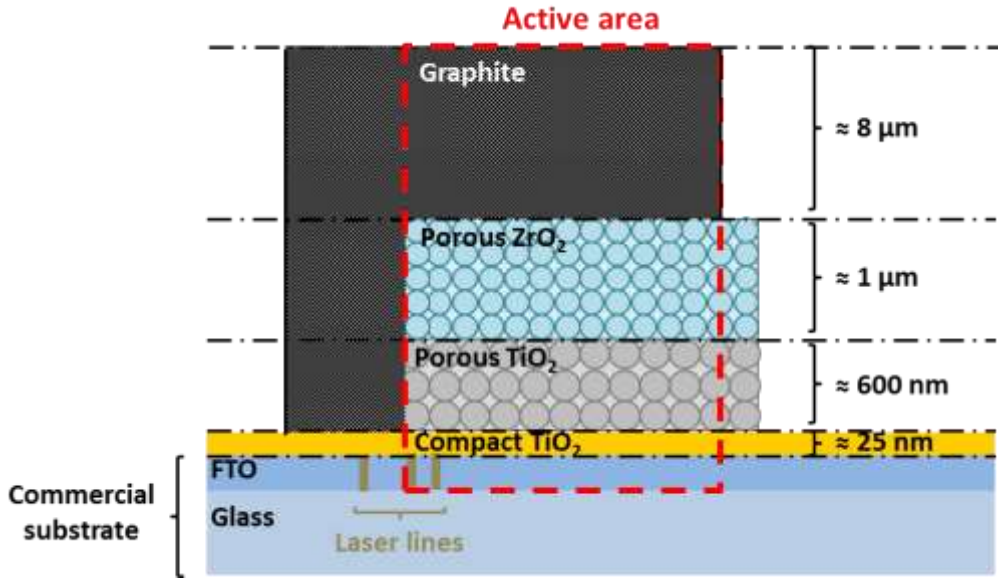

Figure III-5: Representation from the top view of the printed monolithic carbon-based perovskite solar cell

III.1.3. Perovskite Precursors Infiltration

The perovskite crystals formation inside the porous layers is performed by a chemical way using the one step process.

III.1.3.1. The Solution Preparation

The protocol for the perovskite preparation follows the one step deposition process; which means there is only one solution with all needed organic and inorganic precursors. The chemical compound of the perovskite crystals is the common Methyl Ammonium Lead Iodide ($MAPbI_3$ – MAPI). The precursors used for this perovskite formation is the Methyl Ammonium Iodide (commercial MAI salt from Sigma Aldrich), Lead Iodide (PbI_2 product from TCI). Additionally Ammonium Valeric acid iodide (5-AVAI from Sigma Aldrich) completes the preparation. The 5-AVAI helps increasing the connectivity between perovskite crystals and the mesoporous TiO_2, 5-AVAI also acts as a surfactant and modifies the wettability of the components thus increasing the adaptability to surface during the deposition process [71], [122]. The three commercial products are weight and dissolved in gamma-butyrolactone (GBL) solvent to obtain a solution concentrated

at 1.2 M. The solution is prepared in a small vial then stirred with a magnetic barre at room temperature during two hours inside a glovebox, (moisture level < 10 ppm H_2O) to obtain homogenously dispersed precursor in GBL solvent.

III.1.3.2. Perovskite Light Absorber Infiltration Protocol

The drop-casting process is simple, low-cost, versatile, and potentially scalable. The perovskite precursors are infiltrated through the porous layers present in c-PSC structure.

In principle, the film thickness depends on the volume of solution used and the precursors concentration; both of them can be easily varied. The volume is determined by a ratio depending on the area to fill; i.e. 1 µL by 0.1 cm^2 of active area, which corresponds to 4 µL in our monolithic cells configuration. The samples are previously heated at 400 °C and cooled down at room temperature to remove any humidity that could be stored in porous area. Then the first step is to improve the connection of both electrodes by adding an ultrasonically coupled solder alloy (MBR electronics-USS-9210 Ultrasonic Soldering System) (Figure III-6-1). This has to be proceeded before perovskite infiltration due to high temperature process (400 °C). The following step is to delimit the precursor's infiltration zone around the active area and carbon with Kapton® tape (Figure III-6-2). It is essential not to tape on the graphite because it could be completely easily removed with the tape. The solution is dropped out of in glovebox at room temperature on the active area and tilted for 2-3 minutes with an angle about 30° to increase the infiltration to porous layers from the side (Figure III-6-3). Then the sample is annealed at 50 °C for the solvent evaporation and perovskite crystals formation inside the pores of the m-TiO_2 and m-ZrO_2 layers [64], [68], [123]. To complete the cell, a silver large band is deposited on each soldered electrodes to promote a better contact (Figure III-6-4).

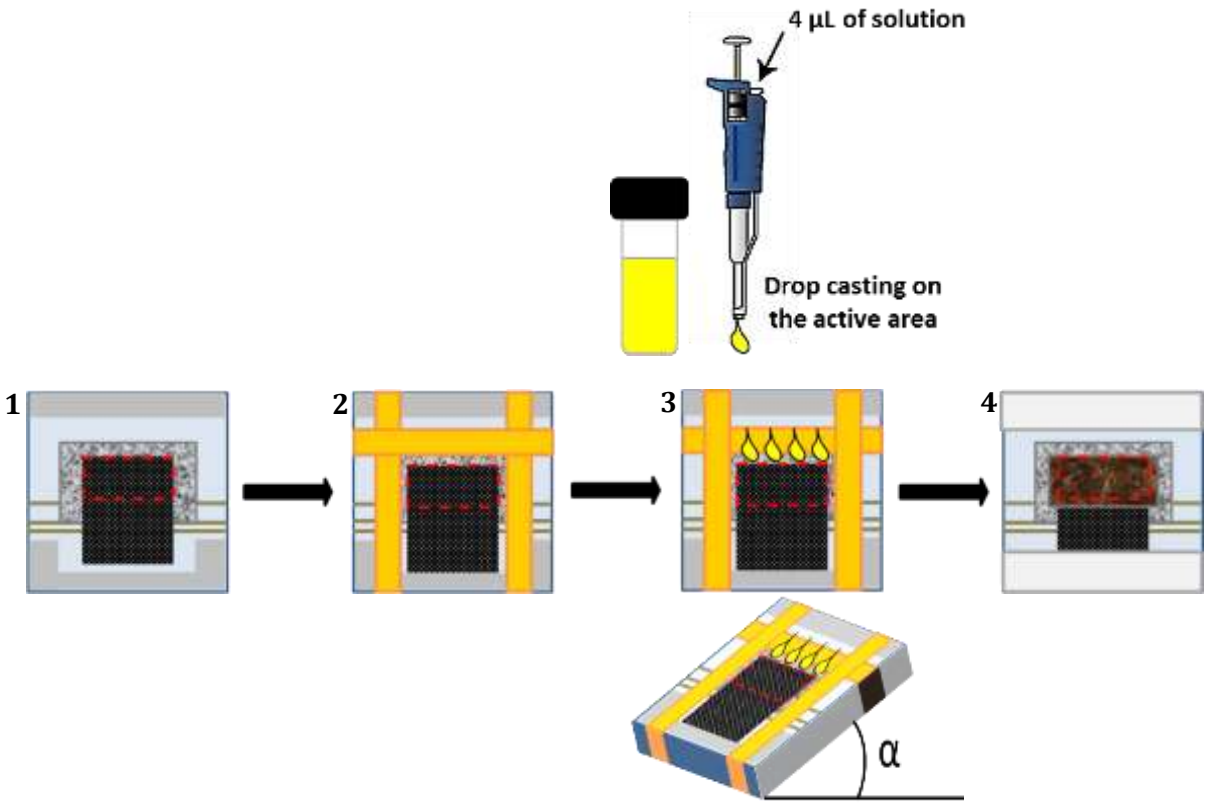

Figure III-6: Scheme illustrating the perovskite precursors infiltration in the porous layers of the solar cell by the drop-casting method

The precursor's infiltration and the crystallization of perovskite crystals after the drop casting process are followed by different steps; first the samples are covered with a glass lid avoiding air contact; for a period of 30 min at room temperature (Figure III-7-1). This allows the precursors solution to go in deep through the different porous layers of the cells. Then the covered samples are placed on a hot plate heated at 50 °C for 30 min with the lid (Figure III-7-2) and for 60 min more without the lid (Figure III-7-3). The lid helps keep the samples in solvent atmosphere to allow a homogeneous crystallization.

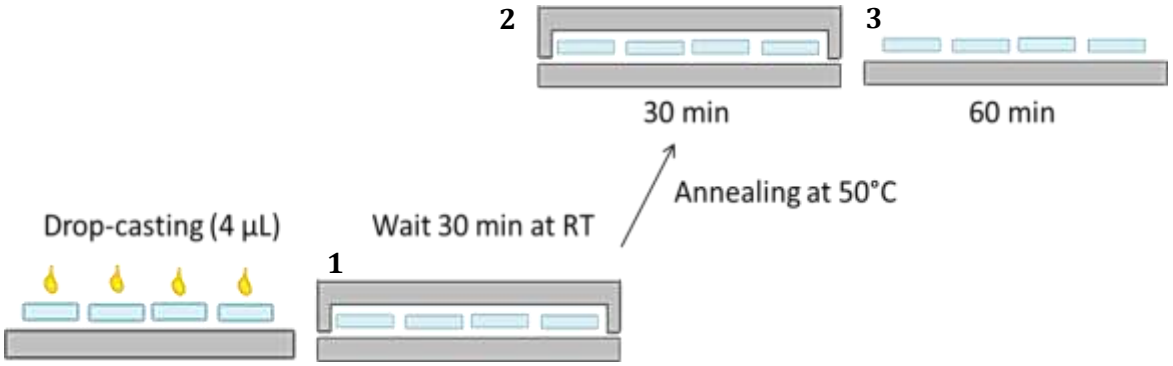

Figure III-7: Scheme explaining the different steps for the perovskite precursor infiltration and the crystals formation in the porous layers of the solar cell by the drop-casting method

III.2. PSC Characterizations Section

The results of characterizations listed below are either for the layers of the PSC or the complete cell. The working principles of all characterization techniques are described in Appendix section. The results shown below concerning the PSC characterization respect the order of the complete cell preparation.

III.2.1. The Compact TiO_2 ETL

The first characterized layer concern the one deposited by spray-pyrolysis on FTO substrate. It is the compact n-type TiO_2 film (ETL-Electron Transporting Layer). The aim is to obtain a homogenous and thin layer conformational to the FTO surface with its important roughness, about ~100 nm (Figure III-8-a). We can clearly observe that the thin ETL layer match properly with the FTO surface (Figure III-8-b).

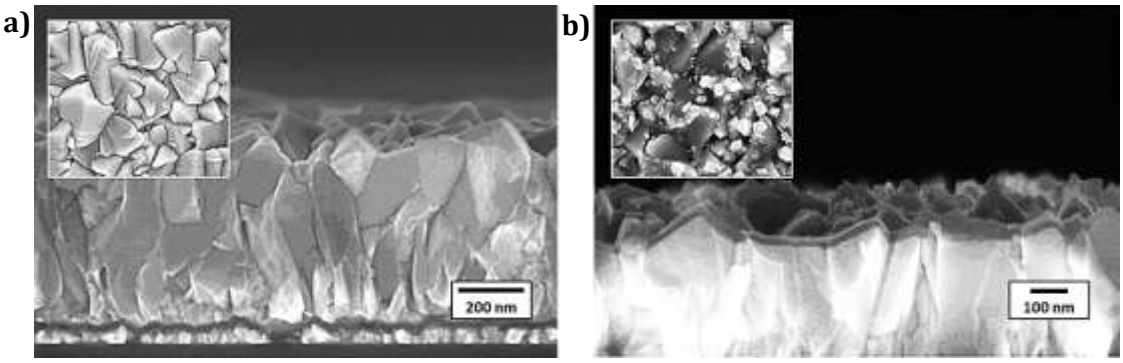

Figure III-8: SEM images of (a) the FTO commercial substrate and (b) c-TiO_2 thin layer after the deposition

The Scanning Electron Microscopy (SEM) technique allows the observation of surface morphology from top and side view and the layer thickness as well (Appendix VIII.1.4.1). In addition, the Atomic Force Microscopy (AFM) in tapping scan mode (Appendix VIII.1.4.2) gives information on surface topography, roughness and phase analyzes. The SEM and AFM images (Figure III-9 and Figure III-10) enable to confirm that we obtained a homogenous c-TiO_2 compact layer that fits closely to the FTO surface.

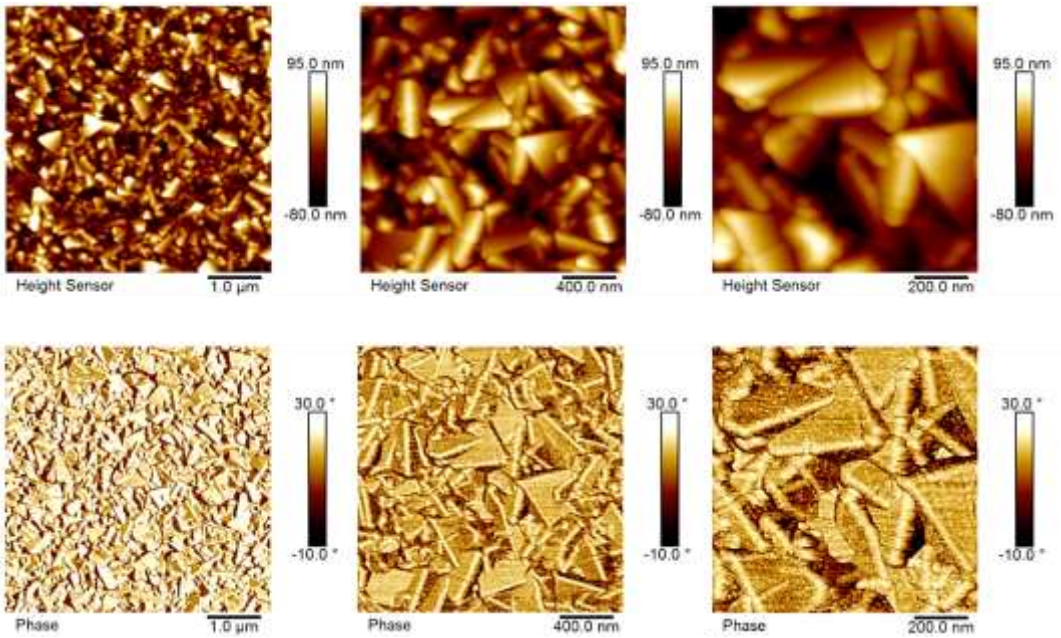

Figure III-9: AFM images of FTO substrate topography (Top images) and phase (bottom images) scans at different scale barre

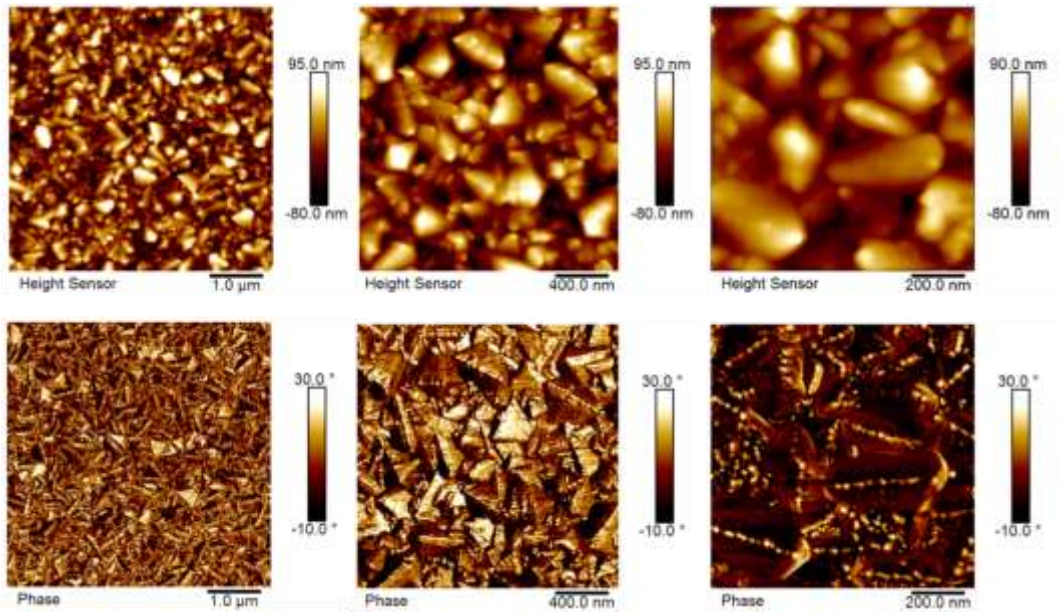

Figure III-10: AFM topography (top images) and phase images (bottom images) of c-TiO_2 deposited by SPD on FTO substrate at different scale barre

The root-mean-square surface roughness is about 33.4 nm for the FTO and 32.1 nm after c-TiO_2 deposition. This small value change means that the surface topography is almost similar before and after the ETL deposition on FTO anode. The phase analyses scan determine the surface composition, from the images we can clearly see a unique phase of c-TiO_2 layers, the unique contrast of the image means an homogenous deposition and covering on the rough FTO surface. Also, the AFM and SEM images of the deposition show small particles formed on the surface due to the spray deposition technique.

The thickness of the c-TiO_2 was measured by spectroscopic ellipsometry technique (Appendix VIII.1.5). The refractive index and the film thickness values are represented in Figure III-11:

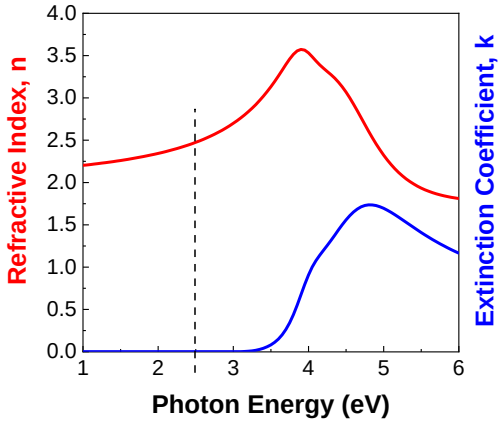

	n (at 2,5 eV)	Thickness (nm)
c-TiO_2	2,47	30.6 ± 1.2

Figure III-11: Ellipsometry measurement of the c-TiO_2 layer thickness and refractive index

The thickness is around 30 nm and the refractive index at 2.5 eV correspond to an anatase TiO_2 [124].

The crystal structure is determined by X-Ray Diffraction (XRD) measurement (Appendix VIII.1.1). The recorded diffractogram (Figure III-12) confirmed that the layer is well crystallized as TiO_2 anatase, which is the most stable phase for photo-active application and n-type conduction [125]. No other phases could be observed in the detection limit of the XRD technique.

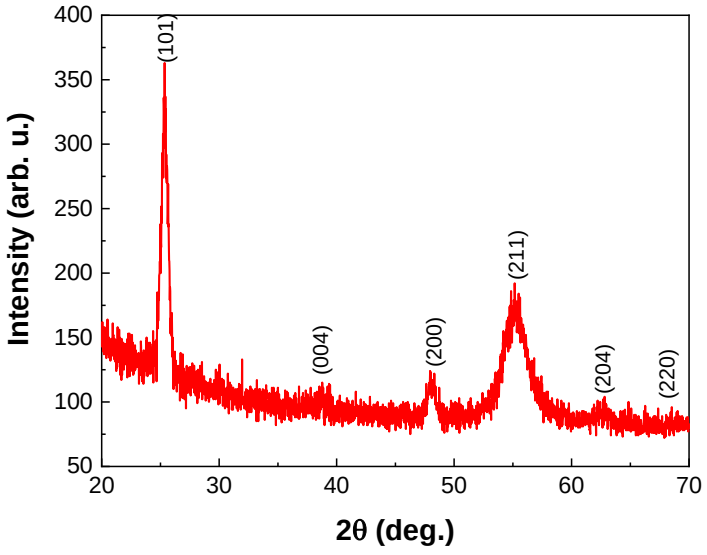

Figure III-12: XRD diffractogram showing the presence of anatase phase obtained for the TiO_2 by spray pyrolysis deposition annealed at 470 °C (JCPDS 00-021-1272)

The transmittance of the titanium dioxide thin film has been determined by the UV-Vis spectroscopy technique (Appendix). The light transmittance of the layer has to be as close as possible to the FTO glass substrates to permit the photons go through the ETL and reach the light absorber material that photo-generate the carriers. The absorbance peak of MAPI is around 750-800 nm [60] and around this value we can observe that the transmittance of c-TiO_2 is near to the FTO/glass substrate with less 5 % of difference (Figure III-13-a). Also, using these data we can determine the optical band gap from the Tauc equation (Figure III-13-b) [126].

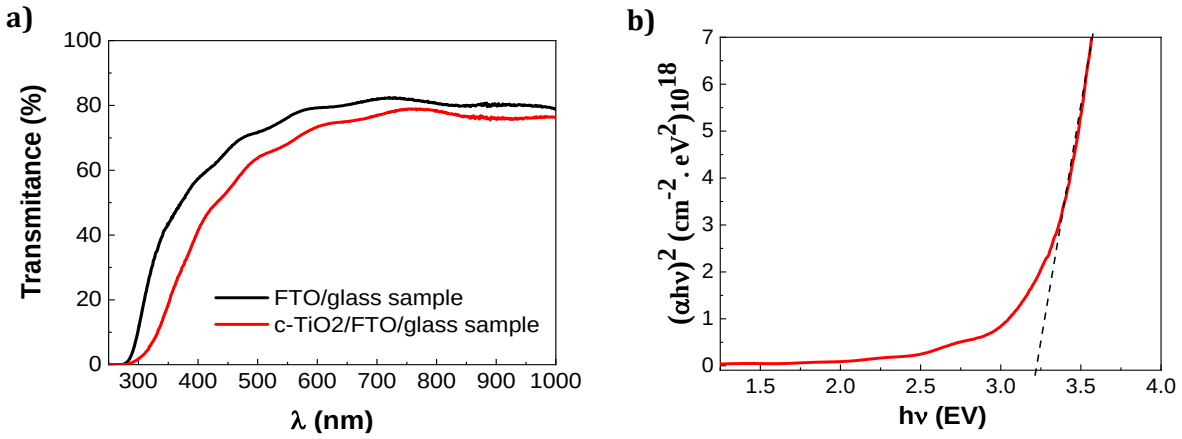

Figure III-13: (a) The Transmittance curve of the c-TiO_2 thin film deposited on FTO/glass substrate (b) Tauc plot of this TiO_2 anatase layer

The optical band gap energy E_g of the layers can be determined with the help of Tauc plots and can be deduced through plotting $(\alpha h\nu)^2$ versus to the band gap energy E_g (α: absorption coefficient, h: Planck constant, ν: photon energy) [127] . The estimated band gap value of the TiO_2 ETL is 3.18 ± 1.2 eV, which is close to the known 3.2 eV value for TiO_2 anatase [125].

III.2.2. The Porous TiO_2, ZrO_2 and Graphite Layers

The subsequent characterization concerns the mesoporous TiO_2 and ZrO_2 layers and graphite film for the HTL and back contact electrode deposited by screen-printing technique and annealed at 500 °C and 400 °C respectively. The structure of the sample following the different scaffolded layers obtained on c-TiO_2/FTO/glass substrate has been observed by SEM in cross section (Figure III-14).

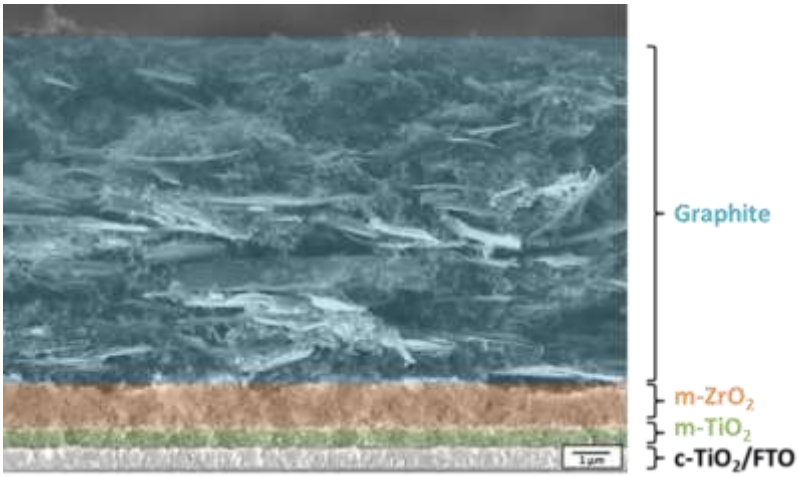

Figure III-14: SEM image of the perovskite cell structure with the different porous layers before light absorber material infiltration trough in

We observe the stacking of different deposited layers with a thickness on average of ~ 600 nm for m-TiO_2, ~ 1 µm for the m-ZrO_2 and ~ 7-8 µm for the graphite.

The mesoporous layers have a pore size around ~ 25 nm (Figure III-15-a-b) and the graphite film shows some porous particles and flakes between the structures (Figure III-15-c).

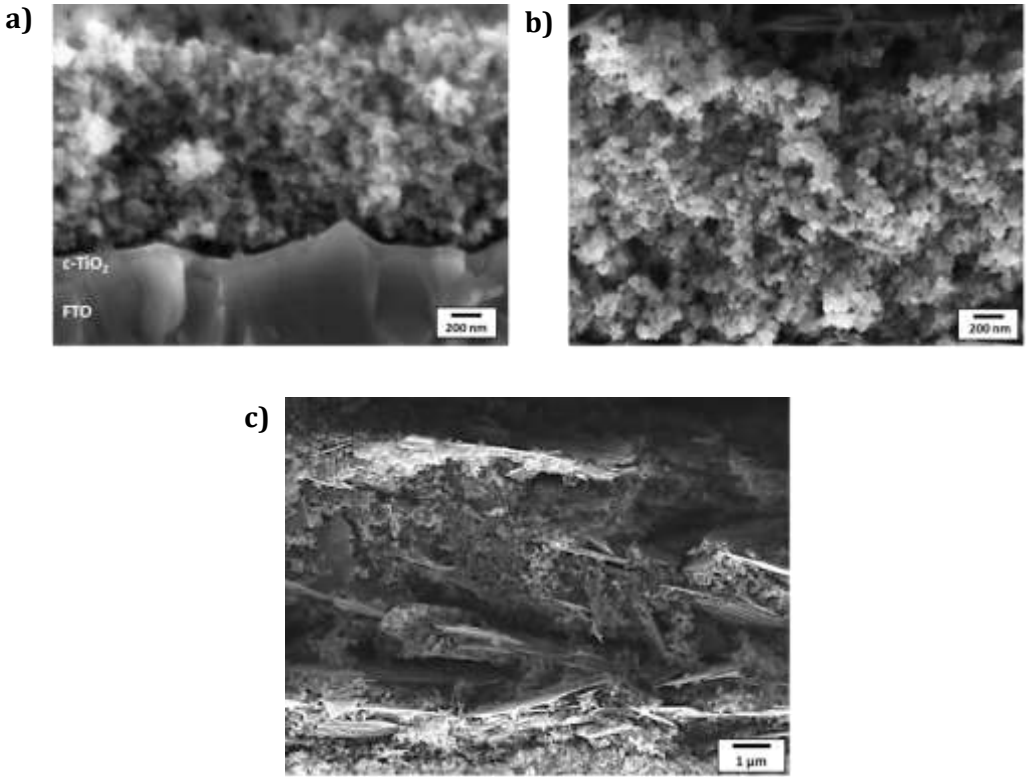

Figure III-15: SEM images of (a) m-TiO_2 (b) m-ZrO_2 and (c) graphite structure present in the PSC before perovskite precursors infiltration

The crystal structure of the stacking was investigated by XRD; the diffractogram in Figure III-16 shows the patterns of TiO_2 anatase, ZrO_2 and graphite. This means that the commercial paste deposited by screen-printing crystalizes well after the different annealing.

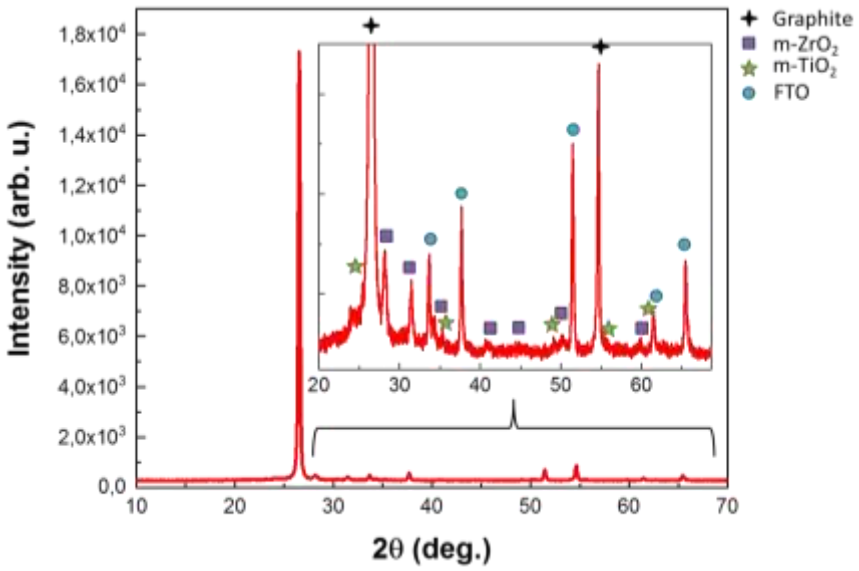

Figure III-16: XRD patterns of the glass/FTO/TiO_2/ZrO_2/graphite stack obtained before perovskite precursors infiltration (JCPDS 00-021-1272/TiO_2 and 00-013-0307/ZrO_2)

To summarize, before the infiltration of the active compound we build the base of perovskite solar cell structure which is composed of:

- glass coated with a FTO conductive layer (commercially available)
- a uniform and dense layer of TiO_2 around 20-30 nm deposited by spray pyrolysis
- a mesoporous TiO_2 layer of about 600 nm, then mesoporous ZrO_2 layer of 1 µm, which serves as spacer layer
- a graphite contact electrode with a thickness larger than 6 µm and processed by screen-printing technique.

III.2.3. Perovskite Light Absorber Characterization

III.2.3.1. Structural Characterization

The up-scaling of the solar cell was carried out in the previous part, with the different structures; the final step will be the infiltration of the perovskite precursors in the porous layers. The perovskite material was first investigated in single layer form in respect to its structural and optical properties. The perovskite material is prepared using the one step method described previously (Figure III-6). The structural properties were characterized by XRD measurement performed on MAPI perovskites film deposited directly on glass substrate. Figure III-17 shows a typical diffractogram recorded on such a layer.

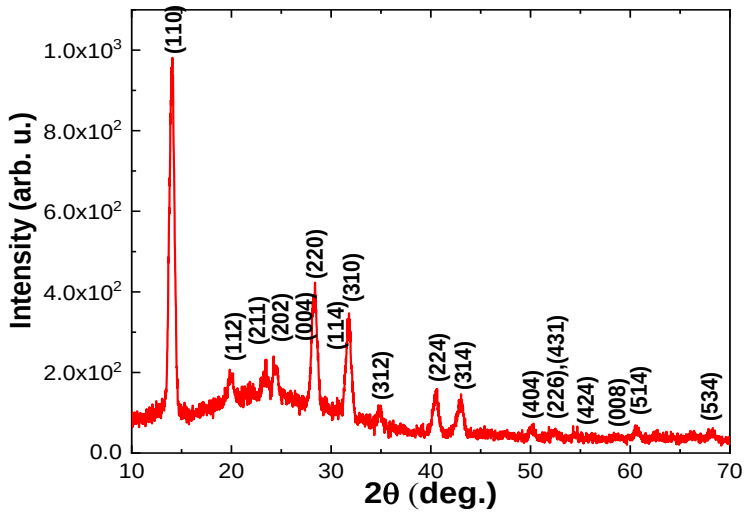

Figure III-17: XRD patterns of the perovskite Methyl-Ammonium Lead Iodide (MAPI) deposited by one-step method on glass substrate (JCPDS 01-084-7607)

The main diffraction observed for a 2θ angle of ~ 14° is specific to the perovskite structure used as light absorber material. The crystallite size estimated from the full width at half maximum of this peak using the Scherrer formula is about 79 ± 4 nm. No peak of PbI_2 at ~ 12 ° indicating that the PbI_2 is well integrated in the MAPI structure. The lattice parameter was determined with the Fullprof software. The parameters values are a = b = 8.859 ± 0.09 Å and c = 12.672 ± 0.08 Å.

These results are in agreement with those reported in JCPDS datasheet on MAPI which indicates a crystalline structure with a I4/mcm (140) space group for this compound and lattice parameters a = b = 8.839 Å and c = 12.695 Å and α = β = γ = 90°. The structure is tetragonal with Pb^{2+} in the octahedral site.

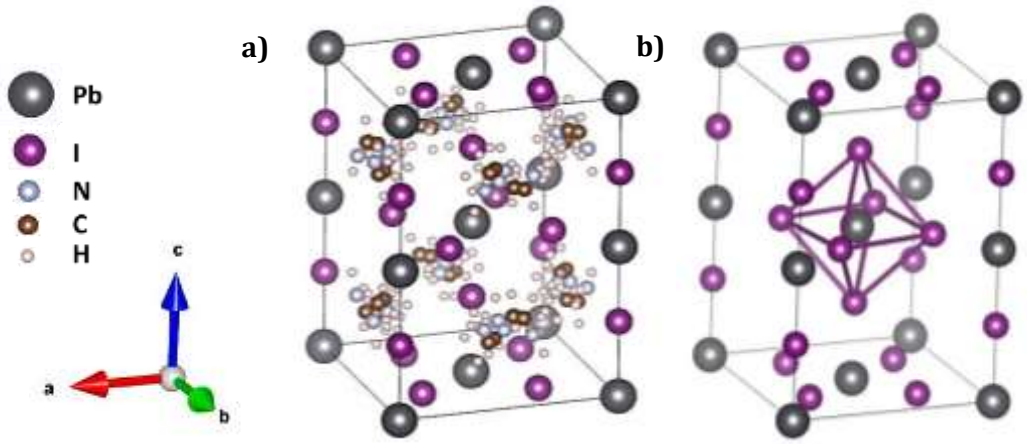

Figure III-18 : Representation of the tetragonal perovskite structure of the MAPI (a) with all elements and (b) without the CH_3NH_3 molecules. The Pb^{2+} ion is well inside the octahedral site (Structural representation realized with Vesta software using JCPDS 01-084-7607 lattice parameters and atoms coordination)

More insight on the structural properties of the MAPI layer was obtained by Transmission Electron Microscopy (TEM). The sample preparation required for such observations is described in Appendix VIII.1.3. High resolution images show clearly that the MAPI is well crystallized, and that the size of the grains is in the order of few tens of nanometer (Figure III-19-a). Atomic planes are easily visible in Figure III-19-b, with an interplanar distance of 3.12 Å corresponding to the (220) plane.

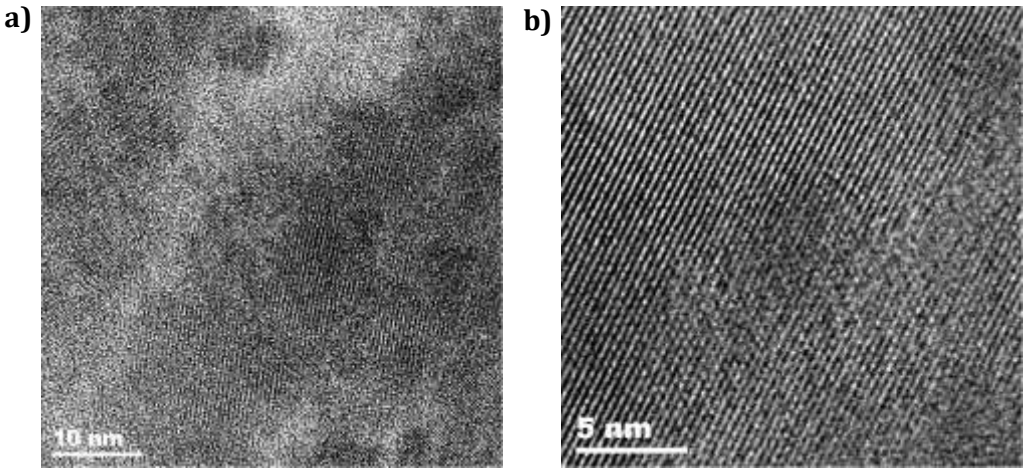

Figure III-19 : TEM images of the MAPI crystals deposited on copper grid

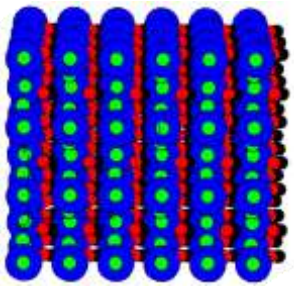

Figure III-20: Illustration of atomic plane in the MAPI structure made with CaRIne software

The crystalline structure has been sketched using the Carine software, which allows calculating: X-Ray diffraction, reciprocal lattices in 3D and 2D etc.

From the JCPDS datasheet parameters we build the atoms order thanks to this software (Figure III-20), the atom disposition are linear and alternated with inorganic (blue-green) and organic (red-dark) elements similar to dark (organic) and bright (inorganic) lines in the TEM images.

Gatan is the industry standard electronic microscope software used for experimental control and analysis to obtain high resolution images at atomic scale, reciprocal lattices patterns… The

crystalline structure of the different grains observed by high resolution TEM can be further examined using FFT (Fast Fourier transform) thanks to this software. This gives the corresponding diffraction pattern (reciprocal space) of some selected region and which can be compared with the theoretical pattern calculated using the Carine software.

Different areas in the high resolution TEM images were selected for the FFT analysis. The results for two such distinct regions are represented in Figure III-21 and Figure III-22. These regions present two different crystal orientations allowing to obtain a, b, c lattice parameters. The first one corresponds to a cubic representation following c axis orientation, so we can observe a cubic patterns (Figure III-21-a). The second one gives rise to a rectangular patterns for both a or b axis orientation (Figure III-22-a) [128]. It is clearly seen that the experimental diffraction patterns match the patterns drawn with Carine software according to the orientation axis and confirm that the perovskite structure is tetragonal (Figure III-21-b and Figure III-22-b).

The Figure III-21-c and Figure III-22-c are a representation of atoms in the lattices structure.

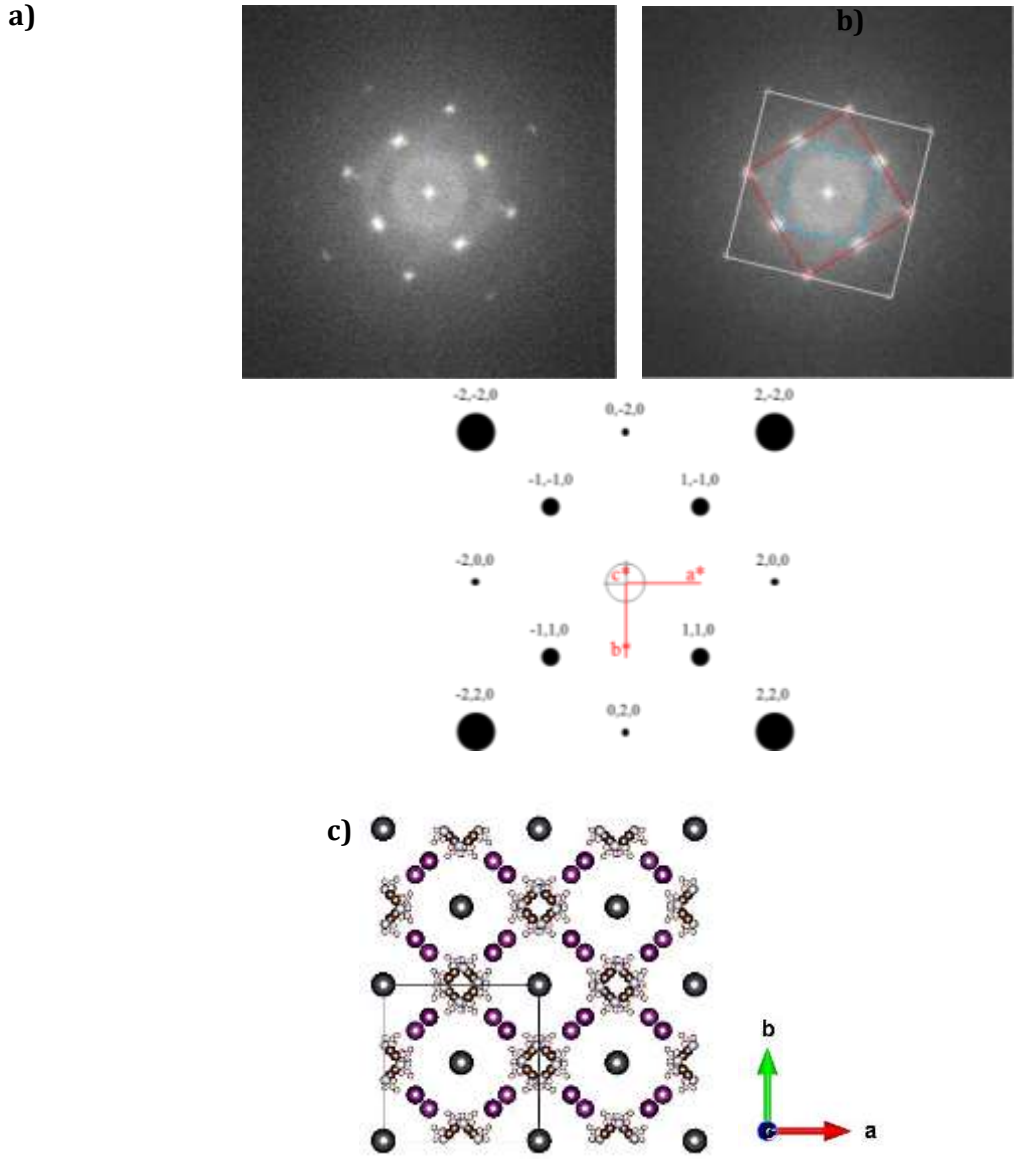

Figure III-21: (a) FFT of the sample at selective area corresponding to c axis with cubic patterns (b) reciprocal space theoretical representation in the same direction (c) atoms position in MAPI lattices according to c axis

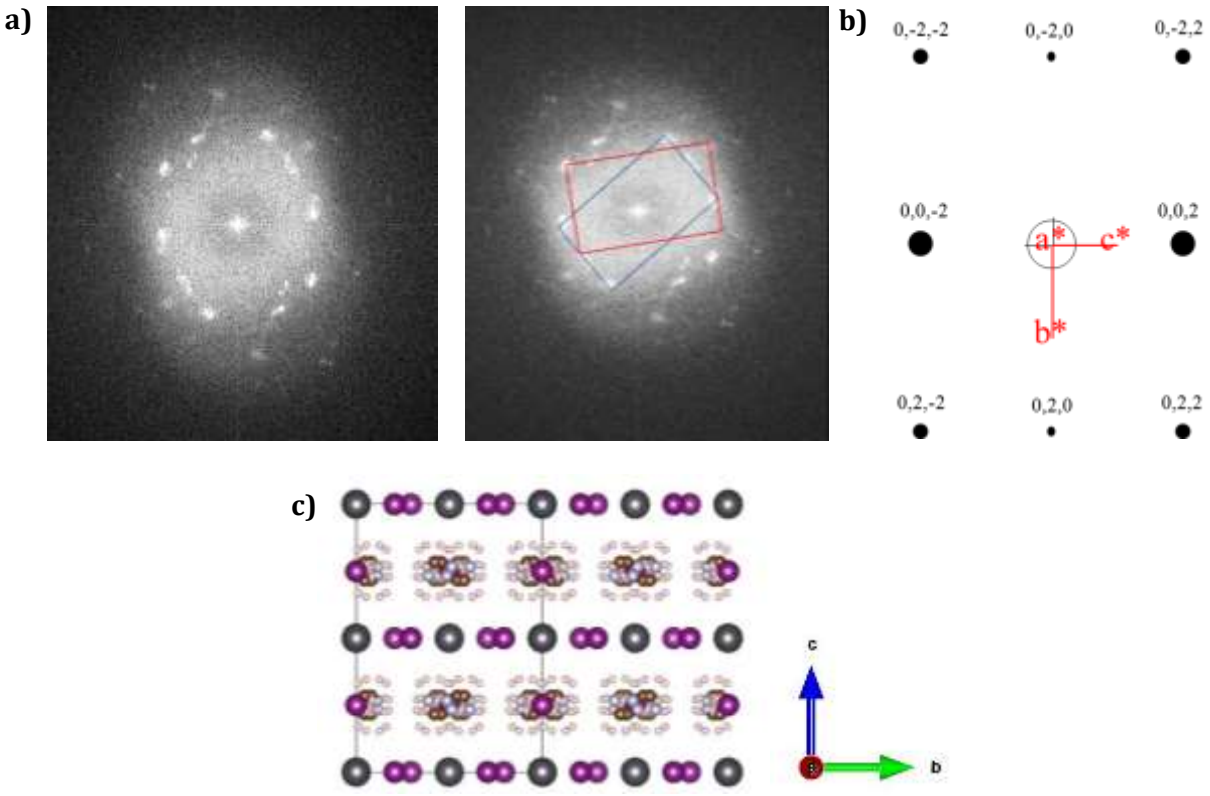

Figure III-22: (a) FFT of the sample at selective area corresponding to a axis with rectangular patterns (b) theoretical reciprocal space representation in the same direction (c) atoms position in MAPI lattices according to a axis

III.2.3.2. Optical Characterization

The optical parameters were obtained by UV-Vis spectroscopy measurements and Photoluminescence (PL) technique (Appendix VIII.1.10). The graphs are represented in Figure III-23:

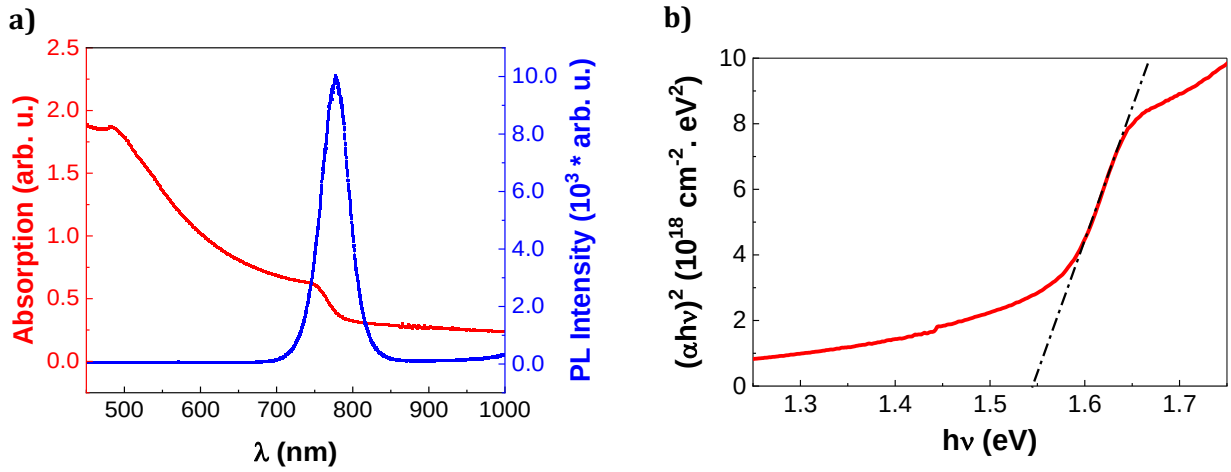

Figure III-23: (a) UV-Vis absorbance of the MAPI film on glass substrate and photoluminescence spectra for the same film (b) Tauc plot of the MAPI film

The PL intensity is maximum for $\lambda \sim 780$ nm and the absorbance step of the MAPI matches with this value as well (Figure III-23-a) [129], [130].

The optical band gap is estimated to be 1.54 ± 0.04 eV, which correspond to the E_g of MAPI in the literature [117].

III.2.4. The Perovskite Solar Cell Characterization

Finally, the fully prepared cell is obtained with the perovskite light absorber infiltration through the porous layers and is ready for measurement of its performance.

III.2.4.1. SEM/EDX Analyzes

The SEM/EDX analyzes confirm that the lead element contained in the MAPI perovskite crystals is present through all scaffolded layers (Figure III-24). This means that the infiltration of the perovskite is homogeneous through the whole stack.

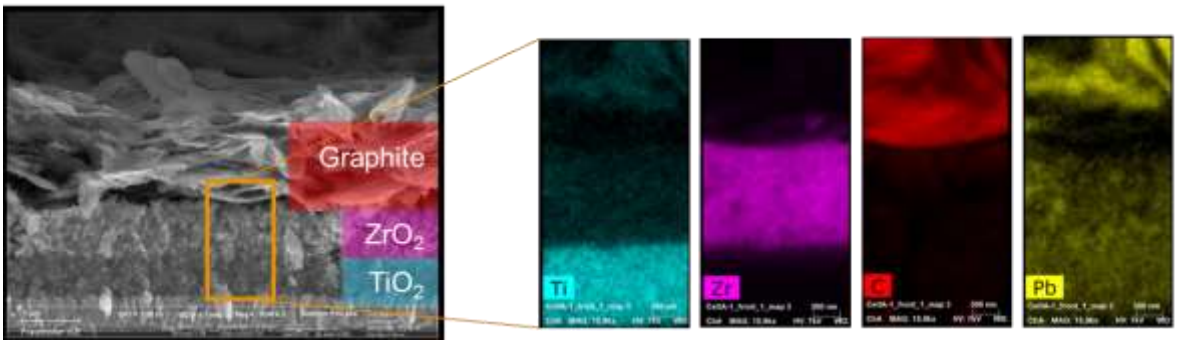

Figure III-24: SEM/EDX in mapping mode images of the complete cell after perovskite precursors infiltration in the porous layers

III.2.4.2. XRD Measurements

The XRD measurements performed on the complete cell confirm that the infiltrated light absorber material has the perovskite structure (Figure III-25). Again we have no indication of PbI_2 or other phases in the detection limit of the XRD technique. The analysis of the HWHM of the perovskite gives a grain size of the order of 28 nm.

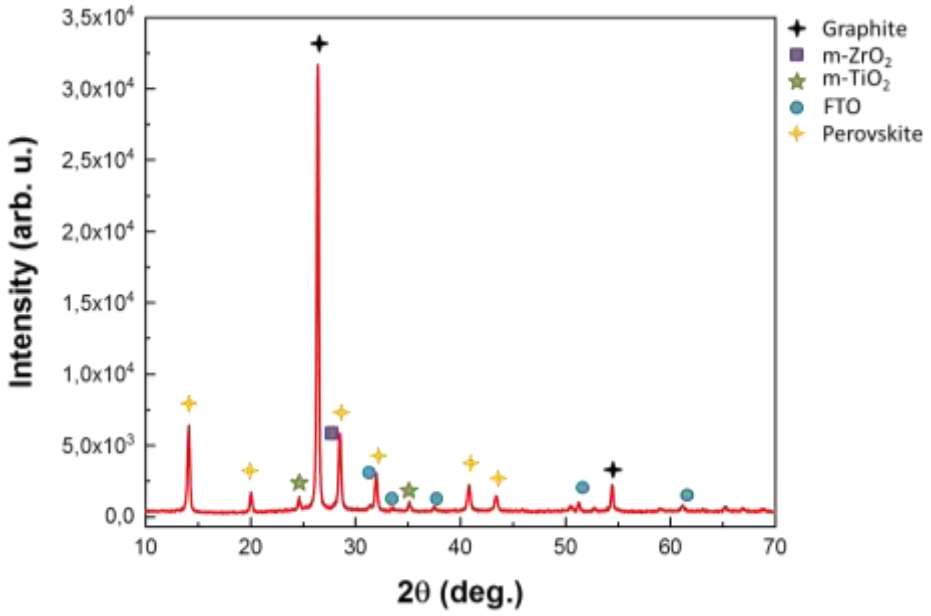

Figure III-25: XRD patterns of the complete cell with all different elements. The mean peaks of perovskite are visible at ~ 14 ° and ~ 20 °, which were not visible before the infiltration (Figure III-16)

III.2.4.3. c-PSC Performances Characterization by I-V Measurements

For the solar cell parameters we use solar sun simulator equipment (Appendix VIII.1.6) to characterize the PSC performance and to determine the efficiency of the cell.

The cell is illuminated from the glass and the contacts are on the top of the cell, while we need to contact them for the electrode in aim to obtain the I-V curve. To allow an optimal illumination and contact of the cell at same time we use a device that permits to fix the cell from the back (Figure III-26). Also, to enhance the contact between the cell and the device two silver bands are deposited on both electrodes of the cell (FTO and graphite).

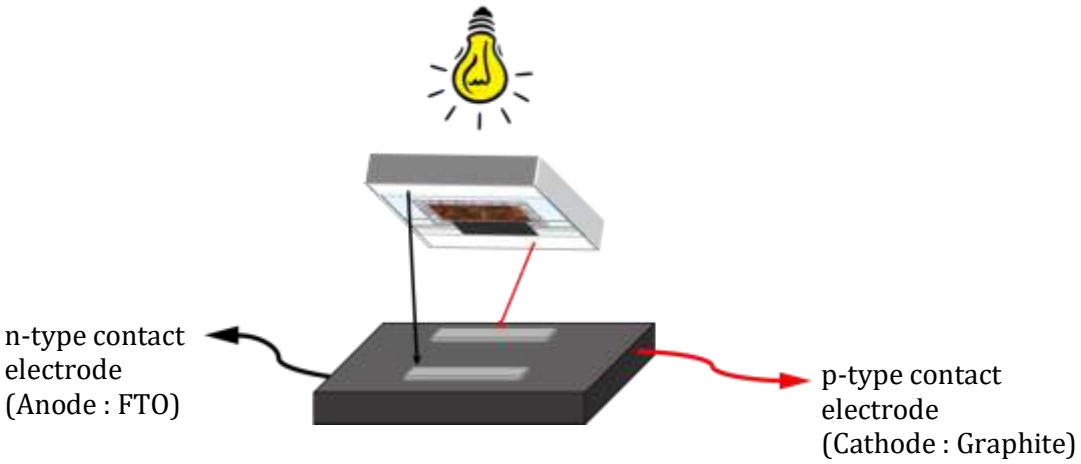

Figure III-26: Illustration of the device used for the I-V curve measurement when the PSC is exposed to light at AM1.5 condition

A series of six reference cells prepared in same conditions was measured to obtain statistics on I-V curves for the determination of solar cell parameters and performances reproducibility. The results are presented in "statistical box mode" and each dot represents a cell value from the series (the data representation style is explained in Appendix VIII.1.7). The graphs in Figure III-27 represent the specific value to characterize solar cells performance measured with an applied bias from 1.1 V to 0.1 V i.e. the open circuit voltage (V_{OC}), the short-circuit current (J_{SC}), the fill factor (FF) and the efficiency (ŋ). The different values obtained give an average for the V_{OC} ~ 900 mV, J_{SC} ~ 19 mA.cm^{-2}, FF ~ 52 % and efficiency around 9 %.

The reproducibilty of the cells is medium with an efficiency that ranges from ~ 8 % to ~ 10 %, which is a no negligeable variation.

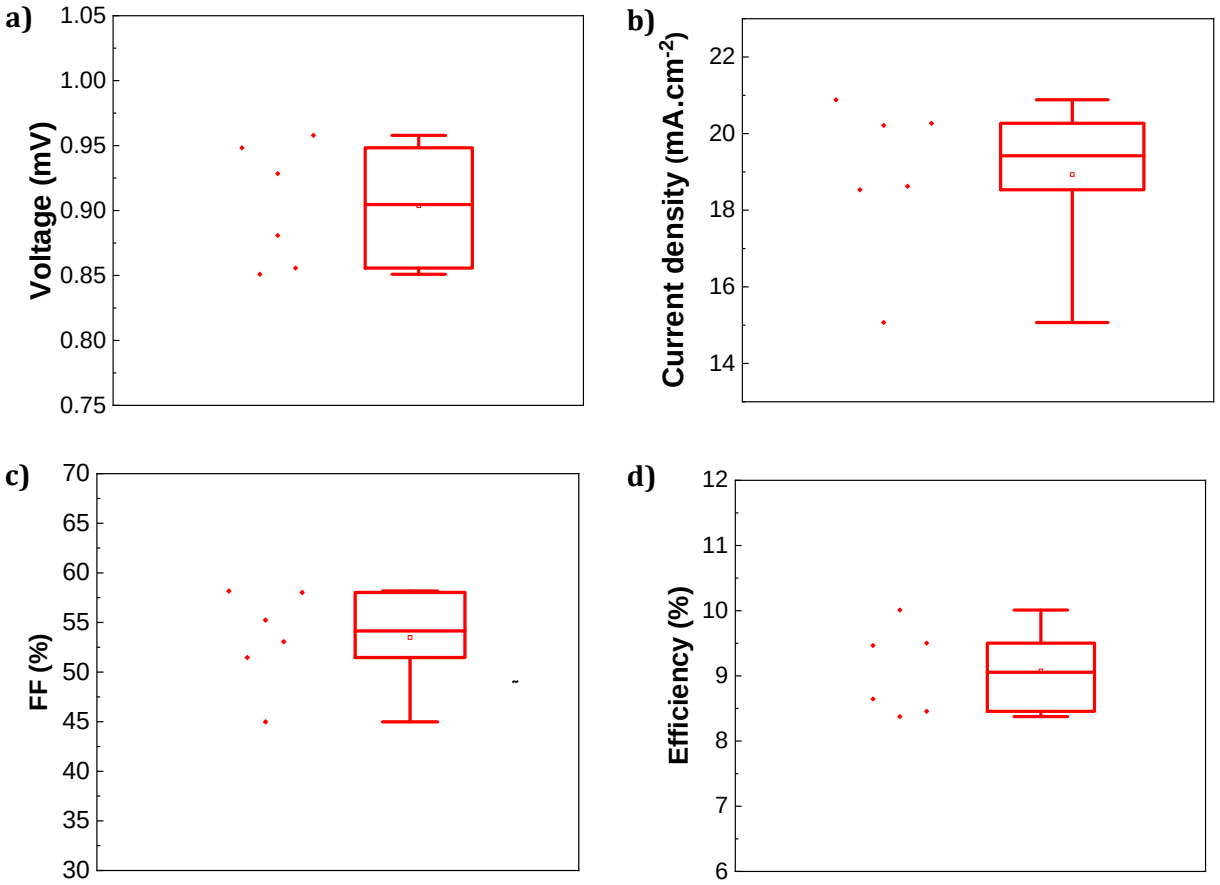

Figure III-27: I-V measurements representing the different specific values for a solar cell as the (a) V_{OC} (Open-Circuit Voltage), (b) J_{SC} (Short-Circuit Courant), (c) FF (Fill Factor) and (d) PCE (Power Conversion Efficiency)

Another important aspect to study related to the PSC characterization is the hysteresis effect with reverse and forward bias. We measured both bias in a cell that matches closely with the experimental PSC parameters values cited above. In the figure below Figure III-28, the I-V curves represent the reverse and forward scans with 50 $mV.s^{-1}$ scan speed (Figure III-28-a). The cell parameters are listed in Figure III-28-b for the reverse scan; we can clearly observe a hysteresis with both scans, the forward curve shows an important decrease of *FF* but small changes for V_{OC} and J_{SC}, which means a drop in efficiency in the forward scan. The hysteresis phenomena result in the overstatement of the performance of PSCs during backward scan, which starts from the bias higher than open voltage and sweeps to voltage below zero. In steady output, the stabilized PCE is lower than the dynamic one, as well as the maximum power point in the I-V curve [61], [131]. The stabilized efficiency (Figure III-28-c) is measured applying a fixed voltage at Maximum Power Point value (V_{MPP}) that corresponds to ~ 600 mV for this cell.

The I-V curve of PSC usually exhibits hysteresis. The hysteresis is generally observed in all three device architectures and regardless of the morphology of the perovskite layer. It is not caused by the presence of a compact TiO_2 layer or due to the hole transport material used and appears to be inherent to the perovskites and associated interfaces. This hysteresis renders standard PCE measurements ambiguous (overall PCE is higher with faster scan rates). Several explanations have been proposed for this phenomenon: very slow trapping and de-trapping of charges, ferroelectric behavior of the perovskites on nanosecond timescale, slow ion migration or displacement, and chemical structural changes [131]–[134]. In this chapter we do not address in detail this explanation.

a)

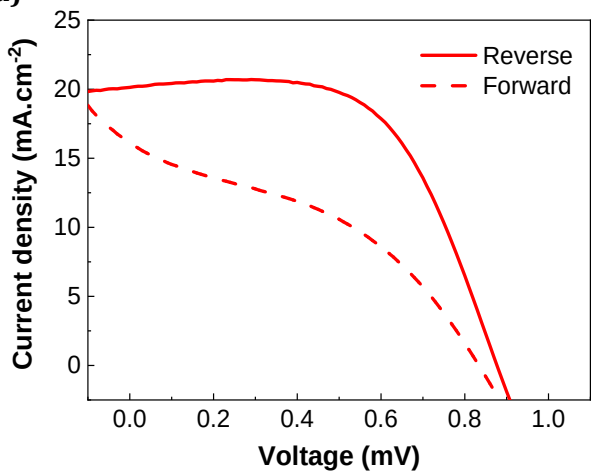

c)

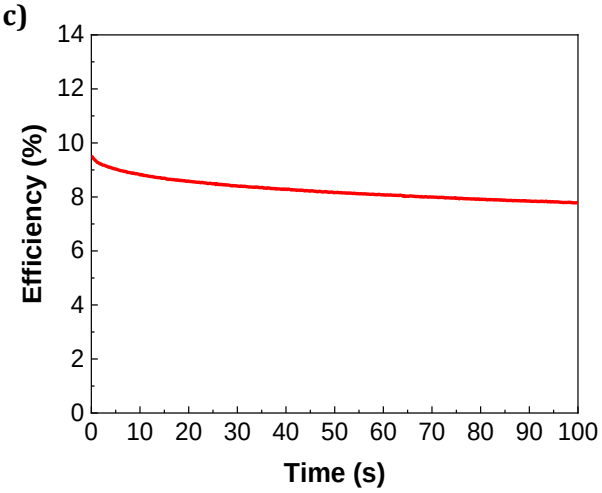

b)

Ref. PSC parameters	
V_{OC} (V)	0,903
J_{SC} (mA/cm²)	18,91
FF (%)	51,06

Figure III-28: (a) I-V curve of a prepared monolithic perovskite solar cell (b) the cell parameters (c) stabilized efficiency

The best efficiencies recorded for fully printable carbon-based PSC in literature are ranging from 15 % to 17 % [95], [96], [135], [136]. The table below (Figure III-29) is a comparison of the reference cell parameters on average that we obtained with similar c-PSC reported in literature.

c-PSC	*Voc (V)*	*J_{SC} (mA/cm²)*	*FF (%)*	*η (%)*
Ref. PSC	0,903	18,9	51,1	9.4
Wu *et al.*	0.990	21.7	70.6	15.1
Hashmi *et al.*	0.875	21.2	74.0	14.3

Figure III-29: Table representing the comparison of fully printable perovskite solar cell parameters with reference cell and c-PSC reported in literature [135], [136]

The comparison of these values shows an important difference concerning the Fill factor (about 20 %). This may explain this efficiency difference as the V_{OC} and J_{SC} remain relatively close. A low FF may be caused by an inhomogeneous interface at the various layers of the cells, improper contact with electrodes, but also by a poor infiltration of the photo-active material which generates resistance in the PSC [34], [45].

Conclusion

This part showed the monolithic carbon based solar cell preparation tools in terms of elaboration and characterization.

We obtained a thin n-type compact TiO_2 layer (~ 30 nm) as ETL deposited by spray pyrolysis. The mesoporous TiO_2 and ZrO_2 films have a thickness of ~ 600 nm and ~ 1 µm respectively and pore size is around 25 nm. The top graphite layer that plays the role of holes transporting layer and back contact is ~ 7-8 µm thick and contains carbon flacks and mesoporous structure in the film.

The perovskite light absorber material has been successfully infiltrated through the different scaffolded layers by the drop-casting technique.

The PSC performances are characterized with I-V measurements, the efficiency ranges from 8 % up to 10 % on average. The reverse and forward scans revealed a hysteresis in the I-V curve. We have no clear explanation to the origin of this effect.

In summary, we have shown in this chapter the complete perovskite solar cell preparation and characterization process. Each layer present in PSC has been characterized in aim to have a reference cell to compare with the new cells coming in next chapters.

IV. Preparation of a TiO_2 Porous Layer by Chemical Coating of PMMA Polymer Beads with a Sol-Gel Solution

The focus of this work is to use cross-linked polymer beads as a template material to build macro-porous film by molding them with a TiO_2 sol-gel precursor solution. Changing the beads size will directly impact the final TiO_2 pore size and morphology of the layer. Porosity becomes easily controllable simply by varying the size of PMMA particles diameter. The pore size will be larger than the mesoporous TiO_2 in order to optimize enhance the infiltration of the perovskite precursors and to obtain larger crystals inside the TiO_2 porous layer and thereby higher efficiency of the PSC.

IV.1. Process Description

The preparation of macro-porous layers by molding polymer beads was carried out in three steps, mostly involving chemical methods. First, the substrate surface is cleaned by plasma treatment, which also helps increase its wettability. Few drops of concentrated bead suspension with a concentration around ~ 20 % in weight are spin-coated on the substrate (2000 rpm during 30 s - Figure IV-1-1). It leads to a thick layer of self-assembled PMMA spheres that is dried for 2 h at room temperature. Next, 150 µL of Ti sol-gel solution (0.5 M) are dropped on the PMMA film. In order to eliminate the excess of solution and to evaporate the solvent, the propionic acid, the sample is spined at 3000 rpm during 180 s (Figure IV-1-2). The self-assembled beads are embedded in the dry sol-gel Ti precursor. A careful heating at 500 °C burns the PMMA and leads to a TiO_2 anatase scaffold film. The voids (macro-pores) are in the same size range as the previous beads. Due to molding of necks in between beads the pores are interconnected (Figure IV-1-3).

The three main steps for the TiO_2 porous layers preparation and characterization will be described in detail now in the next part.

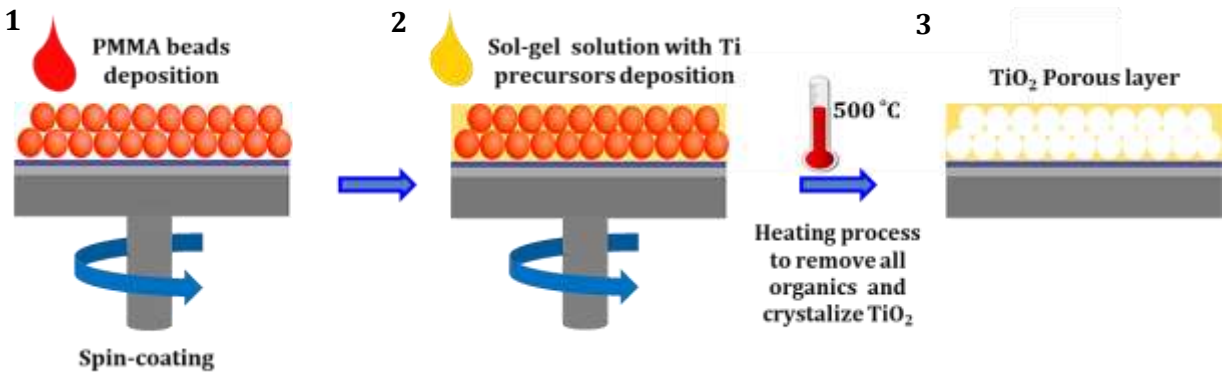

Figure IV-1: Scheme of the different steps to obtain the TiO_2 porous layer by spin-coating with PMMA beads and sol-gel solution [137]

IV.2. PMMA Particles Synthesis and Characterization

Methyl methacrylate (MMA, Aldrich) was passed through a basic alumina column to remove the polymerization inhibitor. Ethylene glycol dimethacrylate (EGDMA, Sigma-Aldrich), poly(vinylpyrrolidone) (PVP, K-90, Sigma, Mw 360000 $g.mol^{-1}$ as given by the supplier), sodium dodecyl sulfate (SDS, ACS Reagent, Sigma-Aldrich, purity > 99 %) and ammonium persulfate (APS, reagent grade, Sigma- Aldrich, purity ≥ 98 %) are used as received. MMA, EDGMA, PVP, SDS, and APS are used respectively as monomer, crosslinker, surfactant for PMMA beads and reaction initiator. The sol-gel solutions is synthetized by the RBnano Company and provided for research purpose [138]. The Ti precursor is based of chelated Ti alkoxide in propionic acid solution.

IV.2.1. PMMA Particles Synthesis Protocol Description

Different syntheses have been performed with an almost similar reaction setup in order to prepare PMMA particles (Figure IV-2) for targeted average diameters of 70, 150 and 280 nm. They will be labelled as P50+, P100+ and P200+ respectively representing the different size range of particles.

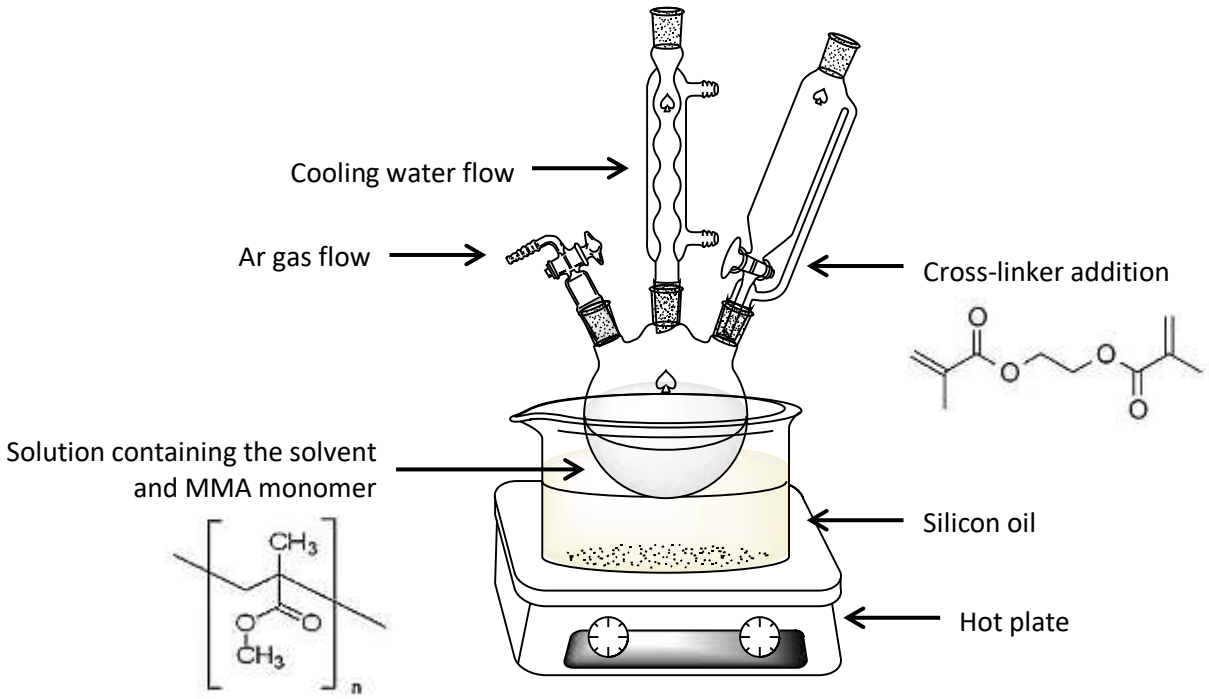

Figure IV-2: Illustration of the general setup for the PMMA polymers beads synthesis in aqueous solution

IV.2.1.1. Small Particles: 50+ nm Diameter

Emulsion polymerization is performed in a double-wall glass reactor. The emulsion polymerization is a type of radical polymerization that usually starts with an emulsion incorporating water, monomer, and surfactant [139]. A solution of 0.8 g SDS (surfactant) in 172.5 mL of distilled water is introduced in the reactor, followed by 62.5 g of the monomer MMA (25 wt % related to total mass) and the 2.5 g of the crosslinker EGDMA (4 wt % related to MMA). An emulsion is obtained by mechanical stirring with a Teflon anchor stirrer and the reaction mixture is heated to 70 °C. 0.35 g of the initiator APS, dissolved in 15 mL water, is then added to the reaction mixture and stirred at 70 °C for 3 hours and then 80 °C for 1 h to finish the polymerization.

IV.2.1.2. Medium Particles: 100+ nm Diameter

150 nm particles are obtained by two step emulsion polymerizations. First 100 nm particles were prepared by emulsion polymerization as described in [140], [141].

For the second step, the particles were grown further by seeded emulsion polymerization. 20 g of the first emulsion were diluted in 100 mL water and placed in a three-necked round bottom flask with magnetic stirring and a condenser. 0.1 g SDS, 9.3 g MMA and 0.6g EGDMA were added to the

reaction mixture. The reaction mixture was heated with an oil bath at 70 °C. After addition of 0.25 g APS, the temperature was maintained at 70 °C during 3 h and 80 °C for 1 h.

IV.2.1.3. Bigger Particles: 200+ nm Diameter

280 nm PMMA particles were synthesized by dispersion polymerization following the protocol of Peng *et al.* [142]. Briefly, a solution of 2.9 wt % PVP in water: methanol (80:20) is prepared. The monomer (2.5 g MMA and the initiator (0.025 g APS) were introduced in two-thirds of volume of the previous mixture and placed in a 250 mL three-necked flask equipped with a gas supply and a magnetic stirrer. After a homogeneous solution is formed at room temperature, nitrogen is bubbled through the reaction system at room temperature for 30 min. The setup is heated at 55 °C while stirring at 100 rpm in oil bath. After nucleation has occurred, approximately 1 hour after the reaction beginning, the cross-linker (0.05 g EGDMA, 2 wt % related to MMA) diluted in the remaining one-third of initial PVP solution was added dropwise to the reaction mixture over 1 hour. The reaction mixture was then maintained at 55 °C for 24 h more before cooling.

IV.2.2. PMMA Particles Characterization

Finally, the obtained beads have been characterized for their sizes, shapes and thermic behavior. The different results obtained for the PMMA beads synthetized and the utilization of thus beads for the TiO_2 porous layers preparation are shown below.

IV.2.2.1. Particles Size Determination with Dynamic Light Scattering

The three PMMA aqueous suspensions have been characterized by Dynamic Light Scattering (DLS) technique (Appendix VIII.1.8). The DLS measurements performed on suspensions confirm the different sets of particles, ranging from 70 nm up to 280 nm (Figure IV-4). DLS data show also an increase of the polydispersity with increasing of the beads target sizes. Nevertheless, this does not affect our work because the main goal was to obtain polymer beads with three different average sizes.

PMMA particles suspension	P50+	P100+	P200+
Diameter size on average (nm)	70 ± 25	150 ± 30	280 ± 60

Figure IV-3: Table resuming the synthetized PMMA suspension and particles diameter sizes

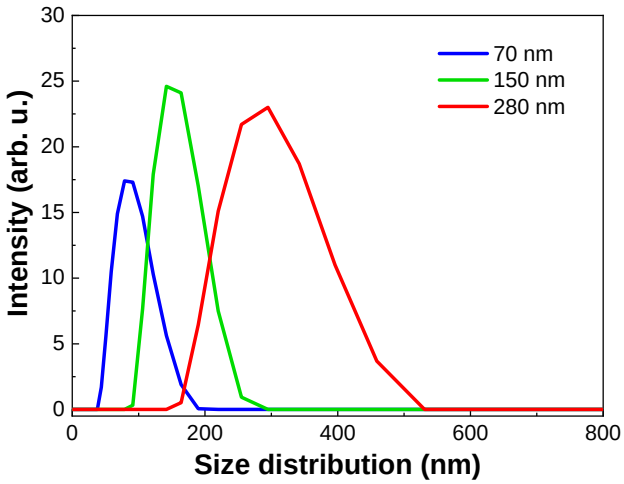

Figure IV-4: Graph representing DLS measurements of the PMMA aqueous suspension with the different sizes from smallest to biggest obtained particles

IV.2.2.2. The Thermogravimetric Analyses (TGA)

A Thermogravimetric Analysis (TGA) on the PMMA particles shows (Figure IV-5) a 100 % weight loss with a heat treatment at 400 °C corresponding to burning of PMMA. This trend is similar for the all synthetized particles. It means that Ti molded beads have completely disappeared at 500 °C , at the last step of our process (Figure IV-1-3) all organic have been removed , giving free open voids.

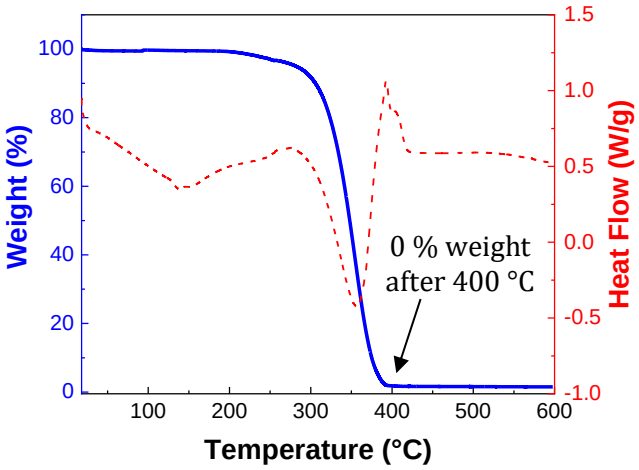

Figure IV-5: Thermogravimetric Analysis of the latex particles from room temperature to 600 °C

IV.2.2.3. PMMA particles deposition by spin-coating on Si substrate

In order to facilitate the characterization, the suspension of PMMA particles was first deposited by spin-coating on (100) silicon substrate for the morphological observation by SEM measurements.

The SEM images below show the top and tilted views of the compact PMMA particles film assembly. It gives an idea of the surface homogeneity and the film thickness. The thickest polymer layer was obtained with the smallest PMMA particles, 70 nm. We evaluate the thickness at approximately 2 µm corresponding to 20 to 25 single layers of beads. For 150 nm beads deposit we measure a thickness of 1 µm corresponding to 5-6 single beads layer. The synthesis has been done with a higher dilution in order to avoid aggregation of particles. For the last layer made of

280 nm beads we obviously observe that we have two single beads layers with an approximate thickness of 300 nm. Again the preparation process should be carried in dilute solution to avoid beads aggregation. Therefore the concentration in number for the suspension decreases drastically from suspension P50+ to P200+.

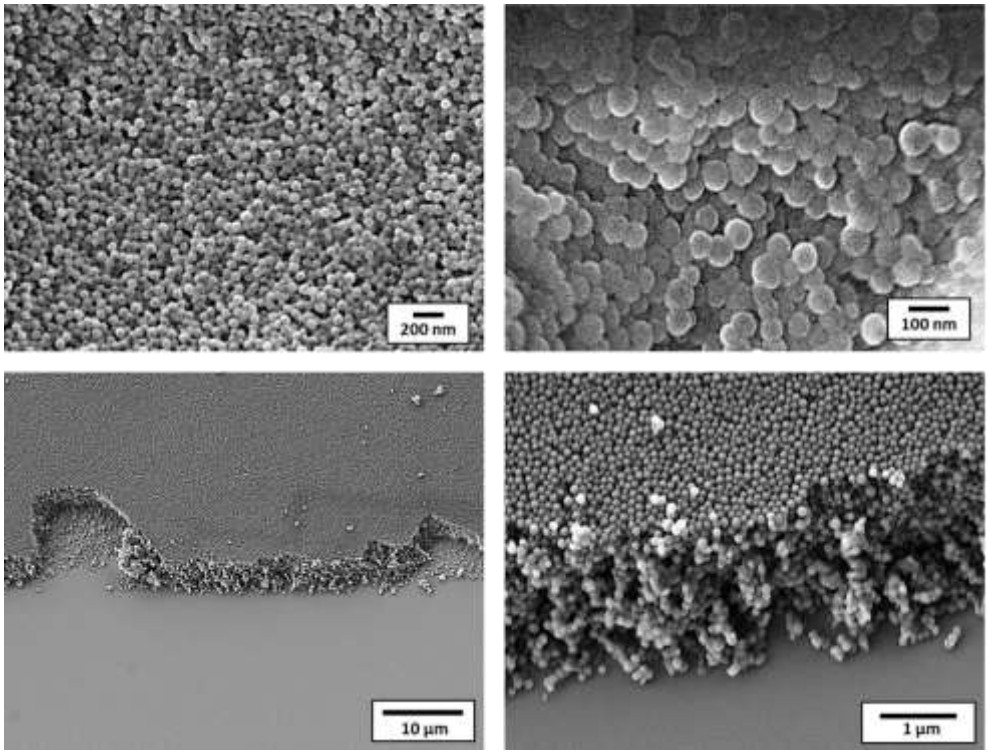

Figure IV-6: SEM images of the 50+ PMMA particles suspension deposited on Si substrate by spin-coating

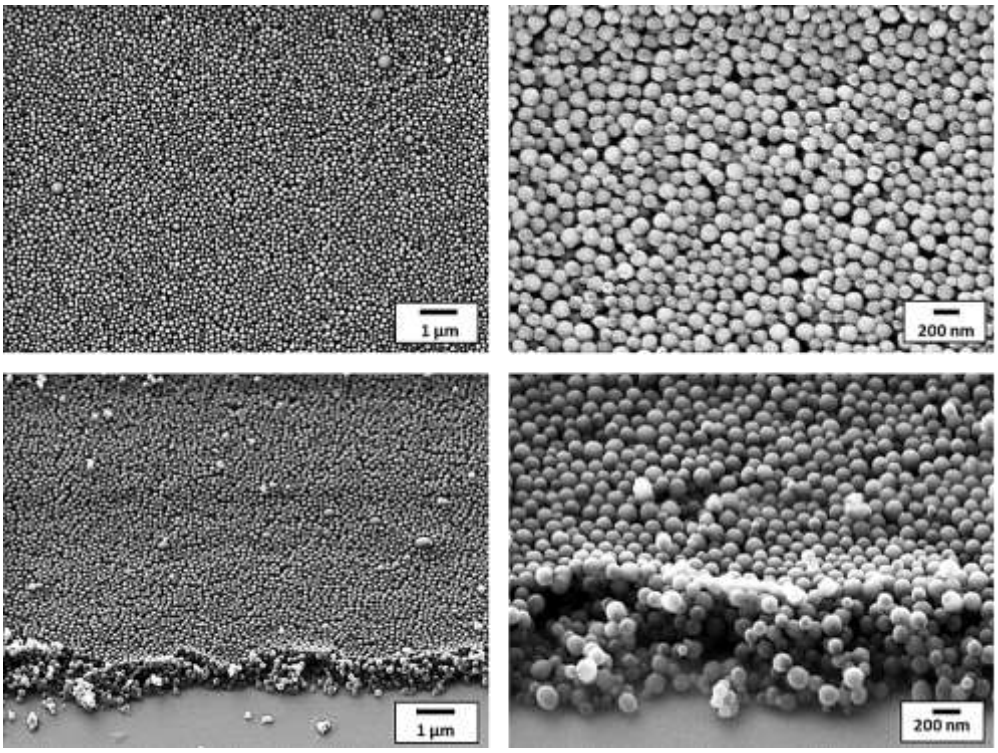

Figure IV-7: SEM images of the 100+ PMMA particles suspension deposited on Si substrate by spin-coating

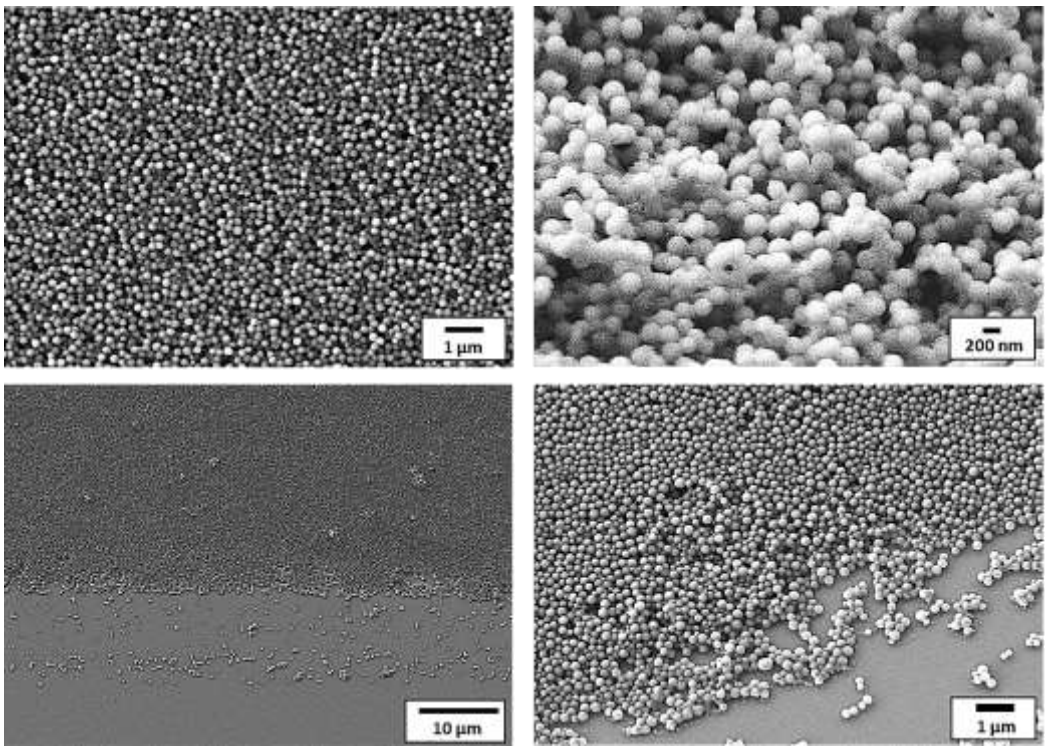

Figure IV-8: SEM images of the 200+ PMMA particles suspension deposited on Si substrate by spin-coating

The surface roughness of the compact PMMA beads film has been measured by AFM. The roughness increases with the particles diameter but stay relatively low, which means a smooth and homogenous surface without particle aggregations.

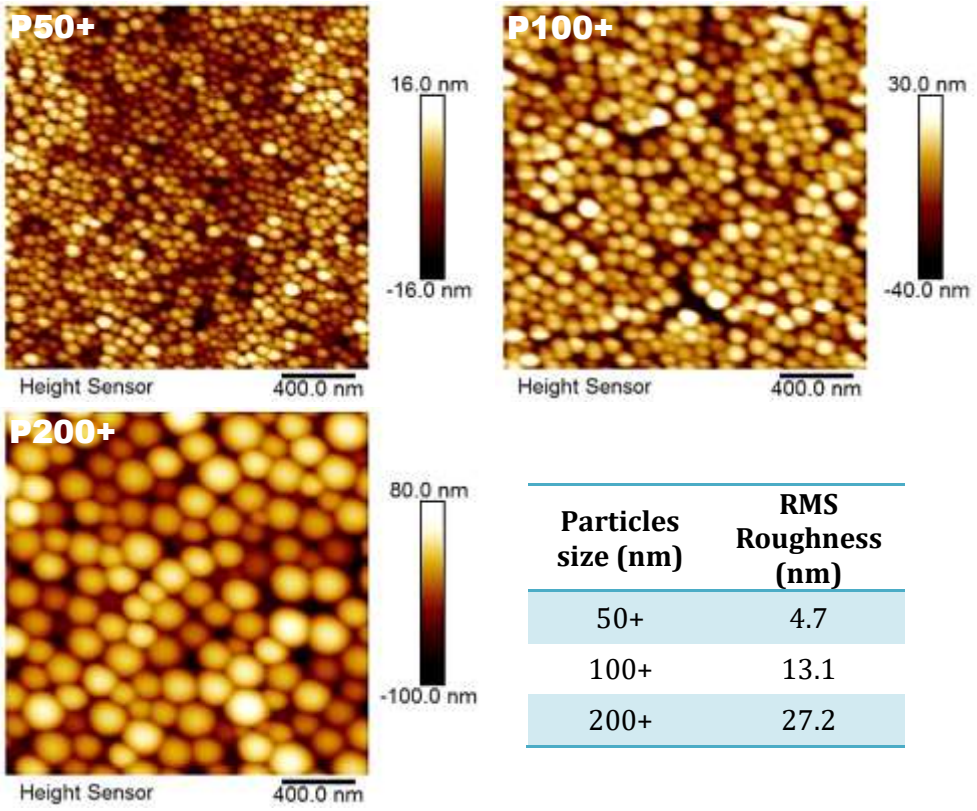

Particles size (nm)	RMS Roughness (nm)
50+	4.7
100+	13.1
200+	27.2

Figure IV-9: AFM images and roughness values of the compact PMMA particles films. The images are recorded at the same scale barre to highlight the beads size increase

IV.3. TiO_2 Porous Layer Characterization

The second step of the TiO_2 porous layer preparation following the PMMA beads deposition is the sol-gel solution deposition by the same technique as for the molding concept (Figure IV-1-2). The next and last step point for obtaining the porous layer is the annealing at high temperature (500 °C) to remove PMMA particles and crystalize the sol-gel solution. Thus different TiO_2 scaffolded layers prepared in the same way are characterized hereunder.

IV.3.1.1. The TiO_2 Porous Layers Morphology

The porous layers morphology is observed on top and section view by SEM technique for the three PMMA size particles molding samples after cleaving of the Si substrate (Figure IV-10). The SEM images show clearly that the pore sizes of the TiO_2 scaffolded layers increase with increasing the initial beads size.

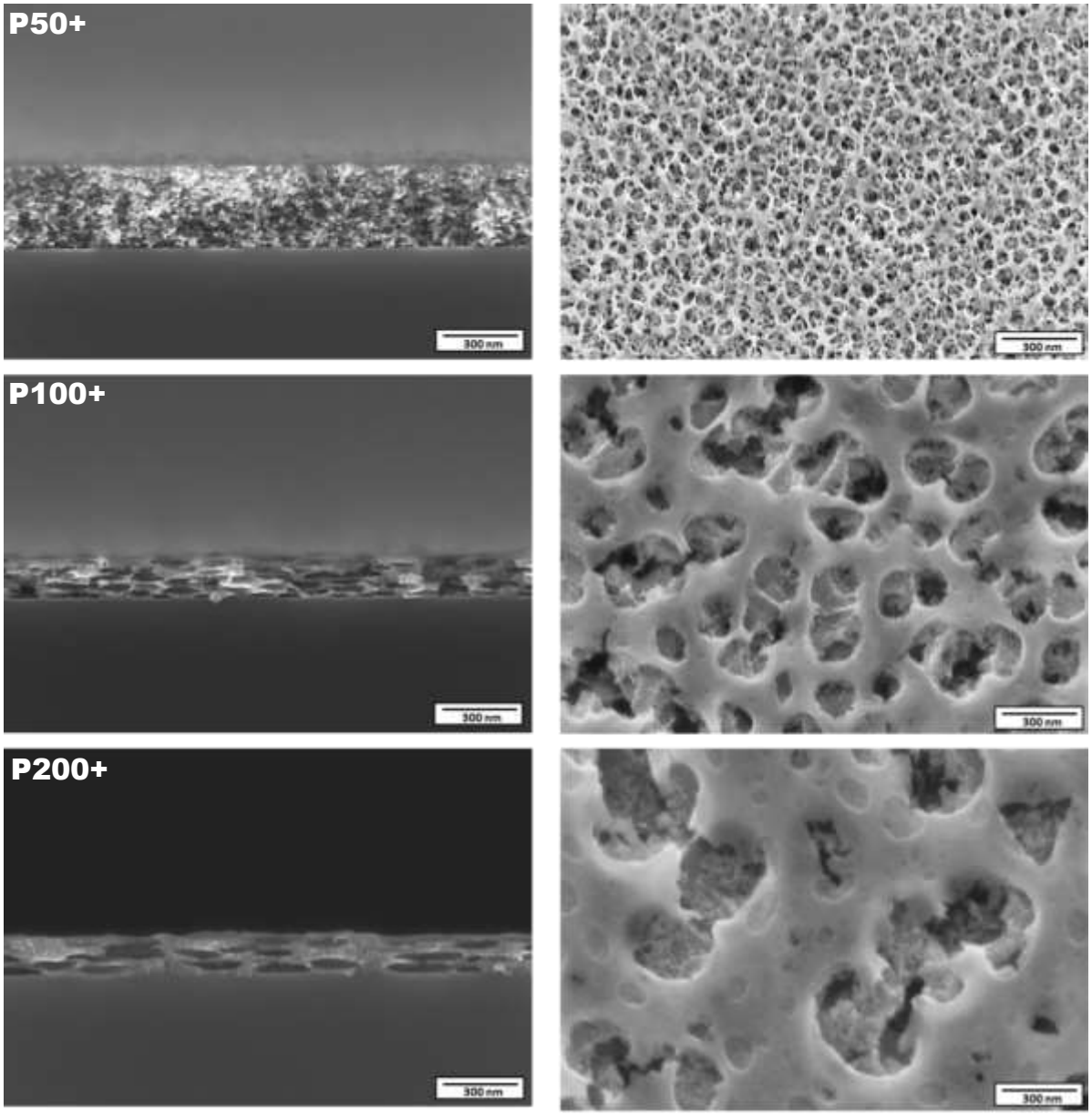

Figure IV-10: SEM images of TiO_2 porous layers obtained by molding of 50+, 100+, 200+ PMMA beads .The images are recorded at the same scale barre (300 nm) to highlight the pore size increase

But, even if the pore sizes are well connected to the PMMA particles sizes on average, we observe a no-spherical shape (Figure IV-11) after the annealing.

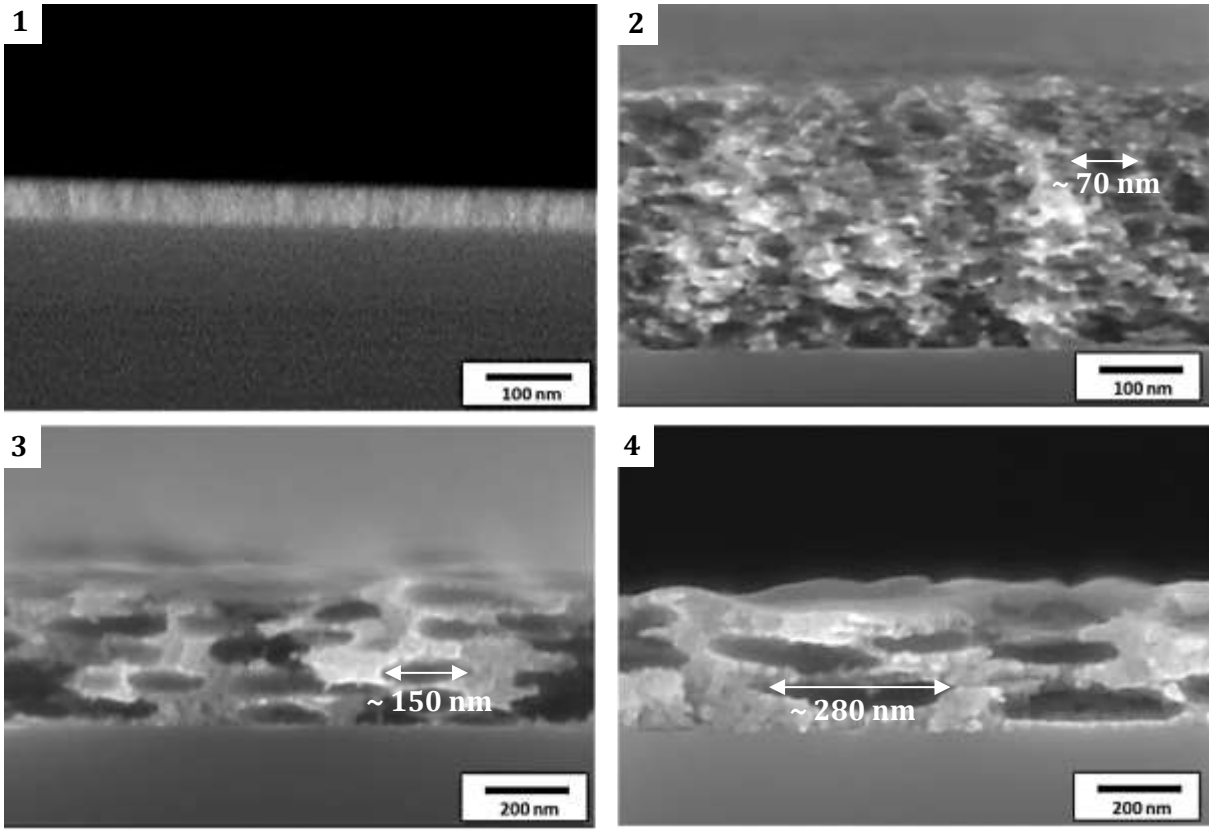

Figure IV-11: SEM images showing the pores shapes on section of the TiO_2 layers obtained after the molding with sol-gel and the annealing process at high temperature 1) no PMMA 2) P50+ 3) P100+ 4) P200+

The pores distribution is relatively homogenous and the deformation could be explained by the fact that the PMMA particles have a tendency to grow by a factor three in diameter in the sol-gel solution (Figure IV-12) and during the heating process all solvent are first evaporated and the beads contracted, which means that the beads are not spherical anymore but more oval-shaped.

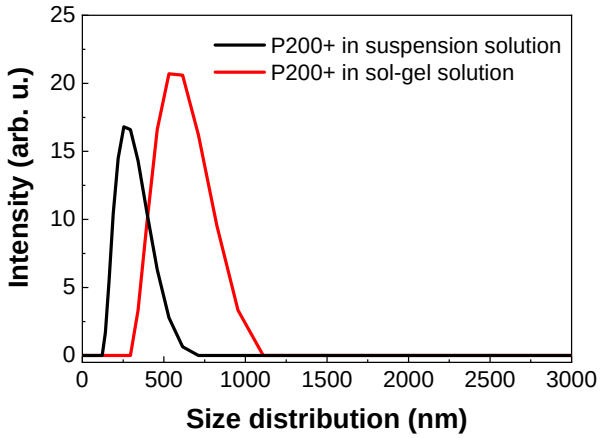

Figure IV-12: DLS graph of the P200+ particles in the suspension solution and the sol-gel solution. The others polymer particles have the similar behavior

Another explanation could be the following: when the sol-gel is removed and the sol-gel is changed from wet to dry there is a retraction, a decrease in volume. The evaporation of the solvent can only occur through the surface and this removal is perpendicular to the deposition surface. The small beads are well crosslinked and harder and therefore resist well to this compression. For large beads this crosslinking is weaker helping the deformation of the beads and giving rise to these lenticular holes.

IV.3.1.2. The Porous Layers Structure

The XRD measurements patterns show that the TiO_2 layer crystallizes into the anatase phase (Figure IV-13-a). No other phases could be observed within the detection limit of the XRD technique.

The SEM/EDX coupled analyzes support that we obtained satisfactory film composed with Ti and O elements (Figure IV-13-b). The Si peak is due to the substrate and the Cu peak to the sample holder from the equipment.

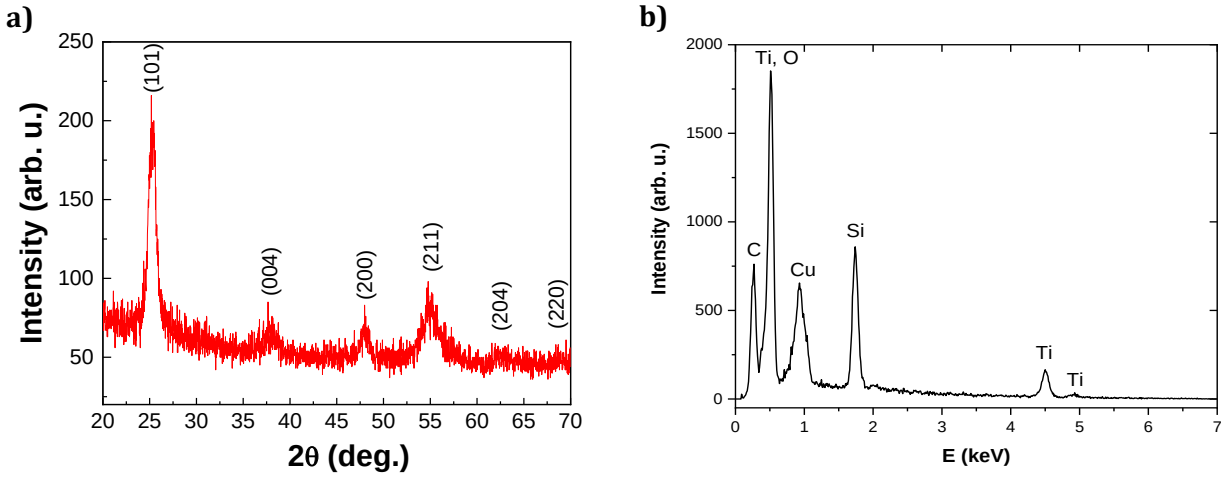

Figure IV-13: a) XRD diffractogram showing the presence of the TiO_2 anatase phase in the scaffold layer obtained after annealing at 500 °C (JCPDS 00-021-1272) b) EDX spectrum recorded on the TiO_2 porous layer

The same layers have been deposited on glass substrates in aim to determine their transmittance, which is an important parameter for the photovoltaic effect. Indeed, to permit a maximum photon transfer to the perovskite light absorber material, the ETL and m-TiO_2 need to allow photons transmission as much as possible. The transmittances of the different TiO_2 porous layers are showed in Figure IV-14. The highest transmittance is achieved with the smallest pore sizes (P50+) and the lowest with the larger pores (P200+). The reason for this difference could be explained by comparing the SEM images (Figure IV-11). Usually, the thinnest layer (P200+) should transmit the most light; but although the porous layer P50+ is the thickest it looks like foam while the P200+ has some compact areas between the pores due the larger particles sizes stacking effect, which reduces its transmittance.

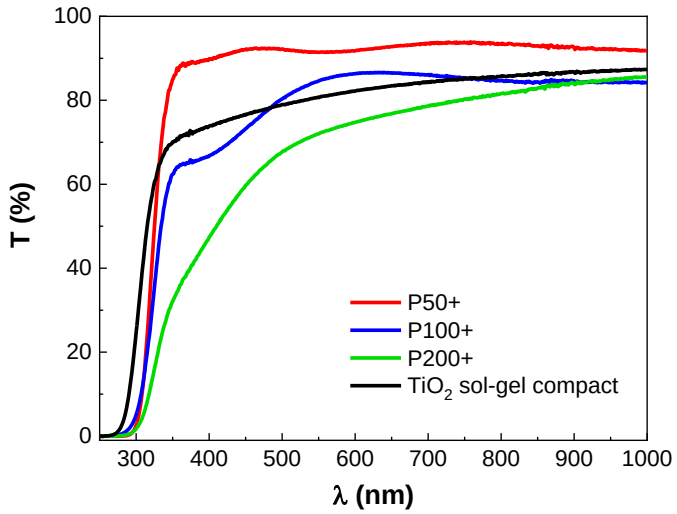

Figure IV-14: Transmittance graph of the different TiO_2 porous layers

IV.3.1.3. The Porosity Volume Estimations

The porosity estimation is important for the TiO_2 scaffolded layers comparison because the void present in the film will consequently correspond to perovskite light absorber material infiltration volume in case of full pore's filling.

Regarding the spherical shape of the polymer particles, which gives place to the pore patterns, we have determined below (Figure IV-15) an hypothetic porosity volume according to the different PMMA beads size for a defined same section:

a)

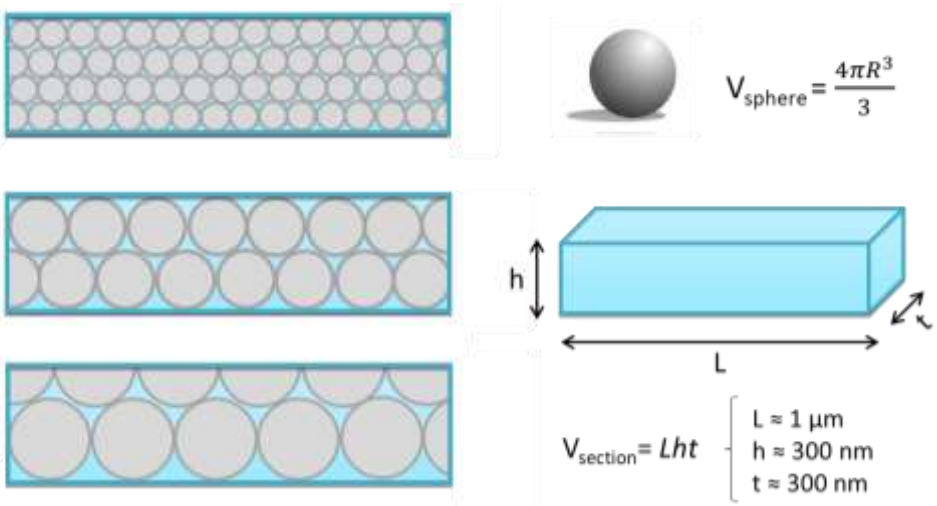

b)

Particles size (nm)	1 Sphere Volume (nm³)	Sphere numbers in the section	Total sphere volume (nm³)	Porosity volume (%)
50+	1 795.94	263.01	472 351.17	52.48
100+	17 671.45	26.68	471 474.51	52.38
200+	114 940.40	4.09	470 106.24	52.23

Figure IV-15: a) Schematic representation of the pore patterns related to the particles size b) Table reporting the theoretical porosity estimation values for the scaffolded TiO_2 layers for each PMMA beads and for a hypothetic section of 9×10^5 nm³ in volume

The porosity volume estimated is almost similar for the three particles sizes; this estimation is correct in case of optimal staking and form of the PMMA beads during the molding process.

One usual method for porosity measurement is the Brunauer-Emmett-Teller (BET) measurement. This method is based on physisorption of N_2. Knowing the volume of supplied N_2 gas and mass of sample, a Langmuir monolayer theory can be applied in order to calculate the specific area and units of monolayer volume of adsorbate gas (N_2). This method is often used to evaluate the porosity of samples in terms of pore surface area and volume. However, the layers that were produced for this method were not of appropriate mass for performing such experiment due to small size of pores and area.

In this thesis, ellipsometry and FIB-3D (Focused Ion Beam) tomography coupled with SEM technique have been used as an alternative for porosity volume measurements.

a. Porosity Volume Measurement by Ellipsometry Technique

The experimental porosity volume estimation has been performed with the ellipsometry technique. The principle is to measure the void corresponding to air refractive index (n = 1) inside the layer. According to the layer thickness and simulation fit it is possible to determine the air volume in the layer. The results are listed hereunder:

Particles size (nm)	Porosity volume (%)
50+	54.0 ± 1.2
100+	54.1 ± 1.1
200+	54.6 ± 1.5

Figure IV-16: Table reporting the experimental porosity estimation values for the scaffolded TiO_2 layers

The measured total porosity volume is more than 50 % in most of case and the porous volume values reached are close to the estimated amount although the no-spherical shape.

b. Porosity Estimation by Tomography: 3D SEM-FIB Construction

An additional method used for the experimental porosity volume estimation is the tomography with a coupled SEM-FIB (Focused Ion Beam) technique (Appendix VIII.1.11). This approach allows us to observe the morphology of the porous layer in depth and thanks to recording SEM images step by step, which makes possible to build the layer in 3D and thereby estimate the porosity volume.

Only the P50+ layer has been characterized with this method, indeed the P100+ and P200+ /TiO_2 porous layers are not dense enough for the tomography and the FIB melted the layers.

The TiO_2 porous film appears dense, homogenous and relatively flat on the top, which makes the sample preparation with FIB easier (Figure IV-17). The tomography process starts from the top of the layer and goes at length. The area is previously defined for a section with 2660.4 nm in large, 3388.4 nm in length and 240 nm in depth (Figure IV-18).

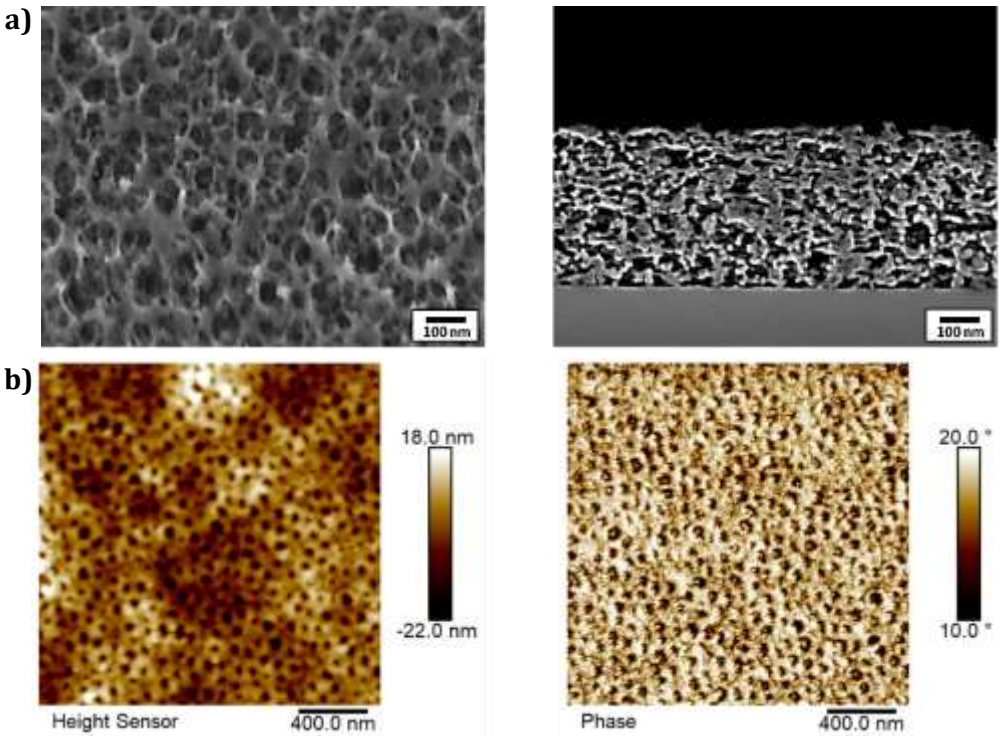

Figure IV-17: a) SEM images from the top and section view. The sample has been polished on the section with an Ar beam. The pores are well defined and the layer quite dense b) AFM images of the TiO_2 porous layer surface in topography and phase analyzes. The average roughness is 5.3 nm and the phase image shows a homogenous distribution, which support that the surface is flat and homogenous

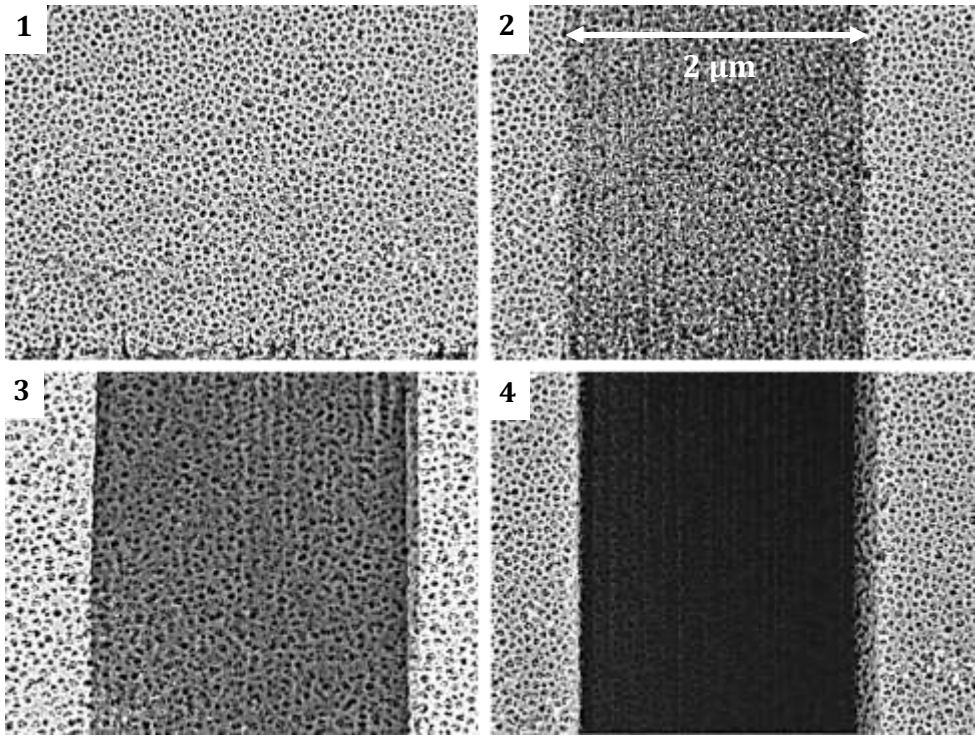

Figure IV-18: SEM images recorded during different steps of the FIB lasering with 1) the start, 2) and 3) are intermediary states and 4) the end. We can clearly observe that the layer in porous homogenously in depth

To gain more quantitative results, an object segmentation procedure has been performed on each image and by combining them together along the image stack; it was possible to compute the pore volumes. The pore volume distribution is presented in Figure IV-20 highlighting that in standard mesoporous TiO_2 layer most of the pores (> 75 %) have volume of less than 250 nm^3, while P50+ /TiO_2 has only pores only larger than this value; more than 60 % of pores have volume between 500 and 1000 nm^3. Due to differences in brightness and contrast there is a small uncertainty in the result. Nevertheless, the pore size difference is rather strong.

These results confirm that P50+ /TiO_2 layer indeed has larger pores and can accommodate more perovskite material than the standard mesoporous TiO_2.

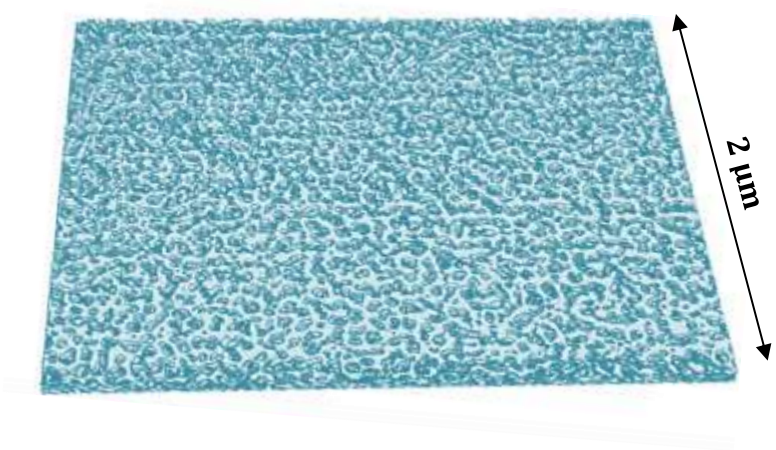

Figure IV-19: Image representing the 3D reconstruction of the section using Image software by collecting SEM images recorded by tomography process

To gain more quantitative results, an object segmentation procedure has been performed on each image and by combining them together along the image stack; it was possible to compute the pore volumes. The pore volume distribution is presented in Figure IV-20 highlighting that in standard mesoporous TiO_2 layer most of the pores (> 75 %) have volume of less than 250 nm^3, while P50+ /TiO_2 has only pores only larger than this value; more than 60 % of pores have volume between 500 and 1000 nm^3. Due to differences in brightness and contrast there is a small uncertainty in the result. Nevertheless, the pore size difference is rather strong.

These results confirm that P50+ /TiO_2 layer indeed has larger pores and can accommodate more perovskite material than the standard mesoporous TiO_2.

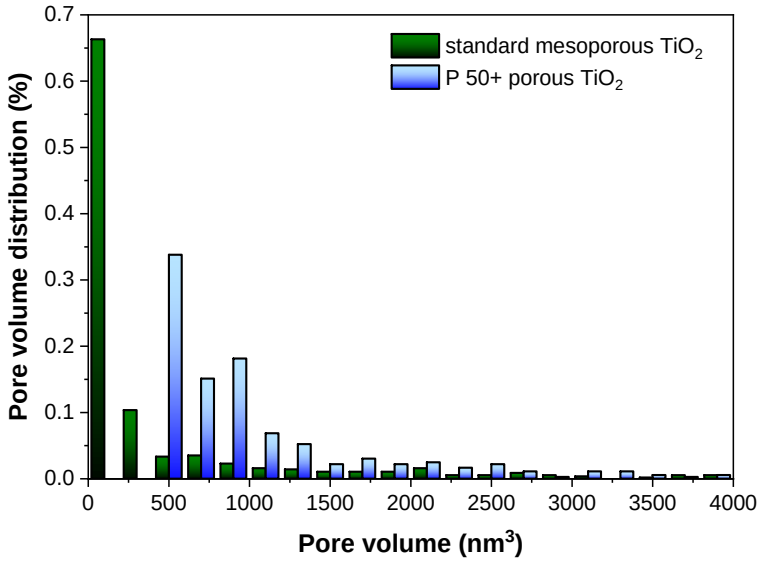

Figure IV-20: Pore volume distribution in mesoporous TiO_2 and P50+ TiO_2 porous layer obtained from FIB-3D tomography

Conclusion

In summary, we have studied the molding of self-assembled PMMA beads by Ti sol-gel solution aiming to obtain TiO_2 anatase layer with large pore size and high porous volume. We have prepared suspensions of PMMA beads with mean size ranging from 80 nm to 280 nm. We have demonstrated that the control of pore sizes can be obtained by varying the initial beads size. A simple three step process was used: deposition of a PMMA beads dense layer, infiltration of Titanium sol-gel solution and a final heat treatment at 500 °C. It leads to thin porous layer with a pore size directly related to initial beads size. Pore volumes in the film are around 50 % for each case. The advantage with larger pores is that they allow the growth of larger crystals in the scaffolded film with less grain boundaries.

Our future work will be to integrate these layers in scaffolded solar cells. In contrast to porous TiO_2 layer obtained by standard techniques using commercial TiO_2-based nanoparticle pastes, our technic should allow improving the amount of infiltrated light absorber materials and thereby increases their power efficiency.

V. Replacing of the m-TiO_2 in the Monolithic Referential Cell Device by Pore Size Engineering of TiO_2 Layer through PMMA Particles Molding

The previous chapter resumes the molding process for the TiO_2 porous with controllable pore sizes. This chapter figures out the integration of this porous layer replacing the standard one for the monolithic perovskite solar cell as described in Part III. The PSC will be also characterized in aim to compare with the referential cell and thereby highlights the enhancement of the PSC performance prepared with this approach.

V.1. Porous Layers Preparation on the c-TiO_2/FTO/Glass substrate with P50+, P100+ and P200+ PMMA Particles

The protocol for the porous TiO_2 layer preparation by molding process on the c-TiO_2/FTO/Glass substrate is similar to what was described in Part III. The only change will be the replacement of the m-TiO_2 film by molded porous TiO_2 layer as represented in Figure V-1. As reminder, the whole structure of the perovskite solar cell is:

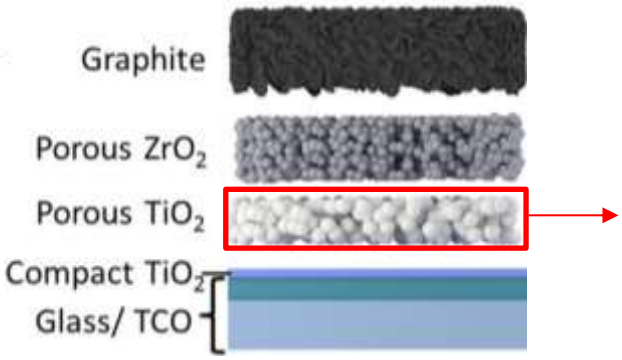

Figure V-1: Scheme of referential structure for a monolithic PSC

V.1.1. The Process Description

The preparation process is similar to that of the reference cell (Figure III-1); the point that differs is that the FTO/Glass plate must be cut into individual cells (sixteen cells of 25 mm size) in the preliminary step following laser ablation. This is due to the spin-coating technique used for molding. The FTO plate is too large and therefore not suitable for this deposition technique. The different stage are illustrated and described below:

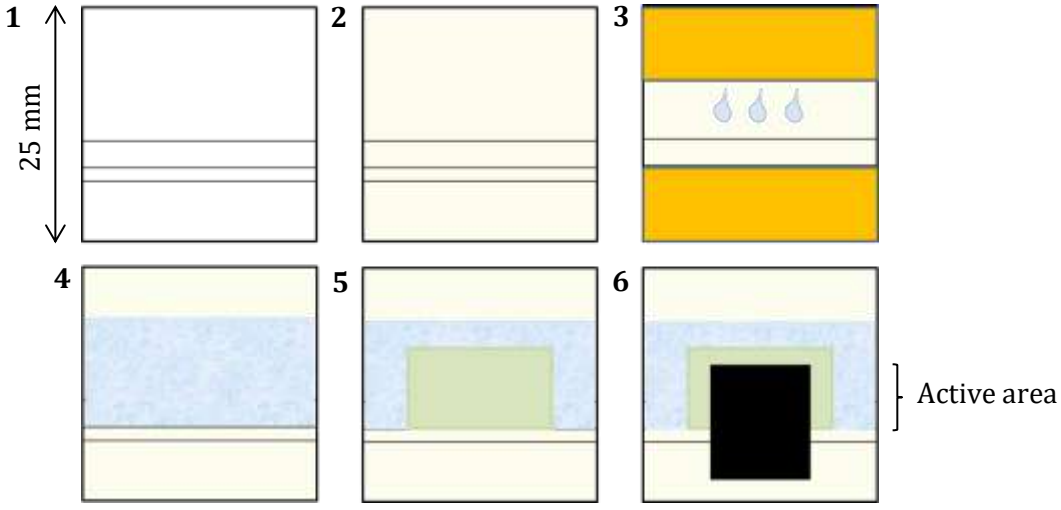

Figure V-2: Schemes of the complete PSC preparation steps using molding process for the porous TiO_2 layer

Once the substrate is ablated with the laser lines and as well has the right size (Figure V-2-1), the first layer applied is the compact TiO_2 by the usual spray pyrolysis method (Figure V-2-2). The next step concerns the preparation of the porous TiO_2 layer by the molding process.

A three step process is carried out:

1. First delimit the deposition area using Kapton® tape
2. PMMA particle deposition and drying at air conditions
3. Infiltration of sol-gel solution followed by a spin-coating (Figure V-2-3)

The next step is the annealing at high temperature to remove the particles that leave the pores and crystallize the porous TiO_2 anatase layer (Figure V-2-4). The ZrO_2 and graphite porous layers are obtained by screen-printing technique to finally define the active area (0.4 cm^2) as for the reference cell (Figure V-2-5 and Figure V-2-6 respectively).

V.1.2. Characterization

The P50+, P100+ and P200+ TiO_2 porous layer obtained on the c-TiO_2/FTO/Glass substrate after the annealing step at 500 °C (Figure V-2-4) have been observed by SEM technique and the obtained images are shown hereunder in Figure V-3:

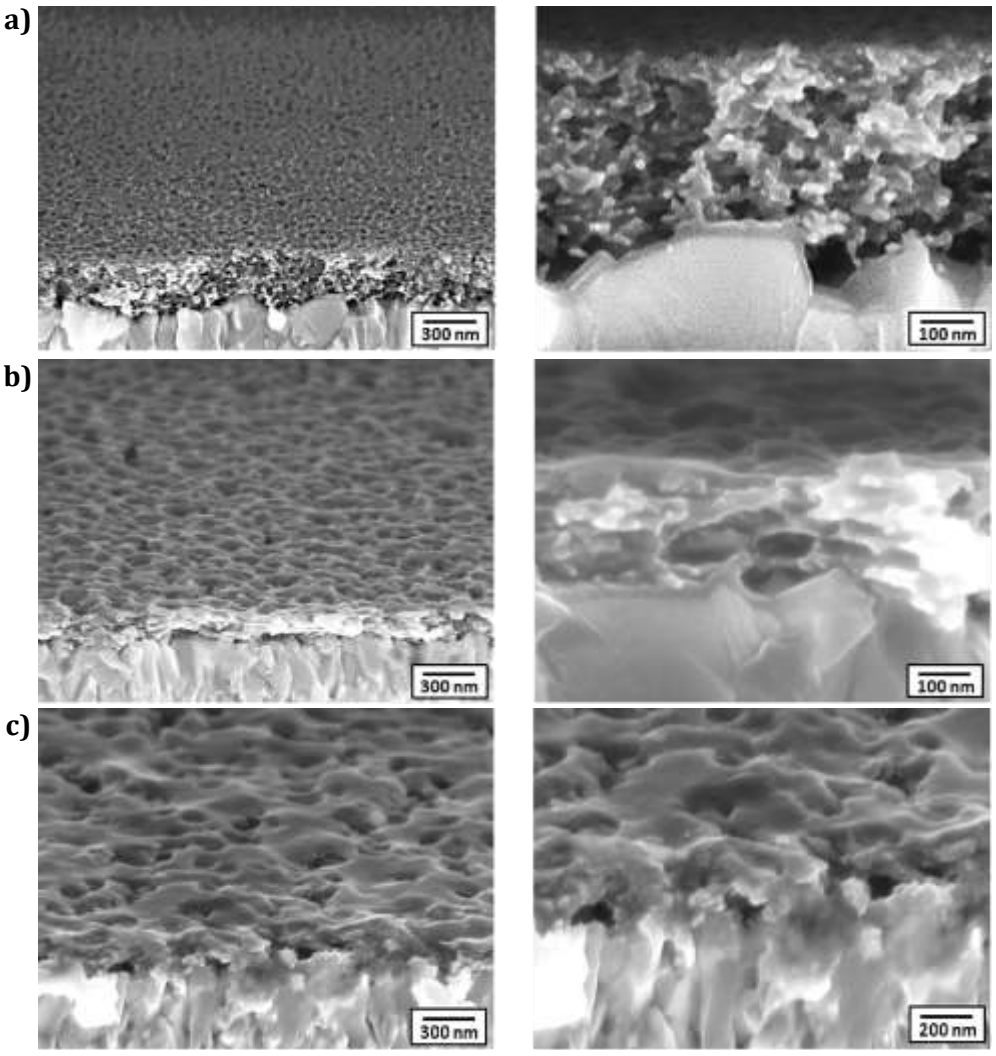

Figure V-3: SEM images from the section view of the TiO_2 porous layer prepared by molding process on the c-TiO_2/FTO/Glass substrate with a) P50+ b) P100+ and c) P200+

The SEM images demonstrate the TiO_2 porous layer with pore size variation obtained by the molding process on c-TiO_2/FTO/Glass substrates. We notice that the thickness of the porous TiO_2 layer decreases as the size of the beads increases. This phenomenon was not clearly visible compared to the depositions on silicon substrates (Figure IV-10); the P50+ porous layer is still around 300 nm and the P200+ is the half of this thickness, also the surface is less smooth with pore size increasing as well. The roughness of the FTO surface can influence the deposition during molding, which affects the final morphology. However, the various range of pore size thus obtained remains very interesting.

As already mentioned, the next step is to deposit the porous ZrO_2 and graphite coatings by screen-printing and then drop-cast the perovskite precursors through the TiO_2 and ZrO_2 porous layers. The following part focused initially on the preparation and characterization of complete cells for the porous TiO_2 P50+ layer.

V.2. Perovskite Solar Cell Characterization with P50+ as Porous TiO_2 Layer

The P50+ monolithic cell was infiltrated according to the procedure described in Part III.1.3. Once the cell was obtained, it was characterized by SEM technique to analyze its morphology and by I-V measurements for its photovoltaic performance.

V.2.1. The P50+ PSC Structure Characterization

The SEM images in cross-section of the complete cell (Figure V-4) display the various layers present in the PSC. We can clearly distinguish the difference in interfaces between the porous layers obtained by the molding and those obtained by screen-printing process. Indeed, the surface of the porous TiO_2 layer is smooth and homogeneous while the surface of ZrO_2 is quite rough.

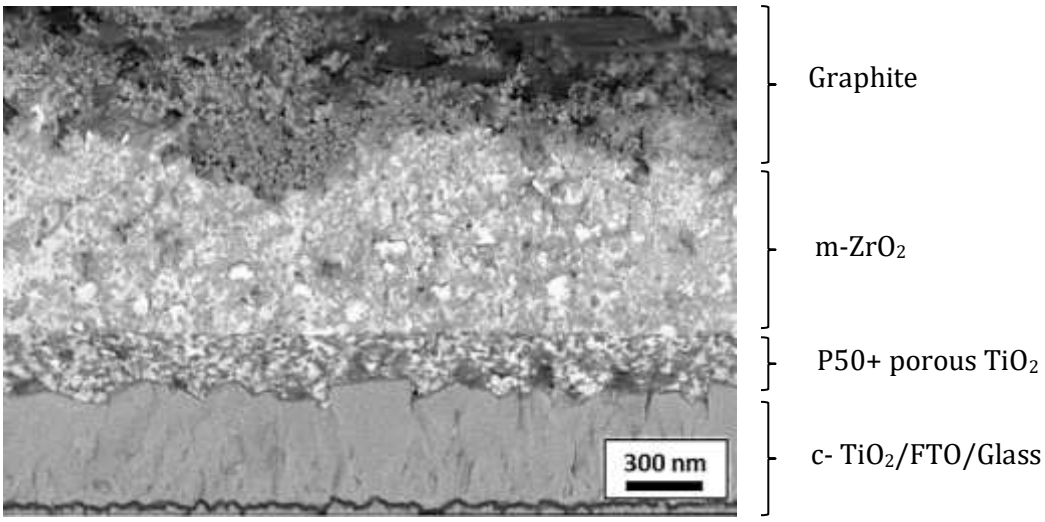

Figure V-4: SEM image on the cross-section of the P50+ monolithic perovskite solar cell

The Improvement of the interface quality of the layers plays a significant role in the infiltration optimization of perovskite precursors into these layers [107], [143], which has a direct impact on the cell's performance [63], [111], [144].

The infiltration of the perovskite photo-active material through the porous films was analyzed by the SEM/EDX mapping technique (Figure V-5).

The collected images show the layers present in the cell and the elements distribution. We notice that lead can be found through these different layers. Comparatively to what was observed in Figure III-24, it seems to be more present in the ZrO_2 intermediate layer and n-type TiO_2 layers and less present in the graphite film. This can be explained by the fact that a TiO_2 layer with better porosity and interface is obtained by molding of P50+ PMMA particles than the commercial paste deposited by the screen-printing technique.

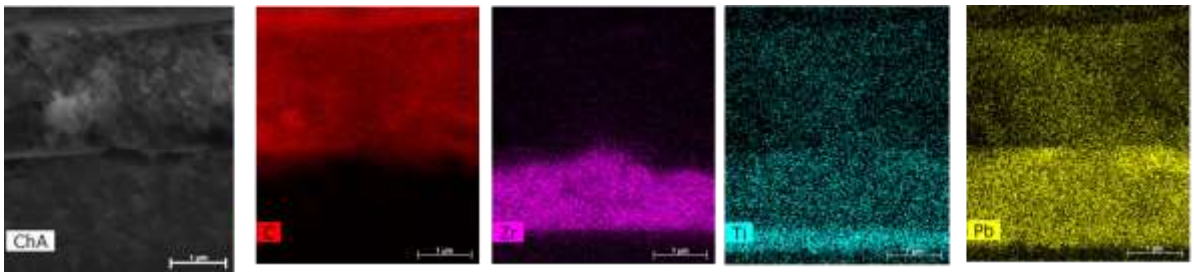

Figure V-5: SEM/EDX mapping recorded on the cross-section of the P50+ monolithic perovskite solar cell

V.2.2. The P50+ Monolithic PSC Photovoltaic Performances

The photovoltaic parameters that define the cell's performance have been obtained by I-V measurements as previously in Part III.2.4. The results of a series of four identical P50+ monolithic cells are shown below in Figure V-6 to assess reproducibility on the performances:

a)

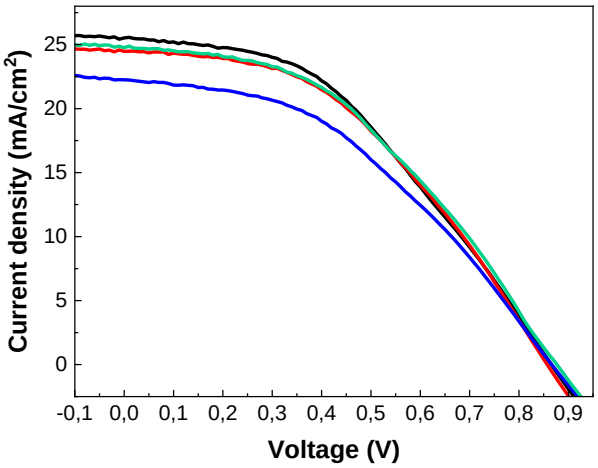

b)

Particles size (nm)	J_{SC} (mA.cm^{-2})	V_{OC} (V)	Fill Factor (%)	Efficiency (%)
PSC- 1	25.25	0.87	42.26	9.34
PSC- 2	24.47	0.86	43.72	9.17
PSC- 3	24.76	0.86	43.87	9.22
PSC- 4	22.26	0.87	41.74	8.25

Figure V-6: a) Graph representing the I-V curves of the cell's series b) PV parameters that are derived from these I-V measurements

The data show an average power efficiency of about 9 % for this series, which remains interesting especially in regards to the short-circuit current (J_{SC}) value, which is higher than 22 mA.cm^{-2} for these cells and higher than the reference cell (Figure III-28). The J_{SC} value can be improved thanks to the better interface quality between the porous TiO_2 and ZrO_2 and the amount of light-absorber material infiltrated in the scaffold architecture due to the larger pores. The fact that there is continuity in the distribution of perovskite photo-active material over the entire cell thickness is probably the reason for the improvement. The larger pores favor the perovskite precursor's infiltration forming crystals with reduced defects and therefore it leads to a higher short-circuit current.

However, it is necessary to measure the efficiency as a function of time at constant V_{MPP} (Voltage at the Maximum Power Point) to characterize the stability of the cell, the outcomes are given in the Figure V-7. The performances of the PSC start high around ≈ 10 % but decreases significantly with time down to ≈ 6 % for the minimum value (Figure V-7). This means that the efficiency is not stable as function of time. To summarize the cells have a good performance and reproducibility regarding the I-V curves but the efficiency are not reliable compared to the stabilized PCE.

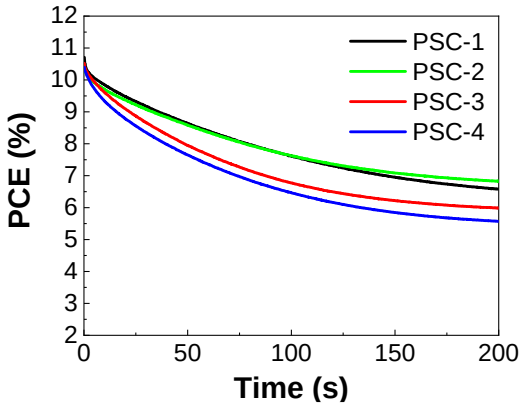

Figure V-7: Graph representing the Power Conversion efficiency (PCE) of the P50+ monolithic perovskite solar cells as function of time (V_{MPP} ≈ 600 mV)

V.3. PSC using the P100+ and P200+ as Porous TiO_2

The previous part focused on the monolithic cell with the molded porous layer TiO_2 50+, which is made using the smallest sizes of synthesized PMMA particles. It is now a natural progression to focus on larger porosity sizes, P100+ and P200+.

This willingness to use larger bead sizes to obtain larger pores was driven by the notion that large pore allows larger crystals into the TiO_2 porous layer in order to reduce the grain boundaries. Grain boundaries are related to the degradation of the photo-active material and therefore of the cell stability [2].

V.3.1. Different Infiltration Ways for the Drop-Casting Technique

Up to now, the technique used for the infiltration of perovskite precursors into porous layers has been the drop-casting (Figure III-6). This technique is quite simple to carry out [64], [91]and the necessary volume for our monolithic cells has been optimized at 1 µL per cm^2, i.e. 4 µL for an active surface of 0.4 cm^2. These parameters are characteristic for the reference cell and have been successfully applied for the P50+ monolithic cell. However, it appears that for cells including the TiO_2 layers with larger pores, infiltration is less intuitive (Figure V-8). We observe on the P100+ PSC's pictures that the infiltration on active area is not homogenous. Indeed, this approach appears to be straightforward but still has sensitive points to be optimized such as volume, distance or dripping angle or even the delimiting zone with tape for the infiltration area.

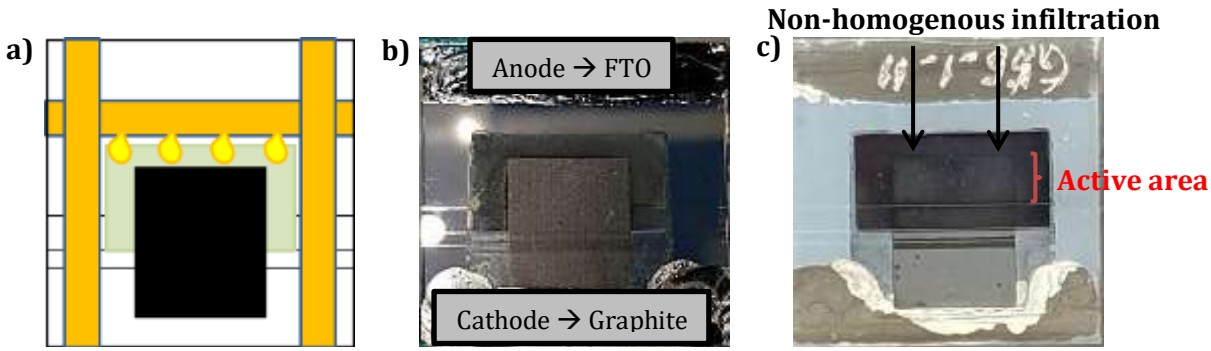

Figure V-8: a) Drop-casting illustration on the P100+ PSC using usual parameters b) Picture of the PSC containing light absorber perovskite crystals (top view) c) view from the glass highlighting the active area

We have tried different ways of infiltration with this technique as represented in the figures below; for example changing the delimiting zone (Figure V-9) or the dripping method (Figure V-10) in order to reduce defects.

Figure V-9: a) Drop-casting illustration on the P100+ PSC with less delimiting zone b) Picture of the PSC from the top view and c) view from the glass side

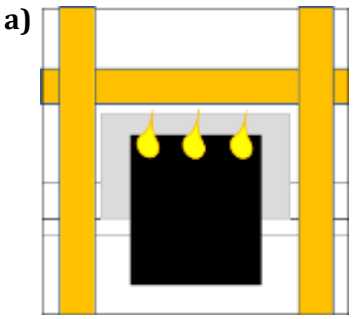

The motivation to reduce the infiltration zone is to reduce defects but this one is not very homogeneous (Figure V-9-c) and the the infiltration zone pictures of the P50+, P100+ and P200+ (Figure V-10) put in evidence a huge difference between the small and large pores. We can observe easily the drop shape for the P100+ and P200+ PSC, while the P50+ cells look quite homogenous on all the area.

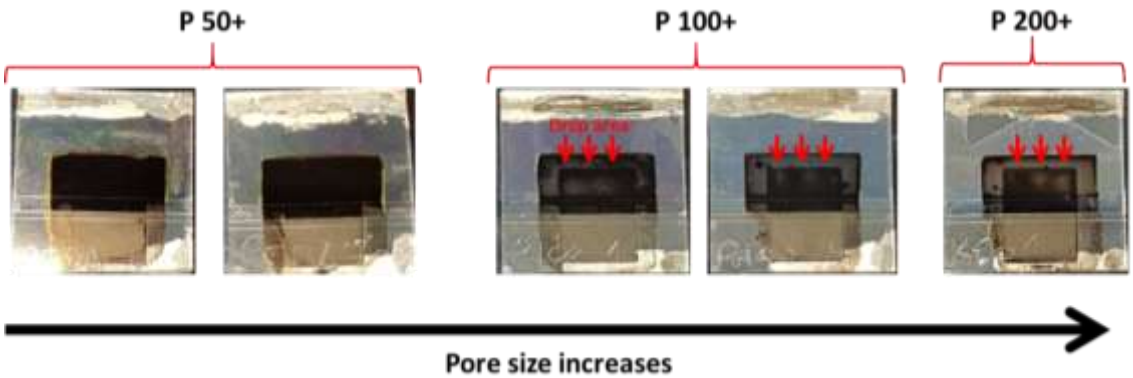

Figure V-10: a) Drop-casting process through the graphite b) Pictures of P50+, P100+ and P200+ PSC from the glass side view

The SEM image obtained on the P100+ (Figure V-11-a) cross-section shows an inhomogeneous TiO_2 porous layer infiltration. The EDX mapping (Figure V-11-b) demonstrates the presence of lead through the scaffolded layers but it is still poor in the porous TiO_2 layer. It is also worth noting that the thickness of porous TiO_2 is lower for P100+ and P200+ (Figure V-3). Therefore, the active area is more limited, which contributes to the decrease in efficiency as well.

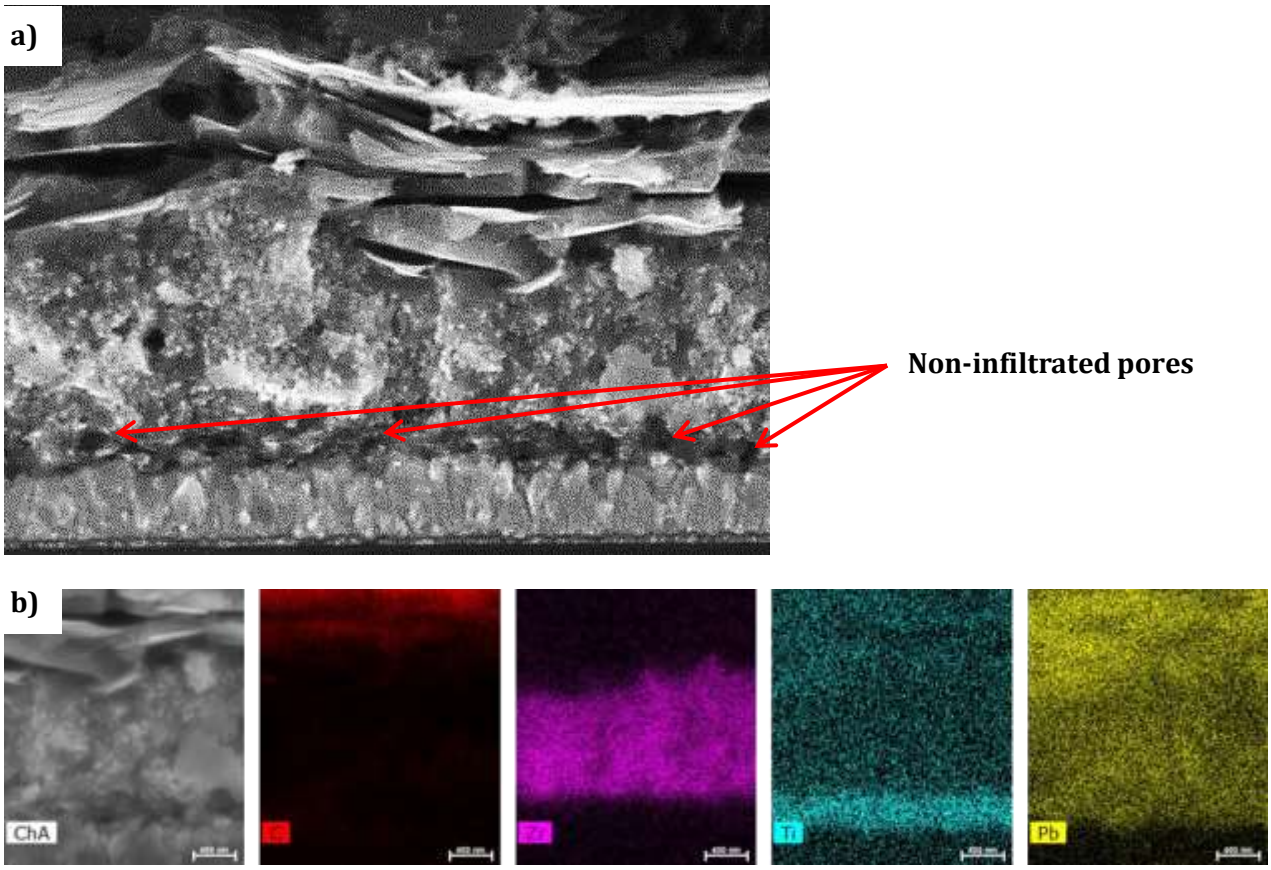

Figure V-11: a) SEM image on the cross-section of the P100+ PSC after the perovskite precursors infiltration. b) EDX mapping recorded on the section

V.3.2. I-V Measurements for the P50+, P100+ and P200+ with MAPI Perovskite Precursors Infiltration

The I-V measurements were performed on the P50+, P100+ and P200+ cells to compare their photovoltaic parameters. The results show a clear decrease in the value of the J_{SC} (Figure V-12).

The photovoltaic efficiencies are therefore lower for P100+ and P200+ cells (from 6 to 4 %) while they remain at around 9 % for the P50+ PSC.

This difference may be directly due to the poor quality and lower quantity of infiltration of the photo-active material.

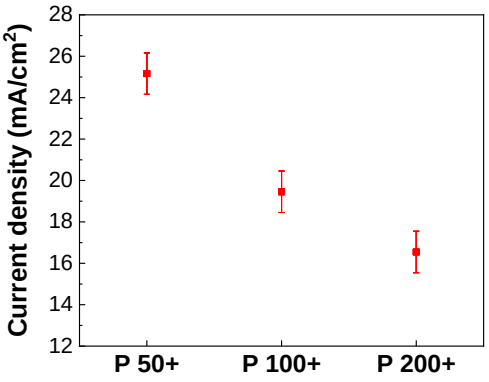

Figure V-12: Graph representing J_{SC} values of the P50+, P100+ and P200+ obtained by I-V measurements

Conclusion

In summary in this part we have demonstrated the direct application in the monolithic perovskite cell of the mesoporous TiO_2 layer replaced by the molding of PMMA particles of P50+, P100+ and P200+ sizes.

The results showed that the P50+ perovskite cell achieved a good improvement on the short-circuit current value (≈ 24 $mA.cm^{-2}$), when compared to the monolithic cell (≈ 19 $mA.cm^{-2}$). However, the Fill Factor remains almost unchanged, while the open-circuit voltage value is less than 900 mV. In addition, the measurement of the PCS as a function of time showed a decrease in performance over time. It is therefore difficult to say at this stage if the P50+ cells are more efficient than the reference cells, but the J_{SC} value and the good reproducibility of PSCs are encouraging for the following part.

Concerning the perovskite cells with the TiO_2 P100+ and P200+ porous layers; the drop-casting technique is obviously not adapted for the optimal infiltration based on the pictures of the cells and the SEM analysis.

From these results we decided to change the infiltration technique of perovskite precursors to the spin-coating technique used more often in planar structure cells. Also, for the PSC performance and stability enhancement we opt for a Formamidinium and cesium-based perovskite to replace the Methylammonium and a mixed halogenated part with iodide and bromide, which formula is: $(CH_5N_2)_xCs_{1-x}PbBr_xI_{3-x}$ - $FA_{0.83}Cs_{0.17}PbBr_{0.8}I_{2.2}$ [9], [118].

VI. Perovskite Light Absorber Replacing for PSC Stabilized Efficiency Enhancement; $MAPbI_3$ by Formamidinium-FA Lead Bromide $(CH_5N_2)_xCs_{1-x}PbBr_yI_{3-y}$) perovskite infiltrated in TiO_2 engineered pore size

This chapter deals with two different aspects, one concerns the replacement of the photo-active material; namely the $FA_{0.83}Cs_{0.17}PbBr_{0.8}I_{2.2}$ instead of the $MAPbI_3$, which is more commonly used, and the technique of infiltration of this new perovskite by a technique other than drop-casting, which is not suitable for larger pore sizes; i.e. the spin-coating method. The motivations to employ the $FA_{0.83}Cs_{0.17}PbBr_{0.8}I_{2.2}$ perovskite have been previously related in Part II.6.1.

We will first compare the PSC for the two perovskites light-absorber material with an infiltration by the usual drop-casting technique on the reference and P50+ cells. In a second step we will focus only on the $FA_{0.83}Cs_{0.17}PbBr_{0.8}I_{2.2}$ perovskite infiltration by spin-coating method on the reference cells, P50+, P100+ and P200+. Finally, we will conclude with the best outcome regarding the photoactive material and the infiltration technique to obtain the more efficient and stable monolithic PSC in our configuration.

VI.1. MAPI vs. $FA_{0.83}Cs_{0.17}PbBr_{0.8}I_{2.2}$: Precursors Infiltration by Traditional Drop-Casting Way for Reference and P50+ PSC

VI.1.1. The Process Description

The process description concerning the $MAPbI_3$ crystals formation has been already depicted in section III.1.3.1. Regarding the $FA_{0.83}Cs_{0.17}PbBr_{0.8}I_{2.2}$ perovskite preparation and infiltration; it differs by the used solvent for the precursor dissolution and by the annealing time and temperature due to this solvent. The protocol has been simply inspired from the literature [118], [145], [146]. The solution preparation and the infiltration carried by the drop-casting method for the $FA_{0.83}Cs_{0.17}PbBr_{0.8}I_{2.2}$ photo-active material are described below.

VI.1.1.1. The Solution Preparation

The protocol for the $FA_{0.83}Cs_{0.17}PbBr_{0.8}I_{2.2}$ perovskite solution preparation follows the one step deposition process like for the MAPI one. This means there is only one solution with all needed organic and inorganic precursors homogenously dispersed in the adapted solvent. The chemical compounds are commercial products either from Sigma Aldrich or TCI.

The solution is prepared in a small vial then stirred with a magnetic barre at room temperature during 30 min inside a glovebox to obtain the homogenous solution containing the perovskite precursor. The amount of all needed products for 1.1 mL of solution at 1.2 M of concentration is listed in Figure VI-1. The solution is prepared in a glovebox where chemical products are stored to avoid humidity storage.

The effect of solvent on perovskite crystals formation also named “solvent engineering” has been investigated in many studies [64], [147]. The most used solvents are the GBL (Gamma-Butyrolactone), DMF (Dimethylformamide) and DMSO (Dimethylsulfoxyde); each of them has different properties regarding solubility, viscosity and volatility. The choice of solvent is an important parameter and it depends also on the structure of the cells (planar or scaffolded) and on the perovskite precursors (high coordination for a homogenous solubilization) [148]. The preference for DMF-DMSO mixture for this preparation is due to the higher solubility of

precursors (strong coordination with solvent) and high crystallization of the perovskite structure [65].

	Compounds	Amount
Solvent	**DMF**: N, N-dimethylformamide	0.88 mL
	DMSO: Dimethylsulfoxyde	0.22 mL
Perovskite precursor	**FAI:** Formamidinium Iodide	0.2049 g
	CsI: Cesium Iodide	0.0633 g
	PbI_2: Lead Iodide	0.3967 g
	$PbBr_2$: Lead Bromide	0.210 g

Figure VI-1: Table resuming the protocol for the $FA_{0.83}Cs_{0.17}PbBr_{0.8}I_{2.2}$ perovskite solution preparation

VI.1.1.2. The Cells Infiltration Protocol by the Drop-Casting Method

The precursor's infiltration and the crystallization of perovskite crystals after the drop casting process are operated out of the glovebox in different steps like for the $MAPbI_3$ crystals but the time and temperature for annealing are different because they are specific to each solvent [63]. First the samples are covered with a glass lid avoiding air contact; for a period of 15 min at room temperature (Figure VI-2-1) that gives time to the solution containing the precursors to go in deep through the different porous layers of the cells. Then the covered samples are placed on a hot plate heated at 100 °C for 15 min with the lid (Figure VI-2-2) and for 30 min more without the lid (Figure VI-2-3). The lid helps keep the samples in solvent atmosphere to allow a homogeneous crystallization.

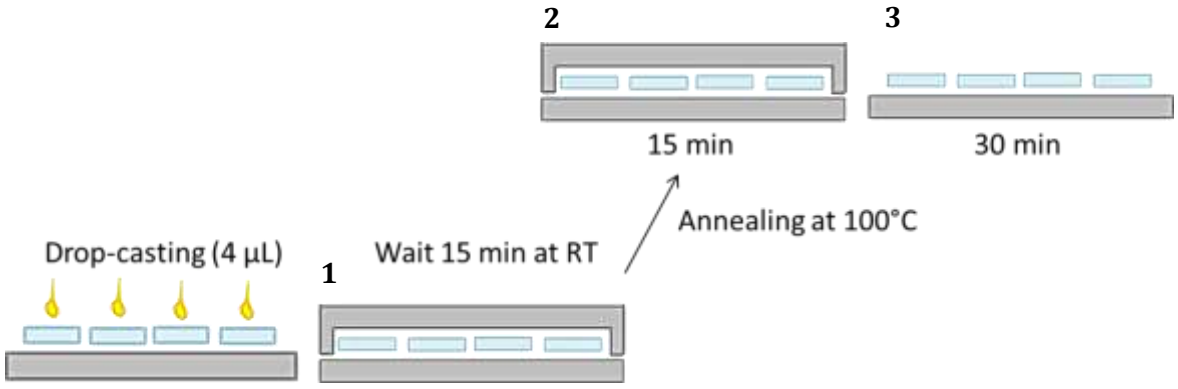

Figure VI-2: Scheme illustrating the different step during the infiltration of the solution by drop-casting way

VI.1.2. PSC Comparison with Different Characterization Tools

After the complete infiltration of the cells with the two different photo-active materials they have been characterized for their morphology, crystal structure, optical parameter as well as their photovoltaic performances in order to be able to carry out a comparison between $MAPbI_3$ and $FA_{0.83}Cs_{0.17}PbBr_{0.8}I_{2.2}$ perovskite light absorber material for reference and P50+ monolithic cells.

VI.1.2.1. The Perovskite Crystals Formation in the PSC Porous Layers

The infiltration of the $FA_{0.83}Cs_{0.17}PbBr_{0.8}I_{2.2}$ perovskite photo-active materials through the porous films was analyzed by the SEM/EDX mapping technique in the cell cross-section for the reference cell (Figure VI-3) and P50+ PSC (Figure VI-4).

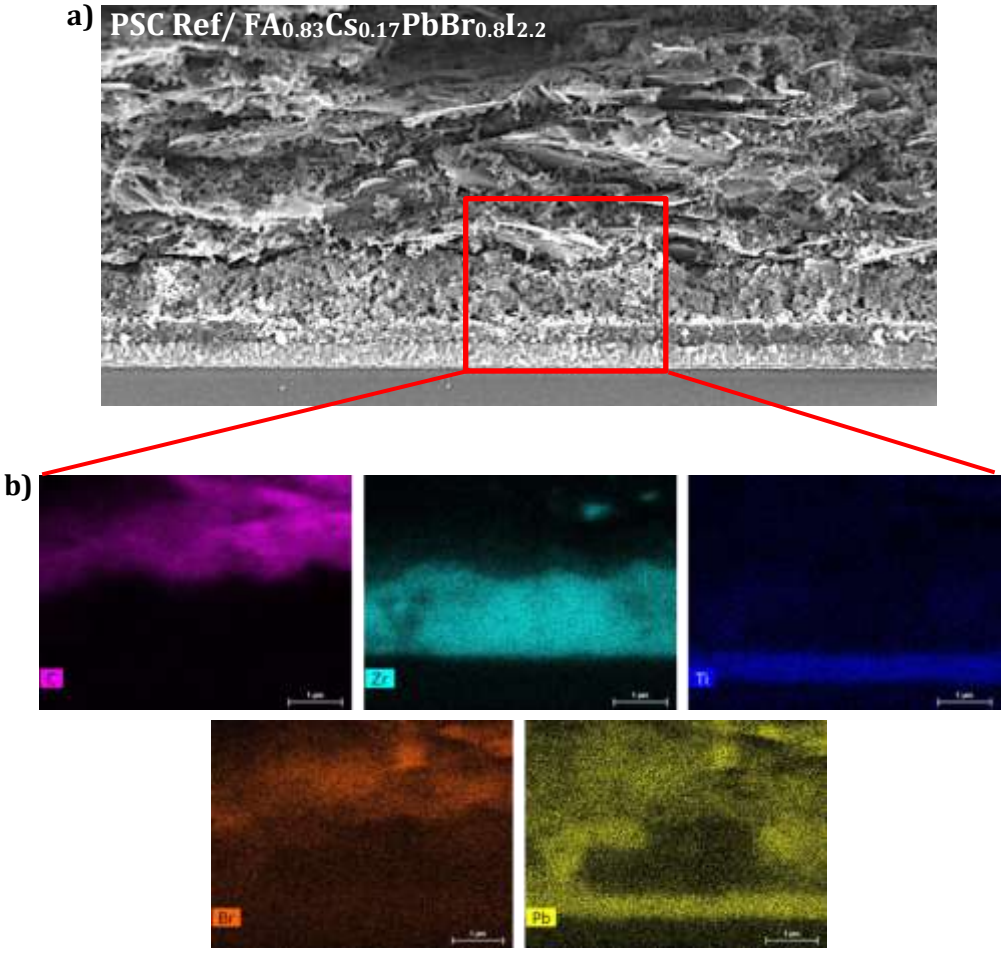

Figure VI-3: a) SEM image on the cross-section of the reference cell with $FA_{0.83}Cs_{0.17}PbBr_{0.8}I_{2.2}$ perovskite b) EDX mapping on the cross-section with layers and elements presents in the PSC

The images obtained for the reference cell clearly demonstrate a non-homogeneous infiltration and formation of perovskite crystals. At the interface of the ZrO_2 and TiO_2 porous layers, a thin layer of perovskite materials can be seen (bright line), while the TiO_2 porous film is modestly filled with photo-active material (dark area means non-infiltrated zone). It seems that the perovskite precursors were difficult to infiltrate into this mesoporous film. This can be supported by EDX mapping, which reveals a random distribution in the scaffolded films of the halogenated elements present in the perovskite crystals.

However, this phenomenon is not observed for the P50+ cell. Effectively the distribution of the perovskite crystals across the different porous layers is more homogeneous (Figure VI-4-a). This is as well demonstrated by the EDX cartography, which reveals a similar distribution of the Pb and Br elements found in the perovskite light-absorber material. This advantageous infiltration of $FA_{0.83}Cs_{0.17}PbBr_{0.8}I_{2.2}$ perovskite precursors in P50+ cell using the DMF/DMSO solvent may be due to the larger pore size and interface quality of the porous TiO_2 layer prepared by PMMA beads molding. This PSC configuration indicates to be more appropriate for this solvent and the precursors.

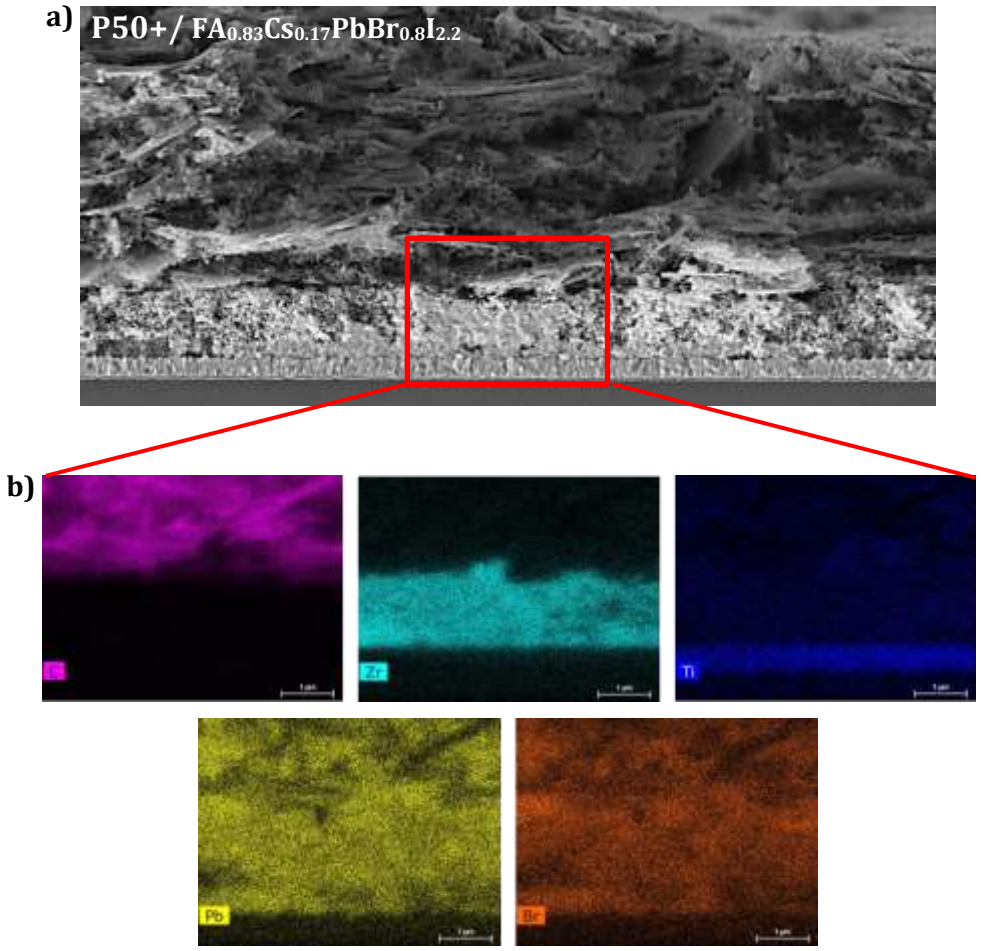

Figure VI-4: a) SEM image on the cross-section of the reference cell with $FA_{0.83}Cs_{0.17}PbBr_{0.8}I_{2.2}$ perovskite b) EDX mapping on the cross-section with layers and elements presents in the PSC

VI.1.2.2. The Optical Parameters Determination

The optical parameters of the different cells were determined by absorbance and photoluminescence measurements. The $FA_{0.83}Cs_{0.17}PbBr_{0.8}I_{2.2}$ and MAPI perovskites solar cells absorbance have been measured through the glass in aim to compare them (Figure VI-5).

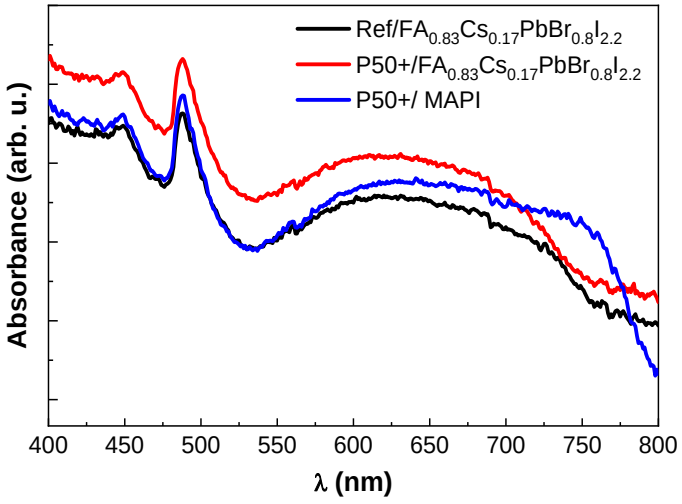

Figure VI-5: Absorbance graph of the $FA_{0.83}Cs_{0.17}PbBr_{0.8}I_{2.2}$ and MAPI perovskites solar cells

The obtained data reveal two interesting information, in particular a shift of the absorbance drops for the two types of perovskites used in the cell; the MAPI is around 750-780 nm, while the $FA_{0.83}Cs_{0.17}PbBr_{0.8}I_{2.2}$ is at a value of 730-750 nm, which means an increase of the optical band gap. The second observation concerns the P50+ cells, which have larger pore sizes and allow better infiltration of the photoactive material; a higher absorbance is observed for this type of structure regardless of the perovskite compared to the reference cell.

The photoluminescence measurement of these cells (Figure VI-6) confirms a modification of the optical band gap with perovskite $FA_{0.83}Cs_{0.17}PbBr_{0.8}I_{2.2}$ as a shift is observed to the left. The peak width is approximately similar for each curve and the highest peak is obtained with the P50+/$FA_{0.83}Cs_{0.17}PbBr_{0.8}I_{2.2}$ cell, while the lowest is obtained with the P50+/MAPI cell.

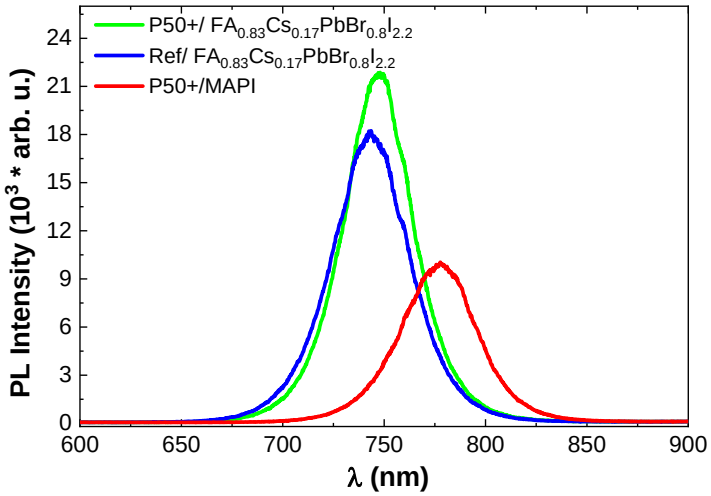

Figure VI-6: Graph representing the photoluminescence of the $FA_{0.83}Cs_{0.17}PbBr_{0.8}I_{2.2}$ and MAPI PSC

In order to experimentally estimate the value of the band gap for perovskite $FA_{0.83}Cs_{0.17}PbBr_{0.8}I_{2.2}$, we have determined its Tauc plot (Figure VI-7). The value obtained of about 1.69 ± 0.05 eV is higher than the MAPI E_g value (≈ 1.55 eV), however it appears consistent with the literature because the presence of the Br element tends to increase the optical band gap [9], [117].

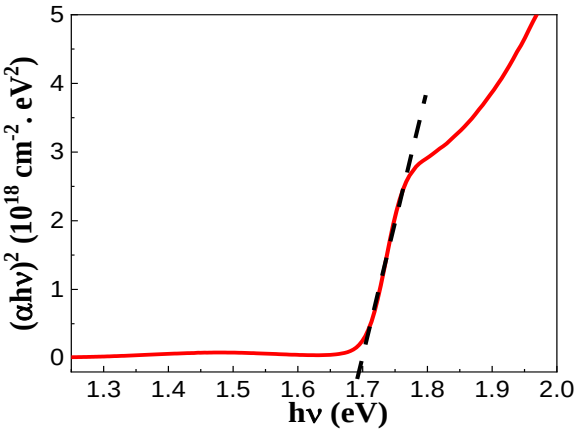

Figure VI-7: The Tauc plot representation for the E_g determination of the $FA_{0.83}Cs_{0.17}PbBr_{0.8}I_{2.2}$ perovskites

VI.1.2.3. The Crystalline Structure Characterization

The crystalline structure of the cells with different perovskite materials and cell configuration were characterized by XRD measurements (Figure VI-8).

The sample of the reference structure does not contain perovskite materials; it allows to highlight the peaks due to the presence of light absorber crystals.

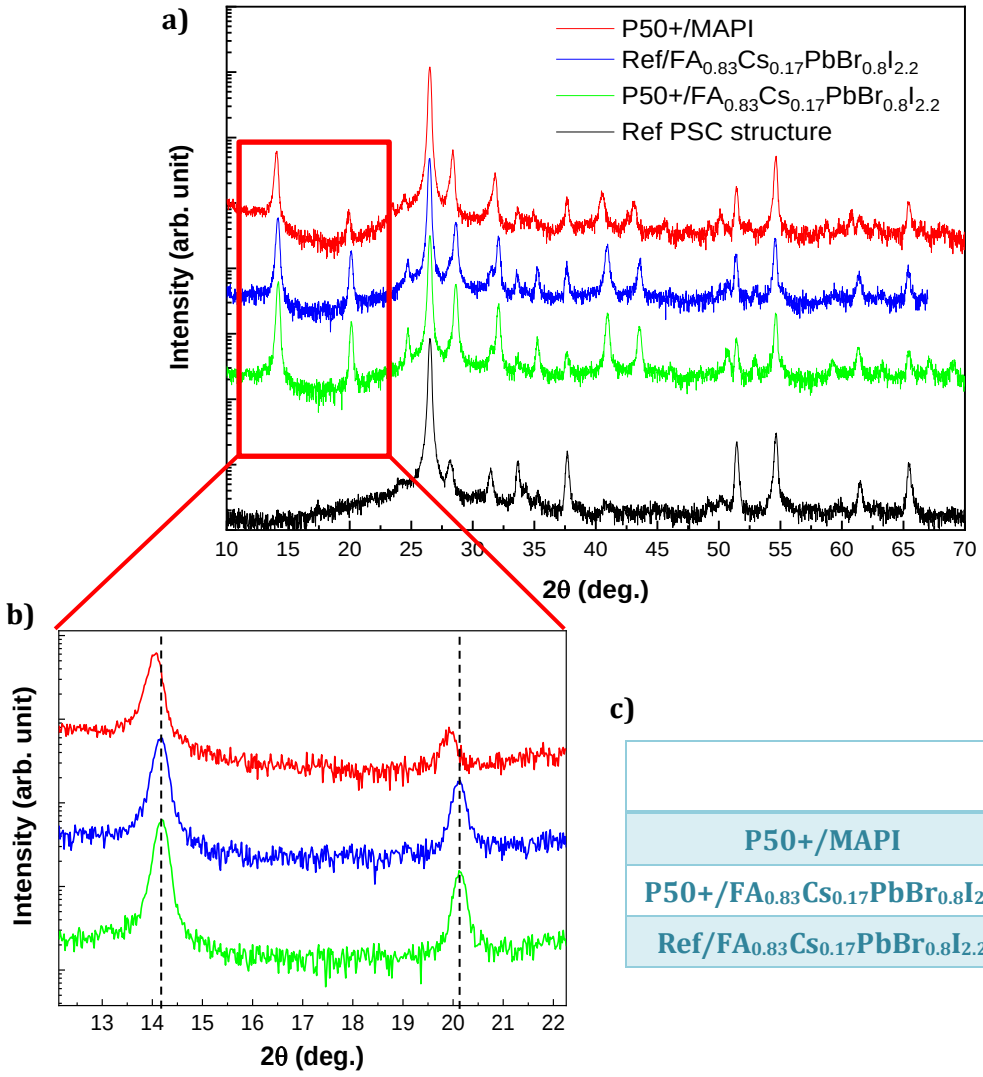

c)

	Crystallite size (nm)
P50+/MAPI	29.5 ± 0.2
P50+/$FA_{0.83}Cs_{0.17}PbBr_{0.8}I_{2.2}$	31.4 ± 0.3
Ref/$FA_{0.83}Cs_{0.17}PbBr_{0.8}I_{2.2}$	30.2 ± 0.2

Figure VI-8: a) XRD patterns of the solar cells with MAPI and $FA_{0.83}Cs_{0.17}PbBr_{0.8}I_{2.2}$ infiltrated perovskites and the reference structure before infiltration of light absorber material b) Zoom on the perovskites significant peaks c) Perovskites crystallite size determined by Scherrer equation

The specific peaks of the perovskite structure occur for each cell (Figure VI-8-a), however for perovskite $FA_{0.83}Cs_{0.17}PbBr_{0.8}I_{2.2}$ a shift of these peaks to the right can be observed. This can result in a modification of the perovskite phase because it can be either tetragonal or cubic (pseudocubic lattice parameter) in most cases depending on its chemical nature [145], [9]. The phase obtained for MAPI perovskite is tetragonal because the peaks correspond to the JCPDS 01-084-7607 as demonstrated previously in Part III.2.3. The crystallite size estimated from the peak at ≈ 14 ° using the Scherrer formula is about 30 nm for each sample (Figure VI-8-c).

In order to refine the characterization of the structure of perovskite $FA_{0.83}Cs_{0.17}PbBr_{0.8}I_{2.2}$, we performed TEM analyses as previously seen for MAPI perovskite in the section III.2.3. We observe the atomically plan position at high resolution as shown in Figure VI-9-a. We selected different areas in the recorded high resolution TEM images for the FFT analysis. The results represented below are from two distinct regions. According to the orientation of the crystals growth we can get FFT from a, b or c axis; cubic representation follows one axis and indeed we observe a cubic patterns (Figure VI-9-b) and rectangular patterns depending on another axis shown in Figure VI-9-c. The experimental diffraction patterns confirm that the perovskite structure is tetragonal and polycrystalline.

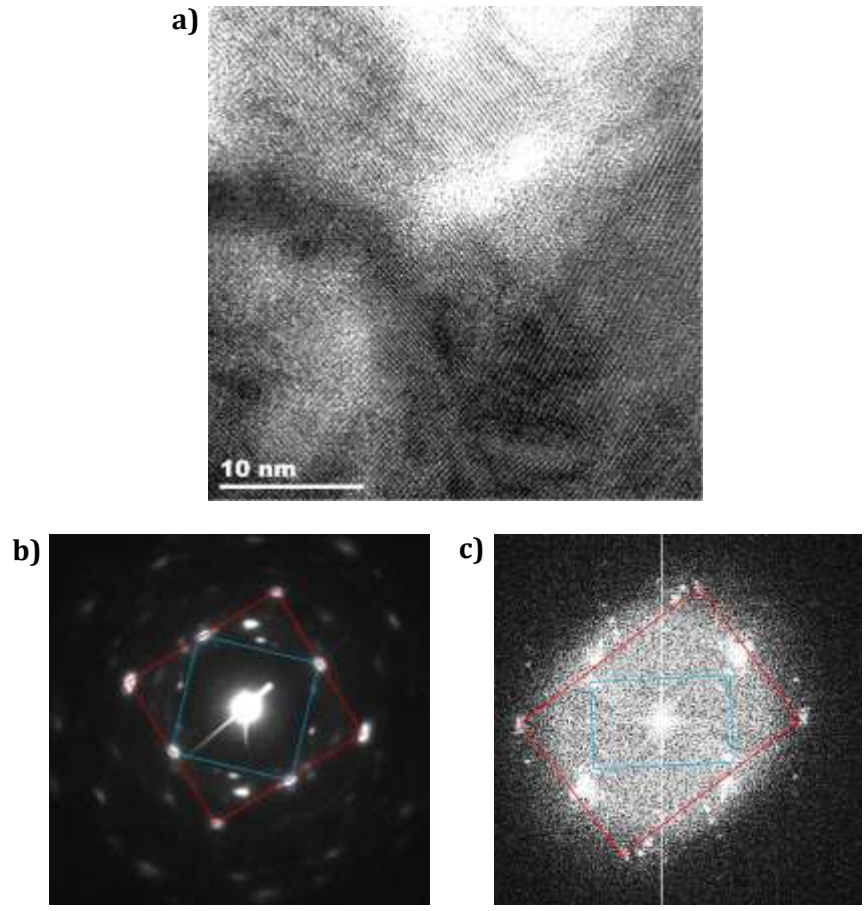

Figure VI-9: a) TEM images of the $FA_{0.83}Cs_{0.17}PbBr_{0.8}I_{2.2}$ crystals deposited on copper grid b) FFT of the sample at selective area corresponding to c axis with cubic patterns c) and rectangular patterns

For the analysis of the homogeneous chemical composition we have used the STEM method (Appendix VIII.1.3) coupled with an EDX detector. The results shown in Figure VI-10-a reveal a homogeneous perovskite $FA_{0.83}Cs_{0.17}PbBr_{0.8}I_{2.2}$ crystal formation (without contrast) and the perovskites precursors elements are all present in the formed material as evidenced by the EDX graph (Figure VI-10-b).

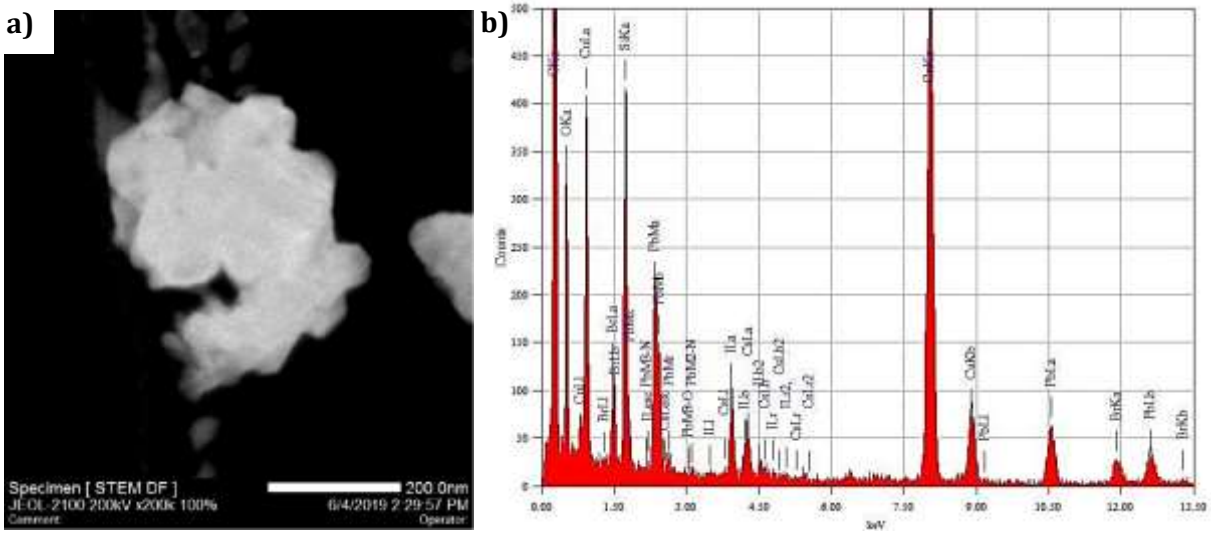

Figure VI-10: a) STEM image of $FA_{0.83}Cs_{0.17}PbBr_{0.8}I_{2.2}$ crystals deposited on Cu grid b) EDX Graph representing the presence of the different chemical element with Br at 1.48 keV, I at 3.94 KeV, Cs at 4.29 KeV and Pb at 2.34 KeV. The elements of C, O, Si and Cu are due to the environment

VI.1.2.4. The $FA_{0.83}Cs_{0.17}PbBr_{0.8}I_{2.2}$ PSC Performances Characterization

The parameters of the perovskite solar cells with the $FA_{0.83}Cs_{0.17}PbBr_{0.8}I_{2.2}$ light-absorber material were determined by I-V measurements (Figure VI-11). There are two cells per similar conditions for the P50+ and references PSC.

The curves obtained indicate a low hysteresis (reverse and forward scans) in contrast to that previously observed for the MAPI cells (Figure III-28). The efficiencies of the P50+ cells are very close to each other and are higher than the reference cells, which provide two different efficiencies and therefore are less reproducible. The low yield for the reference cells can be explained by the poor infiltration of the solution containing perovskite precursors during drop-casting as observed in the SEM images (Figure VI-5).

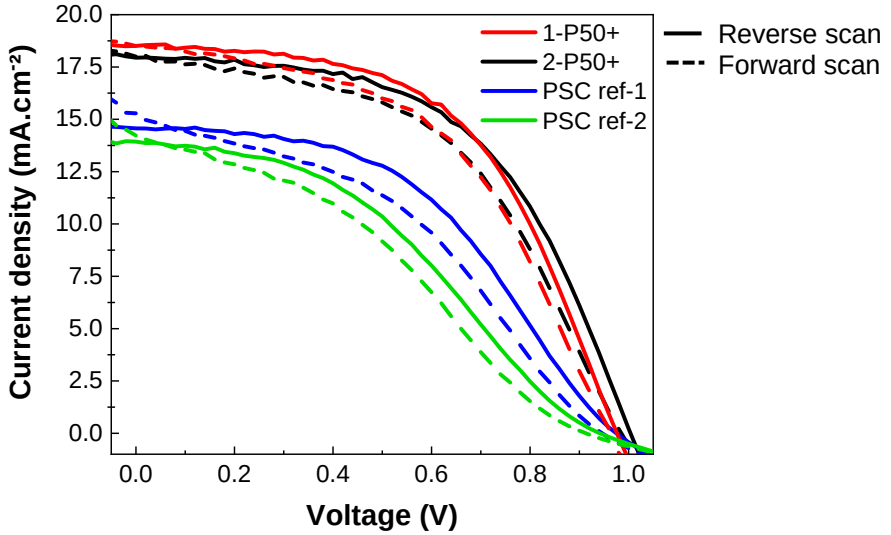

Samples	Scan	V_{OC} (mV)	J_{SC} (mA.cm^{-2})	*FF* (%)	Efficiency (%)
1-P50+	Reverse	976.5	18.5	54.1	**9.8**
	Forward	963.9	18.5	50.2	8.9
2-P50+	Reverse	1004.0	17.9	53.8	**9.7**
	Forward	985.3	18.0	50.1	8.9
PSC ref-1	Reverse	977.7	14.9	46.3	**6.8**
	Forward	953.1	15.1	41.2	5.9
PSC ref-2	Reverse	941.8	13.9	39.5	**5.2**
	Forward	912.9	14.2	35.5	4.6

Figure VI-11: I-V graphs and PV parameters for the forward and reverse scans of the P50+ and reference cells with $FA_{0.83}Cs_{0.17}PbBr_{0.8}I_{2.2}$ perovskites as photo-active material

Nevertheless, it is important to verify the stability of the performance as a function of time. The Figure VI-12 shows the results of the PCE (Power Conversion Efficiency) over time measurements for the cells with perovskite $FA_{0.83}Cs_{0.17}PbBr_{0.8}I_{2.2}$ (P50+ and reference) and a P50+ MAPI cell for comparison purposes. The curves obtained show clearly a difference between the cells containing the traditional MAPI as perovskite and the new used one. Indeed, these cells have a stationary efficiency over the measurement time, while the P50+ MAPI cell decreases considerably as seen above in section IV.

The introduction of $FA_{0.83}Cs_{0.17}PbBr_{0.8}I_{2.2}$ perovskite in c-PSC shows great interest for obtaining stable power efficiency; it is ≈ 9.3 % for the P50+ cell against a value of ≈ 5.9 % obtained with the reference cell. The P50+ PSC efficiency recorded with MAPI perovskite as light absorber does not stabilized and decreases from a PCE of about 10 % to ≈ 7% in short time.

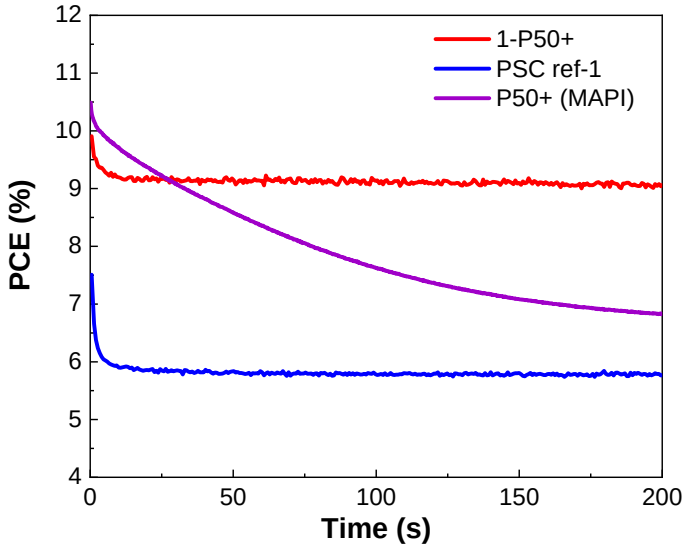

Figure VI-12: Graph representing the stabilized efficiency at MPP of the P50+ MAPI and $FA_{0.83}Cs_{0.17}PbBr_{0.8}I_{2.2}$ and reference perovskite solar cell as function of time

VI.2. Drop-Casting vs. Spin-Coating: New Infiltration Way with the $FA_{0.83}Cs_{0.17}PbBr_{0.8}I_{2.2}$ Perovskite Light Absorber for P50+, P100+ and P200+ PSC

Since the results obtained with the P50+/$FA_{0.83}Cs_{0.17}PbBr_{0.8}I_{2.2}$ cell have been promising, it is natural to focus on the use of this perovskite in larger pore sizes with the P100+ and P200+ cells. However, we have previously seen that the drop-casting technique was not adapted for this type of cell because the infiltration was not uniform (Figure V-8). This is why in this part we have decided to use spin-coating as an alternative technique to replace drop-casting.

The deposition parameters have been optimized and are described below. Then, the cell performances have been characterized in order to estimate their evolution. Finally, we will discuss the results on this use of perovskite in monolithic PSC with the porous TiO_2 layer prepared by PMMA particles molding.

VI.2.1. The Process Description for the Spin-Coating Deposition

The spin-coating technique is mainly used for the planar structure of perovskite solar cells [33], [81], [149]. In the case of monolithic cells, this is a first assay for cells of type P50+, P100+ and P200+. The important parameters to optimize for this kind of deposition method are the volume of solution and the deposition speed, which can be done in multiple steps. For the volume we have tested values ranging from 10 µL up to 100 µL and for the rotation speeds we have experimented from low speed (2000 rpm) up to higher speed (5000 rpm). The results obtained showed that the appropriate volume is less than 50 µL and for the deposition speeds we used a two-step process;

a first fast step for a homogeneous spreading of the solution on the sample and a second slower step for an optimal infiltration in the porous layers.

To resume the volume of solution applied is 30 µL and the deposition conditions are 3500 rpm for 10 s and 2000 rpm for 20 s (Figure VI-13). Following deposition, the sample is directly annealed at 100 °C for 30 min. The sample coverage step as performed for the drop-casting method (Figure VI-2) is not necessary in this scenario because the excess solvent is already evaporated after spin-coating deposition.

The entire process from the preparation of the solution to the deposition by spin-coating and the annealing of the samples is done in glovebox.

In order to observe if the cells were well infiltrated we have taken pictures from the front and from the back through the glass after the annealing of the 30 min at 100 °C (Figure VI-14). The images display a homogeneous formation of $FA_{0.83}Cs_{0.17}PbBr_{0.8}I_{2.2}$ perovskite crystals on the active area for the three type cells of P50+, P100+ and P200+. This deposition technique therefore seems more appropriate for cells containing the larger pore for the scaffolded TiO_2 layer.

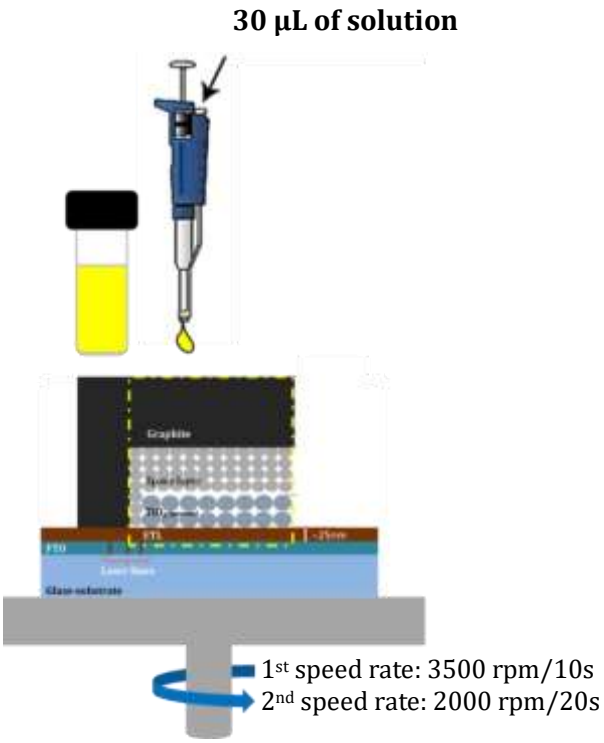

Figure VI-13: Scheme illustrating the protocol of perovskite precursors infiltration by spin-coating deposition respecting the one-step method

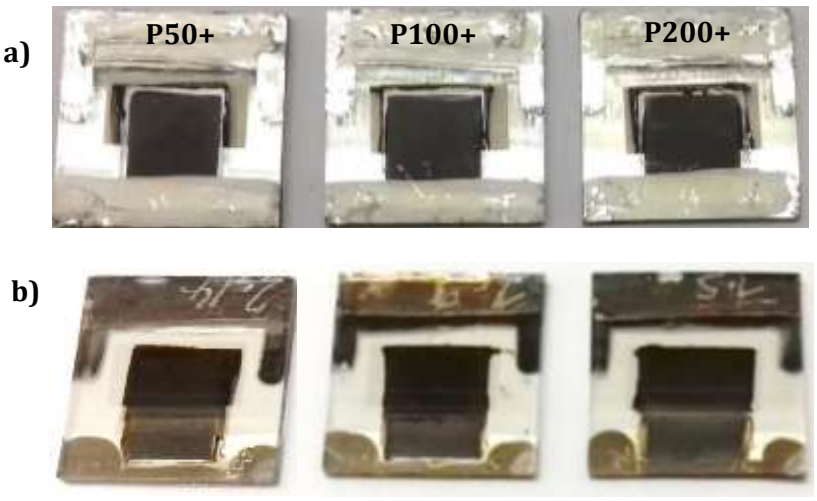

Figure VI-14: a) Pictures from the top view of the PSC after the annealing b) and back view through the glass

For a complete analysis the cells were observed by SEM microscopy on the section followed by EDX mapping. The images recorded for the P50+, P100+ and P200+ PSC infiltrated by spin-coating method are represented in Figure VI-15, Figure VI-16 and Figure VI-17 respectively.

According to the results, the spin-coating technique for infiltrating perovskite precursors is more effective than drop-casting, particularly for larger TiO_2 pore sizes. The distribution of the elements Pb and Br are relatively homogeneous in all the scaffolded layers of the perovskite solar cell regarding the EDX mapping analyzes. Nevertheless, areas of pores that are not completely infiltrated can be observed, such as P100+ and P200+ layers, but it is still less when compared to the drop-casting method (Figure V-11). Infiltration parameters such as volume, deposition rate have been optimized for this spin-coating approach but it can still be further improved. In addition, it is possible to change other parameters such as the concentration of the solution containing perovskite precursors. More insight, another approach that may be considered is the anti-solvent technique after deposition of the solution by spin-coating [63], [65]. In this work we will not investigate more on the infiltration parameters but it is worth knowing that they can be improved, as explained above.

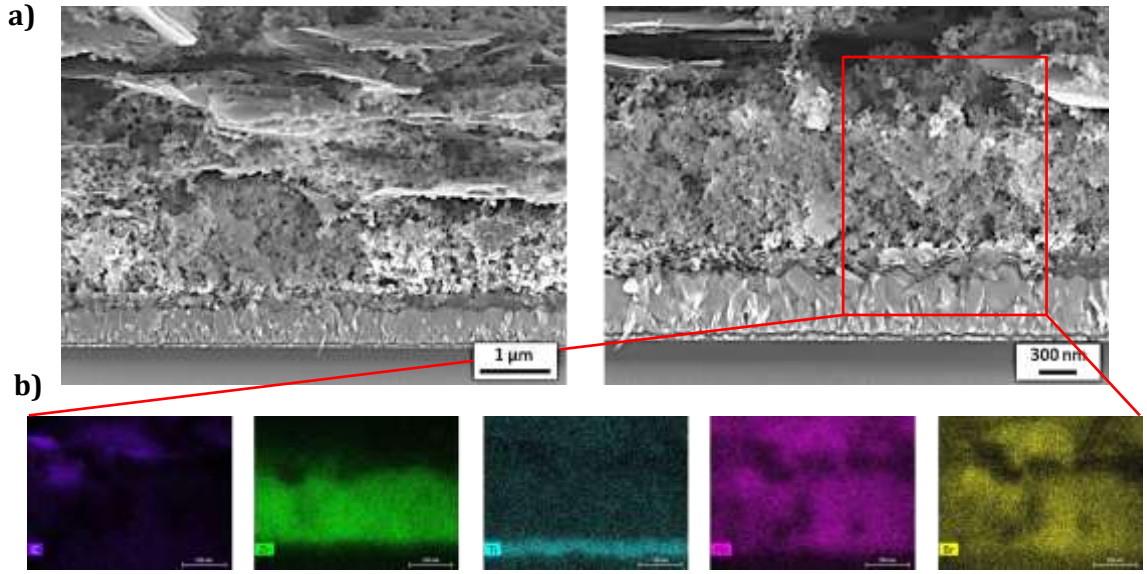

Figure VI-15: a) SEM image on the cross-section of the P50+ perovskite solar cell with $FA_{0.83}Cs_{0.17}PbBr_{0.8}I_{2.2}$ perovskite infiltrated by spin-coating method b) EDX mapping on the cross-section with layers and elements presents in the PSC

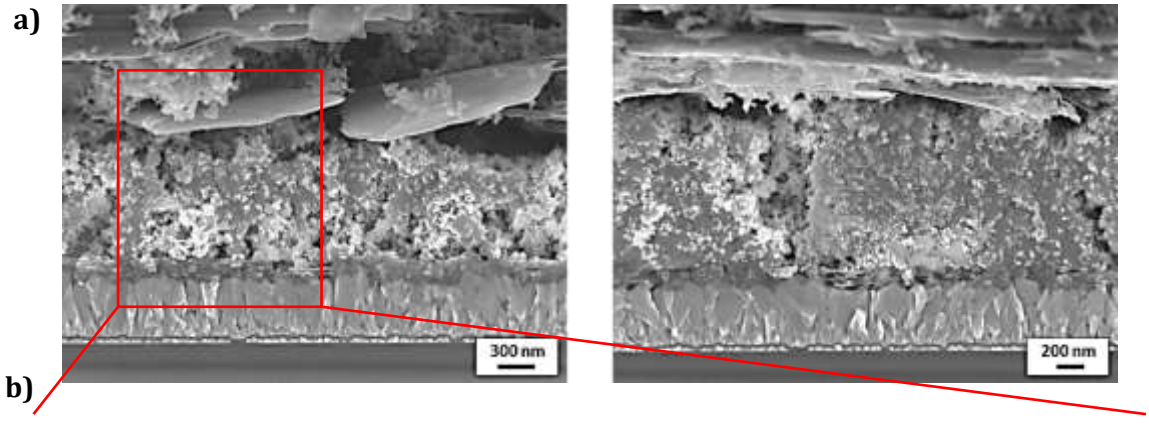

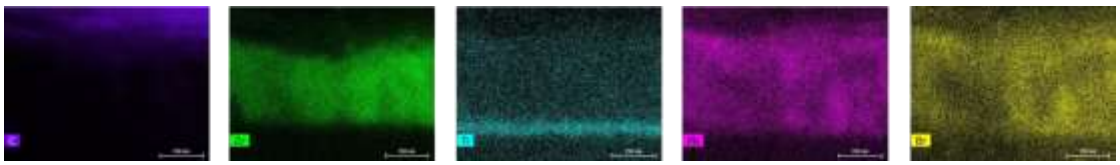

Figure VI-16: a) SEM image on the cross-section of the P100+ perovskite solar cell with $FA_{0.83}Cs_{0.17}PbBr_{0.8}I_{2.2}$ perovskite infiltrated by spin-coating method b) EDX mapping on the cross-section with layers and elements presents in the PSC

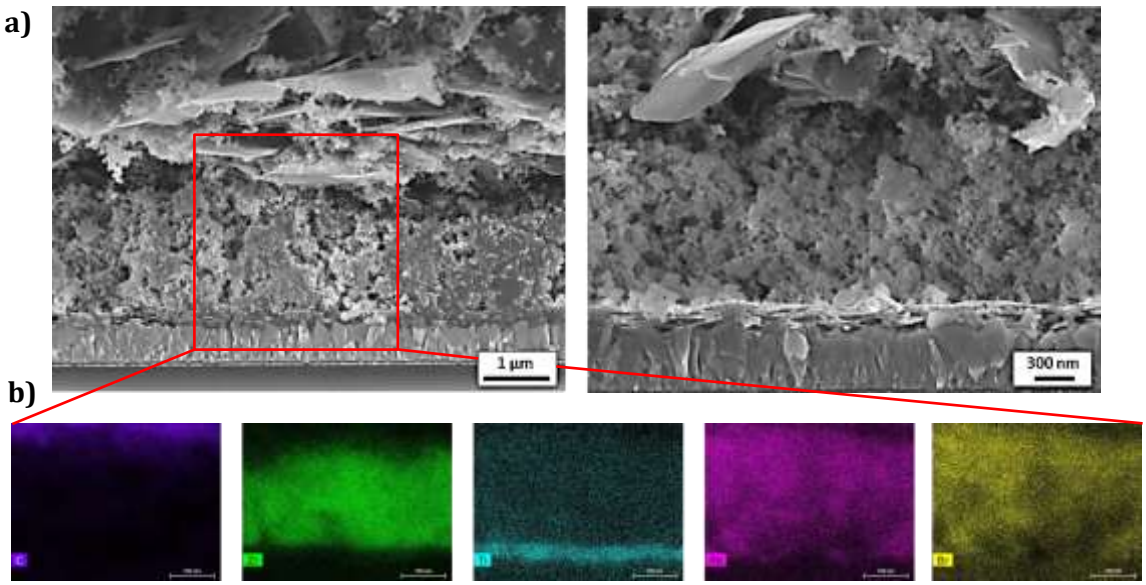

Figure VI-17: a) SEM image on the cross-section of the P200+ perovskite solar cell with $FA_{0.83}Cs_{0.17}PbBr_{0.8}I_{2.2}$ perovskite infiltrated by spin-coating method b) EDX mapping on the cross-section with layers and elements presents in the PSC

VI.2.2. The Crystalline Structure Characterization by XRD

In contrast to the drop-casting technique where the infiltration of the solution containing the perovskite precursors is carried out from the side of the active area (Figure III-6), the spin-coating method consists in depositing directly through the graphite in order to reach and fill the pores of the ZrO_2 and TiO_2 layers. In order to measure the crystalline structure of the perovskite thus formed in the porous layers and not only in the top layer of the graphite, we have removed it by mechanical exfoliation using Kapton® tape. The XRD measurements of a P50+/ $FA_{0.83}Cs_{0.17}PbBr_{0.8}I_{2.2}$ prepared by spin-coating way have been carried out before and after the graphite layer removal to observe the structure of the perovskite crystals present in the scaffolded layers (Figure VI-18).

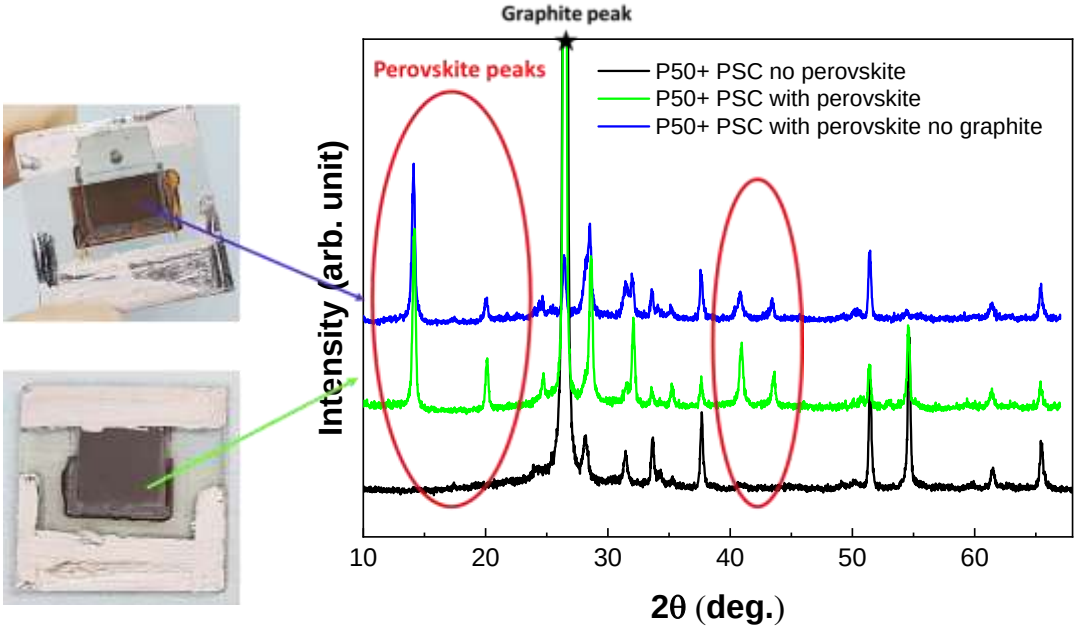

Figure VI-18: XRD diffractogram of the P50+/ $FA_{0.83}Cs_{0.17}PbBr_{0.8}I_{2.2}$ monolithic cell before and after the graphite removing highlighting the presence of perovskite crystals through the porous layers

We have two observations from these measurements: the color of perovskite is different compared to that of MAPI, which is darker while this one tends towards brown color [145]. The second remark concerns the graphite peak, which decreases considerably after it disappears while the perovskite peaks at ≈ 14 ° and ≈ 20 ° are still visible.

VI.2.3. The P50+, P100+ and P200+ / $FA_{0.83}Cs_{0.17}PbBr_{0.8}I_{2.2}$ PSC Performances Characterization and Comparison

The I-V measurements were carried out on a series of cells with about ten PSC per condition in such a way that statistics on their performance and reproducibility could be compiled. The Figure VI-19 represents below the I-V curves and photovoltaic parameters that are obtained on average from each type of cell and the Figure VI-20 shows the PV performances statistics on complete series for the P50+, P100+ and P200+ PSC.

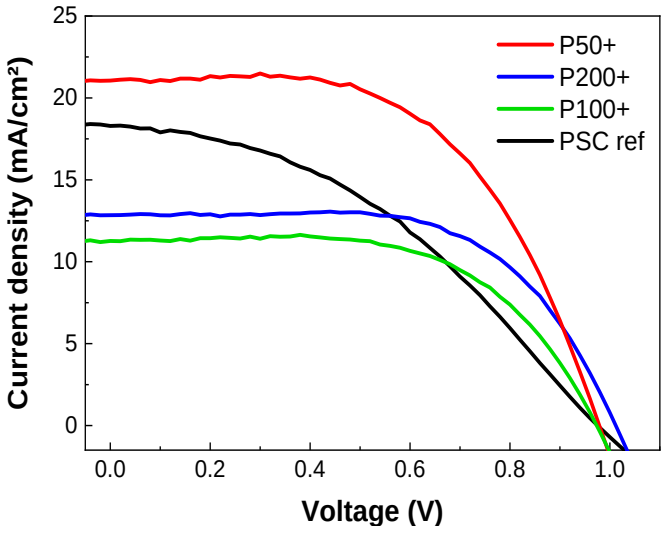

	V_{OC} (mV)	J_{SC} (mA.cm^{-2})	*FF* (%)	Efficiency (%)

P50+	979.0	20.7	57.1	**11.7**
P100+	973.6	11.3	61.1	**6.7**
P200+	1011.9	12.6	62.7	**8.2**
Ref	975.4	18.3	40.5	**7.2**

Figure VI-19: Graph and table representing the results of I-V measurements of the P50+, P100+, P200+ and reference PSC with FA0.83Cs0.17PbBr0.8I2.2 perovskite infiltrated by spin-coating method

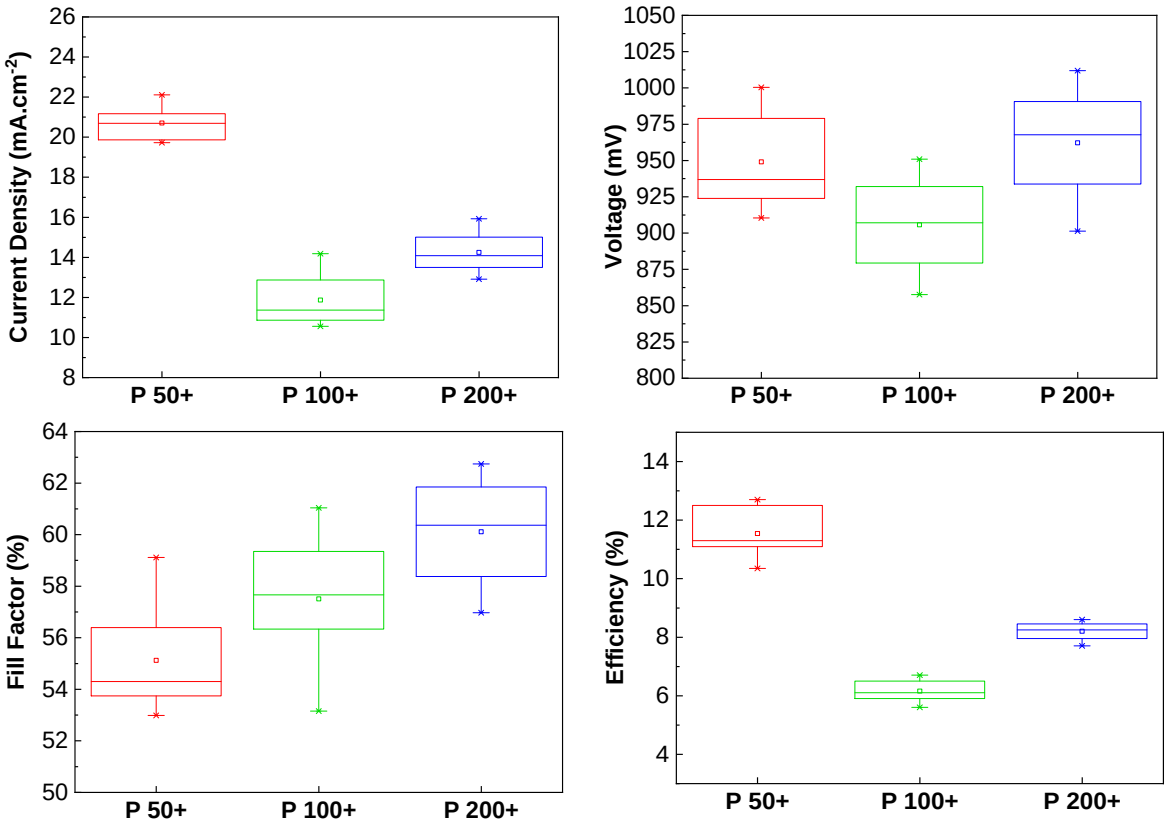

Figure VI-20: Statistical representation of the photovoltaic parameters as J_{SC}, V_{OC}, FF and efficiency of the P50+, P100+ and P200+ solar cells series

The I-V curves achieved demonstrate an improved performance in all solar cells. The P50+ cell has the highest efficiency with an average value of 11.7 %. The P200+ PSC recorded the best V_{OC} and Fill Factor but the J_{SC} value is less than the P50+, which is ≈ 12 mA.cm^{-2} instead of ≈ 20 mA.cm^{-2}. The reference cell obtained has an interesting V_{OC} and J_{SC} but the *FF* is still low.

The statistics on PV parameters of the different PSC have different variations, for example, the current density is considerably greater for P50+ cells, while the fill factor increases with pore size. Nevertheless, what remains interesting is the reproducibility of the cells' performance in terms of efficiency, represented by a narrow box of statistics.

In addition, the performance measurements as a function of time are stable and the results are reliable with I-V measurements with about 11.4 % for P50+ PSC, 8 % for P200+ and 6.6 % for the P100+ perovskite solar cells. The reference cell PCE decreases more than the others cells (> 1 %) at the beginning and then it stabilizes as well. To summarize, the most promising enhancement concerns the P50+ and P200+ PSC.

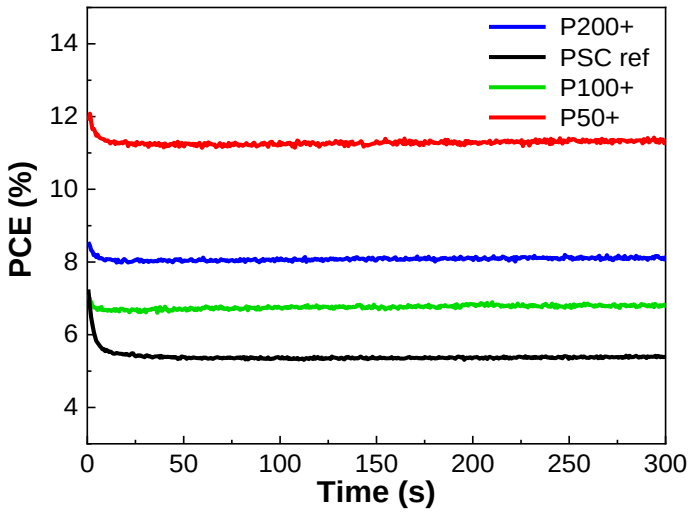

Figure VI-21: Graph representing the stabilized efficiency at MPP of the P50+, P100+, P200+ and reference $FA_{0.83}Cs_{0.17}PbBr_{0.8}I_{2.2}$ perovskite solar cell as function of time

VI.2.4. Preliminary Work on P50+ and P200+ Porous Layers Improvement

Considering the positive results obtained for the P50+ and P200+ cells, it was interesting to investigate whether it was still possible to improve their performance by increasing the TiO_2 porous layers thickness and therefore the amount of infiltrated photo-active $FA_{0.83}Cs_{0.17}PbBr_{0.8}I_{2.2}$ materials. This section discusses the first results obtained for these tests.

The approach to increase the thickness of the porous layers was to double the concentration of the PMMA bead suspension solution, which is initially at 10 % in weight and to maintain similar the molding process parameters. The SEM images below represent the deposition of these concentrated solutions by spin-coating on silicon substrates, which consists in the first step of the molding process (Figure IV-1).

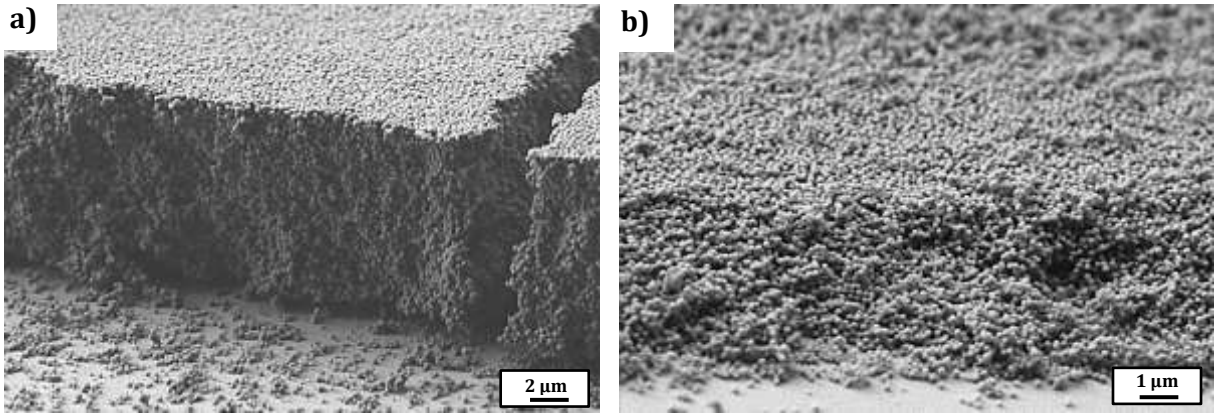

Figure VI-22: SEM images of the PMMA particles concentrated solution deposited by spin-coting on Si substrate for a) P50+ particles size and b) P200+

Figure VI-22-a shows a compact layer of PMMA P50+ particles that are excessively thick and cause cracks. However, the layer of P200+ beads is thicker for the concentrated solution compared to the previous one (Figure IV-8) and moreover it is cracks-free. The next step of the protocol is the deposition and infiltration of the sol-gel solution by spin-coating on the PMMA beads. This is

followed by a slow annealing process for the evaporation of the beads and the crystallization of the sol-gel solution containing the Ti precursors. The results obtained for the concentrated P200+ polymer particles (P200+C) molding are observed by SEM imaging from the top and side view and are reported hereunder.

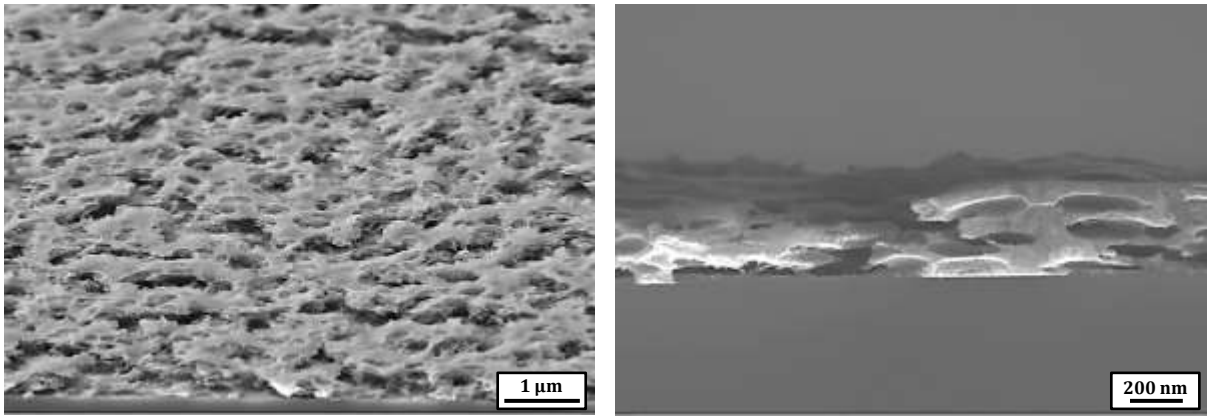

Figure VI-23: SEM images of TiO_2 porous layers obtained by molding of the 200+ PMMA particles and concentrated solution from top view a) and on the cross-section b)

The morphology of the TiO_2 porous layer is different when the PMMA beads film is thicker. The pore size is the same (≈ 260 nm); the porous layer is over 100 nm thicker but has a cracked surface and a high roughness. The film is not uniform but the framework may be relevant for application to the perovskite solar cells. Concerning the concentrated solution of P50+ PMMA particles the initial non-concentrated solution was used and three successive bead layers were deposited to obtain a thicker and more homogeneous film instead of using the concentrated solution. The porous layer using concentrated P50+ and P200+ PMMA particles solution are labeled P50+C and P200+C respectively. These thicker layers were integrated into the monolithic cell as a porous TiO_2 film. Figure VI-24 represent below the P200+C PSC:

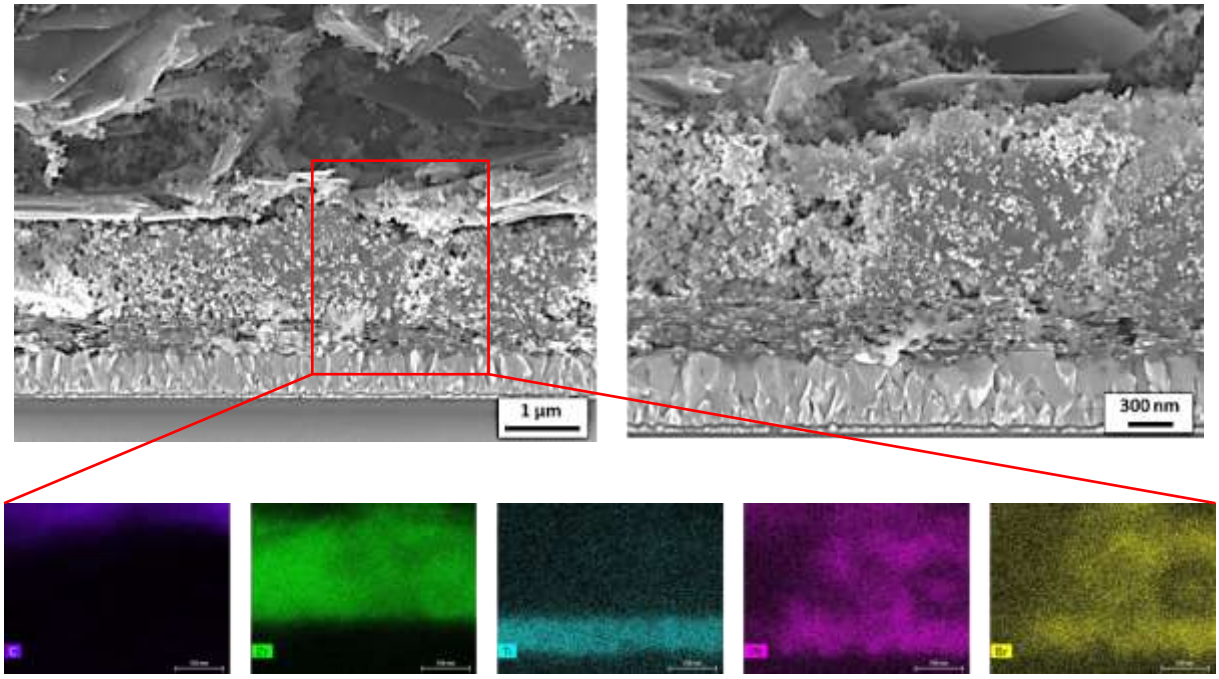

Figure VI-24: SEM image on the cross-section of the P200+C perovskite solar cell with $FA_{0.83}Cs_{0.17}PbBr_{0.8}I_{2.2}$ perovskite infiltrated by spin-coating method b) EDX mapping on the cross-section with layers and elements presents in the PSC

Compared to the previous P200+ PSC SEM/EDX images (Figure VI-17), we can clearly observe that the porous TiO_2 molded layer obtained with the concentrated PMMA particles solution is thicker. The resulting thickness is over than 300 nm instead of ≈ 150 nm for the previous P200+ TiO_2 porous layer. It is therefore possible to increase the thickness of the porous layer by increasing the concentration of PMMA particle solutions. However, this approach may have its limitations as it also influences directly the homogeneity of the porous layer. Indeed, an excessively thick beads layer has cracks which are then replicated on the porous layer after the molding process. This parameter can be further optimized.

The PV performances were characterized by I-V measurements. The graph in Figure VI-25 illustrates the resulting curves. The determined PV parameters indicate a significant increase in efficiency, indeed the values of J_{SC} are higher but the V_{OC} is slightly lower. The J_{SC} improvement could be explained by the light absorber amount increasing in the PSC.

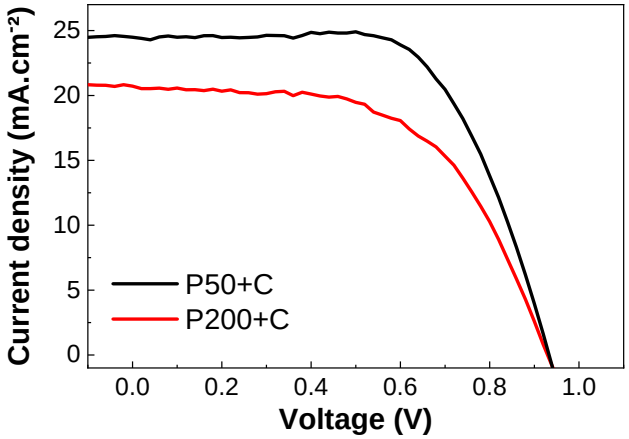

	V_{OC} (mV)	J_{SC} (mA.cm^{-2})	*FF* (%)	Efficiency (%)
P50+C	933.0	24.5	64.3	**14.7**
P200+C	929.6	20.7	56.6	**10.9**

Figure VI-25: Graph and table representing the results of I-V measurements of the P50+C and P200+C perovskite solar cells with $FA_{0.83}Cs_{0.17}PbBr_{0.8}I_{2.2}$ light-absorber infiltrated by spin-coating method

The PCE as a function of time also provides stable values, it is about 13.6 % for the P50+C cell and 10.7 % for the P200+C PSC; this has even a tendency to increase over time.

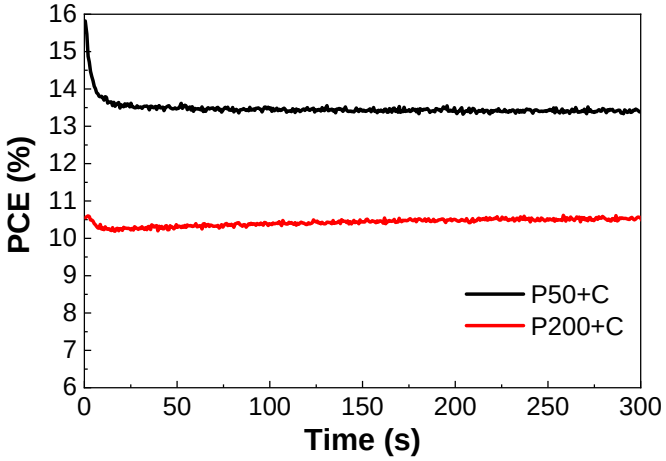

Figure VI-26: Stabilized efficiency measurement at MPP of the P50+C and P200+C / $FA_{0.83}Cs_{0.17}PbBr_{0.8}I_{2.2}$ perovskite solar cell as function of time

These results reveal interesting initial results that still need to be optimized. The investigation on statistical PV parameters measurements and on the PCE analysis over longer time could be necessary as well the study of the cells reproducibility and stability for a more extended period.

Conclusion

To recapitulate, this part is the finalization of the work accomplished during this thesis with the integration of the porous TiO_2 layers prepared by molding and the use of a new type of $FA_{0.83}Cs_{0.17}PbBr_{0.8}I_{2.2}$ perovskites.

The replacement of the $MAPbI_3$ photo-active perovskite material with $FA_{0.83}Cs_{0.17}PbBr_{0.8}I_{2.2}$ crystals has resulted in quasi-stationary time-dependent performance for each type of PSC.

The spin-coating technique to substitute the drop-casting method used traditionally to infiltrate the porous layers with perovskite precursors has proven to be more successful for cells with larger pore sizes for the TiO_2 scaffolded layer.

In general, the P50+, P100+ and P200+ have demonstrated improved photovoltaic performances compared to reference cells. The most important J_{SC} value achieved is for the P50+ cell and the SEM images demonstrated a proper infiltration, while for the reference cell it was non-uniform in the porous TiO_2 layer. However, the value of the Fill Factor had tended to increase with pore size; it reached more than 62 % with the P200+ cell. This can be caused by the reduction of series and shunt resistance in the cell as explained in Part II.3.2.2.

Finally, the part on the preliminary experiments demonstrated that there is still potential for improvement of the performance of the P50+ and P200+ cells, which have already shown promising photovoltaics parameters. The highest stabilized efficiency is obtained for the P50+C type of cell with $FA_{0.83}Cs_{0.17}PbBr_{0.8}I_{2.2}$ light absorber perovskite material infiltrated by spin-coating method; with a recorded stabilized value of ≈ 13.6 %. This is followed by the P200+C cell with a stabilized PCE around 10.7 %.

However, it is important to focus on the study of cell degradation over time because although it shows interesting efficiencies, it is important to study their behavior as time goes on. Even if the P50+ cells have achieved higher efficiencies they can degrade more rapidly than the large pore cells. The influence of pore size as a function of cell stability will be studied in future work.

VII. Conclusions and Perspectives

Conclusions

The thesis topic is about perovskite solar cells based on carbon structure. The choice of such configuration is the simplicity of the elaboration technique because the cells can indeed be screen-printed (using commercial paste for m-TiO_2, m-ZrO_2 and graphite layers) and thus it is easier to manufacture them. Then the perovskite precursor solution is simply filled from the top usually by drop-casting method and following this, the cells are simply annealed at low temperature to promote the perovskites crystals growth through the porous layers. Considering the many advantages of this type of configuration, we have focused the thesis work on the development of the c-PSC structure. Our motivations and strategy for this topic follow the stability challenging aspect and issues points encountered for this PV activity.

In addition, the active material crystals grown in such mesoporous TiO_2 scaffolds often suffer from incomplete crystallite formation, depending on size of the employed TiO_2 nanoparticles. Regarding the current issues and alternative as cited above, it appears interesting to elaborate TiO_2 scaffolds with a macro-porous structure trough a pore size engineering process using sol-gel solution and polymer particles. Another device advantage of the perovskite solar cell is the solution-processing enabling fabrication at low cost and the opportunity to modify easily the perovskite chemical nature and thereby the properties.

Hence, this gives rise to our intuitive strategy where the m-TiO_2 layer is replaced by a porous layer with larger cavities (size ranging over ≈ 50 nm to ≈ 250 nm) prepared by PMMA particles molding with a sol-gel solution containing Ti precursors. Also, the traditional $MAPbI_3$ light harvesting is replaced by a mixed cation and halide perovskite. Regarding positive effect of cations mixture; a small amount of inorganic Cesium is used to improve FA perovskite compounds. The X halide part is combined with Br and I element in order to improve the optical properties. Consequently, the classical previous photo-active material is replaced by $(CH_5N_2)_xCs_{1-x}PbBr_yI_{3-y}$ mixed perovskite where x = 0.83 and y = 0.8.

In summary, in this thesis work I have studied both; the pore size engineering effect of sol-gel solution on self-assembled PMMA particles ranging from 80 nm to 280 nm diameter to obtain scalable pore size of the scaffolded TiO_2 layers, and the integration of this layer in the graphite based perovskite solar cell in order to replace the m-TiO_2 film. For this, we have first successfully synthetized suspensions of PMMA beads. Then, a simple three step process was used: (1) deposition of a PMMA beads dense layer, (2) infiltration of Titanium sol-gel solution and (3) heat treatment at 500 °C to evaporate the PMMA beads. SEM analysis have shown that a uniform and higher porosity than classic mesoscopic TiO_2 layer can be obtained by pore size engineering process.

The results with SEM images showed that the control of pore sizes can be directly controlled by varying the initial beads size. Pore volumes are around 50 % in each case. The advantage of larger pores is the infiltration improvement of the perovskite precursors. Three types of TiO_2 macroporous layers have been prepared; P50+ (pore size over than 50 nm), P100+ (> 100 nm) and P200+ (> 200 nm). In the application of carbon-based PSC configuration these layers have been integrated in order to replace the traditional mesoporous TiO_2 film.

The I-V measurements results showed that the monolithic perovskite cell with P50+ TiO_2 porous layer achieved a good improvement on the short-circuit current value (J_{SC} ≈ 24 mA.cm^{-2}) when compared to the reference monolithic cell (J_{SC} ≈ 19 mA.cm^{-2}) using $MAPbI_3$. However, the Fill Factor remains almost unchanged (below 50 %), while the open-circuit voltage value was less

than 900 mV. In addition, the measurement of the PCE as a function of time (i.e. stabilized efficiency) showed a decrease of its value over time, from ≈ 10 % to ≈ 7 %. Concerning the perovskite cells with the TiO_2 P100+ and P200+ porous layers; the drop-casting technique is obviously not adapted for an optimal infiltration based on the inhomogeneity of absorber infiltration as shown by the SEM analysis. Regarding the last results we have decided to modify the perovskite precursors infiltration method to adopt larger pore sizes; i.e. the spin-coating technique. Also, regarding the positive effects of cations and halide mixture on stabilized efficiency and properties of perovskite materiel; the previous $MAPbI_3$ light harvesting material has been changed to a $FACsPbBr_xI_{(3-x)}$ cation and halide mixed perovskite crystals.

The SEM coupled with EDX analysis on the c-PSC cross-section have shown that the spin-coating technique, which substitutes the drop-casting method used traditionally to infiltrate the porous layers with perovskite precursors has proven to be more successful for the TiO_2 layers with larger pore sizes. Also, the introduction of $FA_{0.83}Cs_{0.17}PbBr_{0.8}I_{2.2}$ photo-active perovskite material has resulted in quasi-stationary time-dependent performance for each type of PSC. The P50+, P100+ and P200+ based porous TiO_2 c-PSC have demonstrated improved photovoltaic performances compared to reference cells (around 11.4 %, 6.6 %, and 8 % of efficiency respectively, against 5.5 % for the reference cell). The highest J_{SC} value achieved (≈ 20 $mA.cm^{-2}$) is for the P50+ cell and the SEM images demonstrated a proper infiltration, while for the reference cell it was non-uniform in the porous TiO_2 layer. However, the value of the Fill Factor had tended to increase with pore size, which reached more than 62 % with the P200+ cell. The *FF* value can be reduced by the presence of series and shunt resistance in the cell. The increase in pore size could decrease this resistance effect in the cell.

Preliminary experiments were carried out in order to improve the P50+ and P200+ porous layer thickness. The I-V measurements have demonstrated that there is still potential to improve the performance of the P50+ and P200+ cells, which have already shown promising photovoltaics parameters. The highest stabilized efficiency is obtained for the P50+ type of cell with $FA_{0.83}Cs_{0.17}PbBr_{0.8}I_{2.2}$ light absorber perovskite material infiltrated by spin-coating method; with a recorded value of ≈ 13.6 %. This is followed by the P200+ cell with a PCE around 10.7 %.

A brief conclusion could be: that both, structural (TiO_2 "macroporous" layer) and perovskite type (mixed cations and halides: $FA_{0.83}Cs_{0.17}PbBr_{0.8}I_{2.2}$) modifications that we applied to a referential monolithic graphite-based perovskite solar cell improve the infiltration of precursors, PV performances and PCE stability over time.

However, the stabilized PCE is measured only for a short period to highlight the difference with used perovskite materials ($MAPbI_3$ and $FA_{0.83}Cs_{0.17}PbBr_{0.8}I_{2.2}$). The next work would be to investigate in long period PCE measurement in order to estimate the different c-PSC stability over 100 hours and interpret the influence of pore size on PV performance stability. Nevertheless, the promising results demonstrated in this thesis work give rise to some suggestions as future work. Additionally, another cation and halide mixed perovskite, as triple mixed cation with different ratios $(MAFACs)PbBr_xI_{3-x}$ could be used in order to improve better the performance and the stability of the cell [9], [80].

Perspective 1

The first intuitive idea would be to increase the thickness of the porous TiO_2 layer because more photo-active materials could be infiltrated into it. However, the deposition parameters to be varied and the protocol have been optimized to obtain a homogeneous and crack-free layer, because an overly concentrated solution of PMMA beads or sol-gel solution, or a slower deposition rate, results in cracked and non-homogeneous porous layers as shown in the figure below:

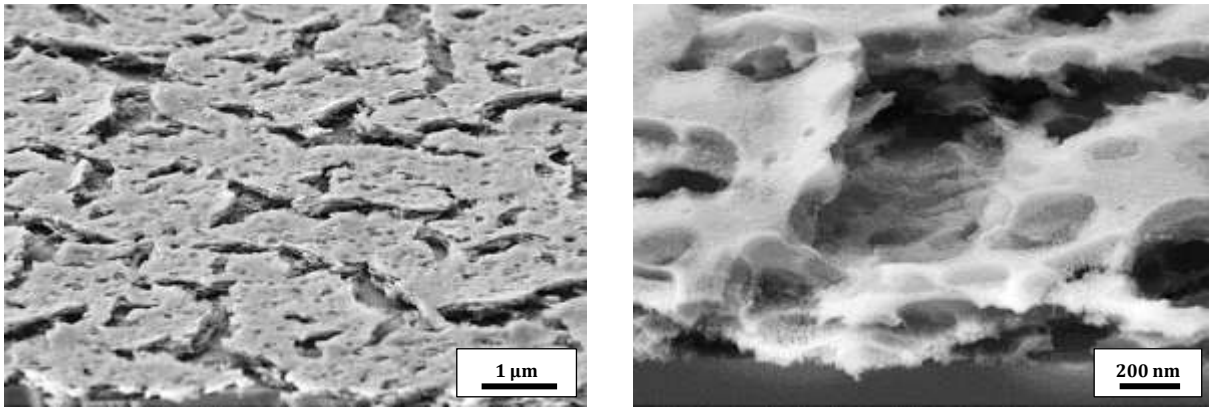

Figure VII-1: SEM images of cracked non-uniform TiO_2 porous layer prepared by PMMA molding method by modifying process parameters

An alternative would be to mix the sol-gel solution containing the TiO_2 precursors with the PMMA solution. A relatively concentrated suspension solution could be used as a mixing base to obtain a paste that could be deposited by screen-printing. As a reminder, one of the advantages of the monolithic cell is its easiness of preparation for commercialization and the screening-printing method is ideal for this purpose. This preparation could also be considered for the ZrO_2 separating layer, which on the one hand is expensive and on the other hand it would be interesting to see the influence on the PV parameters of this layer when improving its porosity.

Perspective 2

According to the obtained results on cell performance, the PMMA bead sizes P50+ and P200+ have demonstrated promising performance. In this perspective we were interested in the preparation of a porous TiO_2 layer with two different sizes. For this purpose, we mixed these two solutions with the same concentration of PMMA particle suspensions (P50+ and P200+) in order to obtain a solution of beads that are bi-dispersed in size. The Figure VII-2-a shows the DLS of this mixture. A stable, non-aggregated solution can be observed with the presence of the two bead sizes. This is supported by the SEM images of the mixed particles solution deposited by spin-coating on silicon substrate (Figure VII-2-b).

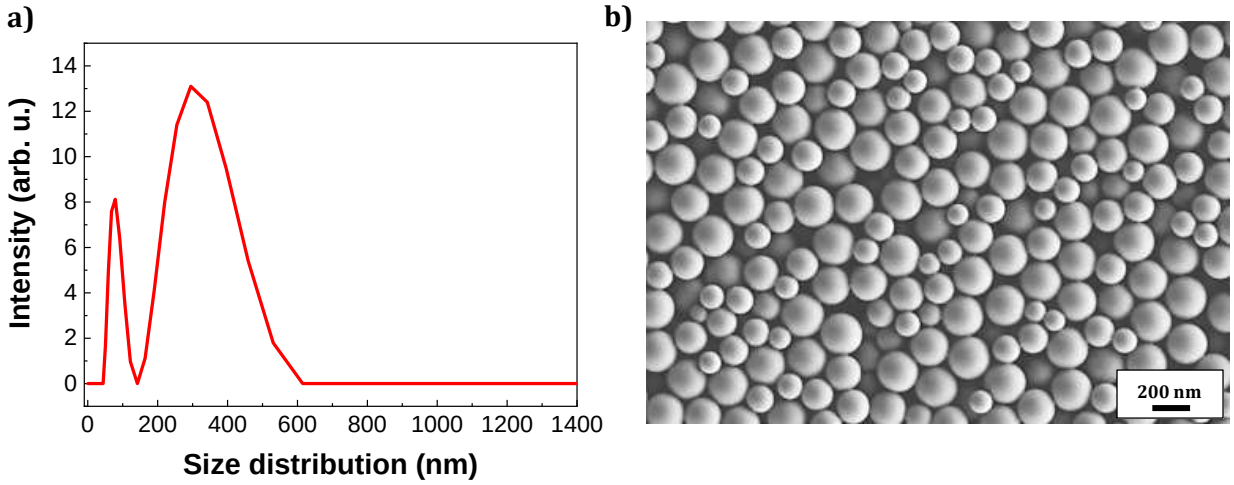

Figure VII-2: a) DLS graph of the mixed P50+ and P200+ PMMA suspension b) SEM image of the solution deposited by spin-coating on Si substrate

For the following the same preparation process of molding by the sol-gel route was applied. The Figure VII-3 represents the SEM image resulting of the "bi-size" PMMA particles molding process.

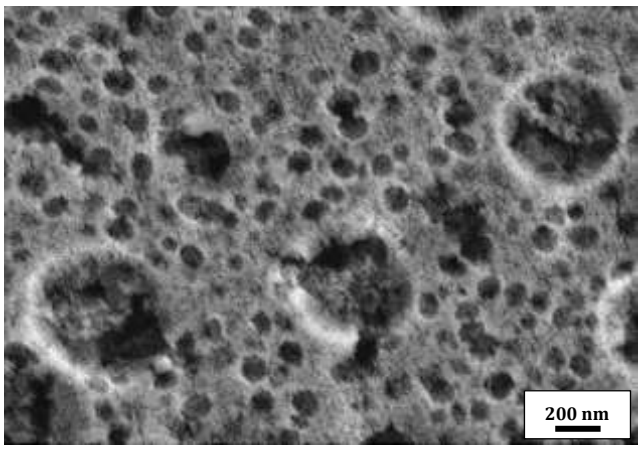

Figure VII-3: a) SEM image on top view of the TiO_2 porous layer prepared by molding process of the mixed P50+ and P200+ PMMA particles suspensions

The obtained porous layer clearly reveals two pore sizes corresponding to the two bead sizes used. The next step would be to integrate this type of layer into the c-PSC in order to further improve the infiltration of perovskite precursors and thus the photovoltaic performance.

Perspective 3

Another scaffold layer issue is related to its electronic structure (defining the output of the cell) and conductivity (related to the ability to evacuate the charges). In this sense, it appeared interesting to replace TiO_2 by SnO_2, which shows well-aligned conduction bands with that of the photoactive material [150], [151].

For this our approach was to introduce Sn precursor in sol-gel solution in order to prepare SnO_2 based porous layer solution. UV-Vis measurements (Figure VII-4) show that the presence of Sn tends to increase the transmittance of the solution. A high transmission for this type of layer is required to allow the photons to pass through to the photo-active material.

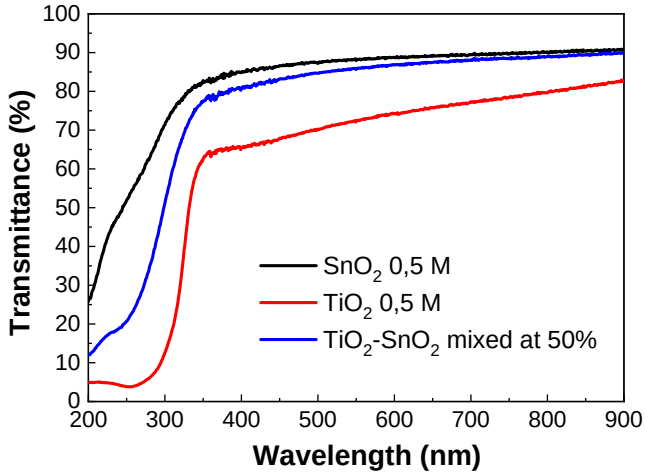

Figure VII-4: Transmittance graph of the sol-gel solution containing titanium and tin precursors

The sol-gel solution combined with 50 % Ti and Sn was used in the molding process with PMMA P50+ suspension. The Figure VII-5 shows the results obtained for this process. The porosity obtained corresponds to the size of the beads, and is therefore uniform. The thickness is around 300 nm.

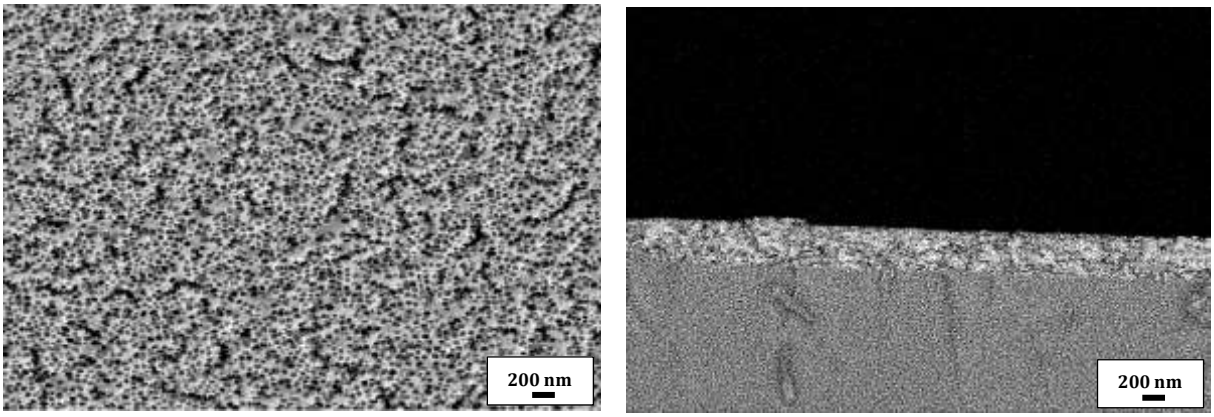

Figure VII-5: SEM images on top view and cross-section view of porous TiO_2-SnO_2 layer prepared by molding of P50+ PMMA beads

EDX analyses have confirmed the presence of Ti and Sn elements as well in the layer (Figure VII-6-a). Also, XRD measurements show peaks corresponding to the anatase phase for TiO_2 and the cassiterite phase for SnO_2 (Figure VII-6-b).

Such layer may improve the optical and electronical properties of the porous layer and thereby enhance the charge transfer.

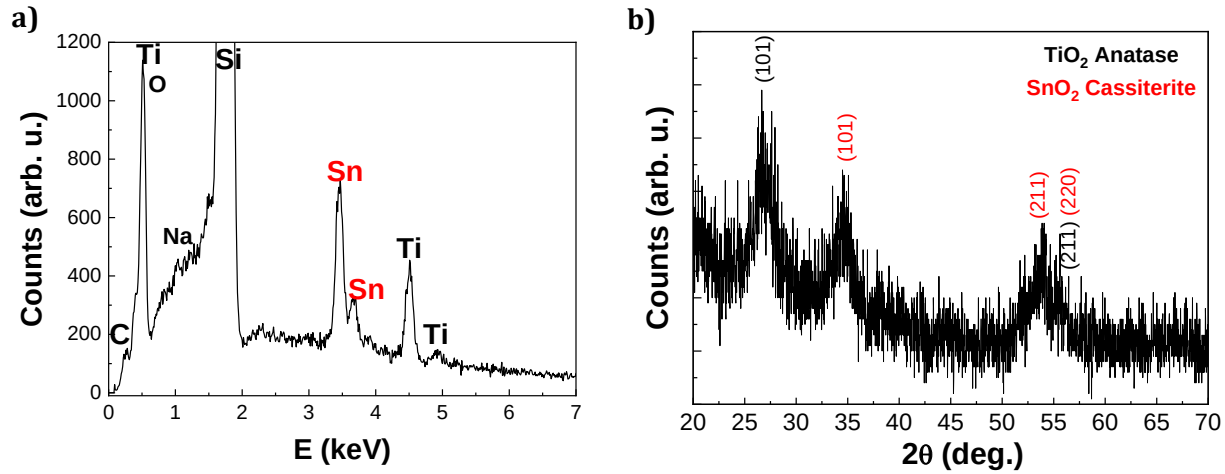

Figure VII-6: a) Graph representing the EDX analysis on the obtained porous layer, Ti and Sn element are well present. b) XRD diffractogram with patterns corresponding to anatase phase for TiO_2 and casserite for SnO_2 (JCPDS: 04-003-0649)

Perspective 4

The last perspective proposed is to increase the size of the pore beads. Given the complex subject of perovskite solar cells we had established that the size of the pore beads ranges from about 50 nm up to 250 nm as a first approach to this infiltration issue.

For a trial we used the synthesis of the P200+ beads by increasing the quantity of PVP in order to obtain larger PMMA particle sizes. The DLS measurement of the solution thus obtained shows a particle size centered at about 400 nm but the monodispersity is very weak (Figure VII-7).

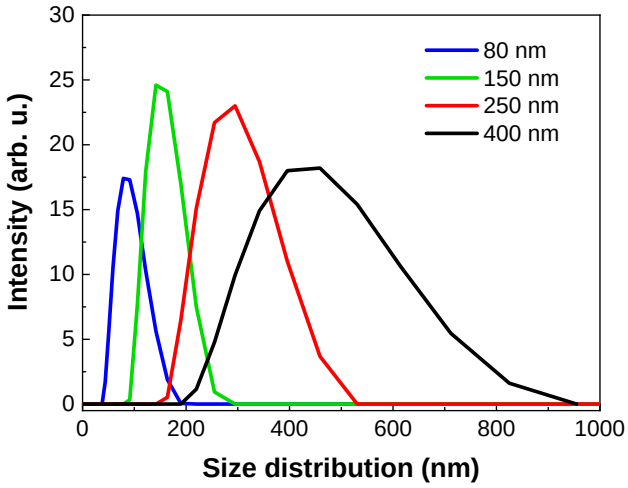

Figure VII-7: DLS of the variety of PMMA particles synthetized solution including the P 400+ new suspension

Nevertheless, we have produced by molding process, a porous TiO_2 layer with this size distribution (Figure VII-8-a). The resulting layer shows a clear pore size correlation with the size of the beads; however the layer is extremely rough. This may be related to the circumstance that the PMMA bead layer deposited by spin-coating is not compact enough and already shows a high roughness at this stage.

The AFM image of the P 400+ bead layer shows a various size and a high roughness (Figure VII-8). Nevertheless, it would be interesting to improve the structure of this porous layer in order to improve its homogeneity and thus integrate it into the perovskite cell.

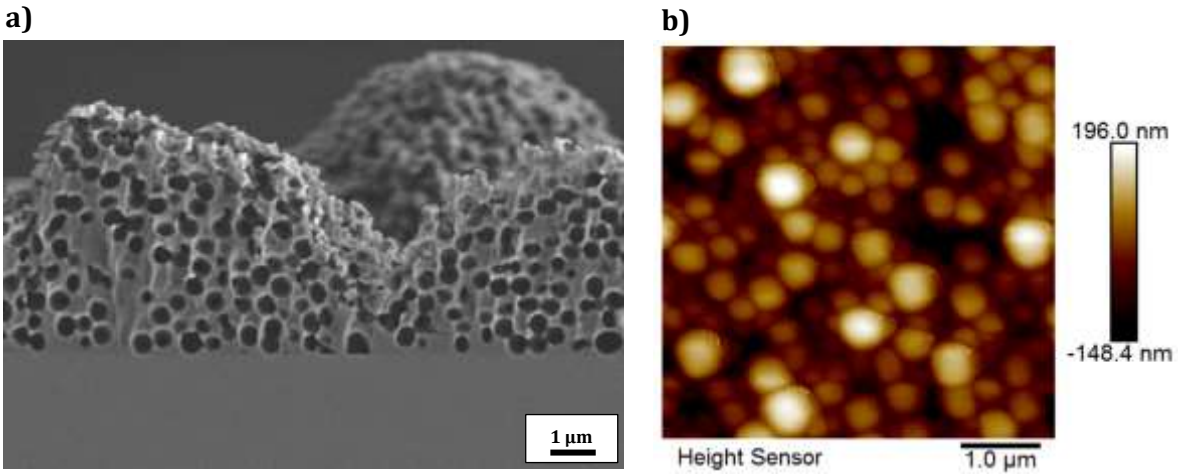

Figure VII-8: a) SEM image on top view of the TiO_2 porous layer prepared by molding process P 400+ PMMA particles suspensions b) AFM image of the P 400+ solution deposited by spin-coating on Si substrate

VIII. Appendix

VIII.1. Appendix 1: Characterization tools

VIII.1.1. X-Ray Diffraction (XRD)

X-ray diffraction (XRD) is a powerful nondestructive technique for characterizing crystalline materials. It provides information on structures, phases, preferred crystal orientations (texture), and other structural parameters, such as average grain size, crystallinity, strain, and crystal defects. X-ray diffraction peaks are produced by constructive interference of a monochromatic beam of X-rays scattered at specific angles from each set of lattice planes in a sample. The peak intensities are determined by the distribution of atoms within the lattice. Consequently, the X-ray diffraction pattern is the fingerprint of periodic atomic arrangements in a given material. The X-Ray diffraction analysis is like a fingerprint test for chemical compounds. It helps determine the materials that compose the tested samples as well as their structural qualities [11]. It follows Bragg's law which consists of:

$$2\,d\sin\theta = n\,\lambda$$

where d is the interplanar spacing, ɵ the angle, n is integer number and λ the wavelength.

The crystalline structure of the final samples was investigated by X-ray diffraction (XRD) recorded in grazing incidence (GI) configuration. The patterns were collected on scaffold layers deposited on silicon or glass substrates using a Rigaku SmartLab diffractometer equipped with a monochromatic source delivering a Cu $K\alpha_1$ incident beam (45 kV, ɵ00mA, 0.154056 nm).

The perovskite crystal with ABX_3 structure has specific diffracted peaks and theses permit to identify the structure of the synthetized light absorber materials. For the characterization of the prepared perovskite, the solution has been deposited by spin-coating (3000 rpm/30 s) on glass or silicon substrate treated with plasma before for wettability improvement on the surface.

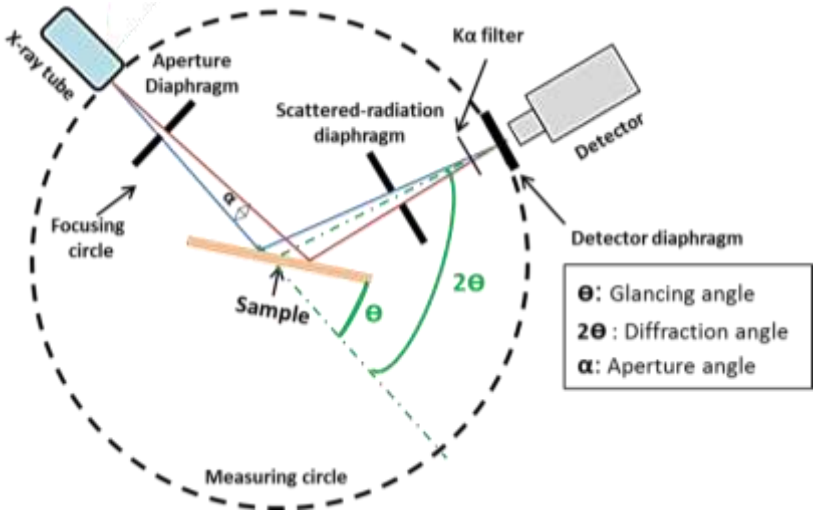

Figure VIII-1: Illustration of the XRD measurements principle

A simple and well-known expression for obtaining a measure of the crystallite size from X-ray diffraction peaks is that of the Scherrer equation [152]

$$FWHM(2\theta) = \frac{b\,\lambda}{D\,cos\theta} \text{ (in terms of } 2\theta)$$

where *FWHM* is the full width of the peak, 2θ is the scattering angle in radians, λ is the wavelength, b is a constant, which normally takes a value between 0.89 and 0.94 depending on the function used to fit the peak, and D is the dimension of the crystallites.

VIII.1.2. UV-Vis Spectroscopy / Tauc Plot (optical measurements)

VIII.1.2.1. Principle

Ultraviolet visible spectroscopy consists of a beam of light passing through or reflecting from the sample surface, and from which absorption measurements of the studied sample are taken, over a spectral wavelength range [153]. Results for both absorbance and transmittance graphs for the samples studied can be obtained (Figure VIII-2).

For our case, the wavelength range taken is of 200 nm to 1000 nm. The equipment is a Perkin-Elmer Lambda spectrophotometer working in the ultraviolet-visible-near infrared (UV-Vis-NIR) range.

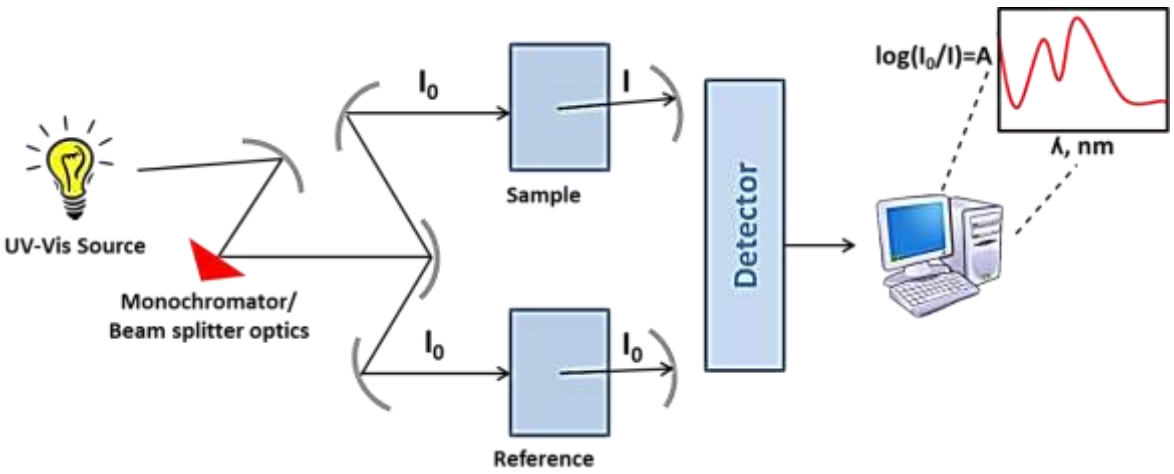

Figure VIII-2: Functional principle of UV-Vis spectroscopy measurement

VIII.1.2.2. Tauc Plot

UV-vis spectroscopy is also used for our project to determine the optical band gap of the elaborated perovskite light harvesting, based on their transmittance graphs. It is essential to note here that corrections are introduced to the transmittance graphs of our samples, considering the automatic change in the filter at the wavelength 860 nm. The corrections consist of calculating the error margin for the transmittance at 860 nm as follows: Error = T(861) – T(859). The error is then subtracted from all the transmittance values from 859 nm to 200 nm, where T(x) = T(x) – [T(861) – T(859)] with x the wavelength value.

The optical band gap energy E_g of the layers can be determined with the help of Tauc plots and can be deduced through plotting $(\alpha h\nu)^2$ with respect to the band gap energy E_g. The absorption coefficient α is calculated following the equation:

$\alpha = \frac{1}{d} ln\left(\frac{1}{T}\right)$ where d is the thickness of the perovskite layer, and T is its transmittance[154].

The Tauc relation gives the correlation between the absorption coefficients that is use for optical band gap determination plot (where E_g is the band gap and $h\nu$ the photon energy):

$$\alpha = \frac{\alpha_0(h\nu - E_g)^2}{h\nu}$$

VIII.1.3. Transmission Electronic Microscope (TEM)

VIII.1.3.1. Principle

Transmission electron microscopy (TEM, an abbreviation which can also stand for the instrument, a transmission electron microscope) is a microscopy technique in which a beam of electrons is transmitted through a specimen to form an image (Figure VIII-3-a). The specimen is most often an ultrathin section less than 100 nm thick or a suspension on a grid. An image is formed from the interaction of the electrons with the sample as the beam is transmitted through the specimen [155].

The contrast between two adjacent areas in a TEM image can be defined as the difference in the electron densities in image plane. Due to the scattering of the incident beam by the sample, the amplitude and phase of the electron wave change, these results in amplitude contrast and phase contrast, correspondingly. Most of images have both contrast components [156].

Different imaging methods therefore attempt to modify the electron waves exiting the sample in a way that provides information about the sample, or the beam itself.

As previously stated, by adjusting the magnetic lenses such that the back focal plane of the lens rather than the imaging plane is placed on the imaging apparatus a diffraction pattern can be generated. For thin crystalline samples, this produces an image that consists of a pattern of dots in the case of a single crystal, or a series of rings in the case of a polycrystalline or amorphous solid material. For the single crystal case the diffraction pattern is dependent upon the orientation of the specimen and the structure of the sample illuminated by the electron beam. This image provides the investigator with information about the space group symmetries in the crystal and the crystal's orientation to the beam path. This is typically done without using any information but the position at which the diffraction spots appear and the observed image symmetries.

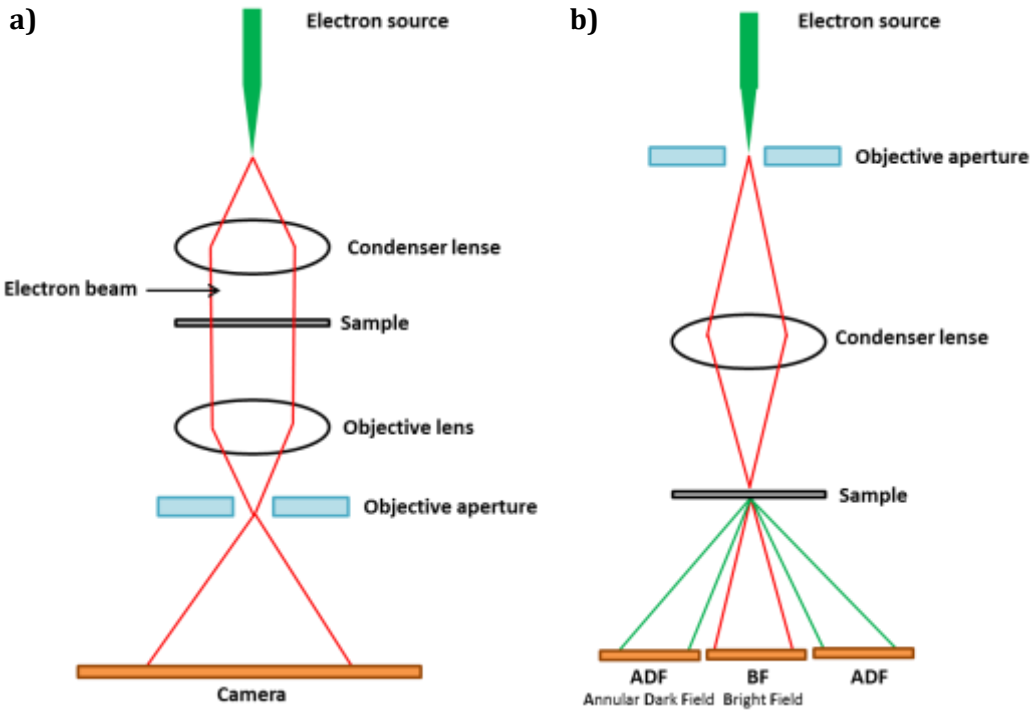

Figure VIII-3: Scheme representing the working principle of a) TEM and b) STEM mode

VIII.1.3.2. Sample Preparation for TEM Analysis

A TEM specimen must be thin enough to transmit sufficient electrons to form an image with minimum energy loss. Therefore specimen preparation is an important aspect of the TEM analysis. Since the grid, which is generally made with copper, is 5 mm long, this preparation step is particularly delicate. In order to deposit the perovskite crystals to be characterized on the grid we have set up a special substrate holder adapted to optimize a homogeneous and thin deposition of crystals film. The solution containing the perovskite precursors (one-step) is w to the one used for solar cells. The deposition on the grid is carried by spin-coating with parameters of 3000 rpm for the rotation speed during 30 seconds. Then the grid is annealed at a temperature suitable for crystallization either for $MAPbI_3$ (50 °C) or $FA_{0.83}Cs_{0.17}PbBr_{0.8}I_{2.2}$ (100 °C).

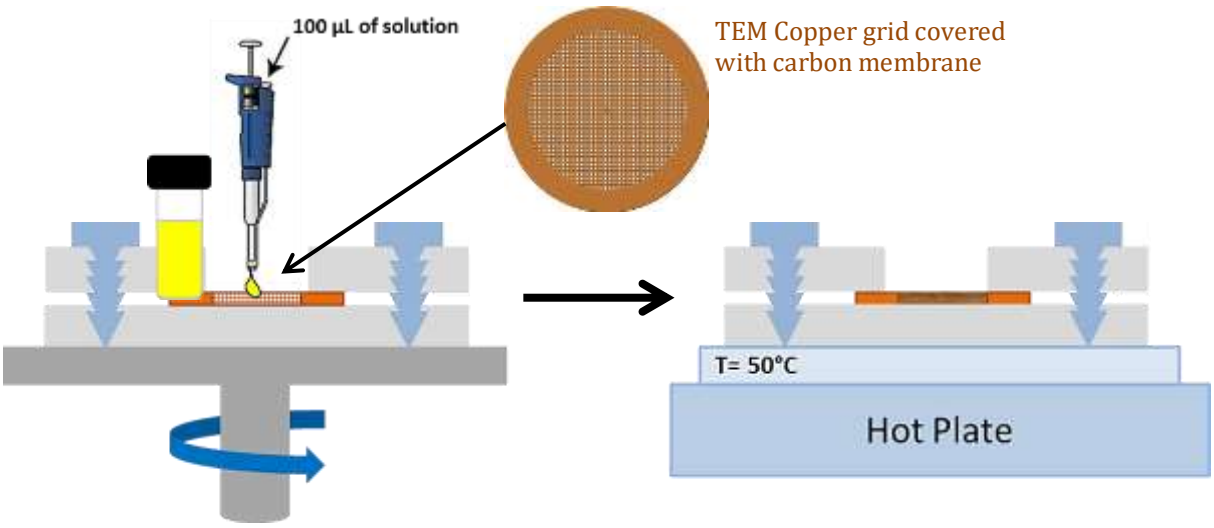

Figure VIII-4: Specimen preparation for perovskite crystals by the TEM or STEM analysis

VIII.1.3.3. Scanning Electron Microscope (STEM)

A scanning transmission electron microscope (STEM) is a type of transmission electron microscope equipped with additional scanning coils, detectors and necessary circuitry, which allows it to switch between operating as a STEM (Figure VIII-3-b),

Scanning transmission electron microscopes are used to characterize the nanoscale, and atomic scale structure of specimens, providing important insights into the properties and behavior of materials. With STEM it is possible to form atomic resolution images where the contrast of an atomic column is directly related to the atomic number (Z-contrast image) [156]. Directly interpretable Z-contrast imaging makes STEM imaging with a high-angle detector an appealing technique in contrast to conventional high resolution electron microscopy, in which phase-contrast effects mean that atomic resolution images must be compared to simulations to aid interpretation.

VIII.1.4. Morphological Characterization

VIII.1.4.1. Scanning Electron Microscope (SEM/EDX)

Scanning electron microscopy (SEM) is a magnification tool that consists of using focused beams of high-energy electrons to obtain high resolution images, that provide information about the morphology as well as the composition of the sample [157]. Zeiss GEMINI scanning electron microscopy (SEM) 500 integrating an InLens/SE2 Detector coupled with an Energy Dispersive X-ray (EDX) analyzer is used. All images were recorded using an acceleration voltage of 5 kV while the EDX analyzes were acquired at 7 kV.

SEM is a non-destructive method. The main types of signals that are detected are the backscattered (BSE) and secondary electrons (SE), which generate a grayscale image of the sample at very high magnifications (Figure VIII-5). These varieties of signals carry different information about the sample. For example, backscattered electrons produce images with contrast that carries information on the differences in atomic number; secondary electrons give topographic information.

In the case of our research project, SEM is used in the purpose of studying the homogeneity as well as the thickness of the layers that form our perovskite solar cells, as well as the infiltration of the perovskite nanocrystallites into porous TiO_2 layer. In order to achieve this, our PSC devices are cut in half with the help of a diamond blade, which allows us to get a clear view of the state of the different thin film layers that form the active area of the solar cell.

However, there are many other signals which can be a product of the electron-matter interaction, and these can provide additional information about the sample as the energy-dispersive X-ray (EDX or EDS) analysis. This X-ray has energy which is characteristic of the energy difference between these two shells. It depends on the atomic number, which is a unique property of every element. In this way, X-rays are a “fingerprint” of each element and can be used to identify the type of elements that exist in a sample.

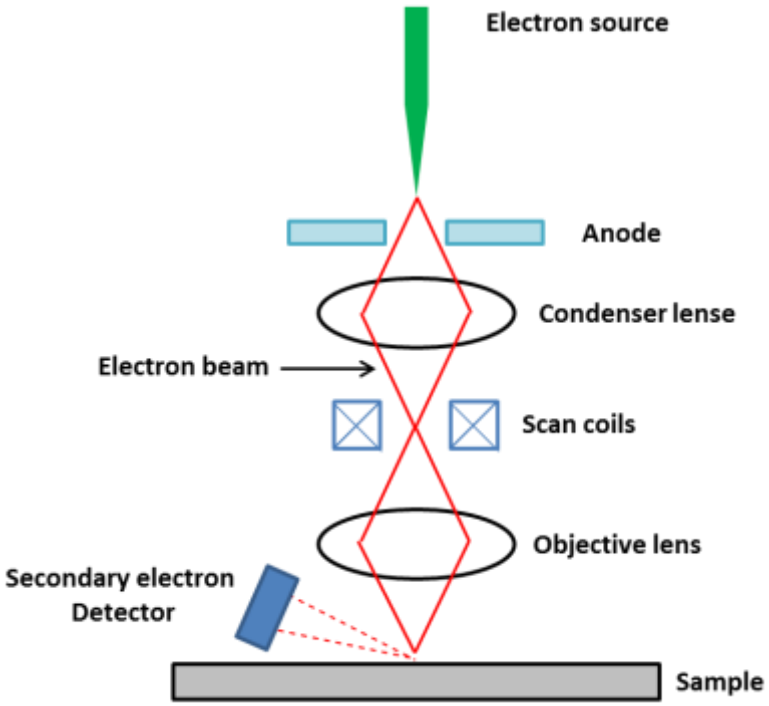

Figure VIII-5: Illustration of Scanning Electronic Microscope working principle

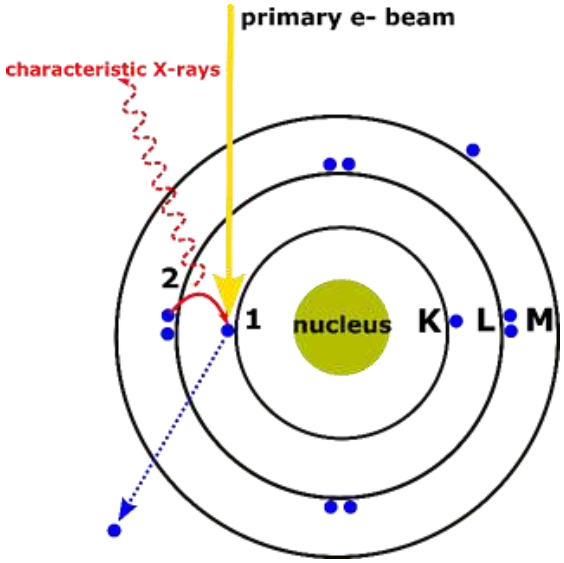

Figure VIII-6: (1) The energy transferred to the atomic electron knocks it off leaving behind a hole, (2) its position is filled by another electron from a higher energy shell and the characteristic X-ray is released [158]

VIII.1.4.2. Atomic Force Microscope (AFM)

An AFM uses a cantilever with a very sharp tip to scan over a sample surface. As the tip approaches the surface, the close-range, attractive force between the surface and the tip cause the cantilever to deflect towards the surface. However, as the cantilever is brought even closer to the surface, such that the tip makes contact with it, increasingly repulsive force takes over and causes the cantilever to deflect away from the surface.

A laser beam is used to detect cantilever deflections towards or away from the surface. By reflecting an incident beam off the flat top of the cantilever, any cantilever deflection will cause

slight changes in the direction of the reflected beam. A position-sensitive photo diode (PSPD) can be used to track these changes. Thus, if an AFM tip passes over a raised surface feature, the resulting cantilever deflection (and the subsequent change in direction of reflected beam) is recorded by the PSPD.

An AFM images the topography of a sample surface by scanning the cantilever over a region of interest. The raised and lowered features on the sample surface influence the deflection of the cantilever, which is monitored by the PSPD. By using a feedback loop to control the height of the tip above the surface, thus maintaining constant laser position, the AFM can generate an accurate topographic map of the surface features. The model equipment is a Brucker Icon using silicon tip in tapping mode.

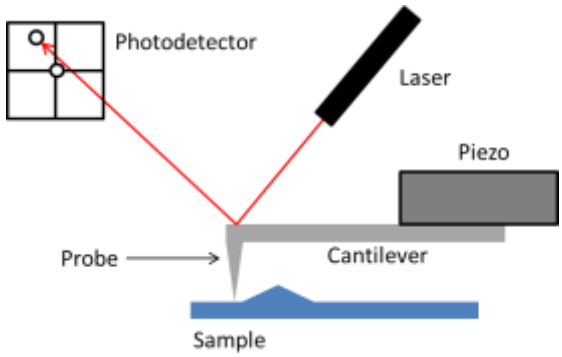

Figure VIII-7: Representation of the Atomic Force Microscope imaging principle

VIII.1.5. Ellipsometry Measurements

Ellipsometry is efficient technique for optical constants, thickness and porosity determination [159], [160]. Ellipsometry is a materials evaluation technique that derives its name from the measurement of the ellipse of polarization generated when a polarized light beam reflects obliquely from the specular surface of a sample. The instrument that performs this measurement is called an ellipsometer. The ellipsometry experiment is processed by five steps: (1) generation of a light beam in a known polarization state using optical components such as polarizers and compensators, (2) oblique specular reflection of the beam from a sample leading to an emergent beam in an altered polarization state, (3) analysis of this new polarization state, (4) determination of parameters that characterize the reflection from the information on the two polarization states, and (5) deduction of sample parameters, such as optical properties and film thicknesses, from the reflection parameters of step (6) [161].

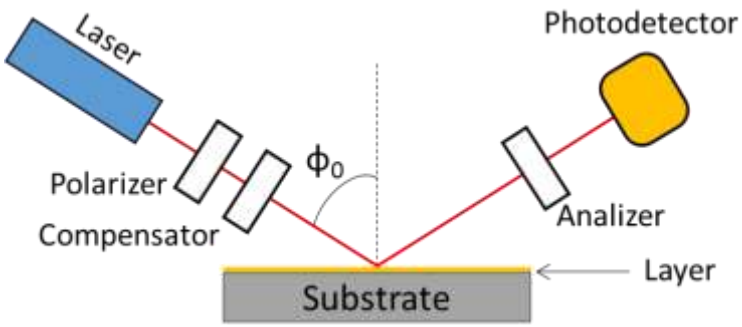

Figure VIII-8: Scheme of the ellipsometry working principle for film thickness and porosity measurements

Ellipsometry measurements for porosity analyses were performed on a HORIBA UV-vis Lt M200 FGMS (210-880 nm) spectroscopic ellipsometer. The ellipsometric dispersion model used for TiO_2 is based on the double amorphous dispersion model on the basis of Forouhi-Bloomer formulation [162]. The samples were measured on crystalline silicon. First a dense layer of TiO_2 of around 20 nm was introduced on top of the silicon. A second TiO_2 rough layer was introduced on top using voids in order to mimic the porosity of the film.

VIII.1.6. Solar Simulator Set-up for I-V Measurements

The solar simulator is a device that helps perform measurements on a solar cell performance in "real conditions" using an artificial sun like illumination [163].

For our samples, the solar simulator is used to deduce the I-V measurements and stabilized efficiency over time for our perovskite solar cells. From the obtained I-V curves, we can deduce the short circuit current (J_{SC}), the open circuit voltage (V_{OC}), the maximum power point (PMPP), the filling factor (*FF*) and the efficiency of the PSC (η).

The substrate holder allows us to flip the PSC sample in order to illuminate through the glass side, after connecting both the front and the back contact electrodes to the fixtures of the holder; this allows maintaining of the needed control over the sample position on the mounted platform under the light source. A silicon reference cell is used as calibrating cell to set the height of the platform and test if the conditions are optimal before each measurement. The I-V curves are recorded with a scan rate of 50 mV per second on a range of -0.1 to 1.1 V.

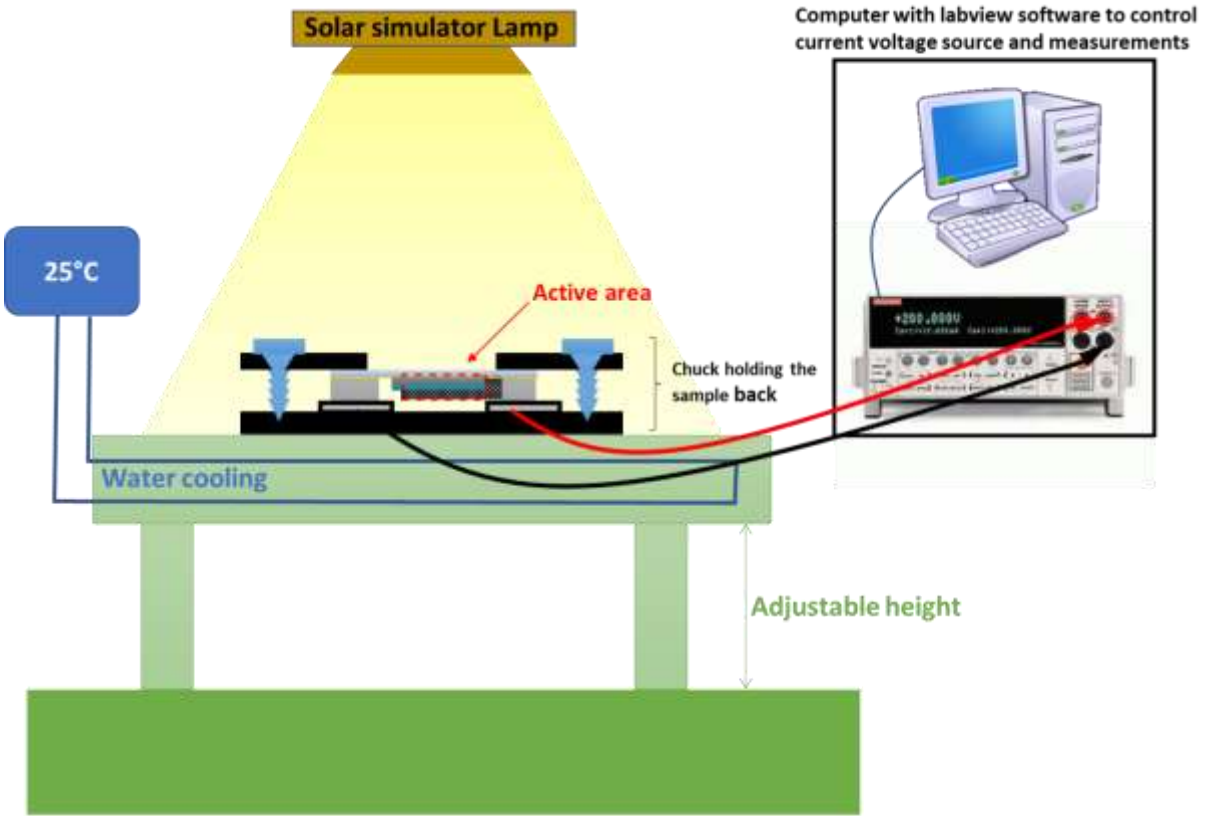

Figure VIII-9: Illustration of I-V characterization Set-up using solar light simulator

VIII.1.7. Statistical Box

The box plot, which is also called a box and whisker plot or box chart, is a graphical representation of key values from summary statistics.

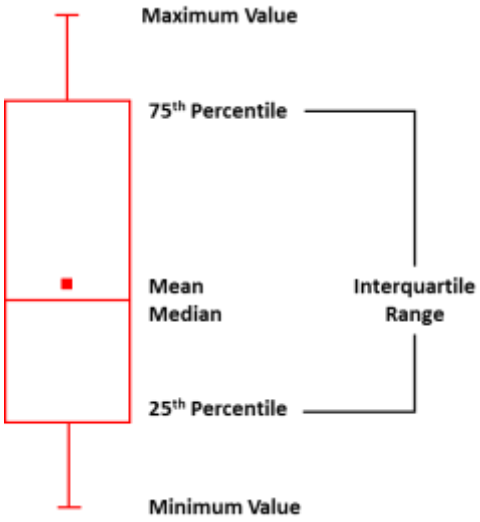

Figure VIII-10: Statistical chart box ratio representation

VIII.1.8. Dynamic Light Scattering (DLS)

The method of dynamic light scattering (DLS) is the most common measurement technique for particle size analysis in the nanometer range.

The basic setup of a DLS instrument is shown in Figure VIII-11. A single frequency laser is directed to the sample contained in a cuvette. If there are particles in the sample, the incident laser light gets scattered in all directions. The scattered light is detected at a certain angle over time and this signal is used to determine the diffusion coefficient and the particle size by the Stokes-Einstein equation [164].

The equipment used is a Malvern Zetasizer. Modern DLS instruments include two, or in the case of Litesizer™ 500 three, detection angles for particle size measurements. Depending on the turbidity of the sample, side scattering (90°) or back scattering (175°) is more suitable. A forward angle (15°) can be used to monitor aggregation.

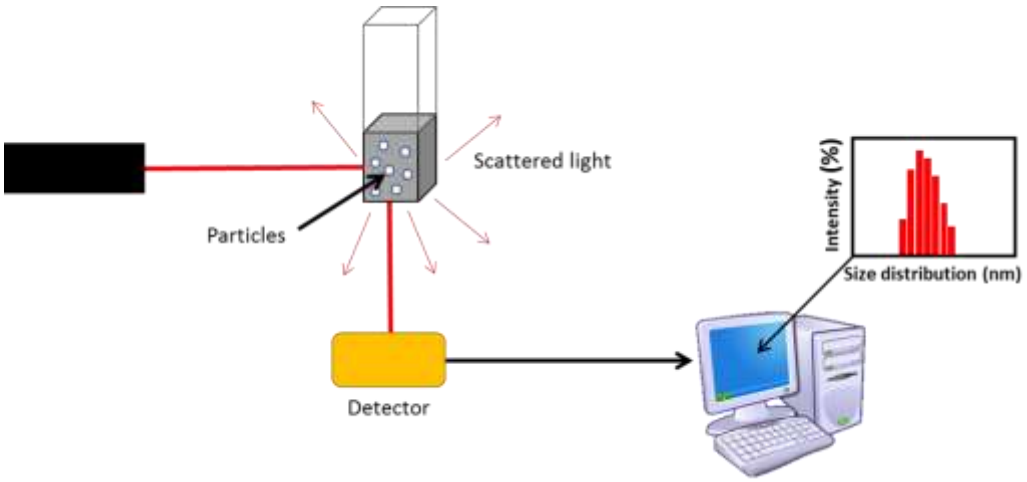

Figure VIII-11: Dynamic Light Scattering measurement working principle for size particles determination

VIII.1.9. Thermogravimetric Analysis (TGA)

Thermogravimetric analysis (TGA) measures weight changes in a material as a function of temperature (or time) under a controlled atmosphere. Its principle uses include measurement of a material's thermal stability, filler content in polymers, moisture and solvent content, and the percent composition of components in a compound [165].

The measurement is performed by gradually raising the temperature of a sample in a furnace as its weight is measured on an analytical balance that remains outside of the furnace (Figure VIII-12). In TGA, mass loss is observed if a thermal event involves loss of a volatile component. Chemical reactions, such as combustion, involve mass losses, whereas physical changes, such as melting, do not. The weight of the sample is plotted against temperature or time to illustrate thermal transitions in the material – such as loss of solvent and plasticizers in polymers, water of hydration in inorganic materials, and, finally, decomposition of the material.

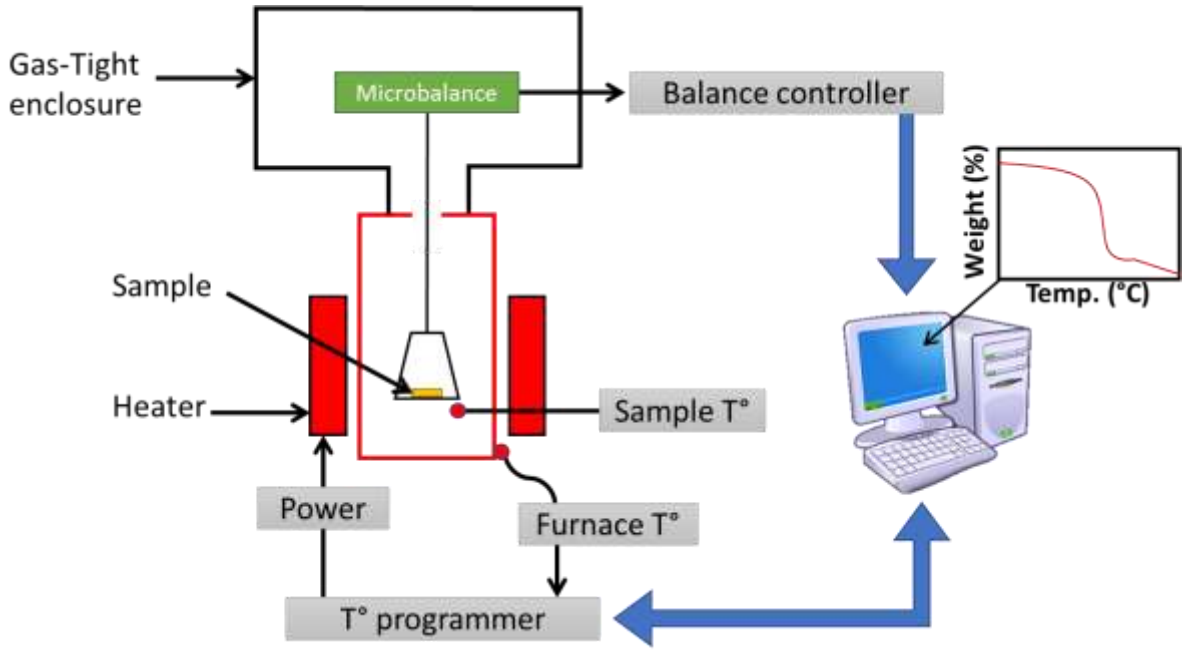

Figure VIII-12: Thermogravimetric Analysis principle used for PMMA particles characterization

VIII.1.10. Photoluminescence Spectroscopy (PL)

Photoluminescence (PL) spectroscopy is a contactless, nondestructive optical method used for photovoltaic solar cells characterization. PL uses a laser beam to capture light generated from a substance as it falls from the excited state to ground state when irradiated by a laser beam [166]. The basic elements of a PL spectroscopy set-up consist in an optical source, a spectrophotometer and a detector. A typical PL set-up is shown in Figure VIII-13. The excitation laser beam is focused on the sample with a lens of typically f = 20-30 cm focal length.

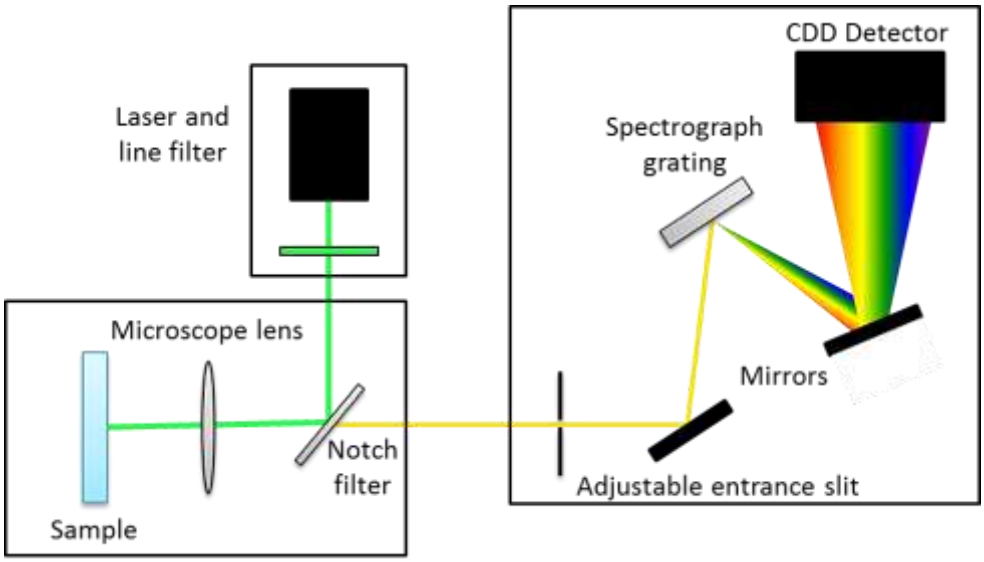

Figure VIII-13: Representation of Photoluminescence measurements on perovskite crystals film or PSC

The PL principle consists of a process called photo-excitation, where the electrons within a substance are brought to excitation by directing light onto the sample. The excess energy is released once the electrons are back to their equilibrium state; this may or may not include the emission of light (radiative or non-radiative combination respectively). Photoluminescence, which is basically the energy of the emitted light (radiative recombination), concerns the difference in energy levels between the two states of the electron, excitation and equilibrium (Figure VIII-14) [157], [167].

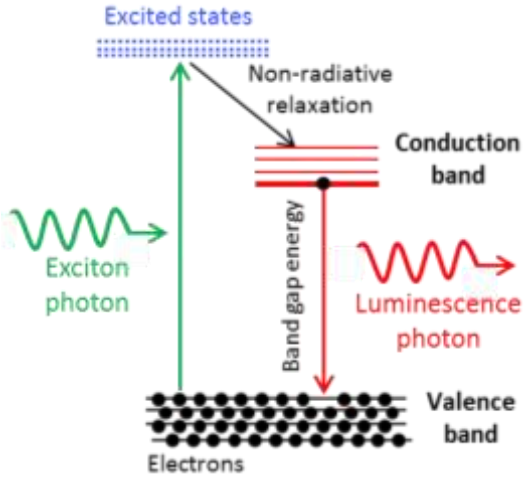

Figure VIII-14: Energy diagram represented exited state of electron and radiative recombination principle

The quantity of PL emitted from a material is directly related to the relative amount of radiative and non-radiative recombination rates. Non-radiative rates are typically associated with impurities and thus, this technique can qualitatively monitor changes in material quality as a function of growth and processing conditions.

Also, the spectral distribution of PL from a semiconductor can be analyzed to nondestructively determine the bandgap. This provides a means to quantify the elemental composition of compound semiconductor, which is parameter influencing solar cell device efficiency. The high sensitivity of this technique provides the potential to identify extremely low concentrations of intentional and unintentional impurities that can strongly affect material quality and device performance.

The samples were measured using photoluminescence spectroscopy at a laser excitation of 532 nm, a detection power of 0.1μW, and an integration time of 1s.

VIII.1.11. FIB-SEM 3D Tomography

Focused Ion Beam (FIB) incorporated into a traditional Scanning Electron Microscope (SEM) constitutes a powerful tool for the observation of internal structures at high resolution in materials science enabling 3D volume analysis with nanoscale resolution.

This instrument is a double column system, which combines a conventional SEM and a second column containing an ion source of Gallium. By combining high resolution imaging using electrons and material removal by an ion beam, such a system can provide a greater variety of applications than when the two sources are used separately, including tomographic acquisition, site specific sample preparation and material manipulation [119], [120].

The FIB-SEM tomography allows acquiring a large representative volume from porous films in order to obtain information on the morphological properties, such as porosity, surface area, and other knowledge required as input parameters for calculations. As we have used with Image software to estimate the distribution of P50+ and mesoporous TiO_2 layers in a specific section.

References

[1] M. A. Green, A. Ho-Baillie, and H. J. Snaith, “The emergence of perovskite solar cells,” *Nat. Photonics*, vol. 8, no. 7, pp. 506–514, Jul. 2014.
[2] Q. Sun *et al.*, “Role of Microstructure in Oxygen Induced Photodegradation of Methylammonium Lead Triiodide Perovskite Films,” *Adv. Energy Mater.*, vol. 7, no. 20, p. 1700977, 2017.
[3] J. M. Azpiroz, E. Mosconi, J. Bisquert, and F. D. Angelis, “Defect migration in methylammonium lead iodide and its role in perovskite solar cell operation,” *Energy Environ. Sci.*, vol. 8, no. 7, pp. 2118–2127, Jul. 2015.
[4] F. Zhang, X. Yang, H. Wang, M. Cheng, J. Zhao, and L. Sun, “Structure Engineering of Hole–Conductor Free Perovskite-Based Solar Cells with Low-Temperature-Processed Commercial Carbon Paste As Cathode,” *ACS Appl. Mater. Interfaces*, vol. 6, no. 18, pp. 16140–16146, Sep. 2014.
[5] A. Mei *et al.*, “A hole-conductor-free, fully printable mesoscopic perovskite solar cell with high stability,” *Science*, vol. 345, no. 6194, pp. 295–298, Jul. 2014.
[6] Z. Ku, Y. Rong, M. Xu, T. Liu, and H. Han, “Full Printable Processed Mesoscopic CH3NH3PbI3/TiO2 Heterojunction Solar Cells with Carbon Counter Electrode,” *Sci. Rep.*, vol. 3, Nov. 2013.
[7] A. Sarkar, N. J. Jeon, J. H. Noh, and S. I. Seok, “Well-Organized Mesoporous TiO_2 Photoelectrodes by Block Copolymer-Induced Sol–Gel Assembly for Inorganic–Organic Hybrid Perovskite Solar Cells,” *J. Phys. Chem. C*, vol. 118, no. 30, pp. 16688–16693, Jul. 2014.
[8] Y. Yue *et al.*, “Polymer-Assisted Construction of Mesoporous TiO_2 Layers for Improving Perovskite Solar Cell Performance,” *J. Phys. Chem. C*, vol. 119, no. 40, pp. 22847–22854, Oct. 2015.
[9] M. Saliba *et al.*, “Cesium-containing triple cation perovskite solar cells: improved stability, reproducibility and high efficiency,” *Energy Environ. Sci.*, vol. 9, no. 6, pp. 1989–1997, 2016.
[10] D. P. McMeekin *et al.*, “A mixed-cation lead mixed-halide perovskite absorber for tandem solar cells,” *Science*, vol. 351, no. 6269, pp. 151–155, Jan. 2016.
[11] “WEO.” [Online]. Available: https://www.iea.org/weo/. [Accessed: 04-Sep-2019].
[12] “Statistics | World - Total Primary Energy Supply (TPES) by source (chart).” [Online]. Available: https://www.iea.org/statistics/?country=WORLD&year=2016&category=Energy%20supply&indicator=TPESbySource&mode=chart&dataTable=BALANCES. [Accessed: 19-Sep-2019].
[13] M. Guarnieri, “More Light on Information [Historical],” *IEEE Ind. Electron. Mag.*, vol. 9, no. 4, pp. 58–61, Dec. 2015.
[14] Richard P. Feynman, *QED: The Strange Theory of Light and Matter*. .
[15] M. Planck and M. Masius, *The theory of heat radiation*. Philadelphia, P. Blakiston’s Son & Co, c1914.
[16] A. Einstein, “Generation and transformation of light,” *Ann. Phys.*, vol. 17, 1905.
[17] F. Kasten and A. T. Young, “Revised optical air mass tables and approximation formula,” *Appl. Opt.*, vol. 28, no. 22, pp. 4735–4738, Nov. 1989.
[18] E. G. Laue, “The measurement of solar spectral irradiance at different terrestrial elevations,” *Sol. Energy*, vol. 13, no. 1, pp. 43–57, Apr. 1970.
[19] S. Rühle, “Tabulated values of the Shockley–Queisser limit for single junction solar cells,” *Sol. Energy*, vol. 130, pp. 139–147, Jun. 2016.
[20] B. G. Yacobi, *Semiconductor Materials: An Introduction to Basic Principles*. Springer US, 2003.
[21] B. Parida, S. Iniyan, and R. Goic, “A review of solar photovoltaic technologies,” *Renew. Sustain. Energy Rev.*, vol. 15, no. 3, pp. 1625–1636, Apr. 2011.
[22] M. P. Paranthaman, W. Wong-Ng, and R. N. Bhattacharya, *Semiconductor Materials for Solar Photovoltaic Cells*. Springer, 2015.
[23] “Solar Cell - an overview | ScienceDirect Topics.” [Online]. Available: https://www.sciencedirect.com/topics/materials-science/solar-cell. [Accessed: 06-Sep-2019].

[24] A. Richter, M. Hermle, and S. W. Glunz, “Reassessment of the Limiting Efficiency for Crystalline Silicon Solar Cells,” *IEEE J. Photovolt.*, vol. 3, no. 4, pp. 1184–1191, Oct. 2013.
[25] S. W. Glunz, S. Rein, W. Warta, J. Knobloch, and W. Wettling, “Degradation of carrier lifetime in Cz silicon solar cells,” *Sol. Energy Mater. Sol. Cells*, vol. 65, no. 1, pp. 219–229, Jan. 2001.
[26] M. Gloeckler, I. Sankin, and Z. Zhao, “CdTe Solar Cells at the Threshold to 20% Efficiency,” *IEEE J. Photovolt.*, vol. 3, no. 4, pp. 1389–1393, Oct. 2013.
[27] M. A. Green *et al.*, “Solar cell efficiency tables (version 50),” *Prog. Photovolt. Res. Appl.*, vol. 25, no. 7, pp. 668–676, 2017.
[28] “Best Research-Cell Efficiency Chart | Photovoltaic Research | NREL.” [Online]. Available: https://www.nrel.gov/pv/cell-efficiency.html. [Accessed: 04-Sep-2019].
[29] G. Allan and C. Delerue, “Optimization of Carrier Multiplication for More Effcient Solar Cells: The Case of Sn Quantum Dots,” *ACS Nano*, vol. 5, no. 9, pp. 7318–7323, Sep. 2011.
[30] J. Gong, J. Liang, and K. Sumathy, “Review on dye-sensitized solar cells (DSSCs): Fundamental concepts and novel materials,” *Renew. Sustain. Energy Rev.*, vol. 16, no. 8, pp. 5848–5860, Oct. 2012.
[31] Y. Yuan *et al.*, “Efficiency enhancement in organic solar cells with ferroelectric polymers,” *Nat. Mater.*, vol. 10, no. 4, pp. 296–302, Apr. 2011.
[32] J. M. Olson, S. R. Kurtz, A. E. Kibbler, and P. Faine, “A 27.3% efficient Ga0.5In0.5P/GaAs tandem solar cell,” *Appl. Phys. Lett.*, vol. 56, no. 7, pp. 623–625, Feb. 1990.
[33] D. Liu and T. L. Kelly, “Perovskite solar cells with a planar heterojunction structure prepared using room-temperature solution processing techniques,” *Nat. Photonics*, vol. 8, no. 2, pp. 133–138, Feb. 2014.
[34] L. Qiu *et al.*, “Engineering Interface Structure to Improve Efficiency and Stability of Organometal Halide Perovskite Solar Cells,” *J. Phys. Chem. B*, vol. 122, no. 2, pp. 511–520, Jan. 2018.
[35] F. A. Lindholm, J. G. Fossum, and E. L. Burgess, “Application of the superposition principle to solar-cell analysis,” *IEEE Trans. Electron Devices*, vol. 26, no. 3, pp. 165–171, Mar. 1979.
[36] F. A. Lindholm, J. G. Fossum, and E. L. Burgess, “Application of the superposition principle to solar-cell analysis,” *IEEE Trans. Electron Devices*, vol. 26, no. 3, pp. 165–171, Mar. 1979.
[37] R. A. Sinton and A. Cuevas, “Contactless determination of current–voltage characteristics and minority-carrier lifetimes in semiconductors from quasi-steady-state photoconductance data,” *Appl. Phys. Lett.*, vol. 69, no. 17, pp. 2510–2512, Oct. 1996.
[38] “sinton-epvsc16-pcd.pdf.” .
[39] E. D. Stokes and T. L. Chu, “Diffusion lengths in solar cells from short-circuit current measurements,” *Appl. Phys. Lett.*, vol. 30, no. 8, pp. 425–426, Apr. 1977.
[40] D. E. Carlson and C. R. Wronski, “Amorphous silicon solar cell,” *Appl. Phys. Lett.*, vol. 28, no. 11, pp. 671–673, Jun. 1976.
[41] W. Shockley and W. T. Read, “Statistics of the Recombinations of Holes and Electrons,” *Phys. Rev.*, vol. 87, no. 5, pp. 835–842, Sep. 1952.
[42] S. Bowden and A. Rohatgi, “Rapid and Accurate Determination of Series Resistance and Fill Factor Losses in Industrial Silicon Solar Cells,” Oct. 2001.
[43] M. Wolf and H. Rauschenbach, “Series resistance effects on solar cell measurements,” *Adv. Energy Convers.*, vol. 3, no. 2, pp. 455–479, Apr. 1963.
[44] G. L. Araujo and E. Sanchez, “A new method for experimental determination of the series resistance of a solar cell,” *IEEE Trans. Electron Devices*, vol. 29, no. 10, pp. 1511–1513, Oct. 1982.
[45] K. Bouzidi, M. Chegaar, and A. Bouhemadou, “Solar cells parameters evaluation considering the series and shunt resistance,” *Sol. Energy Mater. Sol. Cells*, vol. 91, no. 18, pp. 1647–1651, Nov. 2007.
[46] “Mapping of contact resistance and locating shunts on solar cells using Resistance Analysis by Mapping of Potential (RAMP) techniques (Technical Report) | ETDEWEB.” [Online]. Available: https://www.osti.gov/etdeweb/biblio/20098255. [Accessed: 18-Sep-2019].
[47] “Hazardous Materials Used In Silicon PV Cell Production: A Primer.” [Online]. Available: https://www.solarindustrymag.com/online/issues/SI1309/FEAT_05_Hazardous_Materials_Used_In_Silicon_PV_Cell_Production_A_Primer.html. [Accessed: 04-Sep-2019].

[48] M. Kaltenbrunner *et al.*, "Ultrathin and lightweight organic solar cells with high flexibility," *Nat. Commun.*, vol. 3, no. 1, pp. 1–7, Apr. 2012.
[49] J. Gong, K. Sumathy, Q. Qiao, and Z. Zhou, "Review on dye-sensitized solar cells (DSSCs): Advanced techniques and research trends," *Renew. Sustain. Energy Rev.*, vol. 68, pp. 234–246, Feb. 2017.
[50] M.-E. Ragoussi and T. Torres, "New generation solar cells: concepts, trends and perspectives," *Chem. Commun.*, vol. 51, no. 19, pp. 3957–3972, Feb. 2015.
[51] A. Kojima, K. Teshima, Y. Shirai, and T. Miyasaka, "Organometal Halide Perovskites as Visible-Light Sensitizers for Photovoltaic Cells," *J. Am. Chem. Soc.*, vol. 131, no. 17, pp. 6050–6051, May 2009.
[52] I. Chung, B. Lee, J. He, R. P. H. Chang, and M. G. Kanatzidis, "All-solid-state dye-sensitized solar cells with high efficiency," *Nature*, vol. 485, no. 7399, pp. 486–489, May 2012.
[53] N.-G. Park, "Perovskite solar cells: an emerging photovoltaic technology," *Mater. Today*, vol. 18, no. 2, pp. 65–72, Mar. 2015.
[54] P. Gao, M. Grätzel, and M. K. Nazeeruddin, "Organohalide lead perovskites for photovoltaic applications," *Energy Environ. Sci.*, vol. 7, no. 8, pp. 2448–2463, Jul. 2014.
[55] W. Ke and M. G. Kanatzidis, "Prospects for low-toxicity lead-free perovskite solar cells," *Nat. Commun.*, vol. 10, no. 1, pp. 1–4, Feb. 2019.
[56] M. Ye *et al.*, "Recent advances in interfacial engineering of perovskite solar cells," *J. Phys. Appl. Phys.*, vol. 50, no. 37, p. 373002, Aug. 2017.
[57] W. Shockley and H. J. Queisser, "Detailed Balance Limit of Efficiency of p-n Junction Solar Cells," *J. Appl. Phys.*, vol. 32, no. 3, pp. 510–519, Mar. 1961.
[58] A. Goetzberger, C. Hebling, and H.-W. Schock, "Photovoltaic materials, history, status and outlook," *Mater. Sci. Eng. R Rep.*, vol. 40, no. 1, pp. 1–46, Jan. 2003.
[59] W. S. Yang *et al.*, "High-performance photovoltaic perovskite layers fabricated through intramolecular exchange," *Science*, vol. 348, no. 6240, pp. 1234–1237, Jun. 2015.
[60] L. Yue, B. Yan, M. Attridge, and Z. Wang, "Light absorption in perovskite solar cell: Fundamentals and plasmonic enhancement of infrared band absorption," *Sol. Energy*, vol. 124, pp. 143–152, Feb. 2016.
[61] P. Tonui, S. O. Oseni, G. Sharma, Q. Yan, and G. Tessema Mola, "Perovskites photovoltaic solar cells: An overview of current status," *Renew. Sustain. Energy Rev.*, vol. 91, pp. 1025–1044, Aug. 2018.
[62] D. Wang, M. Wright, N. K. Elumalai, and A. Uddin, "Stability of perovskite solar cells," *Sol. Energy Mater. Sol. Cells*, vol. 147, pp. 255–275, Apr. 2016.
[63] N. J. Jeon, J. H. Noh, Y. C. Kim, W. S. Yang, S. Ryu, and S. I. Seok, "Solvent engineering for high-performance inorganic–organic hybrid perovskite solar cells," *Nat. Mater.*, vol. 13, no. 9, pp. 897–903, Sep. 2014.
[64] Y. Rong *et al.*, "Solvent engineering towards controlled grain growth in perovskite planar heterojunction solar cells," *Nanoscale*, vol. 7, no. 24, pp. 10595–10599, Jun. 2015.
[65] P.-H. Huang, Y.-H. Wang, J.-C. Ke, and C.-J. Huang, "The Effect of Solvents on the Performance of CH3NH3PbI3 Perovskite Solar Cells," *Energies*, vol. 10, no. 5, p. 599, May 2017.
[66] M. Liu, M. B. Johnston, and H. J. Snaith, "Efficient planar heterojunction perovskite solar cells by vapour deposition," *Nature*, vol. 501, no. 7467, pp. 395–398, Sep. 2013.
[67] M. Saliba *et al.*, "How to Make over 20% Efficient Perovskite Solar Cells in Regular (n–i–p) and Inverted (p–i–n) Architectures," *Chem. Mater.*, vol. 30, no. 13, pp. 4193–4201, Jul. 2018.
[68] J.-H. Im, H.-S. Kim, and N.-G. Park, "Morphology-photovoltaic property correlation in perovskite solar cells: One-step versus two-step deposition of CH3NH3PbI3," *APL Mater.*, vol. 2, no. 8, p. 081510, Jul. 2014.
[69] T.-B. Song *et al.*, "Perovskite solar cells: film formation and properties," *J. Mater. Chem. A*, vol. 3, no. 17, pp. 9032–9050, Apr. 2015.
[70] M. Xiao *et al.*, "A fast deposition-crystallization procedure for highly efficient lead iodide perovskite thin-film solar cells.," *Angew. Chem.*, vol. 53, no. 37, pp. 9898–9903, 2014.
[71] G. Niu, X. Guo, and L. Wang, "Review of recent progress in chemical stability of perovskite solar cells," *J. Mater. Chem. A*, vol. 3, no. 17, pp. 8970–8980, Apr. 2015.

[72] M. M. Lee, J. Teuscher, T. Miyasaka, T. N. Murakami, and H. J. Snaith, "Efficient Hybrid Solar Cells Based on Meso-Superstructured Organometal Halide Perovskites," *Science*, vol. 338, no. 6107, pp. 643–647, Nov. 2012.
[73] Y. Zhao, A. M. Nardes, and K. Zhu, "Mesoporous perovskite solar cells: material composition, charge-carrier dynamics, and device characteristics," *Faraday Discuss.*, vol. 176, no. 0, pp. 301–312, Mar. 2015.
[74] P. P. Boix, K. Nonomura, N. Mathews, and S. G. Mhaisalkar, "Current progress and future perspectives for organic/inorganic perovskite solar cells," *Mater. Today*, vol. 17, no. 1, pp. 16–23, Jan. 2014.
[75] J. M. Ball, M. M. Lee, A. Hey, and H. J. Snaith, "Low-temperature processed meso-superstructured to thin-film perovskite solar cells," *Energy Environ. Sci.*, vol. 6, no. 6, pp. 1739–1743, May 2013.
[76] C.-G. Wu, C.-H. Chiang, Z.-L. Tseng, M. K. Nazeeruddin, A. Hagfeldt, and M. Grätzel, "High efficiency stable inverted perovskite solar cells without current hysteresis," *Energy Environ. Sci.*, vol. 8, no. 9, pp. 2725–2733, Aug. 2015.
[77] N. J. Jeon *et al.*, "Compositional engineering of perovskite materials for high-performance solar cells," *Nature*, vol. 517, no. 7535, pp. 476–480, Jan. 2015.
[78] "Interface engineering of highly efficient perovskite solar cells | Science." [Online]. Available: https://science.sciencemag.org/content/345/6196/542. [Accessed: 30-Sep-2019].
[79] G. Yang, H. Tao, P. Qin, W. Ke, and G. Fang, "Recent progress in electron transport layers for efficient perovskite solar cells," *J. Mater. Chem. A*, vol. 4, no. 11, pp. 3970–3990, Mar. 2016.
[80] P. Docampo, J. M. Ball, M. Darwich, G. E. Eperon, and H. J. Snaith, "Efficient organometal trihalide perovskite planar-heterojunction solar cells on flexible polymer substrates," *Nat. Commun.*, vol. 4, p. 2761, 2013.
[81] C.-H. Chiang, Z.-L. Tseng, and C.-G. Wu, "Planar heterojunction perovskite/PC71BM solar cells with enhanced open-circuit voltage via a (2/1)-step spin-coating process," *J. Mater. Chem. A*, vol. 2, no. 38, pp. 15897–15903, Sep. 2014.
[82] "Inverted, Environmentally Stable Perovskite Solar Cell with a Novel Low-Cost and Water-Free PEDOT Hole-Extraction Layer - Hou - 2015 - Advanced Energy Materials - Wiley Online Library." [Online]. Available: https://onlinelibrary.wiley.com/doi/abs/10.1002/aenm.201500543. [Accessed: 30-Sep-2019].
[83] C. Wehrenfennig, G. E. Eperon, M. B. Johnston, H. J. Snaith, and L. M. Herz, "High charge carrier mobilities and lifetimes in organolead trihalide perovskites," *Adv. Mater. Deerfield Beach Fla*, vol. 26, no. 10, pp. 1584–1589, Mar. 2014.
[84] F. Fu *et al.*, "High-efficiency inverted semi-transparent planar perovskite solar cells in substrate configuration," *Nat. Energy*, vol. 2, no. 1, p. 16190, Jan. 2017.
[85] P. Ganesan *et al.*, "A simple spiro-type hole transporting material for efficient perovskite solar cells," *Energy Environ. Sci.*, vol. 8, no. 7, pp. 1986–1991, Jul. 2015.
[86] N. J. Jeon *et al.*, "o-Methoxy Substituents in Spiro-OMeTAD for Efficient Inorganic–Organic Hybrid Perovskite Solar Cells," *J. Am. Chem. Soc.*, vol. 136, no. 22, pp. 7837–7840, Jun. 2014.
[87] "Inverted vs standard PTB7:PC70BM organic photovoltaic devices. The benefit of highly selective and extracting contacts in device performance." [Online]. Available: http://www.iciq.org/research/publication/inverted-vs-standard-ptb7pc70bm-organic-photovoltaic-devices-the-benefit-of-highly-selective-and-extracting-contacts-in-device-performance/. [Accessed: 09-Sep-2019].
[88] Q. Wang *et al.*, "Characteristics of High Efficiency Dye-Sensitized Solar Cells," *J. Phys. Chem. B*, vol. 110, no. 50, pp. 25210–25221, Dec. 2006.
[89] M. Grätzel, "Dye-sensitized solar cells," *J. Photochem. Photobiol. C Photochem. Rev.*, vol. 4, no. 2, pp. 145–153, Oct. 2003.
[90] "Recent Advances in Hybrid Halide Perovskites-based Solar Cells," *Sigma-Aldrich*. [Online]. Available: https://www.sigmaaldrich.com/technical-documents/articles/material-matters/hybrid-halide-perovskites-based-solar-cells.html. [Accessed: 08-Sep-2019].

[91] M. Hu, L. Liu, A. Mei, Y. Yang, T. Liu, and H. Han, "Efficient hole-conductor-free, fully printable mesoscopic perovskite solar cells with a broad light harvester NH2CHNH2PbI3," *J. Mater. Chem. A*, vol. 2, no. 40, pp. 17115–17121, Sep. 2014.
[92] M. Lira-Cantú, "Perovskite solar cells: Stability lies at interfaces," *Nat. Energy*, vol. 2, no. 7, pp. 1–3, Jul. 2017.
[93] Y. Liu *et al.*, "Poly(3-hexylthiophene)/zinc phthalocyanine composites for advanced interface engineering of 10.03%-efficiency CsPbBr3 perovskite solar cells," *J. Mater. Chem. A*, vol. 7, no. 20, pp. 12635–12644, May 2019.
[94] "Printable carbon-based hole-conductor-free mesoscopic perovskite solar cells: From lab to market - PDF Free Download," *kundoc.com*. [Online]. Available: https://kundoc.com/pdf-printable-carbon-based-hole-conductor-free-mesoscopic-perovskite-solar-cells-fro.html. [Accessed: 08-Sep-2019].
[95] Shungshuang *et al*., "17% efficient printable mesoscopic PIN metal oxide framework perovskite solar cells using cesium-containing triple cation perovskite", *J. Mater. Chem. A*, vol. 5, pp. 22952-22958, 2017.
[96] C.-M. Tsai *et al.*, "Control of preferred orientation with slow crystallization for carbon-based mesoscopic perovskite solar cells attaining efficiency 15%," *J. Mater. Chem. A*, vol. 5, no. 2, pp. 739–747, Jan. 2017.
[97] H. Zhang *et al.*, "SrCl2 Derived Perovskite Facilitating a High Efficiency of 16% in Hole-Conductor-Free Fully Printable Mesoscopic Perovskite Solar Cells," *Adv. Mater.*, vol. 29, no. 15, p. 1606608, 2017.
[98] Y. Yang *et al.*, "The size effect of TiO_2 nanoparticles on a printable mesoscopic perovskite solar cell," *J. Mater. Chem. A*, vol. 3, no. 17, pp. 9103–9107, Apr. 2015.
[99] "Printable carbon-based hole-conductor-free mesoscopic perovskite solar cells: From lab to market."
[100] Y. Yang *et al.*, "An all-carbon counter electrode for highly efficient hole-conductor-free organo-metal perovskite solar cells," *RSC Adv.*, vol. 4, no. 95, pp. 52825–52830, Oct. 2014.
[101] K. T. Cho *et al.*, "Highly efficient perovskite solar cells with a compositionally engineered perovskite/hole transporting material interface," *Energy Environ. Sci.*, vol. 10, no. 2, pp. 621–627, Feb. 2017.
[102] G. Grancini *et al.*, "One-Year stable perovskite solar cells by 2D/3D interface engineering," *Nat. Commun.*, vol. 8, p. 15684, Jun. 2017.
[103] Q. Chen *et al.*, "Under the spotlight: The organic–inorganic hybrid halide perovskite for optoelectronic applications," *Nano Today*, vol. 10, no. 3, pp. 355–396, Jun. 2015.
[104] T. Leijtens, K. Bush, R. Cheacharoen, R. Beal, A. Bowring, and M. D. McGehee, "Towards enabling stable lead halide perovskite solar cells; interplay between structural, environmental, and thermal stability," *J. Mater. Chem. A*, vol. 5, no. 23, pp. 11483–11500, Jun. 2017.
[105] "Understanding why cesium and rubidium salt improve the yield of perovskite solar cells," *pv magazine International*. [Online]. Available: https://www.pv-magazine.com/2019/02/08/cesium-and-rubidium-salt-improve-yield-of-perovskite-cells/. [Accessed: 09-Sep-2019].
[106] T. Leijtens, B. Lauber, G. E. Eperon, S. D. Stranks, and H. J. Snaith, "The Importance of Perovskite Pore Filling in Organometal Mixed Halide Sensitized TiO2-Based Solar Cells," *J. Phys. Chem. Lett.*, vol. 5, no. 7, pp. 1096–1102, Apr. 2014.
[107] T. Su, Y. Yang, G. Dong, T. Ye, Y. Jiang, and R. Fan, "Improved photovoltaic performance of mesoporous perovskite solar cells with hydrogenated TiO2: prolonged photoelectron lifetime and high separation efficiency of photoinduced charge," *RSC Adv.*, vol. 6, no. 69, pp. 65125–65135, Jul. 2016.
[108] S. Ito *et al.*, "Fabrication of screen-printing pastes from TiO2 powders for dye-sensitised solar cells," *Prog. Photovolt. Res. Appl.*, vol. 15, no. 7, pp. 603–612, 2007.
[109] S. Razza, S. Castro-Hermosa, A. Di Carlo, and T. M. Brown, "Research Update: Large-area deposition, coating, printing, and processing techniques for the upscaling of perovskite solar cell technology," *APL Mater.*, vol. 4, no. 9, p. 091508, Sep. 2016.

[110] K. Domanski *et al.*, "Migration of cations induces reversible performance losses over day/night cycling in perovskite solar cells," *Energy Environ. Sci.*, vol. 10, no. 2, pp. 604–613, Feb. 2017.
[111] L. Wagner, S. Chacko, G. Mathiazhagan, S. Mastroianni, and A. Hinsch, "High Photovoltage of 1 V on a Steady-State Certified Hole Transport Layer-Free Perovskite Solar Cell by a Molten-Salt Approach," *ACS Energy Lett.*, vol. 3, no. 5, pp. 1122–1127, May 2018.
[112] M. Kulbak, D. Cahen, and G. Hodes, "How Important Is the Organic Part of Lead Halide Perovskite Photovoltaic Cells? Efficient CsPbBr3 Cells," *J. Phys. Chem. Lett.*, vol. 6, no. 13, pp. 2452–2456, Jul. 2015.
[113] E. T. Hoke, D. J. Slotcavage, E. R. Dohner, A. R. Bowring, H. I. Karunadasa, and M. D. McGehee, "Reversible photo-induced trap formation in mixed-halide hybrid perovskites for photovoltaics," *Chem. Sci.*, vol. 6, no. 1, pp. 613–617, Dec. 2014.
[114] C. K. Møller, "Crystal Structure and Photoconductivity of Cæsium Plumbohalides," *Nature*, vol. 182, no. 4647, pp. 1436–1436, Nov. 1958.
[115] Y. Bekenstein, B. A. Koscher, S. W. Eaton, P. Yang, and A. P. Alivisatos, "Highly Luminescent Colloidal Nanoplates of Perovskite Cesium Lead Halide and Their Oriented Assemblies," *J. Am. Chem. Soc.*, vol. 137, no. 51, pp. 16008–16011, Dec. 2015.
[116] Z. Guan *et al.*, "Perovskite photocatalyst CsPbBr3-xIx with a bandgap funnel structure for H2 evolution under visible light," *Appl. Catal. B Environ.*, vol. 245, pp. 522–527, May 2019.
[117] "Cation-Induced Band-Gap Tuning in Organohalide Perovskites: Interplay of Spin–Orbit Coupling and Octahedra Tilting | Nano Letters." [Online]. Available: https://pubs.acs.org/doi/10.1021/nl5012992. [Accessed: 09-Sep-2019].
[118] J.-W. Lee, D.-H. Kim, H.-S. Kim, S.-W. Seo, S. M. Cho, and N.-G. Park, "Formamidinium and Cesium Hybridization for Photo- and Moisture-Stable Perovskite Solar Cell," *Adv. Energy Mater.*, vol. 5, no. 20, p. 1501310, 2015.
[119] C. Yi *et al.*, "Entropic stabilization of mixed A-cation ABX3 metal halide perovskites for high performance perovskite solar cells," *Energy Environ. Sci.*, vol. 9, no. 2, pp. 656–662, Feb. 2016.
[120] M. Okuya, N. A. Prokudina, K. Mushika, and S. Kaneko, "TiO2 thin films synthesized by the spray pyrolysis deposition (SPD) technique," *J. Eur. Ceram. Soc.*, vol. 19, no. 6, pp. 903–906, Jun. 1999.
[121] A. I. Martínez, D. R. Acosta, and A. A. López, "Effect of deposition methods on the properties of photocatalytic TiO2thin films prepared by spray pyrolysis and magnetron sputtering," *J. Phys. Condens. Matter*, vol. 16, no. 22, pp. S2335–S2344, May 2004.
[122] L. Xu *et al.*, "Stable monolithic hole-conductor-free perovskite solar cells using TiO2 nanoparticle binding carbon films," *Org. Electron.*, vol. 45, pp. 131–138, Jun. 2017.
[123] N. Ahn, D.-Y. Son, I.-H. Jang, S. M. Kang, M. Choi, and N.-G. Park, "Highly Reproducible Perovskite Solar Cells with Average Efficiency of 18.3% and Best Efficiency of 19.7% Fabricated via Lewis Base Adduct of Lead(II) Iodide," *J. Am. Chem. Soc.*, vol. 137, no. 27, pp. 8696–8699, Jul. 2015.
[124] S. Tanemura, L. Miao, P. Jin, K. Kaneko, A. Terai, and N. Nabatova-Gabain, "Optical properties of polycrystalline and epitaxial anatase and rutile TiO2 thin films by rf magnetron sputtering," *Appl. Surf. Sci.*, vol. 212–213, pp. 654–660, May 2003.
[125] H. Tang, K. Prasad, R. Sanjinès, P. E. Schmid, and F. Lévy, "Electrical and optical properties of TiO2 anatase thin films," *J. Appl. Phys.*, vol. 75, no. 4, pp. 2042–2047, Feb. 1994.
[126] B. D. Viezbicke, S. Patel, B. E. Davis, and D. P. Birnie, "Evaluation of the Tauc method for optical absorption edge determination: ZnO thin films as a model system," *Phys. Status Solidi B*, vol. 252, no. 8, pp. 1700–1710, 2015.
[127] J. B. Coulter and D. P. Birnie, "Assessing Tauc Plot Slope Quantification: ZnO Thin Films as a Model System," *Phys. Status Solidi B*, vol. 255, no. 3, p. 1700393, 2018.
[128] "(10) (PDF) Comparison of scanning tunneling microscope-light emission and photoluminescence from porphyrin films using ultra-high vacuum scanning tunneling microscopy." [Online]. Available: https://www.researchgate.net/publication/257951490_Comparison_of_scanning_tunneling_microscope-light_emission_and_photoluminescence_from_porphyrin_films_using_ultra-high_vacuum_scanning_tunneling_microscopy/figures?lo=1. [Accessed: 13-Sep-2019].

[129] N. K. Noel *et al.*, "Enhanced Photoluminescence and Solar Cell Performance via Lewis Base Passivation of Organic–Inorganic Lead Halide Perovskites," *ACS Nano*, vol. 8, no. 10, pp. 9815–9821, Oct. 2014.
[130] Z. Hameiri *et al.*, "Photoluminescence and electroluminescence imaging of perovskite solar cells," *Prog. Photovolt. Res. Appl.*, vol. 23, no. 12, pp. 1697–1705, Dec. 2015.
[131] E. L. Unger *et al.*, "Hysteresis and transient behavior in current–voltage measurements of hybrid-perovskite absorber solar cells," *Energy Environ. Sci.*, vol. 7, no. 11, pp. 3690–3698, Oct. 2014.
[132] W. Tress, N. Marinova, T. Moehl, S. M. Zakeeruddin, M. K. Nazeeruddin, and M. Grätzel, "Understanding the rate-dependent J–V hysteresis, slow time component, and aging in CH3NH3PbI3 perovskite solar cells: the role of a compensated electric field," *Energy Environ. Sci.*, vol. 8, no. 3, pp. 995–1004, Mar. 2015.
[133] H. J. Snaith *et al.*, "Anomalous Hysteresis in Perovskite Solar Cells," *J. Phys. Chem. Lett.*, vol. 5, no. 9, pp. 1511–1515, May 2014.
[134] S. van Reenen, M. Kemerink, and H. J. Snaith, "Modeling Anomalous Hysteresis in Perovskite Solar Cells," *J. Phys. Chem. Lett.*, vol. 6, no. 19, pp. 3808–3814, Oct. 2015.
[135] X. Wu *et al.*, "Efficient and stable carbon-based perovskite solar cells enabled by the inorganic interface of CuSCN and carbon nanotubes," *J. Mater. Chem. A*, vol. 7, no. 19, pp. 12236–12243, May 2019.
[136] S. Ghufran Hashmi *et al.*, "High performance carbon-based printed perovskite solar cells with humidity assisted thermal treatment," *J. Mater. Chem. A*, vol. 5, no. 24, pp. 12060–12067, 2017.
[137] K. Yasaroglu *et al.*, "Macroporosity Enhancement of Scaffold Oxide Layers Using Self-Assembled Polymer Beads for Photovoltaic Applications," *Phys. Status Solidi A*, vol. 215, no. 17, p. 1700946, 2018.
[138] "R&Dnano | Revêtements & traitements de surface sol-gel pour produits industriels," *R&Dnano*. [Online]. Available: http://www.rdnano.fr/. [Accessed: 11-Sep-2019].
[139] S. Slomkowski *et al.*, "Terminology of polymers and polymerization processes in dispersed systems (IUPAC Recommendations 2011)," *Pure Appl. Chem.*, vol. 83, no. 12, pp. 2229–2259, Sep. 2011.
[140] I. Souilem *et al.*, "A Novel Low-Pressure Device for Production of Nanoemulsions," *Chem. Eng. Technol.*, vol. 35, no. 9, pp. 1692–1698, 2012.
[141] V. Divry, "Mécanismes de formation et relations structure/propriétés de films minces à matrice polymère issus de colloïdes aqueux à séchage rapide," Thesis, Université de Strasbourg, 2016.
[142] B. Peng, E. van der Wee, A. Imhof, and A. van Blaaderen, "Synthesis of Monodisperse, Highly Cross-Linked, Fluorescent PMMA Particles by Dispersion Polymerization," *Langmuir*, vol. 28, no. 17, pp. 6776–6785, May 2012.
[143] X. Li *et al.*, "Improved performance and stability of perovskite solar cells by crystal crosslinking with alkylphosphonic acid ω-ammonium chlorides," *Nat. Chem.*, vol. 7, no. 9, pp. 703–711, Sep. 2015.
[144] T. A. Berhe *et al.*, "Organometal halide perovskite solar cells: degradation and stability," *Energy Environ. Sci.*, vol. 9, no. 2, pp. 323–356, Feb. 2016.
[145] G. E. Eperon, S. D. Stranks, C. Menelaou, M. B. Johnston, L. M. Herz, and H. J. Snaith, "Formamidinium lead trihalide: a broadly tunable perovskite for efficient planar heterojunction solar cells," *Energy Environ. Sci.*, vol. 7, no. 3, pp. 982–988, Feb. 2014.
[146] Y. Yu *et al.*, "Improving the Performance of Formamidinium and Cesium Lead Triiodide Perovskite Solar Cells using Lead Thiocyanate Additives," *ChemSusChem*, vol. 9, no. 23, pp. 3288–3297, 2016.
[147] Z. Li, M. Yang, J.-S. Park, S.-H. Wei, J. J. Berry, and K. Zhu, "Stabilizing Perovskite Structures by Tuning Tolerance Factor: Formation of Formamidinium and Cesium Lead Iodide Solid-State Alloys," *Chem. Mater.*, vol. 28, no. 1, pp. 284–292, Jan. 2016.
[148] Y. Bai *et al.*, "A pure and stable intermediate phase is key to growing aligned and vertically monolithic perovskite crystals for efficient PIN planar perovskite solar cells with high processibility and stability," *Nano Energy*, vol. 34, pp. 58–68, Apr. 2017.

[149] G. E. Eperon, V. M. Burlakov, P. Docampo, A. Goriely, and H. J. Snaith, "Morphological Control for High Performance, Solution-Processed Planar Heterojunction Perovskite Solar Cells," *Adv. Funct. Mater.*, vol. 24, no. 1, pp. 151–157, 2014.
[150] Q. Dong *et al.*, "Insight into Perovskite Solar Cells Based on SnO2 Compact Electron-Selective Layer," *J. Phys. Chem. C*, vol. 119, no. 19, pp. 10212–10217, May 2015.
[151] H.-S. Rao *et al.*, "Improving the Extraction of Photogenerated Electrons with SnO2 Nanocolloids for Efficient Planar Perovskite Solar Cells," *Adv. Funct. Mater.*, vol. 25, no. 46, pp. 7200–7207, 2015.
[152] "Scherrer Equation - an overview | ScienceDirect Topics." [Online]. Available: https://www.sciencedirect.com/topics/materials-science/scherrer-equation. [Accessed: 12-Sep-2019].
[153] H.-H. Perkampus, *UV-VIS Spectroscopy and Its Applications*. Springer Science & Business Media, 2013.
[154] J. Tauc, Ed., *Amorphous and Liquid Semiconductors*. Springer US, 1974.
[155] S. J. Pennycook *et al.*, "Material structure, properties, and dynamics through scanning transmission electron microscopy," *J. Anal. Sci. Technol.*, vol. 9, no. 1, 2018.
[156] J. F. Hainfeld and J. S. Wall, "High Resolution Electron Microscopy for Structure and Mapping," in *Biotechnology and the Human Genome*, 1988, pp. 131–147.
[157] "Photoluminescence Spectroscopy and Its Applications 2 | Spectroscopie ultraviolet-visible | Spectre d'émission," *Scribd*. [Online]. Available: https://www.scribd.com/document/328275247/Photoluminescence-Spectroscopy-and-Its-Applications-2. [Accessed: 12-Sep-2019].
[158] "EDX Analysis with a Scanning Electron Microscope (SEM): How Does it Work?" [Online]. Available: https://blog.phenom-world.com/edx-analysis-sem. [Accessed: 12-Sep-2019].
[159] S. Zangooie, R. Jansson, and H. Arwin, "Ellipsometric characterization of anisotropic porous silicon Fabry–Pérot filters and investigation of temperature effects on capillary condensation efficiency," *J. Appl. Phys.*, vol. 86, no. 2, pp. 850–858, Jun. 1999.
[160] D. Ngo *et al.*, "Spectroscopic ellipsometry study of thickness and porosity of the alteration layer formed on international simple glass surface in aqueous corrosion conditions," *Npj Mater. Degrad.*, vol. 2, no. 1, pp. 1–9, Jul. 2018.
[161] "Ellipsometry - an overview | ScienceDirect Topics." [Online]. Available: https://www.sciencedirect.com/topics/chemistry/ellipsometry. [Accessed: 12-Sep-2019].
[162] M. Gaillet, "Forouhi-Bloomer alias Amorphous Dispersion Formula," p. 5.
[163] "Solar Simulator Components Simulators A Guide." [Online]. Available: http://latt.bestforvstyles.com/index.php?main_page=product_info&products_id=273. [Accessed: 12-Sep-2019].
[164] "Dynamic light scattering: a practical guide and applications in biomedical sciences." [Online]. Available: https://www.ncbi.nlm.nih.gov/pmc/articles/PMC5425802/. [Accessed: 12-Sep-2019].
[165] P. Gabbott, *Principles and Applications of Thermal Analysis*. John Wiley & Sons, 2008.
[166] "Photoluminescence Spectroscopy - an overview | ScienceDirect Topics." [Online]. Available: https://www.sciencedirect.com/topics/chemistry/photoluminescence-spectroscopy. [Accessed: 13-Sep-2019].
[167] E. Diau and P. Chen, *Perovskite solar cells: principle, materials, devices*. 2018.
[168] G. Möbus and B. J. Inkson, "Nanoscale tomography in materials science," *Mater. Today*, vol. 10, no. 12, pp. 18–25, Dec. 2007.
[169] R. Wirth, "Focused Ion Beam (FIB) combined with SEM and TEM: Advanced analytical tools for studies of chemical composition, microstructure and crystal structure in geomaterials on a nanometre scale," *Chem. Geol.*, vol. 261, no. 3–4, pp. 217–229, Apr. 2009.

Résumé en français:

Ces dernières années, les cellules solaires pérovskites (PSC) ont montré un grand potentiel dans le domaine des cellules solaires de nouvelle génération, avec une amélioration rapide du rendement de conversion [1]. Une cellule solaire pérovskite est un type de cellule solaire qui comprend un composé structuré pérovskite (ABX_3 avec X un halogène), le plus souvent composé d'un halogénure hybride organique-inorganique de plomb ou d'étain comme matière active pour la récolte de la lumière. Ces matériaux (c'est-à-dire les halogénures de plomb méthylammonium les plus courants $CH_3NH_3PbI_3$-$MAPbI_3$-MAPI) sont peu coûteux à produire et relativement simples à fabriquer. Bien que l'évolution du rendement de conversion de l'énergie (PCE) ait été extraordinaire, il existe toujours un obstacle à la commercialisation des PCE, à savoir leur grande sensibilité à l'humidité et à l'oxygène, qui entraîne une dégradation rapide du matériau absorbant en pérovskite [2]. Pour résoudre ces problèmes, une idée consiste à utiliser une architecture mésostructuré inorganique en remplacement l'utilisation de couches organiques telles que le spiro-OMeTAD et les électrodes métalliques (or ou argent). Il est bien connu, en effet, que les ions métalliques se diffusent dans le matériau absorbant, provoquant la dégradation de la cellule [3]. Dans la littérature, une telle structure cellulaire a été proposée en utilisant un triple empilement de deux couches inorganiques (par exemple TiO_2 et ZrO_2) et une couche de carbone [4], [5]. La PSC avec une telle conception mésostructurée est composé de différentes couches déposées successivement sur des substrats commerciaux en verre recouverts d'oxyde de fluor et d'étain (FTO). Le FTO joue le rôle d'électrode (anode) transparente et de contact frontal. La première couche déposée est une couche de TiO_2 de type n, mince et compacte ($\sim$ 20 nm) pour l'extraction des électrons du matériau photo-absorbant vers l'anode ; il s'agit généralement d'un film mince obtenu par dépôt par pyrolyse par pulvérisation. Les étapes suivantes consistent à construire les couches poreuses de TiO_2 (m-TiO_2) et de ZrO_2 mésoscopiques, généralement par des techniques de sérigraphie [6]. Pour compléter la structure de la cellule, du graphite est déposé sur le dessus par le même procédé que précédemment ; le graphite est utilisé pour l'extraction des trous et l'électrode de contact arrière (cathode). Enfin, la solution contenant les précurseurs de la pérovskite est infiltrée par une méthode de coulée en goutte-à-goutte à travers les films d'échafaudage pour former les cristaux photo-actifs de pérovskite (sous forme de $MAPbI_3$). La configuration des cellules solaires en pérovskite à base de graphite et les niveaux d'énergie de TiO_2, $CH_3NH_3PbI_3$ et de carbone sont illustrés ci-dessous [6]:

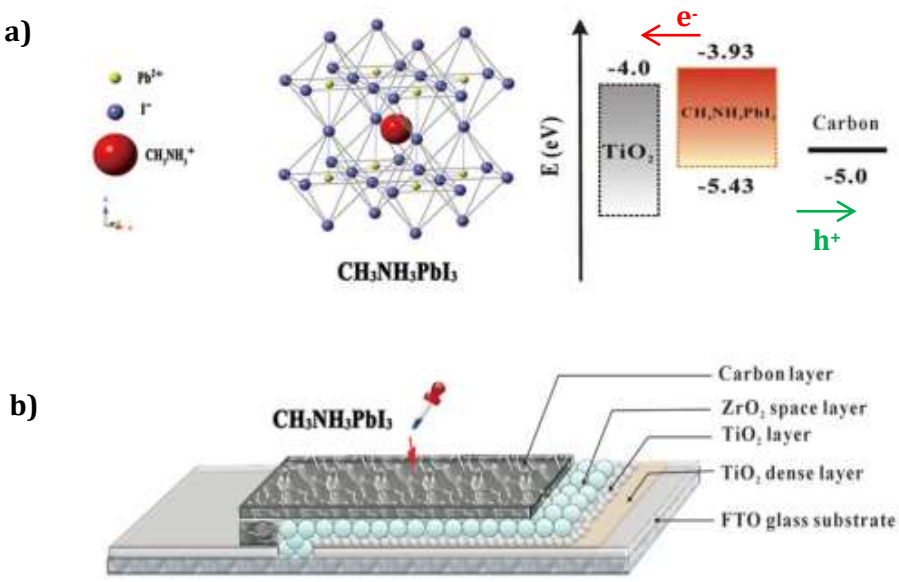

Figure VIII-15: (a) La structure cristalline de la pérovskite CH3NH3PbI3 et les niveaux d'énergie correspondants de TiO2, $CH_3NH_3PbI_3$ et de carbone. (b) Structure schématique d'un dispositif monolithique à base de carbone

La couche de m-TiO_2 est généralement déposée par un procédé d'enduction par centrifugation ou de sérigraphie en utilisant une pâte commerciale contenant des nanoparticules de TiO_2 d'un diamètre d'environ 20 nm pour former un film mésoporeux de 200 à 500 nm d'épaisseur et de grande surface [5]. Les cristaux de pérovskite cultivés dans ces structures mésoporeuses de TiO_2 souffrent souvent d'une formation incomplète de cristallites et d'un remplissage inhomogène des pores [7]. Afin de mieux contrôler les paramètres morphologiques de l'échafaudage et la qualité de la formation de la matière active, différentes stratégies basées sur des réactions sol-gel utilisant des gabarits souples orientant la structure (tels que des tensioactifs et des copolymères séquencés) ont été développées pour préparer une couche de TiO_2 cristallin avec des mésopores bien définis. Yue et ses collègues [8] ont utilisé des couches continues simples de poly(méthacrylate de méthyle) (PMMA) comme agent de modelage pour former des films de TiO_2 mésoporeux sans fissures par une méthode sol-gel. Il a été démontré que la taille des pores et la morphologie obtenues lors du recuit peuvent être contrôlées en faisant varier la quantité de PMMA. Il a été démontré que de plus grands mésopores permettent d'obtenir des rendements plus importants des cellules solaires. Cette morphologie favorise de meilleures performances par rapport à des dispositifs similaires préparés avec des pâtes de nanoparticules de TiO_2 conventionnelles ou par la même méthode sol-gel sans ajout de PMMA.

En ce qui concerne les problèmes décrits et la solution de rechange possible citée ci-dessus, il semble prometteur d'élaborer dans ce travail des échafaudages de TiO_2 à structure macroporeuse, en utilisant l'approche sol-gel assistée par polymère. Pour un meilleur contrôle de la porosité, les particules de polymère sont préférées à des couches continues uniques. Une suspension de perles de polymère de poly(méthacrylate de méthyle) de différents diamètres (de 80 nm à 280 nm) est utilisée comme agent de modelage unique pour former la couche de TiO_2 en échafaudage avec des tailles de porosité contrôlées directement liées à la taille des particules de polymère par le procédé de moulage.

On a constaté que les morphologies des pores de la couche pouvaient être contrôlées avec succès en faisant varier le diamètre des particules de PMMA. Des analyses par microscopie électronique à balayage (MEB) ont été effectuées sur les couches poreuses de TiO_2 (200 - 300 nm d'épaisseur)

obtenues par ce procédé de moulage. Elles ont montré avec succès la relation entre le diamètre des billes de PMMA et la taille des pores. En outre, les mesures de diffraction des rayons X des couches poreuses de TiO_2 ont confirmé que ces dernières sont bien cristallisées sous forme de TiO_2 anatase.

En résumé, dans ce travail, je me suis d'abord concentré sur l'ingénierie de la taille des pores de la couche de TiO_2 par le procédé de moulage des billes de PMMA. Ici, les sphères de polymère sont utilisées comme un modèle de diamètre différent pour contrôler la taille des pores de 80 nm à 280 nm. L'objectif est d'obtenir une couche qui donne naissance à : (i) un transfert d'électrons efficace et (ii) une interface TiO_2/perovskite de haute qualité et (iii) permettant le contrôle d'une infiltration optimale des précurseurs de la perovskite.

La deuxième question scientifique étudiée dans ce travail porte sur la stabilisation de l'efficacité des cellules à court terme. Une alternative prometteuse au $MAPbI_3$ a été largement démontrée dans la littérature via l'utilisation de systèmes à cations mixtes (par exemple, incluant des cations inorganiques tels que le rubidium ou le césium) pour améliorer à la fois la stabilité et l'efficacité à long terme. Les premières cellules pérovskites ayant un rendement énergétique supérieur à 20 % utilisaient un système de cations organiques mixtes, et un grand nombre des systèmes à plus haut rendement récemment publiés utilisent des composants inorganiques [9]. En se basant sur les diverses propriétés des différents composants de la pérovskite, les chercheurs se sont concentrés sur la combinaison de différents cations et halogénures afin de combiner leurs avantages. En outre, l'ajout d'une petite quantité de césium inorganique dans une structure de pérovskite "à double ou triple cation" (Cs-Césium/MA-Méthylammonium/FA-Formamidinium) a permis d'obtenir des grains monolithiques de pérovskite de haute qualité [10]. Dans ce travail, nous avons suivi une approche similaire en remplaçant l'absorbeur de lumière pérovskite $MAPbI_3$ couramment utilisé par un cristal $(CH_5N_2)_xCs_{1-x}PbBr_yI_{3-y}$ (Formamidinium-Césium-Bromure de plomb avec x = 0,83 et y = 0,8).

Pour résumer, dans cette thèse, j'ai développé une couche de TiO_2 "macroporeuse" et j'ai introduit la structure pérovskite de cations/halides mixtes ($FA_{0,83}Cs_{0,17}PbBr_{0,8}I_{2.2}$) dans la PSC à base de graphite. Une caractérisation approfondie a été effectuée pour l'analyse complète des paramètres chimiques et physiques de la cellule dans le but de démontrer les avantages de l'architecture innovante de PSC développée, ses performances accrues et l'amélioration de son efficacité stabilisée. L'intégration de la couche macroporeuse de TiO_2 préparée par l'ingénierie de la taille des pores et l'utilisation de $FA_{0,83}Cs_{0,17}PbBr_{0,8}I_{2,2}$ perovskite ont permis d'améliorer considérablement la CSP à base de graphite avec une efficacité rapportée de 14,7%.

Ce manuscrit est organisé en trois sections distinctes comprenant cinq chapitres au total. Dans la première section, l'état de l'art de la CSP est présenté, qui comprend le principe de fonctionnement des cellules de pérovskite, les configurations cellulaires possibles, les techniques de dépôt de précurseurs, les problèmes de stabilité et enfin l'approche de la thèse. Dans la section expérimentale, les procédés de fabrication de la cellule solaire pérovskite à base de graphite sont décrits avec la préparation de la couche poreuse de TiO_2 par la méthode de moulage de billes de PMMA. La dernière section rapporte le processus expérimental pour l'intégration de la couche poreuse de TiO_2 dans le c-PSC complet et les performances électriques mesurées. Tout au long de ces chapitres, les résultats de la caractérisation seront analysés et discutés. Le synopsis de la thèse est présenté dans le diagramme ci-dessous (Figure I-2).

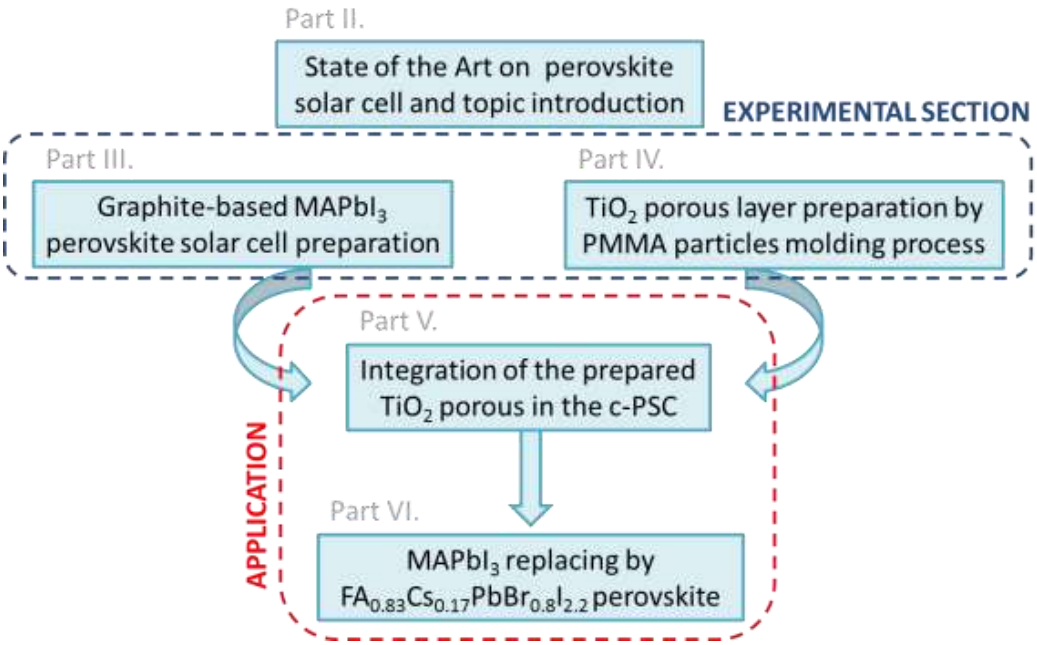

Figure VIII-16: Diagramme représentant le synopsis de la thèse

Le travail de thèse porte sur l'architecture des cellules solaires mésoporeuses et à base de graphite pérovskite dans la configuration directe (n-i-p).

Les cellules solaires hybrides (organiques-inorganiques) à pérovskite sont décrites ici comme une nouvelle technologie photovoltaïque émergente et peu coûteuse qui s'inspire des cellules solaires sensibilisées par des colorants. Les c-PSC peuvent être produites en masse par la technique de sérigraphie, et une variété de matières premières abondantes peuvent être utilisées pour leur élaboration. Avec un rendement théorique de conversion d'énergie de 33 % selon la limite de Shockley Queisser, les cellules solaires hybrides à pérovskite se sont révélées être la technologie photovoltaïque qui se développe le plus rapidement dans l'histoire des panneaux solaires.

Néanmoins, cette activité photovoltaïque est toujours confrontée à un problème majeur, à savoir la grande sensibilité à l'humidité qui provoque la dégradation rapide de la couche de pérovskite. Cela rend les cellules solaires pérovskites instables et peu fiables lorsqu'elles sont exposées à des environnements à air humide, ce qui limite leur mise à l'échelle et leur commercialisation. Un autre problème concerne l'infiltration uniforme et optimale des précurseurs de la pérovskite à l'intérieur de la couche mésoporeuse de TiO2 présente dans le dispositif c-PSC. C'est pourquoi il est devenu un principe de conception important d'améliorer l'infiltration des précurseurs récoltant la lumière et d'utiliser des cations et des halogénures mixtes combinant des propriétés bénéfiques afin d'obtenir des composés de pérovskite avec une stabilité thermique et structurelle améliorée.

Cela justifie donc notre stratégie intuitive où la couche de m-TiO_2 est remplacée par une couche poreuse avec de plus grandes cavités (taille allant de ≈ 50 nm à ≈ 250 nm) préparée par moulage de particules de PMMA avec une solution sol-gel contenant des précurseurs de Ti.

En outre, la récolte traditionnelle de lumière $MAPbI_3$ est remplacée par une perovskite mixte de cations et d'halogénures. En ce qui concerne l'effet positif du mélange de cations, une petite quantité de césium inorganique est utilisée pour améliorer les composés de perovskite FA. La partie halogénure X est combinée avec l'élément Br et I afin d'améliorer les propriétés optiques.

En conséquence, le matériau photo-actif classique précédent devient une perovskite mixte $(CH_5N_2)_xCs_{1-x}PbBr_yI_3$-y où x = 0,83 et y = 0,8.

Des modifications structurelles (couche "macroporeuse" de TiO_2) et de type pérovskite (cations et halogénures mixtes : $FA_xCs_{1-x}PbBr_yI_{3-y}$) seront appliquées à une cellule solaire pérovskite monolithique de référence à base de graphite/$MAPbI_3$ afin d'étudier l'amélioration des performances et du rendement stabilisé.

Nous avons obtenu une couche mince de TiO_2 compact de type n (~ 30 nm) sous forme d'ETL déposée par pyrolyse par pulvérisation. Les films mésoporeux de TiO_2 et de ZrO_2 ont une épaisseur de ~ 600 nm et ~ 1 µm respectivement et la taille des pores est d'environ 25 nm. La couche supérieure de graphite qui joue le rôle de couche de transport des trous et de contact arrière a une épaisseur de ~ 7-8 µm et contient des paillettes de carbone et une structure mésoporeuse dans le film. Le matériau absorbant la lumière, la pérovskite, a été infiltré avec succès à travers les différentes couches de l'échafaudage par la technique de la coulée en goutte-à-goutte.

Les performances du PSC sont caractérisées par des mesures I-V, l'efficacité varie de 8 % à 10 % en moyenne. Les balayages en marche arrière et en marche avant ont révélé une hystérésis dans la courbe I-V. Nous n'avons pas d'explication claire sur l'origine de cet effet.

Aussi, nous avons montré dans cette thèse le processus complet de préparation et de caractérisation des cellules solaires pérovskites. Chaque couche présente dans la PSC a été caractérisée dans le but d'avoir une cellule de référence à comparer avec les nouvelles cellules à venir dans les prochains chapitres.

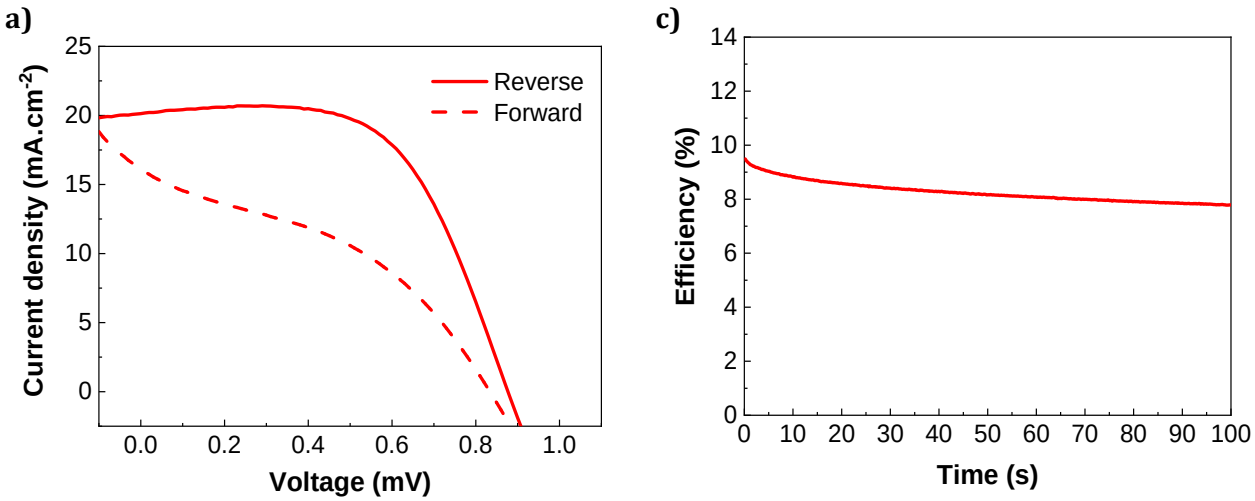

b)

Ref. PSC parameters	
V_{OC} (V)	0,903
J_{SC} (mA/cm²)	18,91
FF (%)	51,06

Figure VIII-17: (a) courbe I-V d'une cellule solaire monolithique préparée en pérovskite (b) les paramètres de la cellule (c) rendement stabilisé

Dans la suite, nous avons démontré l'application directe dans la cellule monolithique de la pérovskite de la couche mésoporeuse de TiO_2 remplacée par le moulage de particules de PMMA de taille P50+, P100+ et P200+.

Les résultats ont montré que la cellule de pérovskite P50+ a obtenu une bonne amélioration de la valeur du courant de court-circuit (≈ 24 mA.cm^{-2}), par rapport à la cellule monolithique (≈ 19 mA.cm^{-2}). Toutefois, le facteur de remplissage reste pratiquement inchangé, tandis que la valeur de la tension de circuit ouvert est inférieure à 900 mV. En outre, la mesure du PCS en fonction du temps a montré une diminution des performances dans le temps. Il est donc difficile de dire à ce stade si les cellules P50+ sont plus efficaces que les cellules de référence, mais la valeur du J_{SC} et la bonne reproductibilité des PSC sont encourageantes pour la partie suivante.

En ce qui concerne les cellules pérovskites avec les couches poreuses TiO_2 P100+ et P200+, la technique de coulée en goutte-à-goutte n'est évidemment pas adaptée pour une infiltration optimale sur la base des images des cellules et de l'analyse MEB.

À partir de ces résultats, nous avons décidé de changer la technique d'infiltration des précurseurs de la pérovskite pour la technique de revêtement par centrifugation utilisée plus souvent dans les cellules à structure plane. De plus, pour améliorer les performances et la stabilité de la PSC, nous avons opté pour une pérovskite à base de Formamidinium et de césium pour remplacer le Méthylammonium et une partie halogénée mixte par de l'iodure et du bromure, dont la formule est la suivante $(CH_5N_2)_xCs_{1-x}PbBr_xI_{3-x}$ - $FA_{0,83}Cs_{0,17}PbBr_{0,8}I_{2,2}$ [9], [118].

Pour résumer la finalisation du travail accompli au cours de cette thèse avec l'intégration des couches poreuses de TiO_2 préparées par moulage et l'utilisation d'un nouveau type de pérovskites $FA_{0,83}Cs_{0,17}PbBr_{0,8}I_{2,2}$.

Le remplacement du matériau pérovskite photo-actif MAPbI3 par des cristaux de $FA_{0,83}Cs_{0,17}PbBr_{0,8}I_{2,2}$ a permis d'obtenir des performances quasi-stationnaires en fonction du temps pour chaque type de PSC.

La technique d'enrobage par centrifugation pour remplacer la méthode de coulée en goutte-à-goutte utilisée traditionnellement pour infiltrer les couches poreuses avec des précurseurs de la pérovskite s'est avérée plus efficace pour les cellules ayant des pores de plus grande taille pour la couche de TiO_2 échafaudée.

En général, les cellules P50+, P100+ et P200+ ont démontré de meilleures performances photovoltaïques par rapport aux cellules de référence. La valeur J_{SC} la plus importante obtenue est pour la cellule P50+ et les images MEB ont démontré une bonne infiltration, alors que pour la cellule de référence, elle était non uniforme dans la couche poreuse de TiO_2. Cependant, la valeur du facteur de remplissage avait tendance à augmenter avec la taille des pores; elle atteignait plus de 62 % avec la cellule P200+. Cela peut être dû à la réduction de la résistance en série et en dérivation dans la cellule, comme expliqué dans la partie II.3.2.2.

Enfin, la partie sur les expériences préliminaires a démontré qu'il existe encore un potentiel d'amélioration des performances des cellules P50+ et P200+, qui ont déjà montré des paramètres photovoltaïques prometteurs. Le rendement stabilisé le plus élevé est obtenu pour le type de cellule P50+C avec du $FA_{0,83}Cs_{0,17}PbBr_{0,8}I_{2,2}$ matériau absorbant la lumière en pérovskite infiltré par la méthode de revêtement par centrifugation ; avec une valeur stabilisée enregistrée de ≈ 13,6 %. Vient ensuite la cellule P200+C avec un PCE stabilisé autour de 10,7 %.

Cependant, il est important de se concentrer sur l'étude de la dégradation des cellules dans le temps car, bien qu'elle montre des rendements intéressants, il est important d'étudier leur comportement au fil du temps. Même si les cellules P50+ ont atteint des efficacités plus élevées, elles peuvent se dégrader plus rapidement que les cellules à larges pores. L'influence de la taille des pores en fonction de la stabilité des cellules sera étudiée dans le cadre de travaux futurs.

Université de Strasbourg

Kubra YASAROGLU UNAL

UNI FREIBURG

« Préparation de couche poreuse de TiO_2 par moulage de billes de polymères pour des applications dans des cellules solaires à base de perovskites »

Résumé

Les cellules solaires à base de pérovskite sont considérées comme cellules de nouvelles génération, les cristaux de pérovskite jouent le rôle de matériaux photo-générateurs de charges avec des éléments organiques et inorganiques plus communément appelés « perovskite hybride halogéné » (ABX_3 avec avec A la partie organique, B la partie inorganique et X un halogène). De plus, ce sont des matériaux à faible coût et simple à élaborer ce qui présente un avantage majeur pour ce genre de cellule.
Il existe différents types de cellules à base perovskite (PSC) avec différentes architectures. Ce travail porte plus particulièrement sur la configuration de PSC dite « monolithique » qui est composée de différentes couches poreuses, dont le TiO_2 déposé à partir de pâtes commerciales par « screen-printing » dans lesquelles s'infiltrent les cristaux de perovskite. Dans cette cellule le graphite (type p) est utilisé comme cathode tandis que le FTO (Fluorine Tin Oxide, type n) sur verre est utilisé comme anode.
Le but est d'obtenir une couche TiO_2 avec un volume poreux plus important par rapport à celui réalisé par voie commerciale, afin d'augmenter la quantité de matériaux photo-actifs qui s'y infiltre et d'atteindre ainsi un rendement supérieur. En effet, jusqu'à environ 13 % a été obtenu pour les cellules optimisées avec la nouvelle configuration de couche poreuse de TiO_2 obtenue par moulage de billes contre 8 % pour les cellules références (couche poreuse élaboré par voie commerciale).

Mot-clés : cellule solaire pérovskite, couche poreuse TiO_2, billes de polymères, voie sol-gel

Résumé en anglais

The perovskite based solar cells is a new generation solar cell type, the perovskite crystals act as photo-charge-generating materials with organic and inorganic elements more commonly referred to as "halide hybrid perovskite" (ABX_3 with A the organic part, B the inorganic part and X an halogen). In addition, they are low-cost materials that are easy to develop, which is a major advantage for this type of cell. There are different types of perovskite-based solar cells (PSC) with different designs. This work focuses on the so-called "monolithic" PSC configuration, which is composed of different porous layers; including TiO_2 deposited from commercial pastes by "screen-printing" technique into perovskite crystals infiltrate. In this cell graphite (p type) is used as cathode while FTO (Fluorine Tin Oxide, n type) on glass is used as anode.
The aim is to obtain a TiO_2 layer with a higher porous volume with respect to the one done commercially, so the quantity of photo-active materials that infiltrates it can be increased and in this sense higher efficiency could be reached. Indeed, up to 13 % has been obtained for the optimized cells with the new configuration of porous TiO_2 layer obtained by bead molding in comparison with a 8 % for reference cells (commercially produced porous layer).

Keywords: perovskites solar cells, TiO_2 porous layer, polymer beads, sol-gel method